FREE ELECTRON QUANTUM OPTICS

Research Thesis

Submitted in partial fulfillment of the requirements for the degree of Doctor of Philosophy

Ron Ruimy

Submitted to the Senate of the Technion – Israel Institute of Technology

Av 5785 August 2026 Haifa

The Research Thesis Was Done in the Faculty of Electrical and Computer Engineering Under The Supervision of Prof. Ido Kaminer.

Ethics Declaration

The author of this thesis states that the research, including the collection, processing and presentation of data, addressing and comparing to previous research, etc., was done entirely in an honest way, as expected from scientific research that is conducted according to the ethical standards of the academic world. Also, reporting the research and its results in this thesis was done in an honest and complete manner, according to the same standards.

Acknowledgments & Financial Support

The generous financial help of the ADAMS foundation and the Technion is gratefully acknowledged.

List of Publications

1. R. Ruimy†, A. Gorlach†, C. Mechel, N. Rivera, I. Kaminer. "Toward atomic-resolution quantum measurements with coherently shaped free electrons". *Physical Review Letters*. 126, 233403 (2021).

2. G. Baranes, R. Ruimy, A. Gorlach, I. Kaminer. "Free electrons can induce entanglement between photons". *npj Quantum Information*. 8, 1-9 (2022).

3. R. Shiloh, Y. Adiv, A. Arie, D. Black, R. Byer, J. England, P. Hommelhoff, T. Hughes, I. Kaminer, A. Karnieli, K. Leedle, P. Musumeci, R. Ruimy, N. Schonenberger, Z. Zhao. "Miniature light-driven nanophotonic electron acceleration and control". *Advances in Optics and Photonics*. 14, 862 (2022).

4. R. Ruimy†, A. Gorlach†, G. Baranes, I. Kaminer. "Superradiant Electron Energy Loss Spectroscopy". *Nano Letters*. 23, 3, 779 (2023).

5. R. Dahan†, G. Baranes†, A. Gorlach, R. Ruimy, N. Rivera, I. Kaminer. "Creation of optical cat and GKP states using shaped free electrons". *Physical Review X*. 13, 031001 (2023).

6. G. Baranes†, S. Even-Haim†, R. Ruimy†, A. Gorlach, R. Dahan, A. A. Diringer, S. Hacohen-Gourgy, I. Kaminer. "Free-electron interactions with photonic GKP states: Universal control and quantum error correction". *Physical Review Research*. 5, 043271 (2023).

7. T. Bucher†, R. Ruimy†, S. Tsesses, R. Dahan, G. Bartal, G. M. Vanacore, I. Kaminer. "Free-electron Ramsey-type interferometry for enhanced amplitude and phase imaging of nearfields". *Science Advances*. 9, adi5729 (2023).

8. A. Gorlach†, O. Reinhardt†, A. Pizzi, R. Ruimy, G. Baranes, N. Rivera, I. Kaminer. "Double-superradiant cathodoluminescence". *Physical Review A*. 109, 023722 (2024).

9. N. Gutman, A. Gorlach, O. Tziperman, R. Ruimy, I. Kaminer. "Universal control of symmetric states using spin squeezing". *Physical Review X*. 132, 153601 (2024).

10. T. Bucher†, H. Nahari†, H. H. Sheinfux†, R. Ruimy†, A. Niedermayr, R. Dahan, Q. Yan, Y. Adiv, M. Yannai, J. Chen, Y. Kurman, S. T. Park, D. J. Masiel, E. Janzen, J. H. Edgar, F. Carbone, G. Bartal, S. Tsesses, F. H. Koppens, G. M. Vanacore, I. Kaminer. "Coherently amplified ultrafast imaging using a free-electron interferometer". *Nature Photonics*. 18, 809 (2024).

11. R. Ruimy†, O. Tziperman†, A. Gorlach, K. Mølmer, I. Kaminer. "Many-body entanglement via 'which-path' information". *npj Quantum Information*. 10, 121 (2024).

12. M. Yannai†, M. Haller†, R. Ruimy†, A. Gorlach, N. Rivera, D. N. Basov, I. Kaminer. "Opportunities in nanoscale probing of laser-driven phase transitions". *Nature Physics*. 20, 1383 (2024).

13. S. Hazanov, A. Gorlach, R. Ruimy, D. Yakushevskiy, M. E. Tzur, M. F. Ciappina, I. Kaminer. "High Interharmonic Generation from Isolated Bound States". *ACS Photonics*. 12, 2440 (2025).

14. A. Balanov, R. Ruimy, I. Kaminer. "Toward high-gain laser-driven electron undulators". *Optica*. 12, 360 (2025).

15. O. Tziperman, G. Baranes, A. Gorlach, R. Ruimy, C. Mechel, M. Faran, N. Gutman, A. Pizzi, I. Kaminer. "Nonlinear Quantum Light Generation in Collective Spontaneous Emission". *ACS Nano*. 19, 21260 (2025).

16. R. Ruimy†, A. Karnieli†, I. Kaminer. "Free-electron quantum optics". *Nature Physics*. 21, 193 (2025).

17. F. J. García de Abajo, A. Polman, C. I. Velasco, M. Kociak, L. H. G. Tizei, O. Stéphan, S. Meuret, T. Sannomiya, K. Akiba, Y. Auad, A. Feist, C. Ropers, P. Baum, J. H. Gaida, M. Sivis, H. Lourenço-Martins, L. Serafini, J. Verbeeck, B. M. Ferrari, C. J. R. Duncan, M. G. Bravi, I. Ostroman, G. M. Vanacore, A. Konečná, N. Talebi, E. Nussinson, R. Ruimy, Y. Adiv, A. Niedermayr, I. Kaminer, V. D. Giulio, O. Kfir, Z. Zhao, R. Shiloh, Y. Morimoto, M. Kozák, P. Hommelhoff, F. Barantani, F. Carbone, F. Chahshouri, W. Albrecht, S. Rey, T. Coenen, E. Kieft, H. L. L. Robert, F. de Jong, M. Solà-Garcia. "Roadmap for Quantum Nanophotonics with Free Electrons". *ACS Photonics*. 12, 4760 (2025).

18. S. Even-Haim, A. A. Diringer, R. Ruimy, G. Baranes, A. Gorlach, S. Hacohen-Gourgy, Ido. Kaminer "Generalized Conditional Displacement". *Quantum*. 9, 1934 (2025).

19. O. Tziperman, D. Nabben, R. Ruimy, J. Holder, E. Nussinson, Y. Fang, A. Gorlach, D. Kazenwadel, A. Karnieli, I. Kaminer, P. Baum. "Two-electron quantum walks can probe entanglement and decoherence in an electron microscope". *Nature Physics*. 22, 763–769 (2026).

20. T. Bucher†, A. Gorlach†, A. Niedermayr, Q. Yan, H. Nahari, K. Wang, R. Ruimy, Y. Adiv, M. Yannai, T. Lenkiewicz Abudi, E. Janzen, C. Spaegele, C. Roques-Carmes, J. Edgar, F. Koppens, G. Vanacore, H. H. Sheinfux, S. T., Ido Kaminer. "Superluminal Correlations in Ensembles of Optical Phase Singularities". Nature *Nature.* 651, 920–926 (2026).

Works in progress

1. T. Shpiro, R. Ruimy, Q. Yan, T. Bucher, A. Shultzman, H. H. Sheinfux, I. Kaminer. "Toward Photon-Induced Near-Field Electron Tomography". arXiv:2510.24648.
2. S. Even-Haim†, E. Nussinson†, R. Ben-Maimon, A. Gorlach, R. Ruimy, E. Shahmoon, O. Schwartz, I. Kaminer. "Spin Squeezing in Electron Microscopy". arXiv:2507.09243.
3. R. Ruimy, Z. Zhao, I. Kaminer, A. Karnieli. "Engineering Free-Electron Entanglement via Virtual Cavity-Photon Exchange.

† *These authors contributed equally to this work.*

Conference talks

1. Coherently-Shaped Free Electrons as High-Resolution Probes of Coherence in Quantum Systems, Conference on Lasers and Electro-Optics, San-Jose, California (2021).
2. Superradiant Electron Energy Loss Spectroscopy, Conference on Lasers and Electro-Optics, San-Jose, California (2022).
3. Free-electron entanglement and non-Gaussian photonic states through 'which-path' information, OASIS 8 (2022).
4. Out-Of-Equilibrium Electron Energy Loss Spectroscopy, Conference on Lasers and Electro-Optics, San-Jose, California (2023).
5. Single-electron Single-photon coupling. NanoP, Barcelona, Spain (2023).
6. Creating Entanglement Through a Joint Decay Channel, Conference on Lasers and Electro-Optics, Charlotte, North-Carolina (2024).
7. Two-electron quantum walk, Electron Photons and Plasmons, Nyon, Swiss (2024).
8. Two-electron quantum walk, Conference on Lasers and Electro-Optics Europe, Munich, Germany (2025).

Contents

List of Figures

Abstract **1**

List of Abbreviations **2**

1 Introduction **3**
1.1 The Dual Nature of the Electron: From Vacuum Tubes to Matter Waves 3
1.2 The Second Quantum Revolution and the Ultrafast Era 4
1.3 The Emergence of Free-Electron Quantum Optics 5
1.4 Overview of the Thesis and Original Contributions 8

2 Methodology **11**
2.1 Free-Electron Interactions With Classical Nearfields 11
2.2 Free-Electron Interactions With Bound Quantum Systems 14
2.3 Macroscopic Quantum Electrodynamics (MQED) 18
2.4 Single-Electron QPINEM and the S-Matrix 20
2.5 Multi-Electron QPINEM and the Modified Coulomb Interaction 21

3 First-Author Publications **23**
3.1 Towards Atomic-Resolution Quantum Measurements with Coherently Shaped Free Electrons 24
3.2 Superradiant Electron Energy Loss Spectroscopy 32
3.3 Many-Body Entanglement via 'Which-Path' Information 40

4 Co-First-Author Publications **49**
4.1 Free-Electron Interactions with Photonic GKP States: Universal Control and Quantum Error Correction 50
4.2 Free-Electron Ramsey-Type Interferometry for Enhanced Amplitude and Phase Imaging of Nearfields 58
4.3 Coherently Amplified Ultrafast Imaging Using a Free-Electron Interferometer . . 66

5 Unpublished Works **76**
5.1 Engineering Free-Electron Entanglement via Virtual Cavity-Photon Exchange . . 77
5.2 Additional Theoretical Derivations 88
5.2.1 The Kapitza-Dirac Effect and Stimulated Compton Scattering in the PINEM Formalism 88
5.2.2 Single-Mode Toy Model of Electron-Cavity Interactions 90
5.2.3 Classical vs. Quantum Regimes of Free-Electron Bunching 91
5.2.4 Photon Statistics in Free-Electron Lasers 93
5.2.5 Electrostatic Fields as Vacuum Displacement in QED 95
5.2.6 Quantum Noise Limits and Correlated Electron Imaging 97

5.2.7 Electron Mass Renormalization in a Macroscopic Medium 99

6 Discussion **101**
6.1 The Electron-Matter Edge: From Single Qubits to Macroscopic Ensembles 101
6.2 The Electron-Light Edge: Enhanced Metrology and Quantum State Engineering 102
6.3 Multi-Electron Entanglement 103
6.4 Future Outlook: Experimental Realization and Technological Roadmaps 104
6.5 Broader Impacts: Bridging Quantum Optics and Materials Science 105
6.6 Concluding Remarks 105

References **106**

Section Hebrew

List of Figures

1.1 The triangle of interactions in free-electron quantum optics. 6
1.2 The electron microscope as a quantum-optical lab. 10

3.3 Coherently shaped free electrons as high-resolution probes of coherence in quantum systems. 27
3.4 Extraction of the relaxation (T_1) and decoherence (T_2) times from a sequence of delayed electron energy spectra. 28
3.5 A scheme for measuring the qubit state on the Bloch sphere. 29
3.6 Free-electron-qubit interactions for studying superradiance and mapping the local density of photonic states. 30
3.7 Superradiant electron energy loss spectroscopy (EELS): Systems containing multiemitter correlations that can be investigated using EELS. 33
3.8 Phase-matched interaction between multiple emitters distributed over an extended area and a single electron that mediates their collective interaction. . . . 36
3.9 Extracting the population of the superradiant states from EELS measurements. . 37
3.10 Extracting information about the superradiance dynamics from EELS. 38
3.11 The multi-particle 'which-path' experiment: implementations in double-slit setups, with analog quantum circuit representations. 42
3.12 Quantum correlations in the particles and in the detector. Particle correlations: Comparing the "which-path" variants with classical (a) and quantum (b) detectors. 44
3.13 Implementation of the multi-particle 'which-path' scheme using split-illumination off-axis electron holography. 46
3.14 Implementation of the multi-particle 'which-path' scheme using waveguide-QED with quantum emitters such as atoms in a Λ configuration. 47

4.15 The free-electron-photon interaction as a fundamental building block for quantum information processing 51
4.16 Single-qubit gates induced by the free-electron ancilla. 53
4.17 Creation of multiqubit entanglement using free electrons. 54
4.18 Using flying qubits for the generation of cluster states. 55
4.19 FERI: Leveraging the complex free-electron interaction with confined fields for enhanced imaging. 60
4.20 FERI measurement scheme. 62
4.21 Phase-resolved optimization. 63
4.22 Enhanced nearfield imaging using FERI. 64
4.23 FERI: utilizing electron modulation for coherently amplified imaging of optical near fields. 67
4.24 Time- and phase-resolved imaging of polariton wavepackets. 70
4.25 Intrinsic phonon-polariton properties extracted via FERI: direct measurement of the polariton phase velocity and identification of a vortex–anti-vortex pair. . . . 72
4.26 Prospects of FERI for precision measurements of weak fields, and comparison between classical and quantum regimes. 73

5.27 Conceptual framework of cavity-mediated free-electron entanglement. 79
5.28 Deterministic energy entanglement mediated by optical cavities. 84
5.29 Spatial entanglement and quantum metrology using microwave cavities. 86

Abstract

For over a century, the free electron has driven profound technological revolutions, most notably as the foundational element of the electron microscope. Traditionally treated as a classical point charge or a simple matter wave, the electron has primarily served as a passive probe for structural imaging. However, the recent convergence of ultrafast laser technology and advanced microscopy has birthed the field of free-electron quantum optics. This paradigm shift elevates the free electron to an active, highly tunable quantum resource—a flying quantum entity capable of carrying, processing, and transferring quantum information with atomic spatial resolution and sub-picosecond temporal precision.

This thesis explores the theoretical boundaries and experimental potential of this emerging field by systematically investigating the quantum interactions of free electrons with light, matter, and one another. Utilizing the framework of macroscopic quantum electrodynamics, this work establishes new methodologies to harness coherently shaped electron wavepackets for advanced quantum metrology, many-body spectroscopy, and continuous-variable quantum information processing.

First, the thesis explores the interaction between free electrons and bound quantum systems. It demonstrates that free electrons can act as ultrafast probes to read and write quantum information directly onto atomic-scale qubits, effectively executing coherent quantum logic operations. Scaling this interaction to macroscopic ensembles, a novel spectroscopic framework is introduced, allowing a single grazing electron to simultaneously measure complex many-body dynamics—such as superradiance—that remain strictly inaccessible to conventional optical probes due to diffraction limits.

Second, the research investigates the coherent exchange between free electrons and the quantized electromagnetic field. It shows that free electrons can serve as deterministic tools to generate and manipulate complex, non-classical states of light, including those required for quantum error correction. Furthermore, by exploiting the electron's longitudinal quantum coherence, advanced free-electron interferometry techniques are developed. These interferometric methods coherently amplify the electron's interaction with weak optical near-fields, drastically enhancing the sensitivity and contrast of ultrafast imaging without the need for destructive, high-intensity pump lasers.

Finally, the thesis addresses the fundamental challenge of generating robust multi-electron entanglement. While native Coulomb repulsion between electrons in free space yields purely classical correlations, this work proposes a paradigm shift utilizing engineered nanophotonic environments. We demonstrate how utilizing cavity-mediated interactions enables the generation of strong, controllable entanglement between electrons.

Altogether, the theoretical frameworks and diagnostic techniques developed in this thesis highlight the vast, untapped potential of the free electron, laying the foundation for next-generation quantum-enhanced electron microscopy and establishing the electron microscope as a fully coherent quantum laboratory.

List of Abbreviations

PINEM	Photon-induced near-field electron microscopy
QPINEM	Quantum photon-induced near-field electron microscopy
QED	Quantum electrodynamics
MQED	Macroscopic quantum electrodynamics
cQED	Cavity quantum electrodynamics
EELS	Electron energy-loss spectroscopy
SREELS	Superradiant electron energy-loss spectroscopy
FEBERI	Free-electron–bound-electron resonant interaction
TLS	Two level system
GHZ	Greenberger–Horne–Zeilinger state
GKP	Gottesman–Kitaev–Preskill state
TEM	Transmission electron microscopy
UTEM	Ultrafast transmission electron microscopy
SEM	Scanning electron microscopy
STEM	Scanning transmission electron microscopy
EFTEM	Energy-filtered transmission electron microscopy
CV	Continuous variable
hBN	Hexagonal boron nitride
TDSE	Time-dependent Schrödinger equation
ZLP	Zero-loss peak
FEL	Free-electron laser
LDOS	Local density of states
CL	Cathodoluminescence
SCQD	Site controlled quantum dots
CD	Conditional displacement
FERI	Free-electron Ramsey interferometry
IR	Infrared
MLE	Maximum likelihood estimator
QEC	Quantum error correction
FTQC	Fault tolerant quantum computation

Chapter 1

Introduction

The evolution of the free electron in modern physics is a story of continuous conceptual elevation. From its origins as a classical point charge to its current status as a highly tunable, coherent quantum resource, the free electron has driven technological revolutions for over a century. In recent years, a convergence of ultrafast laser technology, advanced electron microscopy, and quantum information science has birthed the new field of free-electron quantum optics [1]. In this regime, the electron is no longer merely a classical probe; it is a flying quantum entity capable of entangling with light, matter, and other electrons. This thesis explores the boundaries of this emerging field, establishing the theoretical framework and proposing concrete experimental pathways to harness the free electron for advanced quantum metrology, spectroscopy, and quantum information processing.

1.1 The Dual Nature of the Electron: From Vacuum Tubes to Matter Waves

The discovery of the electron by J.J. Thomson in 1897 marked the dawn of subatomic physics [2]. Heated cathodes in vacuum tubes can "strip" the electron from the confining potential of the atom, creating a stream of energetic charged particles which can be guided and manipulated in free-space, the "free-electrons". In its unbound, "free" state, the electron was initially understood entirely through the lens of classical electrodynamics. Propelled and guided by macroscopic electromagnetic fields in vacuum tubes, the free electron became the workhorse of the early 20th century. The ability to manipulate classical electron trajectories catalyzed a technological revolution that birthed modern electronics, radar, microwave ovens, and eventually, high-energy particle accelerators and free-electron lasers [3]. In all of these applications, the electron was treated as a localized point charge, and its radiation was governed by the classical Maxwell equations.

A profound paradigm shift occurred thirty years later. Building upon Louis de Broglie's hypothesis of wave-particle duality [4], George Paget Thomson (J.J. Thomson's son), alongside Clinton Davisson and Lester Germer, experimentally demonstrated the diffraction of electrons [5, 6]. This monumental discovery promoted the free electron from a classical point charge, into a quantum mechanical matter wave.

The realization that electron matter waves could be focused and interfered using magnetic lenses, similarly to ligh waves, led directly to the invention of the electron microscope by Ernst Ruska in 1931 [7]. Because the de Broglie wavelength of high-energy electrons (typically 10-300 keV) is on the order of picometers—orders of magnitude smaller than visible light—the electron microscope shattered the optical diffraction limit. Over the ensuing decades, it became the most powerful analytical tool in the arsenal of biologists, chemists, and materials scientists, enabling

the structural mapping of crystalline structures, complex macromolecules, and viral structures via techniques such as cryo-electron microscopy (Cryo-EM) [8].

1.2 The Second Quantum Revolution and the Ultrafast Era

Concurrent with the maturation of electron microscopy, the theoretical understanding of quantum mechanics deepened significantly. Early debates regarding the nature of quantum superposition and entanglement [9] eventually gave way to Bell's theorem [10] and the realization that quantum correlations are a tangible, exploitable resource. This catalyzed the "second quantum revolution," driving the development of quantum metrology, secure quantum communication, and quantum computing [11]. However, for many years, the primary systems used to explore quantum mechanics were bound atomic systems (such as trapped ions and superconducting qubits), relying on advances in coherent control techniques that utilize coherent laser pulses in order to interogate and manipulate the quantum states of the systems. Such coherent control techniques remained disconnected entirely from the world of free-electron physics.

This disconnect was bridged in 2009 by a revolution in electron microscopy. By successfully integrating ultrafast femtosecond laser pulses into a Transmission Electron Microscope (TEM), Ahmed Zewail and his colleagues invented the Ultrafast Transmission Electron Microscope (UTEM) [12]. The UTEM added a temporal dimension to the unrivaled spatial resolution of the TEM, making it possible to interrogate electron wavefunctions in entirely new ways.

The hallmark discovery of the UTEM was Photon-Induced Near-field Electron Microscopy (PINEM) [12–14]. In the PINEM interaction, the longitudinal wavepacket of the free electron is coherently modulated by the optical near-fields of a nanostructure illuminated by a laser. By exchanging multiple photons with the optical field, the electron's continuous energy spectrum is split into a discrete, highly controllable energy ladder—a Dirac comb separated by the photon energy $\hbar\omega$. This ability to precisely shape the longitudinal and transverse distribution of the electron marked the beginning of a new era of coherent control.

The hallmark discovery of the UTEM was Photon-Induced Near-field Electron Microscopy (PINEM) [12–14]. In the PINEM interaction, the longitudinal wavepacket of the free electron is coherently modulated by the optical near-fields of a nanostructure illuminated by a laser. By exchanging multiple photons with the optical field, the electron's continuous energy spectrum is split into a discrete, highly controllable energy ladder—a Dirac comb separated by the photon energy $\hbar\omega$. This ability to precisely shape the longitudinal distribution of the electron marked the beginning of a new era of coherent control.

Building upon this foundation together with other rapid developments, the subsequent decade witnessed a rapid expansion of wave-shaping techniques, demonstrating that the electron wavepacket possesses multiple internal degrees of freedom that can be isolated and tailored. While PINEM demonstrated control over the longitudinal energy-momentum phase space, parallel efforts revolutionized the control of the electron's transverse spatial coherence. For example, researchers successfully implemented nanoscale holographic masks, biprisms, and programmable phase plates to sculpt the electron's spatial wavefront [15, 16]. This enabled the creation of free-electron vortex beams carrying quantized orbital angular momentum (OAM) [17, 18], paving the way for probing magnetic dichroism and symmetries in localized plasmonic modes with unprecedented spatial resolution [19].

As the tools for manipulating these transverse and longitudinal degrees of freedom matured, the electron microscope evolved from a passive imaging device into a platform for testing fundamental quantum mechanics. Free electrons were utilized to demonstrate matter-wave Talbot interferometry [20], interaction-free measurements (often referred to as quantum seeing-in-the-dark) [21], and the dynamical Aharonov-Bohm effect via ultrafast electron diffraction [22].

Furthermore, techniques originally developed for atomic and optical systems were adapted for electrons, such as free-electron Rabi oscillations [23] and Ramsey-type interferometry [24–26].

These milestones demonstrated that the free electron could be controlled with the same precision historically reserved for photons and bound atomic systems. The electron was no longer merely a semi-classical illuminating wave; it could be treated as a "flying qubit" or "qudit" [27, 28], capable of carrying, processing, and transferring quantum information with atomic spatial resolution and sub-picosecond temporal precision.

1.3 The Emergence of Free-Electron Quantum Optics

Prior to these developments, the field of quantum technologies primarily focused on either: (1) Quantized excitations in matter (dominantly those described as a quantum two-level system or a qubit), (2) Quantized photons (described as a quantum harmonic oscillator), or (3) Composite systems of the two (typically described using the Jaynes-Cummings model [29]).

The realization that the free electron could be controlled with atomic spatial resolution and sub-picosecond temporal precision fundamentally disrupted this binary paradigm. Since the discovery of PINEM, the field has rapidly expanded beyond semi-classical models into the regime of *free-electron quantum optics* [1].

The theoretical and experimental frontiers of this field can be universally understood through what we define as the "triangle of quantum interactions" (Figure 1.1). The vertices of this conceptual triangle consist of:

- **The Photon:** Modeled as a quantum harmonic oscillator, representing the quantized electromagnetic field.
- **The Emitter:** Modeled as a quantum two-level system, representing bound electrons in atoms, molecules, or artificial qubits.
- **The Free Electron:** Modeled as a doubly infinite energy ladder (or quantum rotor), owing to its continuous energy spectrum and ability to exchange discrete quanta via periodic interactions.

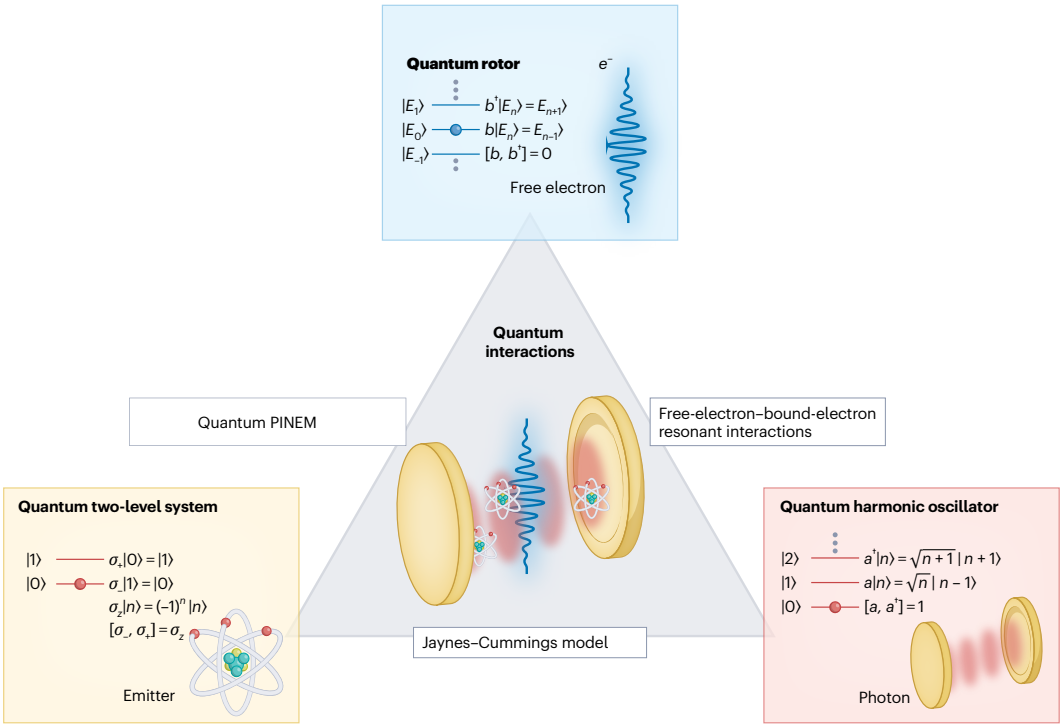


Figure 1.1: The triangle of interactions in free-electron quantum optics. The interactions of the free electron (blue) with the previous building blocks of quantum science—the photon (or generally, harmonic oscillator; red) and the emitter (or generally, two-level system; yellow). These interactions form a triangle, unifying the recent developments in free-electron physics under a single, extended framework of quantum optics. The photon vertex is described by the quantum harmonic oscillator, forming a semi-infinite energy ladder of states $|n\rangle$, where n is an integer. The emitter vertex is described by a quantum two-level system with the states $|0\rangle$ and $|1\rangle$. And finally, the electron vertex is described using a doubly infinite energy ladder known as a quantum rotor. Each edge in the triangle describes an interaction between two of these particles, providing a simple classification of the phenomena arising from their interactions.

The base of this triangle—the interaction between photons and bound emitters—is the well-established domain of cavity quantum electrodynamics (cavity QED). Free-electron quantum optics completes the triangle by activating the remaining edges: the coherent quantum interaction between free electrons and photons (Electron-Light), and the resonant interaction between free electrons and bound-electron emitters (Electron-Matter).

In this thesis, we utilize this foundational triangle to structure our investigation into the quantum nature of the free electron, exploring how to leverage the electron to generate and manipulate quantum light, and how to utilize it as an ultrafast probe for interrogating quantum matter. Finally, we expand upon this framework by introducing multi-electron dynamics—moving beyond the single-electron triangle to target the long-standing challenge of generating entangled free-electrons inside an electron microscope.

Electron-Light Interactions

The interaction between free electrons and photons (right edge of the triangle) has been historically studied via spontaneous emission processes like cathodoluminescence[30] and Cherenkov radiation[31]. However, modern quantum-optical treatments reveal that electron-emitted radi-

ation is not merely classical light. Recent photon-coincidence measurements have shown that the underlying quantum statistics of the light are influenced by the electron's emission regime, demonstrating tunable sub- to super-Poissonian photon bunching [32, 33]. Furthermore, when the electron's initial energy uncertainty is smaller than the emitted photon energy, the spontaneous emission process generates strong electron-photon entanglement [34, 35], fundamentally tying the coherence of the generated light to the quantum state of the emitting particle [36].

In the stimulated regime, the fully quantized PINEM framework has demonstrated that electrons are sensitive to the underlying quantum statistics of the light they interact with [37]. This interaction works both ways: coherently shaped free electrons can act as conditional displacement operators to sculpt the electromagnetic vacuum. Recent proposals and experiments have shown that measuring the electron's energy loss can herald the non-deterministic generation of exact, high-number Fock states [38]. By utilizing shaped electron wavepackets and post-selecting on the electron's final energy parity, researchers have proposed mechanisms to generate complex non-classical light, including photonic cat states and continuous-variable error-correcting codes, such as Gottesman-Kitaev-Preskill (GKP) states [39, 40].

Electron-Matter Interactions

Moving to the left edge of the triangle, free electrons can undergo coherent quantum interactions directly with bound-electron systems, such as atoms, molecules, or quantum dots. Originally proposed as the Free-Electron-Bound-Electron Resonant Interaction (FEBERI) [41], this mechanism allows a free electron passing in the near-field of a quantum emitter to directly drive its transitions.

Unlike conventional electron energy loss spectroscopy (EELS), where excitations are often mediated incoherently via bulk plasmons or phonons, FEBERI relies on direct near-field dipole coupling. The fully quantum formulation of this interaction predicts the generation of hybrid entanglement between the flying electron and the stationary material qubit [42, 43]. While challenging due to inherently weak interaction strengths and fast decoherence rates in solid-state samples, the experimental realization of such interactions is rapidly approaching. In a major milestone toward this goal, recent efforts by the Haslinger group propose the integration of trapped-ion architectures directly into the vacuum chamber of an electron microscope. This active experimental push aims to provide the pristine, isolated two-level systems necessary for the first true physical realization of FEBERI [**haslinger2026**].

Beyond the Triangle: Multi-Electron Dynamics

While the interaction triangle describes the dynamics of a single free electron with its environment, the next major frontier in the field requires moving beyond this framework to consider the interactions between multiple free electrons.

Electrons naturally interact via strong, long-range Coulomb repulsion. Recent experiments utilizing nanotip photoemission have successfully generated energy-correlated multi-electron states, demonstrating tunable sub- and super-Poissonian electron statistics [44, 45]. However, relying on this native free-space interaction to generate usable quantum entanglement has proven exceedingly difficult. Theoretical and experimental diagnostics have recently demonstrated that native Coulomb interactions in free space fundamentally fail to produce measurable electron energy entanglement, resulting instead in purely classical correlations [46]. Overcoming this profound limitation requires moving away from the free-space vacuum and engineering complex nanophotonic environments to artificially mediate and dress the electron-electron interaction.

1.4 Overview of the Thesis and Original Contributions

This thesis seeks to elevate the free electron from a passive classical probe to an active, highly controllable quantum resource. By applying the frameworks of quantum electrodynamics to ultrafast near-field interactions and multi-electron dynamics, we mathematically formalize the missing links in the free-electron quantum optics triangle. The theoretical frameworks and diagnostic techniques developed in this work demonstrate how coherently shaped electrons can be harnessed to push the boundaries of quantum-enhanced electron microscopy, many-body spectroscopy, and continuous-variable quantum information processing.

My original contributions are organized into five primary areas of research:

1. Atomic-Resolution Quantum Measurements via FEBERI

In the first part of this thesis, we explore the theoretical bounds of the Free-Electron-Bound-Electron Resonant Interaction (FEBERI). We demonstrate that a coherently shaped free electron can act as an ultrafast, atomic-resolution probe to read and write quantum information directly onto a two-level bound-electron system. By structuring the longitudinal phase profile of the electron into a Dirac quantum comb, we show that the electron-qubit S-matrix can be engineered to perform operations mathematically equivalent to collective spin rotations (such as the Mølmer-Sørensen gate) on the material qubit [42]. This establishes the free electron as a flying ancilla capable of executing ultrafast quantum logic gates on the atomic scale.

2. Superradiant Electron Energy Loss Spectroscopy (SREELS)

Building upon single-emitter interactions, the second part of this thesis scales the electron-matter interaction to macroscopic atomic ensembles. We introduce Superradiant Electron Energy Loss Spectroscopy (SREELS) [47]. In this paradigm, a single free electron traveling at a grazing angle sequentially interacts with multiple quantum emitters. We demonstrate that the electron effectively acts as a diagnostic tool that simultaneously reads out the collective state of the entire ensemble. By analytically deriving the scattered electron's energy-loss spectrum, we show that the electron can capture complex many-body dynamics, including Dicke superradiance, subradiance, and high-order collective correlations that are strictly inaccessible to conventional photonic probes due to the optical diffraction limit.

3. Creating and Manipulating Quantum Light with Free Electrons

We investigate the use of the free electron as a deterministic source and manipulator of continuous-variable quantum light. Utilizing the generalized quantum PINEM scattering matrix, we present unified strategies for generating quantum superposition states in optical cavities. We outline how post-selection on the electron's final energy state can act as a non-Gaussian operation to generate photonic cat states and continuous-variable error-correcting codes (GKP states) [39]. Furthermore, we see how by manipulating the free-electron wavepackets, they can act as a universal tool to manipulate such error-correcting codes [40].

4. Enhanced Sensing of Optical Fields Using Electron Interferometry

In addition to generating and manipulating quantum states, the coherent control of free electrons opens new frontiers in ultrafast metrology. We leverage the longitudinal quantum coherence of the free electron to develop advanced interferometric sensing techniques. By placing the electron in a coherent superposition of energy states—analogous to a Ramsey interferometer for bound atomic systems—we demonstrate enhanced sensitivity to both the amplitude and phase of optical near-fields. We introduce a coherent amplification mechanism for ultrafast electron microscopy. By utilizing a free-electron interferometer setup, we show that it is possible to coherently amplify the electron's interaction with weak optical fields. This technique significantly improves image contrast and signal-to-noise ratio without requiring high-intensity pump lasers, providing a non-destructive imaging modality for highly sensitive or fragile samples [48]. We experimentally demonstrate this concept using phonon-polariton excitation in hexagonal boron nitride micro-cavities [26].

5. Free-Electron Entanglement and Cavity-Mediated Interactions

Finally, this thesis tackles one of the most fundamental challenges in the field: generating and controlling entanglement between free electrons. We approach this challenge on two distinct fronts.

First, we explore the fundamental role of which-path information and the generation of path entanglement in free-electron interactions [49]. By analyzing the coherent interaction between free electrons and spatially separated quantum systems, we delineate how which-path information is transferred to the environment, and critically, how the interactions can be engineered to induce non-local path entanglement.

Second, we address the generation of robust entanglement between distinct free electrons. Motivated by the recent demonstration that native free-space Coulomb interactions cannot generate energy entanglement [46], we propose a paradigm shift utilizing macroscopic quantum electrodynamics. We develop a theoretical framework for nanophotonic-mediated interactions between paraxial free electrons. By tuning the interaction within a photonic cavity to highly detuned phase-matching conditions, we demonstrate how to suppress real photon emission (environmental decoherence) while maximizing the exchange of virtual photons.

Altogether, the frameworks and applications developed in this thesis highlight the vast, untapped potential of the free electron. By mastering its interactions with light, matter, and the structured vacuum, we pave the way toward a future where the electron microscope serves not only as an imaging device, but as a fully coherent quantum laboratory (Figure 1.2).

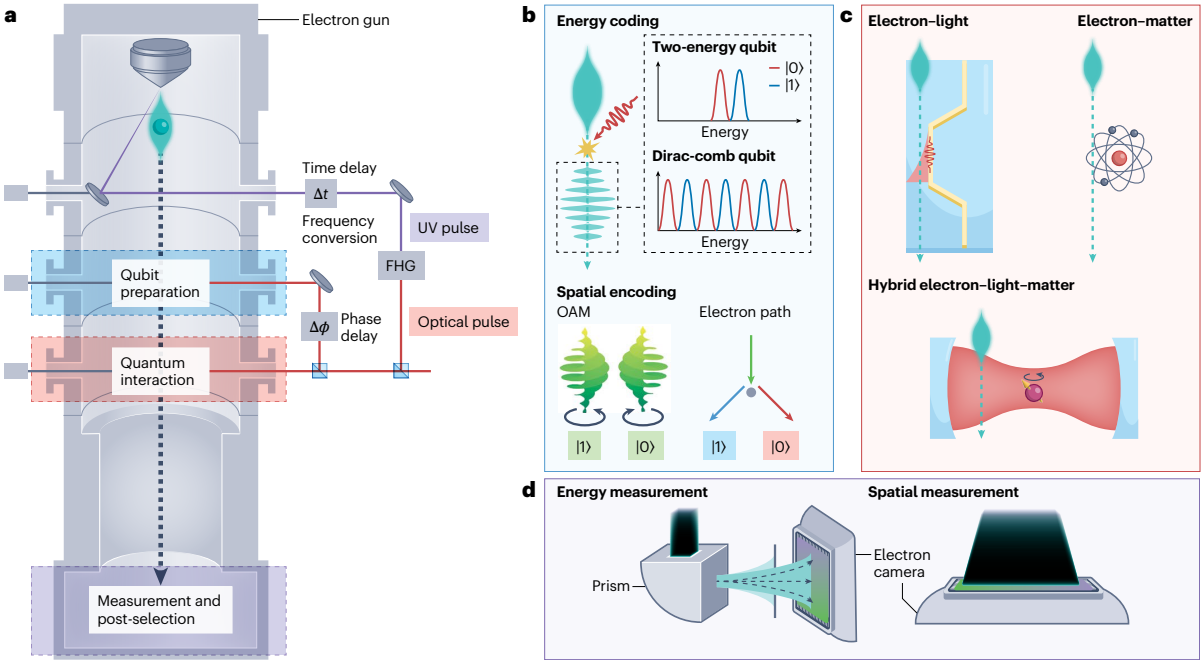


Figure 1.2: The electron microscope as a quantum-optical lab. (a) Advanced electron microscopes, and especially the heavily modified ultrafast electron microscopes, contain the necessary ingredients to become quantum-optical labs. The illustrated microscope contains two interaction points with laser pulses, which have a relative phase delay $\Delta\phi$. It is photoemitted using a shorter-wavelength pulse (denoted UV) generated from the same laser pulse (for example, via fourth-harmonic generation, FHG). Temporal resolution is achieved using a controlled stage for relative time delay Δt. (b) The free electron can encode quantum information on a few different degrees of freedom, including its energy levels, its path in space and its orbital angular momentum (OAM). (c) The electron carrying the quantum information can later coherently interact with light, matter or hybrid light–matter excitations. (d) The quantum information encoded on the electron is then measured by measuring either its energy or its spatial distribution, enabling post-selection and heralding.

Chapter 2

Methodology

In this chapter I derive from first principle the core theory behind all of the works in the PhD. The point is to present a self-contained fully rigorous theoretical framework for the emerging field of free electron quantum optics.

2.1 Free-Electron Interactions With Classical Nearfields

The foundational interaction in free-electron quantum optics is the coherent exchange of energy between a swift electron and illuminated nano-structures, a phenomenon universally recognized as Photon-Induced Near-field Electron Microscopy (PINEM) [12–14]. To establish a theoretical foundation for the phenomena discussed throughout this thesis, we first derive the classical-field PINEM interaction starting from the fundamental relativistic wave equations.

The Paraxial Klein-Gordon Equation

Consider a free electron propagating along the z-axis with a highly relativistic initial momentum p_0 and energy $E_0 = \sqrt{p_0^2c^2 + m_0^2c^4}$. In the presence of an external electromagnetic field described by a classical vector potential $\mathbf{A}(\mathbf{r}, t)$. Since spin-effects are generally negligible in TEM energy, the electron dynamics are to a very good approximation governed by the scalar Klein-Gordon equation (under minimal coupling, $\mathbf{p} \to \mathbf{p} - e\mathbf{A}$):

$$\left[\frac{1}{c^2}\left(i\hbar\frac{\partial}{\partial t}\right)^2 - (-i\hbar\nabla - e\mathbf{A})^2 - m_0^2c^2\right]\psi(\mathbf{r}, t) = 0. \tag{2.1}$$

For a highly energetic electron beam in a standard transmission electron microscope (TEM), the electron momentum is overwhelmingly concentrated along the longitudinal axis ($p_z \approx p_0 \gg p_\perp$). This justifies the *paraxial approximation*. We factor out the unperturbed carrier wave by adopting the ansatz $\psi(\mathbf{r}, t) = \phi(\mathbf{r}, t)e^{i(p_0z - E_0t)/\hbar}$, where $\phi(\mathbf{r}, t)$ is a slowly varying envelope.

Substituting this ansatz into the Klein-Gordon equation and discarding the second-order derivatives of the envelope (the slowly varying envelope approximation), the dispersion relation is effectively linearized around the central momentum ($E \approx E_0 + v_0(p_z - p_0)$, where $v_0 = p_0c^2/E_0$). Assuming the vector potential is predominantly longitudinal ($\mathbf{A} \approx A_z\hat{z}$) and operates in the Lorentz gauge, the wave equation drastically simplifies to the paraxial advection equation:

$$\left(\frac{\partial}{\partial t} + v_0\frac{\partial}{\partial z}\right)\phi(\mathbf{r}, t) = \frac{iev_0}{\hbar}A_z(\mathbf{r}, t)\phi(\mathbf{r}, t). \tag{2.2}$$

The S-Matrix and Bessel Amplitudes

This first-order differential equation can be integrated exactly along the unperturbed classical trajectory of the electron, $z(t) = v_0 t$. If the electron interacts with a monochromatic optical field oscillating at frequency ω, the general solution for the wavepacket after traversing the interaction region is given by the application of a semiclassical scattering matrix $\hat{S}$:

$$\phi_{out} = \hat{S}\phi_{in} = \exp\left[\frac{ie}{\hbar}\int_{-\infty}^{\infty} A_z(x, y, z, t = z/v_0)dz\right]\phi_{in}. \tag{2.3}$$

Because the field is time-harmonic, the integral yields a sinusoidal phase modulation. We define the dimensionless, complex PINEM coupling constant g, which captures the total interaction strength:

$$g(x, y) = \frac{e}{2\hbar\omega}\int_{-\infty}^{\infty} E_z(x, y, z)e^{-i\omega z/v_0}dz = |g|e^{i\chi}. \tag{2.4}$$

The magnitude $|g|$ represents the interaction strength, and χ represents the optical phase evaluated at the electron's arrival time. It is imporant to note that g is simply a fourier transform of the electric field at frequency $k_z = \frac{\omega}{v}$. In free space, the longitudinal wave-vector of a plane wave is given by $\frac{\omega}{c} \cdot cos(\theta)$ where θ is the angle of the plane wave compared to the z-axis. Since $v < c$, $\frac{\omega}{c} \cdot cos(\theta) < \frac{\omega}{c} \cdot < \frac{\omega}{v}$, and so g identically vanishes in free-space. This implies that PINEM interactions cannot happen (for linear interactions) in free space, which is why nearfields are required. The semiclassical S-matrix becomes a pure phase operator, $\hat{S} = \exp[2i|g|\sin(\omega t - \omega z/v_0 + \chi)]$.

Using the Jacobi-Anger expansion, this phase modulation can be decomposed into an infinite sum of discrete harmonics:

$$\psi_{out}(\mathbf{r}, t) = \sum_{n=-\infty}^{\infty} J_n(2|g|)e^{in\chi}e^{i(p_0+n\hbar\omega/v_0)z/\hbar}e^{-i(E_0+n\hbar\omega)t/\hbar}. \tag{2.5}$$

The final state of the electron is a coherent superposition of discrete energy sidebands spaced by $\hbar\omega$, with the transition amplitude to the n-th sideband governed by the Bessel function of the first kind, $J_n(2|g|)$. The probability of absorbing or emitting n photons is $P_n = |J_n(2|g|)|^2$.

Free-Electron Ramsey-Type Interferometry

PINEM interactions are originally suggested as a method to measure the nearfields of samples. By measuring the energy of the interacting electrons, a map of $|g(x, y)|$ can be extracted, however, since the energy distribution of the electrons depend only on $|g(x, y)|$, no phase information about the fields can be extracted. One of the core contributions I had in the field is to use electrons which are premodulated with a fixed reference field before interacting with an unknown optical field. This concept forms the basis of Free-Electron Ramsey-type Interferometry (FERI).

Consider an electron passing through two distinct optical fields separated by a drift region: a known reference field and an unknown sample near-field. Because the interaction Hamiltonian is linear in the vector potential, the total coupling constant is the coherent complex sum of the individual interactions:

$$g_{tot} = g_{ref} + g_{sample}e^{i\theta}, \tag{2.6}$$

where θ accounts for the relative optical phase difference and the accumulated electron time-of-flight between the two interactions.

The resulting final energy spectrum is governed by $P_n = |J_n(2|g_{tot}|)|^2$. Crucially, because $|g_{tot}|^2 = |g_{ref}|^2 + |g_{sample}|^2 + 2|g_{ref}||g_{sample}|\cos(\theta)$, the electron sideband populations oscillate as a function of the relative phase θ. By sweeping the phase of the reference field, the electron spectrum acts as a nanoscale interferometer, providing sensitivity to both the amplitude ($|g_{sample}|$) and the exact local phase of the sample field.

The Role of the Zero-Loss Peak and Coherence Length

In a purely idealized theoretical model, the electron energy state is a Dirac delta function, and the interferometric visibility remains perfect regardless of the drift distance between the two fields. However, practical electron beams possess a finite initial energy spread, characterized by the spectral width of the Zero-Loss Peak (ZLP).

To model this physical reality, the final probability distribution must be integrated over the initial energy distribution $f(E)$ of the electron beam:

$$S(E) = \int f(E - E') \sum_n |J_n(2|g_{tot}(E')|)|^2 \delta(E' - E_0 - n\hbar\omega) dE'. \tag{2.7}$$

The finite ZLP introduces a limitation for spatially separated interactions. Due to vacuum dispersion, electrons with slightly different initial energies travel at slightly different velocities. To quantify this, we Taylor-expand the accumulated phase $\theta(E) = \omega L/v(E)$ around the central energy E_0:

$$\theta(E) \approx \theta(E_0) + \left.\frac{\partial\theta}{\partial E}\right|_{E_0} (E - E_0) = \theta_0 + \frac{\omega L}{m_0\gamma^3 v_0^3}\Delta E. \tag{2.8}$$

Because $|g_{tot}|^2$ depends on $\cos(\theta(E))$, this energy-dependent phase shift leads to a smearing of the interference fringes. Assuming the initial ZLP is a Gaussian distribution with a standard deviation σ_E, integrating the interference term over the energy distribution yields the Fourier transform of the Gaussian. The coherent cross-term is exponentially suppressed:

$$\langle\cos(\theta)\rangle = \cos(\theta_0)\exp\left(-\frac{1}{2}\left(\frac{\omega\sigma_E L}{m_0\gamma^3 v_0^3}\right)^2\right) \equiv \cos(\theta_0)\exp\left(-\frac{L^2}{2L_c^2}\right). \tag{2.9}$$

This derivation formally defines the longitudinal coherence length of the electron wavepacket, $L_c = \frac{m_0\gamma^3 v_0^3}{\omega\sigma_E}$. When the drift distance L approaches L_c, the arrival-time jitter washes out the relative phase, leading to total decoherence of the interferometric signal.

Extracting the Signal: The Energy Gain Measurement

To practically extract the sample field parameters from this smeared spectrum, one must select a robust experimental observable. In standard transmission electron microscopy, the zero-loss peak (ZLP) and the energy-loss sidebands ($n < 0$) are often heavily contaminated by sample-induced inelastic background scattering (e.g., bulk plasmons and phonon excitations). Therefore, the cleanest and most reliable signal is the total electron *energy gain*, obtained by integrating only the positive energy sidebands ($n > 0$).

Due to the unitarity of the S-matrix and the symmetry of the Bessel functions ($J_{-n}(x) = (-1)^n J_n(x)$), the total probability of an electron gaining energy from the optical field is analytically tied to the zeroth-order Bessel function:

$$P_{gain}(\theta_0) = \sum_{n=1}^{\infty} P_n = \frac{1 - P_0}{2} \approx \frac{1 - J_0^2(2|g_{tot}|)}{2}. \tag{2.10}$$

(where the approximation holds in the highly coherent regime, $L \ll L_c$, where phase smearing is negligible).

In a standard single-interaction PINEM experiment, the energy gain induced by a weak sample field ($|g_{sample}| \ll 1$) scales quadratically, $P_{gain} \propto |g_{sample}|^2$, making it practically undetectable against classical background noise. However, in the interferometric scheme, the reference field acts as a local oscillator. Expanding the total coupling constant to first order

in $|g_{sample}|$, we find $|g_{tot}| \approx |g_{ref}| + |g_{sample}|\cos(\theta_0)$. The resulting change in the energy gain signal becomes strictly linear with respect to the weak sample field:

$$\Delta P_{gain} \approx \frac{\partial P_{gain}}{\partial |g_{tot}|} |g_{sample}| \cos(\theta_0) = 2J_0(2|g_{ref}|)J_1(2|g_{ref}|)|g_{sample}|\cos(\theta_0). \tag{2.11}$$

This linear cross-term demonstrates that the sensitivity of the measurement is entirely dictated by the amplitude of the reference field. The signal-to-noise ratio is analytically maximized when the reference amplitude $|g_{ref}|$ is tuned to the global maximum of the derivative term $J_0(2|g_{ref}|)J_1(2|g_{ref}|)$ (which occurs at approximately $|g_{ref}| \approx 0.54$).

2.2 Free-Electron Interactions With Bound Quantum Systems

While the PINEM formalism describes the modulation of a free electron by an external, classical field, we are interested to understand how electron interact with quantum systems. The simple quantum system to considered, is a quantum emitter interacting with the electron trough dipole interactions.

Free-Electron Bound-Electron Resonant Interaction (FEBERI)

To describe the scattering of a swift electron by a single localized emitter, we model the emitter as a two-level system (TLS) with a ground state $|g\rangle$, an excited state $|e\rangle$, and a transition frequency ω_0.

Assuming the electron is relativistic and its energy loss is negligible compared to its initial kinetic energy ($E_0 \gg \hbar\omega_0$), we maintain the paraxial approximation. The electron moves along a deterministic classical trajectory $\mathbf{r}_e(t) = \mathbf{b} + \mathbf{v}t$, where $\mathbf{b}$ is the transverse impact parameter and $\mathbf{v} = v\hat{z}$ is the electron velocity. In the non-retarded (near-field) limit, the moving electron generates a localized, transient electric field $\mathbf{E}_{el}(\mathbf{r}, t)$ evaluated at the position of the TLS ($\mathbf{r}_0$).

The unperturbed Hamiltonian of the combined system is $H_0 = v\hat{p}_z + \frac{1}{2}\hbar\omega_0\hat{\sigma}_z$, where $\hat{\sigma}_z$ is the Pauli z-matrix. Under the dipole approximation, the interaction Hamiltonian is given by:

Using the Liénard-Wiechert potentials for a relativistically moving point charge, the time-dependent electric field evaluated at the position of the TLS is strongly peaked around the time of closest approach ($t = 0$). The transverse and longitudinal field components are:

$$E_x(t) = \frac{-e\gamma b}{4\pi\varepsilon_0(b^2 + \gamma^2 v^2 t^2)^{3/2}}, \tag{2.12}$$

$$E_z(t) = \frac{e\gamma v t}{4\pi\varepsilon_0(b^2 + \gamma^2 v^2 t^2)^{3/2}}. \tag{2.13}$$

Notice the distinct temporal symmetries: the transverse field $E_x(t)$ is an even function of time (a symmetric pulse), while the longitudinal field $E_z(t)$ is an odd function (a bipolar transient).

Under the dipole approximation, the interaction Hamiltonian in the interaction picture is given by:

$$H_I(t) = -\left(\mathbf{d}_{eg}\hat{\sigma}_+ e^{i\omega_0 t} + \mathbf{d}_{eg}^*\hat{\sigma}_- e^{-i\omega_0 t}\right) \cdot \mathbf{E}(t), \tag{2.14}$$

where $\mathbf{d}_{eg}$ is the transition dipole moment, and $\hat{\sigma}_\pm$ are the atomic raising and lowering operators. To simplify the time-evolution algebra, we define a time-dependent complex driving parameter:

$$A(t) = -\frac{i}{\hbar}\mathbf{d}_{eg} \cdot \mathbf{E}(t)e^{i\omega_0 t}, \tag{2.15}$$

such that the scaled Hamiltonian is simply $\frac{1}{i\hbar}H_I(t) = A(t)\hat{\sigma}_+ - A^*(t)\hat{\sigma}_-$.

The time-evolution operator for the target system is given by the time-ordered exponential $U = \mathcal{T}\exp\left(\frac{1}{i\hbar}\int H_I(t)dt\right)$. Because the interaction Hamiltonian does not commute with itself at different times, we must evaluate this evolution using the Magnus expansion, $U = \exp(\Omega_1 + \Omega_2 + \ldots)$.

The first-order term (Ω_1) is simply the time integral of the Hamiltonian. This yields the linear Free-Electron Bound-Electron Resonant Interaction (FEBERI) coupling constant:

$$\Omega_1 = \int_{-\infty}^{\infty} \left(A(t)\hat{\sigma}_+ - A^*(t)\hat{\sigma}_-\right) dt = g_{TLS}\hat{\sigma}_+ - g_{TLS}^*\hat{\sigma}_-, \tag{2.16}$$

where g_{TLS} is defined as the Fourier transform of the electron's field evaluated at the transition frequency:

$$g_{TLS}(\mathbf{b}, \omega_0) \equiv \int_{-\infty}^{\infty} A(t)dt = -\frac{i}{\hbar}\int_{-\infty}^{\infty} \mathbf{d}_{eg} \cdot \mathbf{E}(t)e^{i\omega_0 t}dt. \tag{2.17}$$

Substituting the explicit Liénard-Wiechert field components into this integral allows it to be evaluated exactly. The coupling constant is strictly governed by the modified Bessel functions of the second kind:

$$g_{TLS}(\mathbf{b}, \omega_0) = \frac{e\omega_0}{2\pi\varepsilon_0\hbar v^2\gamma}\left[d_x K_1\left(\frac{\omega_0 b}{v\gamma}\right) + \frac{i}{\gamma}d_z K_0\left(\frac{\omega_0 b}{v\gamma}\right)\right]. \tag{2.18}$$

While the first-order term captures the resonant driving, the second-order term (Ω_2) captures the non-linear phase dynamics. It arises strictly from the commutator of the Hamiltonian at different times (t_1 and t_2). Using the standard Pauli commutation relation $[\hat{\sigma}_+, \hat{\sigma}_-] = \hat{\sigma}_z$, we find:

$$\Omega_2 = \frac{1}{2}\int_{-\infty}^{\infty} dt_1 \int_{-\infty}^{t_1} dt_2 \left[H_I(t_1), H_I(t_2)\right] = -i\Phi\hat{\sigma}_z. \tag{2.19}$$

Here, Φ represents the transient AC Stark shift dynamically induced by the near-field of the passing electron:

$$\Phi = -\int_{-\infty}^{\infty} dt_1 \int_{-\infty}^{t_1} dt_2 \mathrm{Im}\left(A(t_1)A^*(t_2)\right). \tag{2.20}$$

Crucially, because the Pauli matrices form a closed algebra, any higher-order nested commutators in the Magnus expansion evaluate strictly to linear combinations of $\hat{\sigma}_+$, $\hat{\sigma}_-$, and $\hat{\sigma}_z$. Therefore, the analytical scattering matrix for the two-level system takes the *exact* form of a detuned Rabi rotation across all orders of interaction:

$$\hat{S} = \exp\left(\tilde{g}\hat{\sigma}_+ - \tilde{g}^*\hat{\sigma}_- - i\tilde{\Phi}\hat{\sigma}_z\right). \tag{2.21}$$

Here, the fully renormalized coupling constant $\tilde{g} = g_{TLS} + \mathcal{O}(|E|^3)$ and the fully renormalized dynamic detuning $\tilde{\Phi} = \Phi + \mathcal{O}(|E|^4)$ absorb all higher-order mathematical corrections. Truncating the Magnus expansion simply isolates their leading physical contributions: the linear geometric drive (g_{TLS}) and the primary transient AC Stark shift (Φ). In typical cases, $g_{TLS} \ll 1$ and we can write a simplified version of the scattering matrix:

$$\hat{S} = \exp\left(g_{TLS}\hat{\sigma}_+ - g_{TLS}^*\hat{\sigma}_-\right). \tag{2.22}$$

This formalism encapsulates the interaction between free-electron and quantum emitters in a simple operator-level terminology, and lay the basis for the investigation of free-electron manipulation and interrogation of quantum emitters.

Qubit Tomography, and Coherent Qubit Driving

When we single quantum modulated free electron wavepackets, the interaction of free-electrons with such bound quantum system drastically change. By pre-modulating the electron using an optical laser (via the standard PINEM interaction), the electron wavepacket is cast into a coherent superposition of discrete energy sidebands, $|\psi_e\rangle = \sum_n c_n |E_0 + n\hbar\omega_0\rangle$.

To mathematically formalize this, we define the electron energy-lowering operator, $\hat{b} = \sum_n |E_{n-1}\rangle\langle E_n|$, which annihilates a quantum of energy from the electron. For a continuous, unmodulated electron beam, the state is approximated by a delta function on the energy basis, yielding a zero expectation value ($\langle\hat{b}\rangle = 0$). However, for a PINEM-modulated electron combined with free-space propagation, the wavepacket can possess a non-zero quantum bunching factor:

$$b \equiv \langle\psi_e|\hat{b}|\psi_e\rangle = \sum_n c_n^* c_{n-1} \neq 0. \tag{2.23}$$

Physically, b represents the off-diagonal coherence of the electron's density matrix.

By transitioning to the joint energy basis, the effective interaction Hamiltonian between the quantum electron and the two-level system (TLS) under the rotating wave approximation becomes a pure exchange of excitations:

$$H_{eff} = g_{TLS}\hat{\sigma}_+\hat{b} + g_{TLS}^*\hat{\sigma}_-\hat{b}^\dagger, \tag{2.24}$$

where $\hat{\sigma}_\pm$ are the raising/lowering operators of the target qubit. This fully quantized Hamiltonian fundamentally alters the scattering dynamics, giving rise to two distinct physical consequences:

1. Extraction of Off-Diagonal Qubit Coherence

Consider a target qubit prepared in an arbitrary mixed state, characterized by a density matrix ρ_q with a non-zero off-diagonal coherence $\rho_{eg} = \langle e|\rho_q|g\rangle$. If we probe this qubit with a pre-bunched electron ($\langle\hat{b}\rangle = b$). We can calculate the energy transfer between the emitter and the electron (to first order in g) and get:

$$\Delta P_e \approx i\left(g_{TLS} b\rho_{eg} - g_{TLS}^* b^* \rho_{ge}\right) = -2\mathrm{Im}(g_{TLS} b\rho_{eg}). \tag{2.25}$$

For an unbunched electron ($b = 0$), the linear term vanishes, and the transition relies entirely on the second-order standard EELS probability ($|g_{TLS}|^2$). However, because the bunched electron possesses a defined phase, the energy transfer is directly proportional to the off-diagonal element ρ_{eg}. Thus, by measuring the energy loss/gain spectrum of a pre-bunched free electron, one effectively performs Quantum State Tomography on the target—extracting not just population levels, but the exact quantum phase of the atomic qubit.

2. Quadratic Superradiant Excitation Scaling

Furthermore, this quantum bunching dictates the macroscopic scaling when the target is driven by a beam of N_e independent, sequential PINEM-modulated electrons. The total electron lowering operator for the beam is the collective sum $\hat{B} = \sum_{j=1}^{N_e} \hat{b}_j$.

If the target qubit is initialized in the ground state ($\rho_{eg} = 0$), the linear cross-term vanishes, and the total excitation probability P_{exc} is governed by the second-order term of the collective Hamiltonian:

$$P_{exc} \approx |g_{TLS}|^2 \langle\hat{B}^\dagger\hat{B}\rangle = |g_{TLS}|^2 \sum_{i=1}^{N_e}\sum_{j=1}^{N_e}\langle\hat{b}_i^\dagger\hat{b}_j\rangle. \tag{2.26}$$

Because the electrons are independent, the expectation value of the cross terms factors out ($\langle\hat{b}_i^\dagger\hat{b}_j\rangle = b^*b = |b|^2$ for $i \neq j$). Separating the diagonal terms ($i = j$, where $\langle\hat{b}_i^\dagger\hat{b}_i\rangle \approx 1$) from the off-diagonal terms yields the exact scaling law:

$$P_{exc} \approx |g_{TLS}|^2 \left[N_e + N_e(N_e - 1)|b|^2\right]. \tag{2.27}$$

This derivation reveals a superradiant scaling. The N_e term represents the standard incoherent addition of probabilities—the electrons acting as independent particles. However, the presence of the quantum bunching factor ($b \neq 0$) generates an interference term that scales as N_e^2. A beam of N_e bunched electrons acts collectively to superradiantly pump a single atom. After some time, the quantum emitter will decay via spontanous emission, with the intensity of this emission proportional to the population of the excited state. Therefore, quantum emitters excited via bunched electron beams could demonstrate emission quadratic in the electron beam, compared to the typical linear dependence of cathodoluminescence (CL).

Superradiant Electron Scattering and Collective Coherence

While FEBERI governs the interaction with a single, isolated emitter, profound new physics emerges when the free electron interacts with a macroscopic ensemble of N identical emitters. To model this many-body scattering event, the interaction Hamiltonian is extended by summing over all individual atomic dipoles located at positions $\mathbf{r}_j$:

$$H_{int}(t) = -\sum_{j=1}^{N} \left(\mathbf{d}_{eg} \hat{\sigma}_+^{(j)} e^{i\omega_0 t} + \text{h.c.} \right) \cdot \mathbf{E}_{el}(\mathbf{r}_j, t). \tag{2.28}$$

By applying first-order perturbation theory, the total probability of the electron losing a quantum of energy ($\hbar\omega_0$) to the ensemble is dictated by the expectation value of the collective transition operator over the initial state of the material. Crucially, this mathematically separates the total Electron Energy Loss Spectroscopy (EELS) probability into two distinct physical regimes—the diagonal and off-diagonal sums:

$$P_{EELS} = \underbrace{\sum_{j=1}^{N} |g_j|^2 \langle \hat{\sigma}_+^{(j)} \hat{\sigma}_-^{(j)} \rangle}_{\text{Incoherent Scattering } (\propto N)} + \underbrace{\sum_{j \neq k}^{N} g_j g_k^* \langle \hat{\sigma}_+^{(j)} \hat{\sigma}_-^{(k)} \rangle}_{\text{Coherent Scattering } (\propto N^2)}, \tag{2.29}$$

where $g_j \equiv g_{TLS}(\mathbf{r}_j, \omega_0)$ is the local coupling constant between the electron and the j-th emitter.

This equation encapsulates the essence of Superradiant Electron Energy Loss Spectroscopy (SREELS). The first term represents independent, spontaneous scattering; if the atoms are unentangled and possess no mutual phase coherence, the off-diagonal terms vanish, and the energy loss scales linearly with the number of emitters ($P \propto N$).

However, if the ensemble is prepared in a macroscopically entangled state—such as a Dicke superradiant state—the atoms share a collective phase coherence ($\langle \hat{\sigma}_+^{(j)} \hat{\sigma}_-^{(k)} \rangle \neq 0$). Under these conditions, the electron does not scatter off N individual atoms; it scatters off the macroscopic quantum coherence of the entire ensemble, triggering the second term and unleashing a massive, quadratically enhanced transition probability ($P \propto N^2$).

Confined vs. Extended Superradiant Geometries

The exact manifestation of this N^2 superradiant enhancement depends heavily on the spatial geometry of the ensemble relative to the transition wavelength $\lambda_0 = 2\pi c/\omega_0$.

1. The Confined Regime ($V \ll \lambda_0^3$): If the emitters are packed into a deeply sub-wavelength volume, the electron's evanescent field addresses them all with identical amplitude and phase ($g_j \approx g_k$). In this limit, any perfectly symmetric state (the classic Dicke state) maximizes the coherent cross-terms, yielding an unconditional N^2 superradiant burst in the EELS spectrum.

2. The Extended Regime ($V \gtrsim \lambda_0^3$) and Phase-Matching: For realistic macroscopic materials, the ensemble spans distances much larger than the optical wavelength. Here, the

spatial phase of the moving electron becomes critical. Because the electron propagates at a velocity v, its near-field carries a strict longitudinal momentum $q = \omega_0/v$, encoding a deterministic spatial phase into the coupling constant: $g_j \propto e^{iqz_j}$.

Consequently, for extended geometries, the product $g_j g_k^* \propto e^{iq(z_j - z_k)}$ oscillates wildly, washing out the superradiant N^2 scaling for a standard symmetric Dicke state. To recover superradiance, the material must be prepared in a *Timed-Dicke state*—a phased coherent superposition where the macroscopic excitation itself propagates through the material with wavevector k_0:

$$|\psi_{Timed}\rangle = \frac{1}{\sqrt{N}} \sum_{j=1}^{N} e^{-ik_0 z_j} |g_1, g_2, \ldots, e_j, \ldots, g_N\rangle. \tag{2.30}$$

Evaluating the SREELS probability for this extended state yields a coherent interference condition:

$$P_{EELS}^{(coherent)} \propto \sum_{j \neq k} e^{i(q-k_0)(z_j - z_k)}. \tag{2.31}$$

This establishes a fundamental resonance condition for extended macroscopic quantum systems. The N^2 superradiant scaling is only unlocked when the electron's longitudinal momentum perfectly phase-matches the spatial phase of the quantum entanglement ($q = k_0$, or equivalently $v_{electron} = v_{phase}$).

2.3 Macroscopic Quantum Electrodynamics (MQED)

Thus far, the free electron has been treated as a quantum wavepacket interacting with classical optical fields (PINEM) or discrete atomic qubits (FEBERI). However, to rigorously describe the interaction between a free electron and the quantized vacuum of a complex, dispersive, and absorbing nanophotonic environment, we must transcend standard vacuum QED.

The Temporal Gauge and the Classical Green's Tensor

To quantize the electromagnetic field in an arbitrary environment characterized by a complex, frequency-dependent dielectric function $\varepsilon(\mathbf{r}, \omega)$, we begin with the macroscopic Maxwell's equations. We adopt the temporal gauge (Weyl gauge), defined by setting the scalar potential to zero ($\Phi = 0$).

In this gauge, the electric field is strictly determined by the time derivative of the vector potential:

$$\mathbf{E}(\mathbf{r}, t) = -\partial_t \mathbf{A}(\mathbf{r}, t) \implies \mathbf{E}(\mathbf{r}, \omega) = i\omega \mathbf{A}(\mathbf{r}, \omega). \tag{2.32}$$

Consequently, the quantum vector potential operator must satisfy the exact same boundary conditions as the classical electric field. By taking the curl of the magnetic field $\nabla \times \mathbf{B} = -i\frac{\omega}{c^2}\varepsilon(\mathbf{r}, \omega)\mathbf{E} + \mu_0 \mathbf{J}_{\text{noise}}$, we find the field is governed by the classical dyadic electric Green's tensor $\mathbf{G}(\mathbf{r}, \mathbf{r}'; \omega)$, defined as the solution to the macroscopic Helmholtz equation:

$$\left[\nabla \times \nabla \times - \frac{\omega^2}{c^2}\varepsilon(\mathbf{r}, \omega)\right] \mathbf{G}(\mathbf{r}, \mathbf{r}'; \omega) = \mathbf{I}\delta(\mathbf{r} - \mathbf{r}'). \tag{2.33}$$

The Noise-Current Formalism

Because $\varepsilon(\mathbf{r}, \omega)$ is complex, the environment absorbs energy. A standard mode expansion would result in exponentially decaying operators, violating the conservation of the canonical commutation relations over time. To rigorously preserve unitarity, we employ the Gruner-Welsch

noise-current formalism. The dielectric medium is treated as a continuous reservoir of harmonic oscillators, and a continuous bosonic bath acts as a Langevin noise source, balancing the macroscopic dissipation.

We introduce the bosonic noise-current operators $\hat{\mathbf{f}}(\mathbf{s},\omega)$, where $\mathbf{s}$ represents a spatial coordinate within the lossy dielectric volume. These satisfy the standard continuous bosonic commutation relations:

$$[\hat{f}_\mu(\mathbf{s},\omega),\hat{f}_\nu^\dagger(\mathbf{s}',\omega')]=\delta_{\mu\nu}\delta(\mathbf{s}-\mathbf{s}')\delta(\omega-\omega'),\quad [\hat{f}_\mu,\hat{f}_\nu]=0. \tag{2.34}$$

The macroscopic noise current is directly proportional to these bosonic operators and the local absorption:

$$\hat{\mathbf{J}}_{\text{noise}}(\mathbf{r},\omega)=-i\omega\sqrt{\frac{\hbar\varepsilon_0}{\pi}\text{Im}[\varepsilon(\mathbf{r},\omega)]}\hat{\mathbf{f}}(\mathbf{r},\omega). \tag{2.35}$$

The fully quantized electric field is obtained by propagating this source current via the Green's tensor:

$$\hat{\mathbf{E}}(\mathbf{r},\omega)=i\mu_0\omega\int d^3\mathbf{s}\,\mathbf{G}(\mathbf{r},\mathbf{s};\omega)\cdot\hat{\mathbf{J}}_{\text{noise}}(\mathbf{s},\omega). \tag{2.36}$$

Using $\hat{\mathbf{A}}=\hat{\mathbf{E}}/(i\omega)$, the exact time-domain vector potential is constructed as:

$$\hat{\mathbf{A}}(\mathbf{r},t)=\int_0^\infty d\omega\int d^3\mathbf{s}\sum_k\left[\mathbf{A}_k(\mathbf{r},\mathbf{s};\omega)\hat{f}_k(\mathbf{s},\omega)e^{-i\omega t}+\text{h.c.}\right], \tag{2.37}$$

where the mode amplitude $\mathbf{A}_k$ is properly normalized to match the vacuum zero-point energy:

$$\mathbf{A}_k(\mathbf{r},\mathbf{s};\omega)=\sqrt{\frac{\hbar}{\pi\varepsilon_0}}\frac{\omega}{c^2}\sqrt{\text{Im}[\varepsilon(\mathbf{s},\omega)]}\mathbf{G}_k(\mathbf{r},\mathbf{s};\omega). \tag{2.38}$$

Derivation of the Vacuum Auto-Correlation and Field Commutator

To express quantum interactions purely in terms of classical Green's functions, we analytically derive the vacuum auto-correlation function, $\langle 0|\hat{A}_\mu(\mathbf{r},t)\hat{A}_\nu(\mathbf{r}',t')|0\rangle$.

Substituting the vector potential expansion into the expectation value yields a double integral. Because the annihilation operator acts on the vacuum ($\hat{f}|0\rangle=0$), only the normally ordered cross-term survives. Applying the commutation relation collapses the integral over $\mathbf{s}'$ and ω':

$$\langle\hat{A}_\mu(\mathbf{r},t)\hat{A}_\nu(\mathbf{r}',t')\rangle=\frac{\hbar}{\pi\varepsilon_0c^4}\int_0^\infty d\omega\,\omega^2e^{-i\omega(t-t')}\int d^3\mathbf{s}\text{Im}[\varepsilon(\mathbf{s},\omega)]\sum_k G_{\mu k}(\mathbf{r},\mathbf{s};\omega)G^*_{\nu k}(\mathbf{r}',\mathbf{s};\omega). \tag{2.39}$$

We now utilize the fundamental integral identity of the macroscopic dyadic Green's tensor, which physically states that integrating over all localized lossy sources identically reproduces the imaginary part of the total Green's tensor:

$$\frac{\omega^2}{c^2}\int d^3\mathbf{s}\text{Im}[\varepsilon(\mathbf{s},\omega)]\mathbf{G}(\mathbf{r},\mathbf{s};\omega)\cdot\mathbf{G}^*(\mathbf{s},\mathbf{r}';\omega)=\text{Im}[\mathbf{G}(\mathbf{r},\mathbf{r}';\omega)]. \tag{2.40}$$

Substituting this identity collapses the spatial integration entirely, yielding the exact vacuum correlation:

$$\langle\hat{A}_\mu(\mathbf{r},t)\hat{A}_\nu(\mathbf{r}',t')\rangle=\frac{\hbar}{\pi\varepsilon_0c^2}\int_0^\infty d\omega\,e^{-i\omega(t-t')}\text{Im}\left[G_{\mu\nu}(\mathbf{r},\mathbf{r}';\omega)\right]. \tag{2.41}$$

Because the field operators represent an unbroken bosonic algebra, the unequal-time commutator is a strict c-number given by $[\hat{A}_\mu,\hat{A}_\nu]=2i\text{Im}\langle\hat{A}_\mu\hat{A}_\nu\rangle$. Applying Euler's formula gives the fundamental commutator:

$$[\hat{A}_\mu(\mathbf{r},t),\hat{A}_\nu(\mathbf{r}',t')]=-\frac{2i\hbar}{\pi\varepsilon_0c^2}\int_0^\infty d\omega\sin[\omega(t-t')]\text{Im}\left[G_{\mu\nu}(\mathbf{r},\mathbf{r}';\omega)\right]. \tag{2.42}$$

2.4 Single-Electron QPINEM and the S-Matrix

Consider a paraxial electron with initial momentum p_0 propagating along the z-axis with velocity v. In the interaction picture, its trajectory is $\mathbf{r}_e(t) = \mathbf{r}_T + vt\hat{z}$, where $\mathbf{r}_T$ is the transverse coordinate. Under the minimal coupling scheme, the interaction Hamiltonian is:

$$\hat{V}_I(t) = -e\mathbf{v} \cdot \hat{\mathbf{A}}(\mathbf{r}_e(t), t) = -ev\hat{A}_z(\mathbf{r}_e(t), t). \tag{2.43}$$

To find the final state, we evaluate the time-ordered S-matrix: $\hat{S}_1 = \mathcal{T} \exp\left[-\frac{i}{\hbar}\int dt\, \hat{V}_I(t)\right]$. Because the commutator of the Hamiltonian at two different times is a c-number (from Eq. 2.42), the Magnus expansion terminates exactly after the second order:

$$\hat{S}_1 = \exp\Big(\hat{\Omega}_1 + \hat{\Omega}_2\Big). \tag{2.44}$$

This naturally splits the QPINEM interaction into real photon emission ($\hat{\Omega}_1$) and virtual vacuum self-phase ($\hat{\Omega}_2$).

Part I: Real Emission and the Discrete Mode Limit

The first-order term generates linear displacements of the environmental modes:

$$\hat{\Omega}_1 = -\frac{i}{\hbar}\int_{-\infty}^{\infty} \hat{V}_I(t)dt = \frac{iev}{\hbar}\int_{-\infty}^{\infty} \hat{A}_z(\mathbf{r}_e(t), t)dt. \tag{2.45}$$

By integrating the squared norm of the displacement amplitude over all modes k and positions $\mathbf{s}$, we can express the total emission probability. Applying the MQED Green's tensor identity established previously, the spontaneous photon-emission probability density evaluates exactly to:

$$\frac{dP_{\text{em}}}{d\omega} = \frac{e^2v^2}{\pi\hbar\varepsilon_0 c^2}\int_{-\infty}^{\infty} dt \int_{-\infty}^{\infty} dt' e^{-i\omega(t-t')} \text{Im}G_{zz}\left[\mathbf{r}_e(t), \mathbf{r}_e(t'); \omega\right]. \tag{2.46}$$

Real photon emission is governed exclusively by $\text{Im}[G_{zz}]$, representing the Local Density of Optical States (LDOS) sampled along the trajectory.

The Narrow Resonance Limit: This continuous formulation bridges seamlessly to discrete single-mode interactions. In a high-Q lossless cavity ($\text{Im}[\varepsilon] \to 0$), the LDOS condenses into discrete resonance peaks:

$$\text{Im}[G_{zz}(\mathbf{r}, \mathbf{r}'; \omega)] \propto \sum_m E_{z,m}(\mathbf{r}) E^*_{z,m}(\mathbf{r}')\delta(\omega - \omega_m). \tag{2.47}$$

Substituting this delta function collapses the continuous frequency integral. The macroscopic field reduces to discrete bosonic cavity modes ($\hat{a}_m$). Defining an energy ladder operator $\hat{b}$ for the electron state, the first-order Magnus term yields the generalized QPINEM S-matrix:

$$\hat{S}_{QPINEM} = \exp\left(\sum_m g_m \hat{a}^\dagger_m \hat{b} - g^*_m \hat{a}_m \hat{b}^\dagger\right), \tag{2.48}$$

where g_m is the effective coupling constant for the m-th mode.

Part II: The Coherent AB Phase

The second-order term captures the virtual dynamics and non-linear phase accumulation. It is generated by the time-ordered commutator of the interaction Hamiltonian:

$$\hat{\Omega}_2 = -\frac{1}{2\hbar^2}\int_{-\infty}^{\infty} dt \int_{-\infty}^{t} dt' [\hat{V}_I(t), \hat{V}_I(t')] = -\frac{e^2 v^2}{2\hbar^2}\int_{-\infty}^{\infty} dt \int_{-\infty}^{\infty} dt'\, \Theta(t-t')[\hat{A}_z(t), \hat{A}_z(t')]. \quad (2.49)$$

Combining the exact MQED field commutator with the time-ordering domain precisely reconstructs the full retarded Green's tensor in the frequency domain:

$$[\hat{A}_z(\mathbf{r}, t), \hat{A}_z(\mathbf{r}', t')]\Theta(t-t') = -\frac{i\hbar}{\pi\varepsilon_0 c^2}\int_{-\infty}^{\infty} d\omega\, e^{-i\omega(t-t')} G_{zz}(\mathbf{r}, \mathbf{r}'; \omega). \quad (2.50)$$

Substituting this directly back into the Magnus term and changing variables from time to position along the trajectory ($z = vt$, $z' = vt'$), the operator evaluates to:

$$\hat{\Omega}_2 = \frac{ie^2}{4\pi\hbar\varepsilon_0 c^2}\int_{-\infty}^{\infty} d\omega \int_{-\infty}^{\infty} dz \int_{-\infty}^{\infty} dz'\, e^{i\omega(z-z')/v} G_{zz}(\mathbf{r}_T, z; \mathbf{r}_T, z'; \omega). \quad (2.51)$$

To isolate the physical phase, we split the frequency integration into positive and negative domains. By applying the crossing symmetry of the Green's tensor, $G_{zz}(\mathbf{r}, \mathbf{r}'; -\omega) = G^*_{zz}(\mathbf{r}, \mathbf{r}'; \omega)$, the negative-frequency contribution becomes the complex conjugate of the positive-frequency contribution. Their sum exactly yields the real part, resulting in a purely anti-Hermitian operator $\hat{\Omega}_2 \equiv -i\Phi_{\text{self}}$:

$$\Phi_{\text{self}}(\mathbf{r}_T) = -\frac{e^2}{2\pi\hbar\varepsilon_0 c^2}\int_0^{\infty} d\omega \int_{-\infty}^{\infty} dz \int_{-\infty}^{\infty} dz'\, e^{i\omega(z-z')/v} \text{Re}\left[G_{zz}(\mathbf{r}_T, z; \mathbf{r}_T, z'; \omega)\right]. \quad (2.52)$$

While $\text{Im}[G]$ governs irreversible emission, this rigorous derivation proves that $\text{Re}[G]$ governs reversible, virtual photon exchanges. For a coherent superposition of electron trajectories, Φ_{self} manifests as a measurable topological Aharonov-Bohm-like phase shift.

2.5 Multi-Electron QPINEM and the Modified Coulomb Interaction

We generalize the formalism to an ensemble of N paraxial electrons. The macroscopic current operator is a sum over individual trajectories, where each electron j has a transverse coordinate $\mathbf{r}_{Tj}$ and an arrival coordinate z_j:

$$\hat{\mathbf{J}}(\mathbf{r}, t) = -ev\sum_{j=1}^{N} \delta^{(2)}(\mathbf{r}_\perp - \mathbf{r}_{Tj})\delta(z - vt - z_j)\hat{\mathbf{z}}. \quad (2.53)$$

The total interaction Hamiltonian becomes the sum over individual electrons:

$$\hat{V}_I^{(N)}(t) = \sum_{j=1}^{N} \hat{V}_{I,j}(t) = -ev\sum_{j=1}^{N} \hat{A}_z(\mathbf{r}_{Tj}, z_j + vt, t). \quad (2.54)$$

Because the collective Hamiltonian remains linear in the bosonic field, the Magnus expansion once again terminates exactly at the second order: $\hat{S}_N = \exp\left(\hat{\Omega}_1^{(N)} + \hat{\Omega}_2^{(N)}\right)$.

Collective Emission and Decoherence

The first Magnus term ($\hat{\Omega}_1^{(N)} = \sum_j \hat{\Omega}_{1,j}$) represents collective real energy exchange. Expanding its squared norm to find the total emission probability yields diagonal terms and collective cross-terms ($i \neq j$):

$$\frac{dP_{\rm em}^{(N)}}{d\omega} = \sum_{i,j=1}^{N} \frac{e^2 v^2}{\pi\hbar\varepsilon_0 c^2} e^{-i\omega(z_i - z_j)/v} \int_{-\infty}^{\infty} dt \int_{-\infty}^{\infty} dt' e^{-i\omega(t-t')} \mathrm{Im} G_{zz}(\mathbf{r}_{Ti}, t; \mathbf{r}_{Tj}, t'; \omega). \tag{2.55}$$

The cross-terms, governed by $\mathrm{Im}[G_{zz}]$ evaluated between different trajectories, demonstrate that multi-electron superradiance and environmental decoherence are direct consequences of cross-correlations in the MQED vacuum state. The environment effectively traces out electronic coherences when the bunch leaves distinguishable photon states.

The Nanophotonic Modification of the Coulomb Phase

The physical modification to the electron-electron interaction occurs in the second Magnus term:

$$\hat{\Omega}_2^{(N)} = -\frac{1}{2\hbar^2} \sum_{i,j=1}^{N} \int_{-\infty}^{\infty} dt \int_{-\infty}^{t} dt' [\hat{V}_{I,i}(t), \hat{V}_{I,j}(t')]. \tag{2.56}$$

By inserting the field commutator, we see that the interaction depends on the spatial separation between the i-th and j-th electrons:

$$[\hat{V}_{I,i}(t), \hat{V}_{I,j}(t')] = e^2 v^2 [\hat{A}_z(\mathbf{r}_{Ti}, z_i + vt, t), \hat{A}_z(\mathbf{r}_{Tj}, z_j + vt', t')]. \tag{2.57}$$

Applying the exact same time-ordering and frequency-folding procedure used for the single electron, this operator mathematically separates into single-particle self-phases ($i = j$) and a macroscopic coherent pair-phase ($\Phi_{\rm pair}$) generated by the cross terms ($i < j$). For reciprocal structures, the pair-phase evaluates to:

$$\Phi_{\rm pair} = -\frac{e^2}{\pi\hbar\varepsilon_0 c^2} \sum_{i<j} \int_0^{\infty} d\omega \int_{-\infty}^{\infty} dz \int_{-\infty}^{\infty} dz'\, e^{-i\omega(z_i - z_j)/v} \mathrm{Re}\left[G_{zz}(\mathbf{r}_{Ti}, z; \mathbf{r}_{Tj}, z'; \omega)\right]. \tag{2.58}$$

To understand what is this interaction term we look at the free-space limit. In a perfect vacuum, $G_{zz}^{(0)}$ admits no real photon emission for uniformly moving electrons ($v < c$) because phase-matching cannot be met; thus $\mathrm{Im}[G] \to 0$ and $\Omega_1 \to 0$. However, substituting the real part of the free-space retarded Green's tensor into the pair-phase integral analytically recovers the classical Liénard-Wiechert potential. Taking the non-relativistic limit ($\gamma \to 1$), it collapses perfectly into the standard electrostatic Coulomb phase:

$$\Phi_{\rm pair}^{(0)} \xrightarrow{\gamma \to 1} \sum_{i<j} \frac{e^2 T}{4\pi\varepsilon_0 \hbar} \frac{1}{|\mathbf{r}_i - \mathbf{r}_j|}. \tag{2.59}$$

By separating the general Green's tensor into a vacuum component and a scattered material component ($G_{zz} = G_{zz}^{(0)} + G_{zz}^{(\rm sc)}$), we isolate the core mechanism: the real part of the macroscopic Green's tensor mathematically describes how the structured nanophotonic vacuum modifies the long-range Coulomb interaction, providing a dressed, controllable knob for creating strong electron-electron entanglement.

Chapter 3

First-Author Publications

3.1 Towards Atomic-Resolution Quantum Measurements with Coherently Shaped Free Electrons

This section is based on the publication:
Ron Ruimy†, Alexey Gorlach†, Chen Mechel, Nicholas Rivera, and Ido Kaminer.
Physical Review Letters 126, no. 23 (2021): 233403.
† *These authors contributed equally to this work.*

Abstract

Free electrons provide a powerful tool for probing material properties at atomic resolution. Recent advances in ultrafast electron microscopy enable the manipulation of free-electron wave functions using laser pulses. It would be of great importance if one could combine the spatial resolution of electron microscopes with the ability of laser pulses to probe coherent phenomena in quantum systems. To this end, we propose a novel concept that leverages free electrons that are coherently shaped by laser pulses to measure quantum coherence in materials. We develop the quantum theory of interactions between shaped electrons and arbitrary qubit states in materials, and show how the postinteraction electron energy spectrum enables measuring the qubit state (on the Bloch sphere) and the decoherence or relaxation times (T_1/T_2). Finally, we describe how such electrons can detect and quantify superradiance from multiple qubits. Our scheme can be implemented in ultrafast transmission electron microscopes (UTEM), opening the way toward the full characterization of the state of quantum systems at atomic resolution.

Introduction

Electron microscopy and spectroscopy are powerful methods to extract information about quantum emitters such as atoms, molecules, and solids [50]. State-of-the-art techniques include cathodoluminescence (CL) [50–52] and electron energy-loss spectroscopy (EELS) [50, 53, 54], which measure excitation energies, band gaps, and the local density of photonic states (LDOS) [55] with high spatial resolution. However, much information cannot normally be extracted: for example, the quantum state of material excitations, decoherence times (T_2), and generally any information associated with off-diagonal density-matrix elements of quantum systems.

Looking beyond electron microscopy, it is of fundamental interest to determine the quantum information that is exchanged in the interaction of free electrons and quantum emitters. For brevity, we refer to the quantum systems as "qubits," since we focus on a single material excitation that corresponds to a fixed electron transition. In the case of qubits in the optical range, their quantum state and decoherence times can be analyzed using laser-based coherent control [56] and pump-probe laser experiments [57–62]. Yet, the probing of individual qubits in optical experiments has limited spatial resolution set by the optical wavelength: measuring an individual emitter, rather than an ensemble, requires a dilute sample. Dilute ensembles render the acquisition of sufficient signals a substantial challenge. Frequently, high densities of qubits are intrinsic to their fabrication and important for applications [63–65], such as semiconductor quantum dot (SCQD) devices for quantum science and technology [66–68] or applications involving qubit-qubit interactions for quantum gates and quantum information processing [69–71].

The ability to distinguish between homogeneous and inhomogeneous broadening in emitters is highly desired [72]. It is especially important to have ways to measure the decoherence rates

of individual emitters (T_2) and differentiate them from the ensemble collective decoherence rate (T_2^*) that relates to inhomogeneous broadening. Such a distinction is also of technological relevance, e.g., in high color-contrast displays [73]. Usually, in dense emitter ensembles, T_2 can only be measured through indirect techniques such as spin echo, giving the ensemble average of many different T_2 values [74, 75]. These challenges motivate the use of free electrons as highly localized probes that can quantify the quantum properties of individual qubits.

Here we propose a scheme to access coherent quantum information of qubits using coherently shaped free electrons. We show how controlling the incident-shaped electron enables measurement of the qubit state and the extraction of the longitudinal (T_1) and transverse (T_2) relaxation rates of the qubit. Such measurements can be performed using a pump-probe scheme in which the pump is a laser pulse and the probe is the electron. We develop a theory to describe the interaction of electrons with a two-level system characterized by a transition dipole moment, relevant to many types of excitations in different systems (e.g., defect centers and direct band-gap transitions). The results are stronger for larger dipoles, as with excitons in 2D semiconductor heterostructures [76], perovskites [77–79], and Rydberg state atoms [80, 81].

Our work is motivated by advances in ultrafast electron spectroscopy and microscopy [50], especially photon-induced nearfield electron microscopy (PINEM) [12, 14, 23, 82], which demonstrated how femtosecond-pulsed lasers can shape free-electron wave functions transversely [83] and longitudinally [84, 85] (i.e., coherently modulated electrons). These advances reveal various new applications in condensed matter physics, quantum technology, and even nuclear physics. Interestingly, the PINEM theory was recently extended to capture the interaction of free electrons with quantized light [34, 35, 86] revealing new applications such as free-electron entanglement [34].

We propose a method that takes advantage of shaped electrons to extract the coherent state and decoherence rates of qubits. We quantify how this concept can be implemented in electron microscopes using EELS and CL and how it can enhance their signals. These enhancements agree with some of the semiclassical predictions presented in Ref. [41], based on the classical modulation of free electrons. We show how the quantum description goes beyond this theory and provides capabilities that cannot be modeled semiclassically.

Apart from T_2, our scheme can also measure T_1, which provides information about the LDOS. Importantly, T_1 can also be extracted at high spatial resolution using recent advances in time-resolved CL [50, 51]. In comparison, our scheme could provide a femtosecond (and eventually attosecond) temporal resolution. Such short timescales enable probing phenomena such as superradiance [87, 88]. Altogether, our schemes could lead to a full toolbox of high-resolution capabilities for reading and writing arbitrary states of qubits in materials.

Quantum Interaction of Qubits and Free Electrons

We can model the electron-qubit interaction by the Hamiltonian [89]:

$$\mathcal{H} = -i\hbar v\partial_z + \frac{\hbar\omega_0}{2}\sigma_z + \frac{e}{4\pi\epsilon_0}\frac{(d_\perp \cdot r_\perp + d_\parallel z)\sigma_+ + (d_\perp^* \cdot r_\perp + d_\parallel^* z)\sigma_-}{(r_\perp^2 + z^2)^{3/2}} \tag{3.60}$$

where the first two terms describe the Hamiltonians of the electron and the qubit. The average velocity of the electron wave packet is v. The qubit has an energy separation of $\hbar\omega_0$; σ_+, σ_z are Pauli matrices. The third term in Eq. (1) describes the interaction with the transition dipole moment $d = \langle g|er|e\rangle$, with components $d_\parallel = \hat{z}d_z$ and $d_\perp = \hat{x}d_x + \hat{y}d_y$. The distance between the center of the electron wave packet and the center of the qubit (the impact parameter) is $r_\perp$, and the vacuum permittivity is ϵ_0.

The approximations behind Eq. (1) are: (I) Paraxial approximation for the electron is valid since the energy of the electron is much larger than that of the excitation. (II) External

decoherence channels by other material excitations [90], such as Bremsstrahlung radiation [91] and characteristic x-ray [92], occur at probabilities much smaller than unity. Thus, the reduced density matrix of the electron and the qubit (for the excitation of interest) will be the same as if the external channels are not considered at all.

The scattering matrix can be found from the Magnus expansion [93] as:

$$S = e^{-i(g\sigma_+ b + g^* b^+ \sigma_- + \chi\sigma_z)} \tag{3.61}$$

Here, the operators b and b^+ are momentum translation operators for the electron and $b = e^{i\omega_0 z/v}$ [94] (for sufficiently fast electrons, they equivalently describe energy translation); g and χ are the interaction parameters. The interaction strength g is typically small ($|g| \ll 1$) and then can be approximated as:

$$g = \frac{ed_x\omega_0 K_1\left(\frac{\omega_0 r_\perp}{v}\right)}{2\pi\epsilon_0\hbar v^2} + i\frac{ed_z\omega_0 K_0\left(\frac{\omega_0 r_\perp}{v}\right)}{2\pi\epsilon_0\hbar v^2} \tag{3.62}$$

where $K_0(x)$ and $K_1(x)$ are modified Bessel functions of the second kind. The interaction constant χ in Eq. (2) under the approximation of $|g| \ll 1$ can be neglected:

$$S \approx \cos|g| - i\cdot\sin|g|\left(e^{i\phi_g}\sigma_+ b + e^{-i\phi_g}\sigma_- b^+\right) \tag{3.63}$$

where ϕ_g is the phase of the interaction constant g.

Consider a qubit prepared (e.g., by an optical pulse) in a coherent superposition $|\psi\rangle = a_1|g\rangle + a_2|e\rangle$. The qubit undergoes decoherence and relaxation, leading to a density matrix at time t [95]:

$$\rho_a(t) = \begin{pmatrix} 1-|a_2|^2 e^{-t/T_1} & a_1 a_2^* e^{i\omega_0 t} e^{-t/T_2} \\ a_1^* a_2 e^{-i\omega_0 t} e^{-t/T_2} & |a_2|^2 e^{-t/T_1} \end{pmatrix} \tag{3.64}$$

A shaped electron interacts with this qubit. The density matrix after the electron-qubit interaction is $\rho_f = S^\dagger \rho_i S$, where $\rho_i = \rho_a \otimes \rho_e$ and ρ_e are the initial density matrices of the joint system and electron, respectively. We measure the EELS of the postinteraction electron, which provides the diagonal of the electron density matrix after the interaction $tr_{qubit}\rho_f$. This measurement contains information about the off-diagonal terms of Eq. (5) if the initial electron is a superposition of several energies that differ by the qubit energy gap $\hbar\omega_0$. Such shaped electrons can be generated via PINEM.

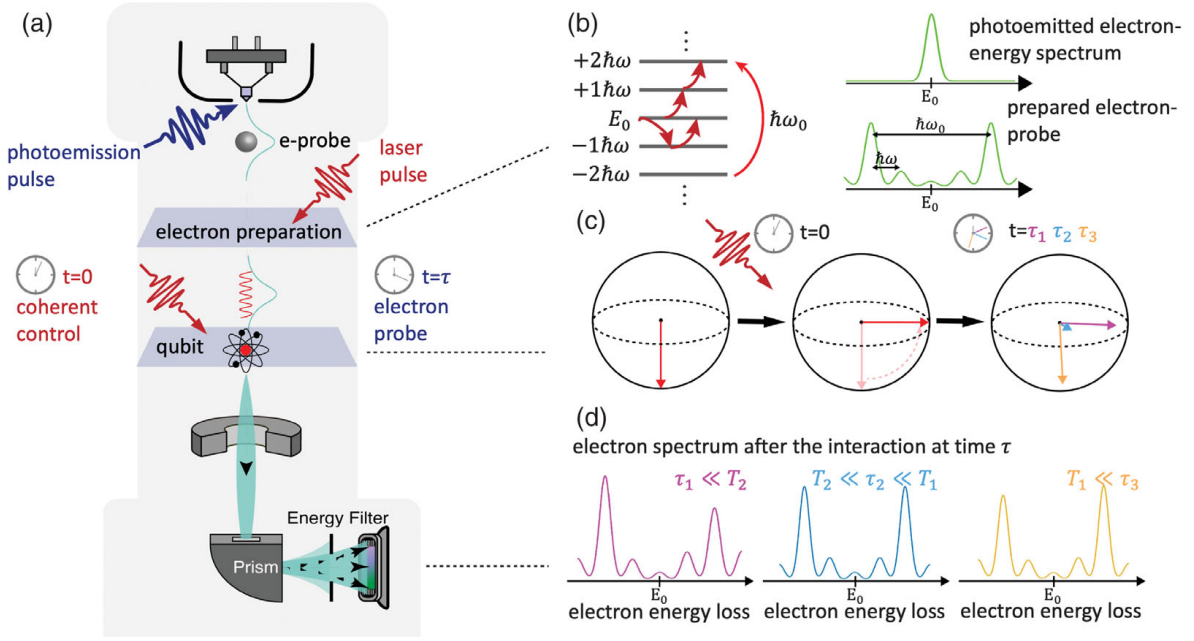


Figure 3.3: Coherently shaped free electrons as high-resolution probes of coherence in quantum systems. (a) An ultrafast transmission electron microscope where (b) electrons are coherently shaped by a PINEM interaction, creating a superposition of energies spaced by integer multiples of the driving laser frequency ω, chosen so the gap between a certain pair of electron energies matches the qubit energy $\hbar\omega_0$. (c) The qubit is excited to $1/\sqrt{2}|g\rangle + i/\sqrt{2}|e\rangle$ and interacts with the electron after time delay τ. (d) The postinteraction electron is measured as a function of τ, using electron energy loss spectroscopy (EELS). This scheme enables measuring different qubit properties, e.g., extracting T_2 from the asymmetry of the spectrum.

Measurement of Relaxation and Decoherence Times

We first consider the interaction of a conventional electron that was not pre-shaped by the laser (i.e., "unshaped electron," or zero-loss peak). The EELS features of unshaped electrons interacting with a qubit are proportional to $|g|^2$. For example, a pump-probe scheme with unshaped electrons can measure T_1. Since in realistic scenarios the coupling constant $|g| \ll 1$ (a typical value is $|g| \sim 10^{-3}$), the qubit features could be very difficult to see.

This problem can be resolved by shaped electrons, for which the interaction creates EELS features that are proportional to $|g|$ instead of to $|g|^2$. Moreover, several qubit properties remain inaccessible for unshaped electrons. One such property is T_2. To probe T_2, we take a superposition electron state of two (or more) different energies. Such electrons lead to interference in the electron-qubit interaction, depending on the phases (in the rotating frame of reference): ϕ_g of the coupling constant, ϕ_e between the relevant electron energies (determined by the modulating laser), and ϕ_a between the excited and ground qubit states. We denote the phase difference by $\Phi = \phi_a - \phi_e - \phi_g$.

The EELS probabilities of electron energy gain P_+ and energy loss P_- depend on the phase difference Φ. Their difference $\Delta P = P_+ - P_-$, to first order in the coupling strength $|g|$, is:

$$\Delta P = (P_+ + P_-)|g|e^{-\tau/T_2}\sin(\Phi) \tag{3.65}$$

The maximal EELS signal is for $\Phi = \pi/2 + \pi\mathbb{Z}$. The maximal contrast can be found without explicit knowledge of $\phi_{a,e}$ by scanning over different electron phases. Repeating this experiment

for different delays enables measuring the decoherence time T_2. We emphasize that T_2 is the individual decoherence time of the given qubit, which usually cannot be measured directly (e.g., in dense ensembles). Only its average over multiple qubits can be found through collective measurement methods such as spin echo [74]. We can also use a broad electron wave function to probe many emitters simultaneously, in which case, the relevant decoherence time will be the typically much smaller collective T_2^* [74].

Equation (6) shows a remarkable quality: interference enables obtaining a net energy gain or loss proportional to $|g|$ rather than to $|g|^2$, which increases the EELS sensitivity. This quality can be exploited in multiple ways. We propose a sensitive T_1 measurement scheme in which a $\pi/2$ pulse is applied immediately before the interaction with the shaped electron. Then, we extract T_1 via a similar scheme.

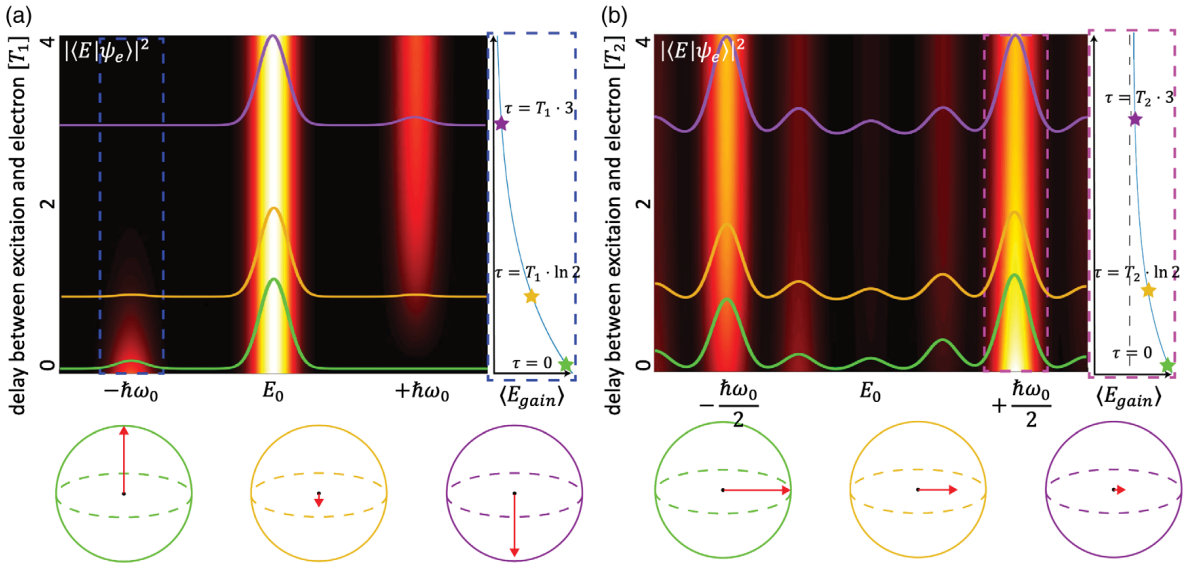


Figure 3.4: Extraction of the relaxation (T_1) and decoherence (T_2) times from a sequence of delayed electron energy spectra. (a) A laser pulse excites the qubit to $|e\rangle$, which then relaxes back. T_1 is extracted from the sequence of electron energy loss spectroscopy (EELS) measurements of unshaped electrons probing the qubit at different delays τ. $\langle E_{gain}\rangle$ is the average energy gain. (b) A laser pulse excites the qubit to $1/\sqrt{2}(|g\rangle + i|e\rangle)$, which then precesses while decohering. T_2 is extracted from the sequence of EELS measurements of shaped electrons probing the qubit at different delays τ.

Finding the Exact Qubit State on the Bloch Sphere

Our method is of particular interest for setting initial conditions or measuring final states in quantum simulators. Thus far, optical tools can control individual qubits only when they are more than a wavelength apart, limiting qubit-qubit interactions and possible experimental platforms for simulators. Shaped-electron probes could enable new quantum simulator platforms, facilitated by the electrons' spatial resolution.

We present a scheme that utilizes shaped electrons for measuring qubit states on the Bloch sphere. Consider a general state $|\psi_a\rangle = \cos(\theta_a/2)|e\rangle + \sin(\theta_a/2)e^{i\phi_a}|g\rangle$, with θ_a and ϕ_a representing the Bloch sphere angles. The qubit interacts with the electron $|\psi_e\rangle = |E_+\rangle + e^{i\phi_e}|E_-\rangle$. The resulting EELS probability difference $\Delta P = P_+ - P_-$, to first order in $|g|$, is given by:

$$\Delta P = (P_+ + P_-)|g|\sin(\theta_a)\sin(\Phi) \tag{3.66}$$

The value of $\sin(\theta_a)$ can be found by repeating the measurement, scanning over ϕ_e until ΔP is maximized, $\Delta P_{max} = (P_+ + P_-)|g| \cdot \sin(\theta_a)$. To remove the ambiguity regarding whether the qubit is located on the lower or upper half of the Bloch sphere [since $\sin(\theta_a)$ is symmetric around $\theta_a = \pi/2$], one can use an additional $\pi/2$ pulse or measure additional electron spectral peaks.

The same scheme can extract additional information, such as the transition dipole moment size [by extracting g from Eq. (3)], and measure the electron phase ϕ_e (by changing ϕ_a).

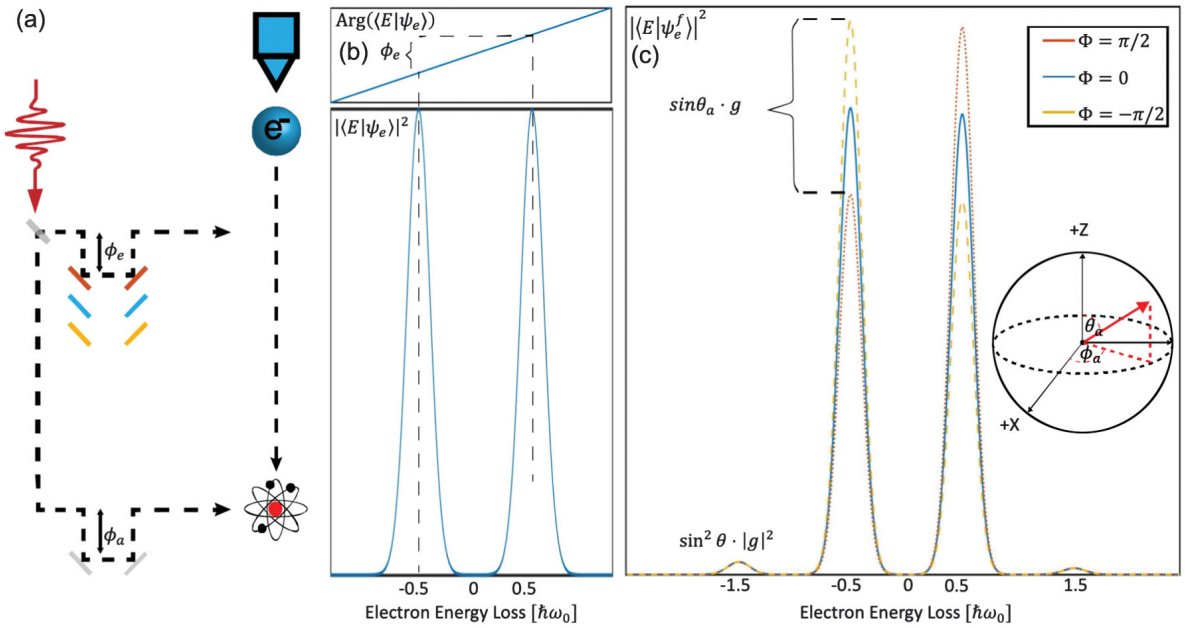


Figure 3.5: A scheme for measuring the qubit state on the Bloch sphere. (a) The electron is coherently shaped by a laser pulse with a tunable optical path length that changes the relative phase ϕ_e between the electron's energy states. The same laser (or another one that is phase-locked) excites the qubit to a state defined by angles θ_a and ϕ_a on the Bloch sphere. (b) The initial electron wave function with relative phase ϕ_e. (c) The resulting EELS spectra for different Φ. We extract the qubit state from the difference between the maximal and minimal EELS peaks.

Probing Superradiance from Multiple Emitters

For qubits with weak nonradiative relaxation, T_1 is related to the qubit's spontaneous emission rate $\gamma = 1/T_1$ influenced by the optical environment through the LDOS. Thus, the shaped-electron-qubit interaction enables measuring the LDOS through a pump-probe scheme. This measurement scheme has a temporal resolution on femtosecond timescales [12, 14, 23, 82, 96, 97], gradually reaching attosecond timescales [82, 98–100].

Consequently, the scheme can be utilized to explore novel emission phenomena on short timescales, such as superradiance, which occurs when a few qubits are bunched together. In superradiance, several excited qubits have a faster emission rate γ than each individual qubit. Our scheme can observe the rapid decay via changes in the EELS peaks. Thus, we can quantify the superradiant decay of any number of emitters. The superradiance implies an enhancement in CL experiments. A different CL enhancement can be created even for a single qubit by using shaped free electrons. The latter corresponds to part of the predictions of a semiclassical theory [41].

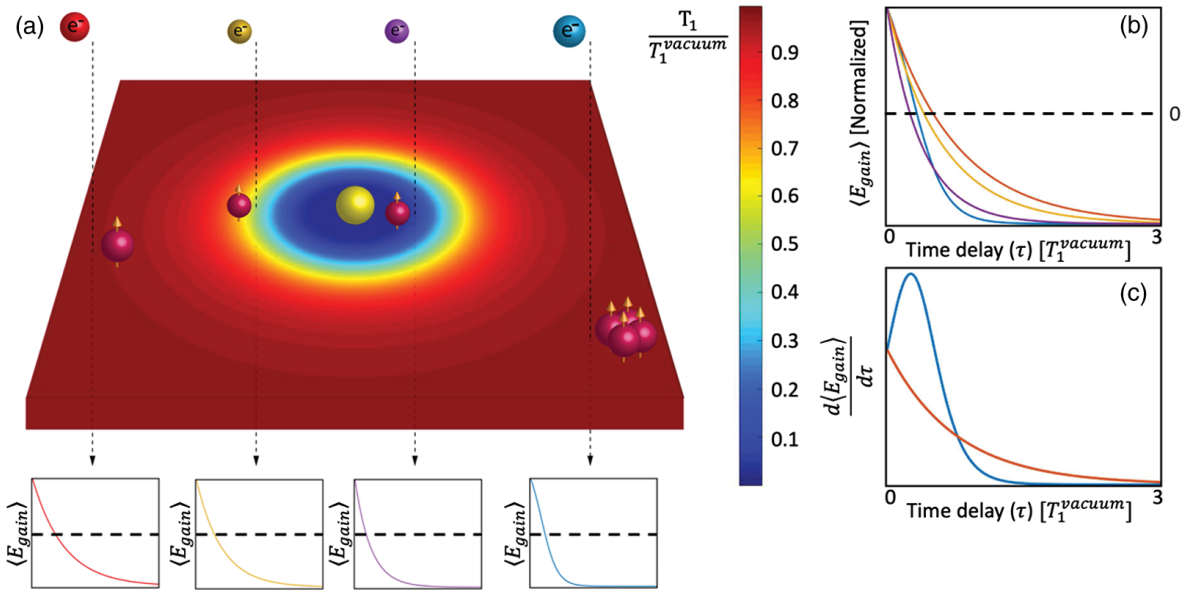


Figure 3.6: Free-electron-qubit interactions for studying superradiance and mapping the local density of photonic states. (a) To exemplify the concept, we place qubits on a membrane surrounding a 10 nm Au nanoparticle, which varies the LDOS and T_1 as a function of position. (b) Comparison of the time decay of normalized $\langle E_{gain} \rangle$ for different qubit positions (the same curves are also shown schematically at the four bottom plots). (c) The emission from a single qubit (orange) vs superradiance from multiple qubits (blue).

Discussion and Outlook

The concepts proposed in our work can be realized in existing materials that have large dipole moments such as perovskite nanocrystals [77–79]. We estimate that temporal resolution of a hundred fs and spatial resolution reaching a single nm is achievable [101, 102], at energy resolution limited by the excitation laser bandwidth (∼10 meV and below [97, 103]). The optimal electron velocity for a transverse dipole is $v \approx (r_\perp \omega_0 / 1.33)$.

For $r_\perp$ smaller than the dipole's size, there could be beyond-dipole corrections to the electron-qubit interaction. Then, the qubit wave function profile cannot be ignored. When the electron spot size is smaller than the qubit, as with SCQDs, we can potentially probe the qubit state and decoherence time as a function of position inside a quantum dot. Such experiments can provide insight into the effects of many-body physics in quantum emitters.

The acquisition of electron spot sizes of a few nanometers opens intriguing possibilities for testing dense ensembles of qubits in systems such as SCQDs [66–68], and for measuring decoherence rates and other quantum properties of individual quantum dots in the ensemble. The combined temporal and spatial resolution can reveal currently unobserved phenomena, such as differences in T_2 of individual qubits in the ensemble and their fluctuations in time. The electron-qubit interaction can also probe the mechanisms differentiating T_2 and T_2^* [74, 75]. High-density SCQDs are of particular interest in areas of quantum technologies, being able to demonstrate fundamental coherent quantum effects such as Rabi oscillations [67, 104], Ramsey fringes, photon echoes, and even quantum coherent revival [105, 106]. Currently, these phenomena are probed optically, which limits researchers' ability to study the properties of single qubits out of a dense ensemble and understand how they vary within the ensemble.

We should also discuss the validity of modeling real materials with a two-level system (qubit)

for interactions with free electrons. Unlike a photon that creates only a single excitation, an electron can set off many material excitations, acting as decoherence channels and becoming entangled with the electron. When the additional excitations are distinct in energy from the qubit energy, one can postselect electrons (using an energy filter) that lose or gain the qubit energy, ensuring that the measured electrons interact with the qubit. This approach is especially accurate in thin samples, where electrons only weakly interact with the decoherence channels. The resulting qubit-electron density matrix is then unchanged by these channels. Future work should further quantify the effect of general decoherence channels on our ability to infer the qubit state from the electron. Looking forward, the determination of material systems that realize the idealized interaction will be a key problem in this field.

From a different perspective, our theory can be seen as a generalization of the well-established EELS theory [30, 107–109] for out-of-equilibrium systems that hold coherence, i.e., described by superposition of different energy states. The standard EELS theory covers a wide variety of interacting systems beyond the two-level system model here. Thus, it will be of great importance to generalize our work to create the unified theory of inelastic electron scattering (or EELS) by general time-dependent out-of-equilibrium systems.

To conclude, we predict that coherently shaped free electrons can determine the qubit state and other quantum characteristics. We envision combining this idea with the proposed methods of coherent control using shaped electrons [41, 110]. Together, they constitute the building blocks to read/write the quantum state of various quantum systems using shaped electrons. Such capabilities, especially if achieved at deep subwavelength and eventually atomic resolutions, are attractive for creating new types of quantum simulators. We envision quantum simulators in which shaped electrons enable the depiction of the initial state of each element and enable reading the final (or intermediate) states using femtosecond (and ultimately attosecond [82, 84, 98–100]) time resolution.

3.2 Superradiant Electron Energy Loss Spectroscopy

This section is based on the publication:
Ron Ruimy†, Alexey Gorlach†, Gefen Baranes, and Ido Kaminer.
Nano Letters 23, no. 3 (2023): 1022-1028.
† These authors contributed equally to this work.

Abstract

We analyze the interaction between a free electron and an ensemble of identical optical emitters. The mutual coherence and correlations between the emitters can enhance the interaction with each electron and become imprinted on its energy spectrum. We present schemes by which such collective interactions can be realized. As a possible application, we investigate free-electron interactions with superradiant systems, showing how electrons can probe the ultrafast population dynamics of superradiance.

Introduction

Electron microscopy and spectroscopy are powerful tools to probe emitters, such as atoms, molecules, vacancy centers, and quantum dots [50–55]. Specifically, electron-based approaches such as cathodoluminescence and electron energy-loss spectroscopy (EELS) can probe excitation energies, atomic bandgaps, the local density of photonic states, and recently even observe phononic phenomena such as vibrational modes in molecules [111]. In all these examples, free-electron probe techniques can provide very high spatial and energy resolutions.

An emerging field of electron microscopy and spectroscopy is imaging the quantum coherence of bound electron systems [42] and even of light [112]. Much theoretical effort in recent years [13, 30, 37, 43, 110, 113–119] investigated the coherent interaction between free electrons and discrete quantum systems with energy gaps and transitions in the optical range. Such interactions have been proposed as a means to measure strong-coupling physics with deep-subwavelength resolution, extract the coherent quantum states of quantum emitters, generate entanglement between them, and even control their quantum state [42]. A key element necessary for these capabilities is the coherent modulation of the free-electron wave function in the time domain, through photon-induced nearfield electron microscopy (PINEM) [12, 14, 23, 82–85, 96, 100]. Such modulated electrons can undergo a coherent resonant interaction with a quantum emitter in a process also called free-electron-bound-electron resonant interaction (FE-BERI) [41] or a quantum klystron in microwave frequencies [110]. So far, due to the intrinsically weak coupling between free electrons and bound electrons [41], experimental realizations of these phenomena have remained beyond reach.

High densities of emitters hold importance for applications [63–65], such as semiconductor quantum dot devices for quantum science and technology [66–68]. High emitter densities are a fundamental aspect of certain light-matter interactions, such as superradiance [87, 88] and superfluorescence [120–123]. Similarly, the existence of multiple emitters interacting with each other is fundamental for quantum information and computation problems, especially ones that involve collective phenomena and correlations between emitters. These kinds of correlations typically occur at the nanometer scale, making it particularly challenging to probe them with optical techniques due to the diffraction limit. Those considerations motivate our proposal to use

free electrons to probe high-density ensembles of emitters, toward the investigation of many-body quantum physics using free-electron probes. However, so far, the coherent interaction between free electrons and ensembles of quantum systems has yet to be described.

Here, we analyze the coherent interaction between free electrons and an ensemble of identical optical emitters (Figure 3.7). The electron interaction can be sensitive to the many-body nature of such an ensemble of emitters, strongly enhanced by multiemitter correlations and mutual coherence. We examine these enhanced interactions for the exemplary case of superradiant dynamics [87, 88], extracting the entire population statistics of the superradiant states using the electrons. These prospects rely on a key realization: that the multiemitter correlations that enable superradiance also enhance their interaction with each free electron. Our work contributes to current efforts toward the investigation of general many-body quantum phenomena using electrons, aiming to achieve simultaneous subnanometer and femtosecond resolution using experimental setups such as ultrafast transmission electron microscopy (UTEM) [12].

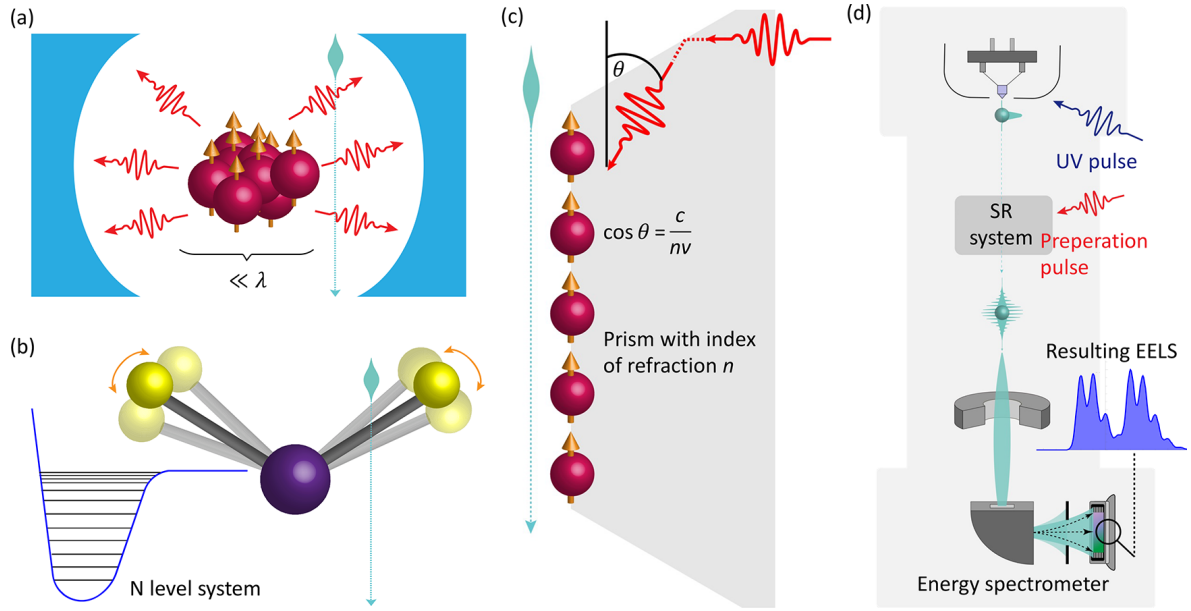


Figure 3.7: Superradiant electron energy loss spectroscopy (EELS): Systems containing multiemitter correlations that can be investigated using EELS. (a) The high density of emitters confined in a small volume compared to the emitted light wavelength can interact superradiantly. (b) Vibrational modes in molecules are often described by anharmonic oscillators, creating effective N-level systems that mimic superradiant phenomena. (c) Identical quantum emitters arranged along a surface can be synchronized to behave superradiantly even when they are relatively far apart, using their joint interaction with a single electron that correlates between them. We propose such a scenario in a grazing-angle configuration and find that it is governed by a Cherenkov-type phase-matching condition. (d) Superradiant EELS can be realized in an ultrafast transmission electron microscope. A pump laser pulse prepares the state of the initial superradiant system, which then interacts with the electron at a delay depicted by a probe pulse. We can extract the state of the superradiant system and its ultrafast dynamics from the EELS measurement.

Theoretical Framework

We model each emitter as a general multilevel system that is small enough to be treated in the dipole approximation. The emitters are coupled to the near-field of the free electron through dipole interaction. The interaction between the emitters is neglected, which is justified when the distance between neighboring emitters is large enough (larger than 5 nm for our characteristic values) or when the interaction is rapid enough to occur before the characteristic decoherence time T_2^* of interemitter interactions.

We calculate the electron-emitters interaction scattering matrix. The i-th emitter is located at position z_i with impact parameter $r_\perp^i$. Each emitter's energy states can be denoted as $|p^i\rangle$, and the energy separation between the states is denoted as $\hbar\omega_i^{pq}$. Assuming paraxiality and weak interaction strength with each individual emitter, the coupling strength between an electron and an emitter is:

$$g_i^{pq} = \frac{ed_{\perp,pq}^i \omega_i^{pq} K_1\left(\frac{\omega_i^{pq} r_\perp^i}{v\gamma}\right)}{2\pi\epsilon_0\gamma\hbar v^2} + i\frac{ed_{z,pq}^i \omega_i^{pq} K_0\left(\frac{\omega_i^{pq} r_\perp^i}{v\gamma}\right)}{2\pi\epsilon_0\gamma^2\hbar v^2} e^{-i\omega_i^{pq} z_i/v} \tag{3.67}$$

Here, v is the average velocity of the electron wavepacket; $d_{pq}^i = \langle p^i|e\mathbf{r}|q^i\rangle$; the vacuum permittivity is ϵ_0; the Lorentz factor is γ; and $K_0(x)$ and $K_1(x)$ are modified Bessel functions of the second kind.

Note that the electron's velocity v plays a few crucial roles: (1) The coupling depends strongly on the electron's velocity and scales as $\sim 1/v$ over the relevant parameters range. Generally, slower electrons are preferred as long as the other conditions are satisfied. (2) The electron velocity affects the phase of the coupling due to the term $\exp(-i\omega_i^{pq} z_i/v)$. This term will define the phase-matching conditions for extended systems that will contribute to the enhanced interaction as discussed below. (3) Other parameters in electron microscopy scale favorably for higher electron velocities, enabling the beam to remain collimated for longer distances, which is important for grazing-angle interactions. The scattering matrix is given by:

$$S = e^{i\sum_{i,p,q} g_i^{pq} t_i^{pq} b_i^{pq}} \tag{3.68}$$

where the operators b_i^{pq} are the momentum translation operators with translation of $-\hbar\omega^{pq}/v$, defined as $e^{i\omega_i^{pq} z/v}$. The operators t_i^{pq} are the emitters' transition operators $|p_i\rangle\langle q_i|$.

The Hilbert space of the emitters is hard to analyze because of its size, which is generally $K^N \times K^N$ where N is the number of emitters and K is the number of energy levels. Note that although the bound-electronic systems are emitters, the emission time-scale is much longer than the free-electron interaction time, and thus, we can neglect the electron interaction with the emitted radiation. We assume that all the emitters are identical in terms of transition dipoles and energy levels, differing only in their location on the z axis, creating an effective 1D structure (Figure 3.7c). Furthermore, we ignore all energy states except the ground state and some excited state with energy separation $\hbar\omega_0$, making the emitters effective two-level systems. In this case, the scattering matrix can be simplified to:

$$S = e^{i(gS_+ b + g^* S_- b^\dagger)} \tag{3.69}$$

g is the coupling strength defined in Eq. (1), and b is the momentum translation operator for the free electron with translation $-\hbar\omega_0/v$, and $S_\pm = \sum_i \sigma_\pm^i e^{\mp i\omega_0 z_i/v}$ where $\sigma_\pm$ are Pauli matrices. These super operators define a superradiant ladder that can be constructed by acting with these operators on the ground state $|m\rangle = \frac{1}{\sqrt{\binom{N}{m}}} S_+^m |gg...g\rangle$. To understand in what sense this ladder is superradiant, we write the $S_\pm$ operators in the interaction picture:

$$S_\pm^I = \sum_i \sigma_\pm^i e^{\pm i\omega_0(t - z_i/v)} \tag{3.70}$$

The electron arrives at the emitter located at z_i at time z_i/v and, thus, experiences a delayed interaction with the different emitters. From the perspective of the electron, all the transition dipoles add up constructively as is the typical case in Dicke superradiance, resulting in an effective dipole with size $N \cdot d$.

The elements of the scattering matrix can be found analytically and are given by:

$$\begin{aligned} s_{nm} &= \langle n|S|m\rangle \\ &= b^{n-m}(\cos|g|)^N(i\tan|g|)^{n-m}\sqrt{m!n!(N-n)!\,(N-m)!} \\ &\quad\times\sum_{k=0}^{m}\frac{(-1)^k(\tan|g|)^{2k}}{k!\,(m-k)!\,(n-m+k)!\,(N-n-k)!}. \end{aligned} \tag{3.71}$$

If we assume that $|g| \ll 1$ and additionally $N-m \gg 1$ and $m \gg 1$, meaning that the state is far from the edges of the ladder, then Eq. (5) can be further simplified:

$$s_{nm} \approx J_{n-m}(2|g|\sqrt{Nm-m^2})e^{i(n-m)\arg(g)} \tag{3.72}$$

In this approximation, the scattering matrix approaches that of a coherent interaction between a free electron and light, as in photon-induced nearfield electron microscopy [12]. The resulting effective coupling equals $g_{eff} = |g|\sqrt{Nm-m^2}$. If we imagine that the emitters are excited using a coherent control ϕ-pulse [124], then the states are narrowly distributed around $m = \sin^2(\frac{\phi}{2})N$, and we can approximate the effective coupling as:

$$g_{eff} = \frac{\sin(\phi)}{2}Ng \tag{3.73}$$

The most important result here is that g_{eff} scales like N and not like $\sqrt{N}$ as expected from noncorrelated interactions. This enhancement is due to the mutual quantum coherence between the emitters and is analogous yet complementary to the effect of free-electron-bound-electron resonant interaction.

Phase-Matched Interaction

For an ensemble of excited emitters to satisfy a phase-matched interaction with the electron, they need to be excited such that they remain inside the superradiant sub-Hilbert space following their interactions with the electron. This implies that the relative phase between emitters separated by Δz should be $\omega_0\Delta z/v$. Since $v < c$, such a relative phase cannot be achieved by a free-space laser excitation, so a material with an index of refraction n can be utilized as illustrated in Figure 3.7c. For a laser excitation propagating through such a material at angle θ, the phase-matching condition translates to the Cherenkov condition [31, 125, 126]:

$$\cos\theta_C = \frac{c}{nv} \tag{3.74}$$

Unlike all previous works in the field, here the phase matching is between the quantum emitters and an electron.

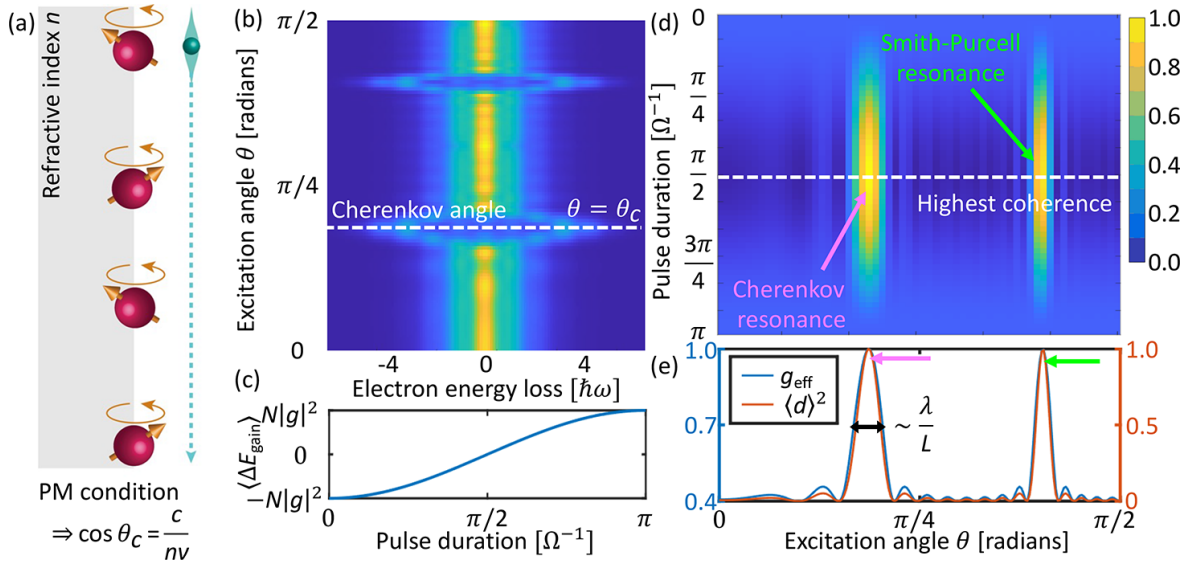


Figure 3.8: Phase-matched interaction between multiple emitters distributed over an extended area and a single electron that mediates their collective interaction. (a) System schematic. Emitters excited by a laser with its wavefront tilted by an angle θ, creating a relative delay between consequent emitters. A free electron interacts with the emitters at a certain phase delay, creating a resonant interaction governed by a Cherenkov-type condition ($n\cos\theta_C/c = 1/v$). (b) EELS as a function of excitation angle by a $\pi/2$ pulse. The strongest interaction is achieved at the Cherenkov angle θ_C. (c) The net energy transfer from the emitters to the electron as a function of the excitation pulse duration. (d) The effective coupling g_{eff} as a function of the excitation pulse duration and angle, showing Smith-Purcell-type resonances. (e) The effective coupling for a $\pi/2$ pulse, in comparison with the expectation value of the dipole as seen by the electron. Parameters: $v = 0.7c$, $N = 10$, $|g| = 0.5$.

To quantify the enhancement in the coupling, we define the effective coupling constant according to:

$$g_{eff} \equiv \frac{\sigma_{EELS}}{\sqrt{2}\hbar\omega_0} \tag{3.75}$$

where σ_{EELS} is the standard deviation of the resulting energy distribution. Figure 3.8d,e shows oscillations in the effective coupling that we attribute to higher-order phase-matching arising from Smith-Purcell-like conditions [127–129] due to the periodicity of the emitters' positions. To understand this effect, we write the dipole expectation value as seen by the moving electron:

$$\langle d\rangle^2 \propto \left|\sum_{j=1}^{N} d_0 \exp\left[i\frac{\omega_0 z_j}{v}\left(1-\frac{nv}{c}\cos\theta\right)\right]\right|^2 \tag{3.76}$$

To find the resonant excitation angles marked in Figure 3.8d,e, we require the arguments of the exponents in Eq. (10) to be multiples of 2π, which yields a hybrid Cherenkov-Smith-Purcell condition:

$$\cos\theta_K = \frac{c}{nv} - \frac{2\pi c}{\Delta z n\omega_0}K \tag{3.77}$$

where Δz is the spacing between emitters, and K is the resonance index, where $K = 0$ corresponds to the Cherenkov resonance.

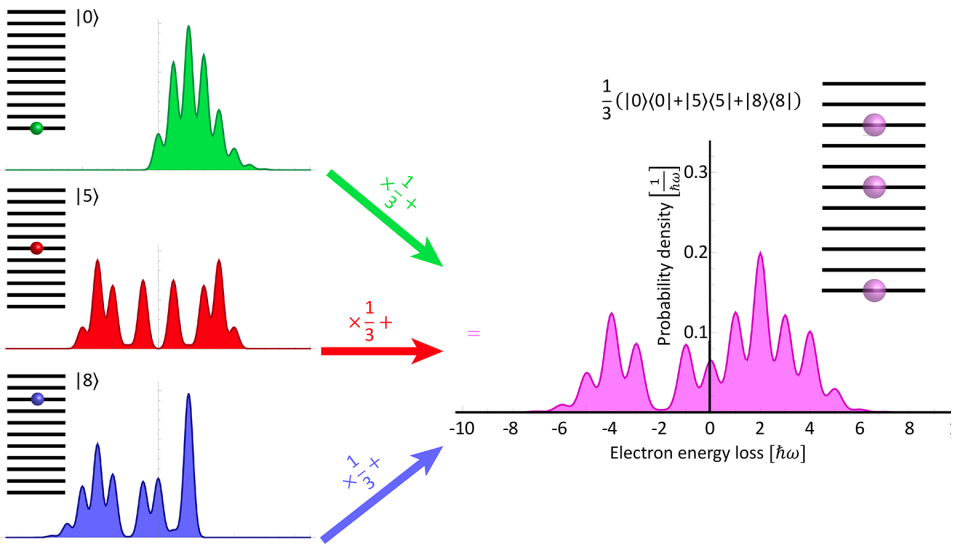


Figure 3.9: Extracting the population of the superradiant states from EELS measurements. The EELS is found to be an incoherent weighted sum of the corresponding electron spectra of the different states on the ladder. Therefore, the population can be inferred by decomposing the spectrum according to Eq. (12). Parameters are the same as in Figure 3.8.

Superradiant Population Dynamics

When the state of the emitters is part of the superradiant ladder, the entire population of the emitters is encoded on the free electron's postinteraction energy spectrum. Consider a general superradiant state $\rho_a = \sum \rho_{mm}|m\rangle\langle m|$ interacting with a free electron. The resulting EELS contains the probability P_{-k} of the electron to lose k quanta of energy:

$$P_{-k} = \sum_m \rho_{mm}|d_{km}|^2 \tag{3.78}$$

where the matrix elements d_{km} (identical to s_{km} from Eq. 5, but without the ladder operators b) govern the transition probabilities. The population statistics ρ_{mm} can be constructed from the energy spectrum by inverting the matrix $|d_{km}|^2$. This process involves exciting the emitters with a laser pulse and waiting a fixed time delay before the electron interaction.

The dynamics of Dicke Superradiance [87] includes a rapid relaxation of the identical emitters to their ground state, accompanied by the emission of a short, intense pulse of light. Typical measurements of superradiance rely on the emitted pulse intensity, which only reveals the mean-field dynamics [88]. However, much interesting information lies beyond the mean-field approximation [130]. Figure 3.10 exemplifies EELS measurements for extracting the transient population statistics of the emitters during superradiance.

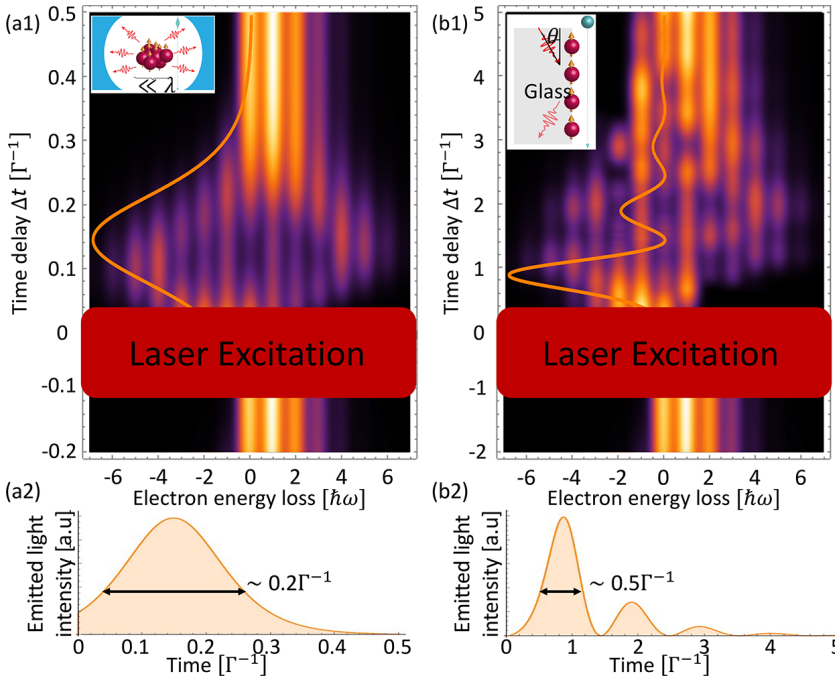


Figure 3.10: Extracting information about the superradiance dynamics from EELS. The emitters are initiated at fully excited states using a π-pulse. Panels (a1) and (b1) show electron energy loss after the interaction with the system of emitters at different delays Δt. A free electron measures their state as a function of the time delay, showing population relaxation during superradiant emission. The delay is shown in units of Γ^{-1}. The EELS at each time delay enables extracting the emitters' population on the superradiant ladder. Panels (a2) and (b2) present the corresponding time-dependent intensity plots. Parameters: $v = 0.7c$, $N = 30$, $|g| = 0.2$.

Discussion and Outlook

Looking at the greater field of EELS gives our theory a wider context: as an instance of EELS for out-of-equilibrium systems, showing the importance of mutual coherence in matter for interactions with free electrons. This goes beyond the conventional theory of EELS that relies on systems in equilibrium and linear response theory [30]. Our work shows that when coherence involves multiple systems, it affects the interaction even with nonmodulated electrons.

The Dicke superradiance process is typically probed optically by measuring the emitted pulse. The electron interaction opens the possibility of using electron pulses to image the dynamics of Dicke superradiance, extracting the intermediate populations on the superradiant ladder with simultaneous high spatial and temporal resolution, as in ultrafast transmission electron microscopy [12].

A realistic system that can demonstrate all the predicted features in an experiment will include high-quality quantum emitters (such as the quantum dots in Refs. [105, 106]) glued on the surface of a glass prism positioned in a similar configuration to that in Ref. [96] (Figure 3.7c). The interaction length of the free electron with the prism can be more than $L = 100\ \mu$m [96]. The distance between neighboring quantum dots can range from 10 nm up to a few microns, which is enough to neglect interactions between emitters. Furthermore, despite the possible effect of disorder in energy, position, orientation, and interaction strength of the emitters, the predicted resonances remain robust. The variation in emitter energies and other harmful effects for the superradiance can be described by the T_2^* decoherence time. Modern fabrication techniques

can achieve long decoherence times on the picoseconds scale even in room temperatures [105, 106], which is longer than the time of interaction (dozens of femtoseconds). Similarly to Ref. [131], the number of emitters with which each electron can interact coherently is approximated by $vT_2^*/\Delta z$, where Δz is the distance between neighboring emitters. This number can range between hundreds to thousands of emitters depending on the specific parameters. Considering characteristic values of the electron-emitter coupling $|g| \sim 10^{-3}$ [42], the resonances presented in this work can enhance the effective electron-emitters coupling to be above unity, resulting in a strong interaction well within the detectable range of free electron pump-probe experiments.

To conclude, our work investigated for the first time the coherent interaction between a free electron and an ensemble of emitters. Free electrons can be utilized to investigate superradiance over spatial and temporal resolutions that are inaccessible to conventional optical techniques. Further information on the quantum state of the emitters, such as their off-diagonal coherences, can be accessed as well by preshaping the electron before its interaction [42], potentially enabling even stronger superradiant-EELS resonances.

3.3 Many-Body Entanglement via 'Which-Path' Information

This section is based on the publication:
Ron Ruimy†, Offek Tziperman†, Alexey Gorlach, Klaus Mølmer, and Ido Kaminer.
npj Quantum Information 10, no. 1 (2024): 121.
† These authors contributed equally to this work.

Abstract

We propose a multi-particle 'which-path' gedanken experiment with a quantum detector. Contrary to conventional 'which-path' experiments, the detector maintains its quantum state during interactions with the particles. We show how such interactions can create an interference pattern that vanishes on average, as in conventional 'which-path' schemes, but contains hidden many-body quantum correlations. Measuring the state of the quantum detector projects the joint-particle wavefunction into highly entangled states, such as GHZ's. Conversely, measuring the particles projects the detector wavefunction into desired states, such as Schrödinger-cat or GKP states for a harmonic-oscillator detector, e.g., a photonic cavity. Our work thus opens a new path to the creation and exploration of many-body quantum correlations in systems not often associated with these phenomena, such as atoms in waveguide QED and free electrons in transmission electron microscopy.

Introduction

The double-slit experiment with matter waves is one of the most famous experiments in the history of physics [132–135]. A core concept behind the double-slit experiment is 'which-path' information. Any attempt to observe the path taken by a particle will inhibit it from forming an interference pattern [136]. The 'which-path' concept became the textbook example of complementarity in quantum mechanics, i.e., the inability to simultaneously measure certain properties of quantum systems, such as a particle's position and momentum [136, 137].

The story of 'which-path' information was later connected to weak measurements [138]. When a measurement device (i.e., detector) provides partial information about a particle trajectory, for example via a weak interaction, it does not fully inhibit the formation of the interference pattern but instead decreases its visibility. Many other variants of 'which-path' experiments have been proposed, such as delayed choice [138, 139] and quantum eraser experiments [140]. These works and many others highlight many of the mysteries of quantum mechanics, and as popularized by Feynman: "it (the double-slit experiment) contains the only mystery" [141].

However, there is a key ingredient to quantum mechanics missing from the conventional which-path experiment: quantum entanglement. The conventional experiment concerns the measurement of single-particle observables, whereas observing entanglement requires the measurement of multi-body correlations. Here we propose a multi-particle which-path experiment, revealing many-body correlations that can be created using the universal concept of 'which-path' information. We show what operations create multi-particle entanglement in the limited space of symmetric states, and what operations reach the full exponentially large many-body Hilbert space [70].

At the heart of every 'which-path' experiment lies the measurement of the path, which causes the collapse of the particle trajectory due to its interaction with the detector. The

detector's state becomes entangled with the particle's trajectory. We show that if the detector preserves its quantum state between its interactions, the trajectories of the different particles can collectively interfere. Then, although the interference pattern still vanishes on average, strong quantum correlations between the particles emerge.

The concept we propose applies to a wide range of quantum systems. Fig. 3.11 illustrates this concept, depicting a double-slit setup together with the analogous quantum circuit. We compare three options: conventional interference pattern with no detector, conventional 'which-path' with a classical detector that destroys the interference, and a quantum detector that preserves coherence between interactions and thus creates multi-particle quantum correlations.

The analog quantum circuit represents the two paths of the particle using qubit states $|0\rangle$ and $|1\rangle$. The splitting and interference of the trajectories are represented by Hadamard gates. The two orthogonal final interference patterns are identified using $|0\rangle$ and $|1\rangle$ after the Hadamard gate, with $|0\rangle$ being the ordinary interference pattern without the detector. The detector's 'which-path' measurement is a conditional operator that entangles the detector with the particle. To model the conventional 'which-path' experiment, we reset the detector state after interacting with each particle. The reset randomizes the particle measurement outcomes and diminishes the interference pattern. In contrast, if the detector preserves its quantum state between interactions with all the particles, their measurement outcome becomes correlated.

We consider two quantum detector models: either a fermionic or a bosonic system. The former is a qubit state describing a binary "yes/no" measurement outcome. The latter is a quantum harmonic oscillator describing a photonic or a vibrational mode excited by the particle. The fermionic detector implements a Pauli X gate, and then the 'which-path' experiment generates the highly entangled Greenberger-Horne-Zeilinger state [137]. The bosonic detector implements a conditional displacement, and then the 'which-path' experiment generates a many-body quantum walk [142, 143].

We focus below on the bosonic detector, which could be implemented in a wide range of systems. We exemplify the implications using two concrete systems: quantum emitters such as atoms or quantum dots emitting light into a common mode, such as a waveguide or cavity [88, 144, 145], or free electrons interacting with a cavity before interfering in a transmission electron microscope (TEM) [146–150]. In both systems, we show how to create many-body correlations and how to control the corresponding detector state, for the generation of desired quantum photonic states.

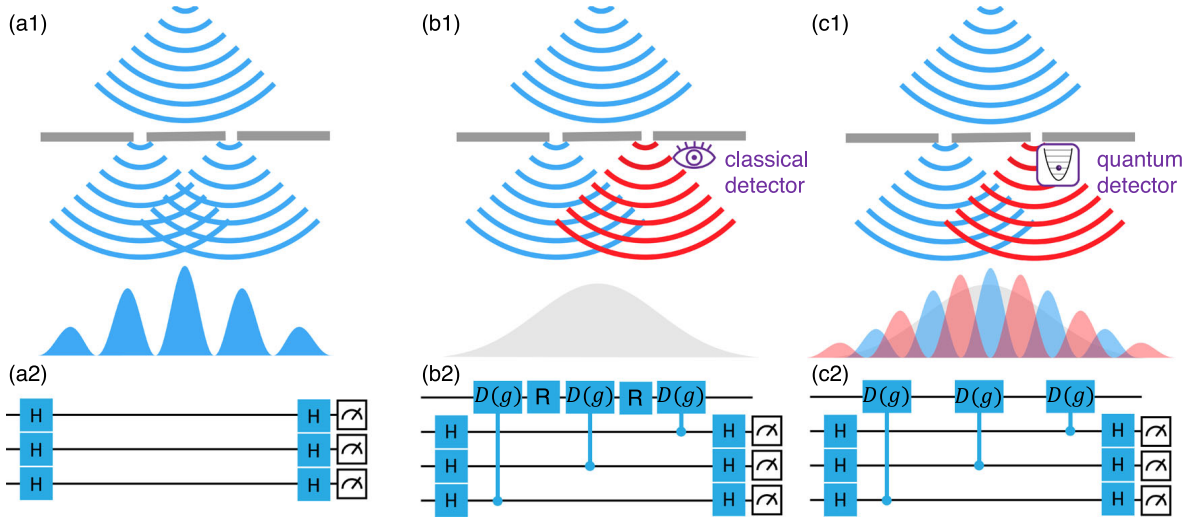


Figure 3.11: The multi-particle 'which-path' experiment: implementations in double-slit setups, with analog quantum circuit representations. (a) Conventional 'which-path' experiment: with no detector, the particle is split into two paths that are later combined, creating an interference pattern. The Hadamard H gate represents both the splitting and combining of the paths. (b) Conventional 'which-path' experiment: a classical detector in one of the paths destroys the interference pattern. The detection can be modeled using a unitary operator changing the detector state conditioned on the particle state. Each R gate resets the detector state such that it has no memory. (c) 'Which-path' experiment with a quantum detector: the detector interaction entangles it with the particles, resulting in multi-particle quantum correlations. Without the R gates, the detector correlates the particles because its state is maintained between its interactions with them. The detector can be modeled by conditional gates such as conditional displacement for a harmonic-oscillator detector, denoted by $D(g)$ with interaction strength g.

Results

Quantum circuit model

The interaction of each particle with the detector's harmonic oscillator state can be modeled using a conditional displacement operator [151]:

$$CD(g) = |0\rangle\langle 0| \otimes I + |1\rangle\langle 1| \otimes D(g), \quad D(g) = e^{ga^\dagger - g^* a} \tag{3.79}$$

Here, $|0\rangle, |1\rangle$ are the particle states corresponding to the different paths, and $a^\dagger, a$ are the creation and annihilation operators that act on bosonic detector states denoted by $|\rangle_{ph}$. The displacement operator $D(g)$ [151] depends on the particle-detector interaction strength represented by the (complex) parameter g, satisfying $D(g)|\alpha\rangle_{ph} = |\alpha + g\rangle_{ph}$ for every coherent state $|\alpha\rangle_{ph} \equiv e^{-|\alpha|^2/2} \sum_{n=0}^{\infty} \frac{\alpha^n}{\sqrt{n!}} |n\rangle_{ph}$, with $|n\rangle_{ph}$ being the number states.

A classical detector is modeled by applying the gates $H \cdot CD(g) \cdot H$ on the joint particle-detector wavefunction and then tracing out its state. Then, using the formula for the inner-product of two coherent states $\langle\beta|\alpha\rangle = e^{-\frac{1}{2}(|\alpha|^2 + |\beta|^2 - 2\beta^*\alpha)}$ [151], the final state of each particle

becomes a mixed density matrix:

$$\rho_f = \frac{1}{2}\begin{pmatrix} 1+e^{-\frac{1}{2}|g|^2} & 0 \\ 0 & 1-e^{-\frac{1}{2}|g|^2} \end{pmatrix} \tag{3.80}$$

The purity of this state is $\gamma_f = tr(\rho_f^2) = \frac{1}{2} + \frac{1}{2}e^{-|g|^2}$. As $|g|$ increases, the state transitions from completely pure (perfect interference fringes, weak or no detection) to completely mixed (no fringes, strong detection). For strong detection (large $|g|$), the chance to measure all the k particles in the original fringe (state $|0\rangle$) is exponentially small in the number of particles (2^{-k}).

Creating the many-body quantum state

We now consider the same experiment but with the quantum detector. The final joint particle-detector state is $|\psi_f\rangle = (H \cdot CD(g) \cdot H)^{\otimes k}|0\rangle^{\otimes k}|0\rangle_{ph}$. It is convenient to define the non-unitary operators $C_\pm \equiv \frac{1}{2}(I \pm D(g))$, in which case the final state can be written as:

$$|\psi_f\rangle = \sum_{n=0}^{k}\sum_{perm}|0\rangle^n|1\rangle^{k-n} \otimes C_+^n C_-^{k-n}|0\rangle_{ph} \tag{3.81}$$

Formally, $\sum_{perm}$ represents the sum over all unique sequences $|s_1 s_2 \dots s_k\rangle$ where each s_i is either 0 or 1, and the total number of zeros is n and the total number of ones is $k-n$. The probability to measure n particles in the state $|0\rangle$ and $k-n$ particles in the state $|1\rangle$ is then:

$$P_{n,k-n} = \frac{(-1)^n}{4^k}\binom{k}{n}\sum_{j=0}^{2n}\sum_{i=0}^{2(k-n)}\binom{2n}{j}\binom{2(k-n)}{i}(-1)^j e^{-\frac{1}{2}|g|^2(k-i-j)^2} \tag{3.82}$$

This process is akin to a random walk with quantum coin tosses [142, 143] deciding whether to displace the detector state at each step. The same final state is reached through different paths, i.e., different sequences of displacements. These paths constructively interfere and thus, for strong interactions, the probability of measuring all k particles in the same final state is approximately $\frac{1}{\sqrt{\pi k}}$, which strongly amplifies the exponentially small probability of the classical detector.

The mathematical reason for this interference can be understood from the norm of the operator $C_+^n C_-^{k-n}$ which equals $\sqrt{\frac{n^n(k-n)^{(k-n)}}{k^k}}$. The norm is maximal when $n = 0, k$ and minimal when $n = k/2$, implying that there is a tendency for the particles to bunch together in one output or in the other. This bunching holds resemblance to bosonic interference phenomena although the particles in our description are distinguishable (either in temporal or spatial degrees of freedom). The bosonic behavior can be understood from the fact that the detector state is symmetric to permutations of the particles, resulting in boson-like interference.

To illustrate the implication of this result, we consider repeating this which-path experiment many times, each with $\sim k = 100$ particles. Both classical and quantum detectors will show no interference pattern on average. However, in each repetition of the experiment, all the $k = 100$ particles will form the same fringe with a probability > 0.1 using a quantum detector rather than 10^{-30} using a classical detector.

The paths of each particle can be described as a spin 1/2 system, and the total state of N particles that are symmetric to permutation can be described in the subspace of maximal total angular momentum or Dicke states. The key component that creates the many-body correlations is a non-destructive measurement of the angular momentum projection, i.e., how many particles pass through each path. Similar correlations can be obtained by measuring in this basis with a classical detector, albeit this cannot create quantum photonic states in the detector (still, previous works showed that such a detection can entangle particles [152–156]).

Since the operator $CD(g)$ is fully entangling in the limit of $g \gg 1$, by measuring the detector's final state, the particles' state can collapse into an entangled state. For example, for $k = 2$, measuring the detector will give a Bell state or a Hadamard state, with a 50%-50% chance. Bell states are important resources for quantum metrology, providing precision beyond the standard quantum limit, as is one of the goals of quantum electron microscopy [146–150]. Going beyond $k = 2$ can create more complex entangled states, similar to N00N states, which can provide Heisenberg-limited scaling for quantum metrology.

We note that the state of the quantum detector can be indirectly measured using post-selection on additional particles. To prove the entanglement of the multi-particle state, we can control the particle interferometry (the final Hadamard gate): measuring the particles in orthogonal bases will break a Bell inequality. For example, measuring the particle states before and after applying the final Hadamard gate, will show correlations that are unobtainable classically.

Furthermore, adjusting the relative phase of the coherent displacements (phase of g), can break the symmetry between the particles. This can be done by tuning the relative arrival time of the particles in the optical cycle. This way we can control the complex quantum state of multiple particles, tapping into the vast potential of their exponential Hilbert space [70]. By controlling the initial conditions and studying the emergent dynamics, our multi-particle 'which-path' implements a quantum simulator.

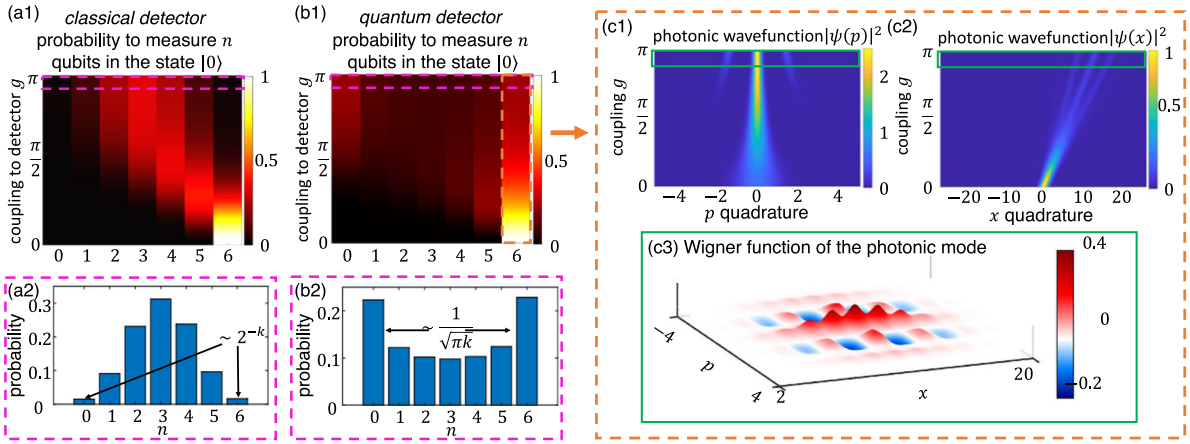


Figure 3.12: Quantum correlations in the particles and in the detector. Particle correlations: Comparing the "which-path" variants with classical (a) and quantum (b) detectors. The probability to measure n of the total $k = 6$ particles in the $|0\rangle$ state is presented as a function of the particle-detector coupling strength g, showing strong anti-correlations in the limit of strong coupling. (c) Detector state: The state of the quantum detector (a quantum harmonic oscillator) presented in the p and x quadratures, as a function of the coupling strength, post-selected on all particles measured in the $|0\rangle$ state. The Wigner function in the limit of strong coupling is highly non-Gaussian, taking the form of a (GKP-like) grid of coherent states.

The detector's quantum state

The 'which-path' experiment can be used to control the quantum state of the detector. If n particles are measured in the state $|0\rangle$ and $k - n$ in the state $|1\rangle$, then the detector state is $|\psi_f\rangle_{ph} \propto C_+^n C_-^{k-n} |0\rangle_{ph}$. This state can be highly non-Gaussian. If the k particles are measured

in $|0\rangle$, the final state takes the form of a 1D grid of coherent states:

$$|\psi_f\rangle_{ph} \propto \sum_{n=0}^{k} \binom{k}{n} |(k-n)g\rangle_{ph} \tag{3.83}$$

Figure 3.12c shows the Wigner function of this state for $g = \pi$, and its x and p quadrature representations as a function of g. The detector state transitions from a Gaussian squeezed state to a non-Gaussian grid state for larger g values. Our scheme can create a Gottesman-Kitaev-Preskill (GKP) detector's state up to Gaussian operations [39, 157–159]. For a GKP state with squeezing r, we can take $g = \sqrt{2\pi e^r}$. The goal of 10dB squeezing, a threshold for fault-tolerant quantum computation [39, 157–159], requires 3 particles with $r = 3$, and then the post-selection probability to create this GKP state is 31.3%.

We find that the limit of weak g creates a squeezed vacuum state with squeezing of $r = \frac{1}{2}\ln\left(\frac{k|g|^2}{2}+1\right)$. The probability to post-select this state depends only on the squeezing, rather than on the number of particles, and is equal to e^{-r}. For larger g values, already a single particle deterministically generates a Schrödinger cat state of the form $|0\rangle_{ph} \pm |g\rangle_{ph}$ where the sign is decided by the particle measurement outcome ($|0\rangle$ or $|1\rangle$) [39].

Physical implementations

This section proposes two implementations of the multi-particle 'which-path' experiment. The first is an electron holography setup with a microwave cavity in one of the paths, resembling the typical image of a double-slit setup (Fig. 3.13). The second is a waveguide-QED setup in which multiple emitters interact with the same mode (Fig. 3.14). In this case, the "paths" are taken by electrons of the emitters in different internal states.

Any implementation requires the realization of two components with sufficiently high fidelity: (1) Hadamard gate: To combine or separate the particle states into two distinct states representing the logical states. (2) Conditional displacement gate: State-selective interaction between the particle and the detector, displacing the detector state without back-action on the particle.

Our first proposed implementation relies on split-illumination holography in a transmission electron microscope [160–163] (Fig. 3.13). Denoting the electron's left and right paths by $|0\rangle$ and $|1\rangle$, their interference creates the fringe pattern that corresponds to the state $|0\rangle + |1\rangle$. The orthogonal state is the fringe with a quarter of a wavelength offset that corresponds to the state $|0\rangle - |1\rangle$. Then, dividing the measurement screen into equal sections quarter wavelength apart enables observing the correlation between the final states of the electrons. Fig. 3.13b shows that the overlap between the fringes limits their distinguishability, smearing the measured anti-correlations [164].

Figure 3.13a shows that using an electron beam-splitter to convert the fringes into separate paths creates more pronounced anti-correlation. The electron beam-splitter can be realized in many different ways such as crystals, diffraction gratings, and more advanced phase masks [21, 165–167], each with different pros and cons like limited fidelity. Additional proposed realizations include laser or microwave fields [168] and electron mirrors [169]. The electron beam-splitters could be optimized to have two inputs and outputs, as expected from true Hadamard gates. The electron beam-splitters can also be used for splitting the electron before the cavity interaction (e.g., instead of a bi-prism). There, the electron beam-splitter should not be optimized for fidelity but used to provide round spot size enabling precise electron beam overlap and better transverse coherence. If the initial beam-splitter is lossy or has more than two outputs, then they can be eliminated by measuring them, essentially post-selecting only electrons that passed through the desired outputs. In the second electron beam-splitter, this could not be tolerated as lost electrons destroy the many-body entanglement.

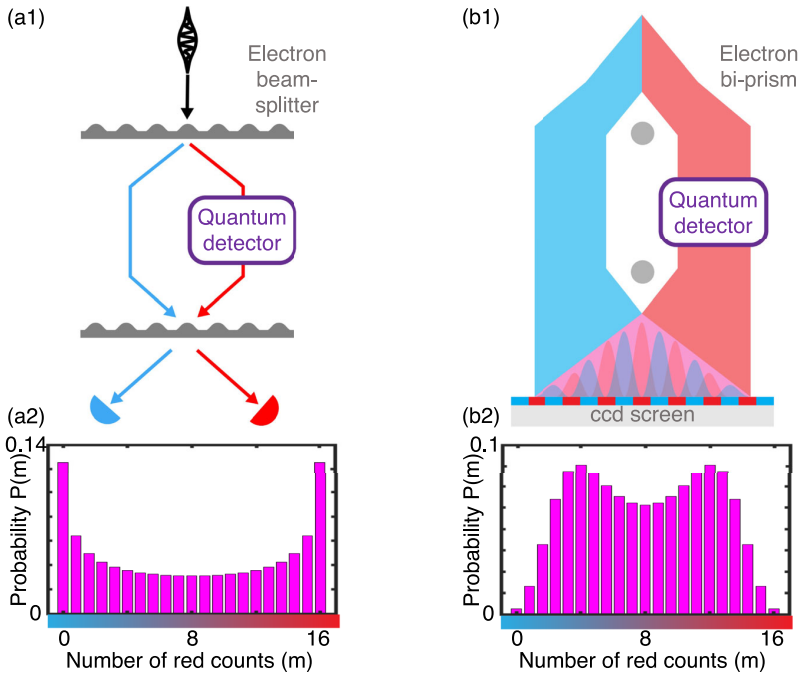


Figure 3.13: Implementation of the multi-particle 'which-path' scheme using split-illumination off-axis electron holography. The setup splits and then combines back an electron beam. A microwave cavity is placed in one of the paths. The two paths interfere either on a two-port beam-splitter (a) or on screen (b) divided into colored sections that denote the two-port outputs. The beam-splitter output results in pronounced anti-correlated distribution, while the interference on a screen result in a less pronounced but still clear anti-correlated distribution.

For this implementation to work, the quantum detector must satisfy several conditions: (1) The cavity lifetime (T_1) and coherence time (T_2) should be long enough such that it interacts with all the electrons before losing the quantum nature of its state. (2) The cavity should be cooled to limit thermal fluctuations. (3) The coupling strength g of the electron with the photonic mode should be strong enough. (4) A single-mode of the cavity should dominate its interaction with the electron. (5) All the electrons arrive either at the same time to the detector, or periodically in time such that they are locked with the cycle of the mode. (6) The photonic mode frequency ω should be of sufficiently low such that it does not induce back-action on the electron, i.e., satisfying $\omega \ll \frac{v}{(kg)^2\sigma_z}$ where k is the number of electrons, v is the electron velocity and σ_z is the spatial extent of the free-electron wavepacket along its direction of motion z. (7) The electron is paraxial, and its energy is much higher than that of the photon, implying that the scattering matrix describing their interaction is given by [35, 170]:

$$S \approx D(g) \tag{3.84}$$

and can be reduced to the ordinary displacement operator by assuming negligible photon back-action.

Condition (3) is especially challenging, yet critical for strong entanglement. In recent years substantial effort has been invested to increase the coupling between electrons and photonic modes, primarily in the optical regime, to achieve single-electron-single-photon coupling ($g \sim 1$) [38, 170, 171]. Due to their higher flexibility in design, microwave cavities could lead to breakthroughs in this regard as we recently investigated [172].

Our interferometry proposal closely relates to the works of Okamoto, who proposed interferometry of electrons that strongly interact with superconducting qubits [146–148]. There, the

electrons get entangled to such qubits, creating GHZ states. Our work also relates to interference experiments of electrons passing nearby semiconductors and metallic surfaces, interacting with the electron gas inside them, showing a controllable washing-out of the interference pattern [173, 174]. In contrast to our work, in such experiments, the electron emits distinguishable photons, acting as a classical detector. All these experiments could be viewed as part of the general family of which-path experiments, with various types of detectors.

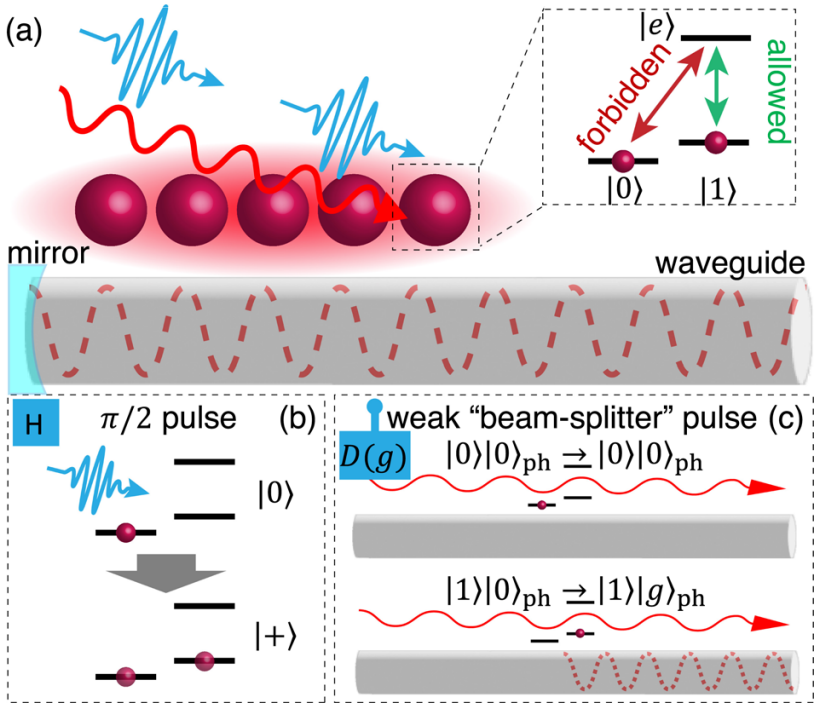


Figure 3.14: Implementation of the multi-particle 'which-path' scheme using waveguide-QED with quantum emitters such as atoms in a Λ configuration. (a) One of the electronic transitions couples to the driving laser. The two ground states represent the two "paths", $|0\rangle$ and $|1\rangle$. (b) Coherent control pulses act as Hadamard gates. (c) Weak illumination pulses couple each emitter in the correct state to the waveguide, creating a conditional displacement.

Our second proposed implementation relies on k emitters such as atoms coupled to a 1D waveguide (Fig. 3.14). In this case, the "two paths" $|0\rangle, |1\rangle$ of our scheme are two hyperfine levels of each emitter. The Hadamard gate can be implemented via a microwave $\pi/2$ pulse resonant with the $|0\rangle$ to $|1\rangle$ transition or using Stimulated Raman Adiabatic Passage [175]. Then, by turning on a laser tuned for the transition between the state $|1\rangle$ and an excited state $|e\rangle$, the emitters begin to populate the excited state and radiate into the waveguide. We assume that the transition $|0\rangle \leftrightarrow |e\rangle$ is forbidden by detuning or selection rules, and in this case, emission into the waveguide is conditioned on the internal state of the emitters.

In the limit where the Rabi frequency associated with the optical transition $|1\rangle \leftrightarrow |e\rangle$ satisfies $\Omega_R \ll k\Gamma_{1D}$ (where Γ_{1D} is the decay rate into the waveguide), the emitters are in their linear regime, and the radiation emitted is a coherent state $|\alpha\rangle$ in a single temporal mode [144, 176–179]. The magnitude of α scales as the number of emitters occupying the state $|1\rangle$. At the end of the process, the number of emitters in each hyperfine state can be measured to herald particular photonic states (indirect post-selection emitter measurements are possible by subsequent excitations). The system should satisfy a few conditions to effectively implement the protocol: (1) The collective decay rate into the waveguide should be sufficiently greater

than the decay rate into free space $\Gamma_{1D} \gg \Gamma'$. (2) The emitters remain in their linear regime. (3) The dephasing time T_2^* must be far larger than the total protocol time.

When all these conditions are met, the laser implements a conditional displacement between the qubit of the hyperfine state and the propagating pulse in the waveguide. For a single emitter, the protocol creates the state $|\psi\rangle \propto |0\rangle_e(|0\rangle+|\alpha\rangle_{v(t)})+|1\rangle_e(|0\rangle-|\alpha\rangle_{v(t)})$, where the indices $e, v(t)$ are for the emitter and photonic state in temporal mode $v(t)$ which, in the linear regime, matches the temporal shape of the driving field [180]. By measuring the internal state of the emitter, its emission is heralded into a cat state. Cat states with large photon numbers are desired for various applications, yet are very challenging to create, especially in the optical range. The maximum magnitude of α that can be achieved is approximately determined by the amplitude of the field emitted to the waveguide mode in the typical timescale of the decoherence channel [176–181]:

$$\alpha \approx \min\left\{\frac{\Gamma_{1D}}{\Gamma'}, \Gamma_{1D}T_2^*\right\} \tag{3.85}$$

Discussion

Our work describes a multi-particle 'which-path' experiment with a detector that interacts with multiple particles while maintaining its quantum state. We find that the particles develop strong correlations due to their path interference. Moreover, measuring the particles generates useful detector states (e.g., cat and GKP photonic states), whereas measuring the detector creates useful entangled particle states. The special case of a fermionic detector that contain a discrete 'yes/no' degree of freedom rather than a full harmonic oscillator can capture a range of schemes used for generating multi-partite entanglement: Consider a quantum detector described by conditional gates (such as CNOT or Controlled Phase gates). In this case, the "path" is encoded on the state of the control qubit, and the detection is performed via an entanglement with the controlled qubit. Such operations are routinely used to generate multi-partite entanglement in quantum information platforms such as superconducting qubits and atom-cavity systems [182–187]. Our gedanken experiment thus provides a description of such experiments in the language of 'which-path' information.

So far, we have shown how to reach entangled particle states in the effective Hilbert space of symmetric states. However, the interactions in any many-body which-path scheme can reach the entire exponentially large Hilbert space. The way to reach the entire Hilbert space we can break the symmetry between the particles, for example, by shifting the arrival time of the electrons relative to the optical cycle, or by shifting the positions of the emitters along the waveguide. This approach can create more complicated entanglement structures [188–191]. For example, the shift of the electron arrival time or emitters position by half the mode cycle creates destructive (rather than constructive) interference between two consequent particles, completely altering the correlations. Another way to access the exponentially large Hilbert spaces is to use a multi-mode quantum detector or multiple detectors.

Due to the universality of the "which-path" concept, our method could potentially be implemented in many physical systems such as trapped ions coupled to joint vibrational modes, arrays of superconducting qubits, quantum dots, atoms in tweezers coupled to a waveguide or to a cavity, atomic ensembles probed by off-resonant light, interferometric experiments with various free particles, and various schemes relying on single-photon nonlinearities [192].

Chapter 4

Co-First-Author Publications

4.1 Free-Electron Interactions with Photonic GKP States: Universal Control and Quantum Error Correction

This section is based on the publication:
Gefen Baranes[†], Shiran Even-Haim[†], Ron Ruimy[†], Alexey Gorlach, Raphael Dahan, Asaf A. Diringer, Shay Hacohen-Gourgy, and Ido Kaminer.
Physical Review Research 5, no. 4 (2023): 043271.
[†] These authors contributed equally to this work.

Abstract

We show that the coherent interaction between free electrons and photons can be used for universal control of continuous-variable photonic quantum states in the form of Gottesman-Kitaev-Preskill (GKP) qubits. Specifically, we find that electron energy combs enable nondestructive measurements of the photonic state and can induce arbitrary gates. Moreover, a single electron interacting with multiple photonic modes can create highly entangled states such as Greenberger-Horne-Zeilinger states and cluster states of GKPs.

Introduction

Quantum error correction is essential for reaching large-scale quantum computation. One prominent approach toward this goal is to encode qubit information on continuous variables [158, 193] in quantum harmonic oscillators, known as bosonic codes. These codes, and most prominently the Gottesman-Kitaev-Preskill (GKP) code [158], facilitate quantum error correction for fault-tolerant quantum computation [194]. The generation and manipulation of GKP states is a formidable challenge, as it necessitates non-Gaussian operations that typically require strong nonlinearities. Creating the required nonlinearity can rely on a wide range of physical mechanisms. The nonlinearity can arise from intrinsically nonquadratic Hamiltonians that can be realized in the optical regime using the Kerr effect [195, 196] or postselection by number-resolving photonic measurements [197–199]. The GKP states can also be deterministically generated from cat states [200, 201], which, however, still require nonlinearity for their generation. Such nonlinearities are typically counterproductive to the stabilization of GKP states since they increase decoherence by coupling to external degrees of freedom, even more so given that such states rely on a large average photon number.

Leading approaches for generating and manipulating GKP states rely on the coupling to matter ancilla qubits, which provide the necessary strong nonlinearity. Such a scheme was demonstrated experimentally with the vibrational motion of trapped ions [202, 203], with cavity photons at microwave frequencies coupled to superconducting qubits in circuit quantum electrodynamics (QED) [204]. A similar ancilla-based scheme was also recently suggested theoretically in optical frequencies using cavity QED [205].

Here we propose a different physical mechanism that provides the needed nonlinear interaction using free electrons that act as ancilla qubits. We show how the fundamental coherent interaction of free electrons and photons, perhaps the most basic interaction in QED, can provide the building blocks for universal quantum computing with GKP states. The interaction provides the strong nonlinearity needed for quantum error correction and universal control of

GKP states. This interaction can be used in gate-based [70] and measurement-based [206] computational protocols. A step in this direction has recently shown the free-electron-based generation of GKP states [39]. We now unveil the complete picture and show that the fundamental electron-photon interaction can be described as a conditional displacement (CD) gate when the free electron is shaped in the rotor GKP encoding [207]. The CD gate is the basic building block for universal computation and error correction with GKP states [204, 208].

The idea to use free electrons in the context of quantum optics is inspired by recent advances in ultrafast electron microscopy. Specifically, our work relies on the inelastic scattering of free electrons by electromagnetic fields, which was famously observed in photon-induced near-field electron microscopy (PINEM) [12–14, 23, 50, 84, 98, 209]. This nonlinear scattering provides the additional degrees of freedom required to encode quantum information on the individual electron by coherent modulation of its wave function [28, 210, 211]. The ability to control the modulated electrons has been studied extensively in theory (e.g., [100, 119]) and experiments (e.g., [85, 96, 212]). The interaction of such modulated electrons enables photon addition and subtraction [213], measurement of light statistics [37], coherent control of two-level systems [41–43, 113, 114, 117], and investigation of ultrafast population dynamics of superradiance. The same underlying theory enables heralded generation of photonic entanglement [115] and heralded generation of Fock states of one or more photons [38, 171, 214, 215]. Such ideas and experimental achievements support the feasibility of the scheme we propose here.

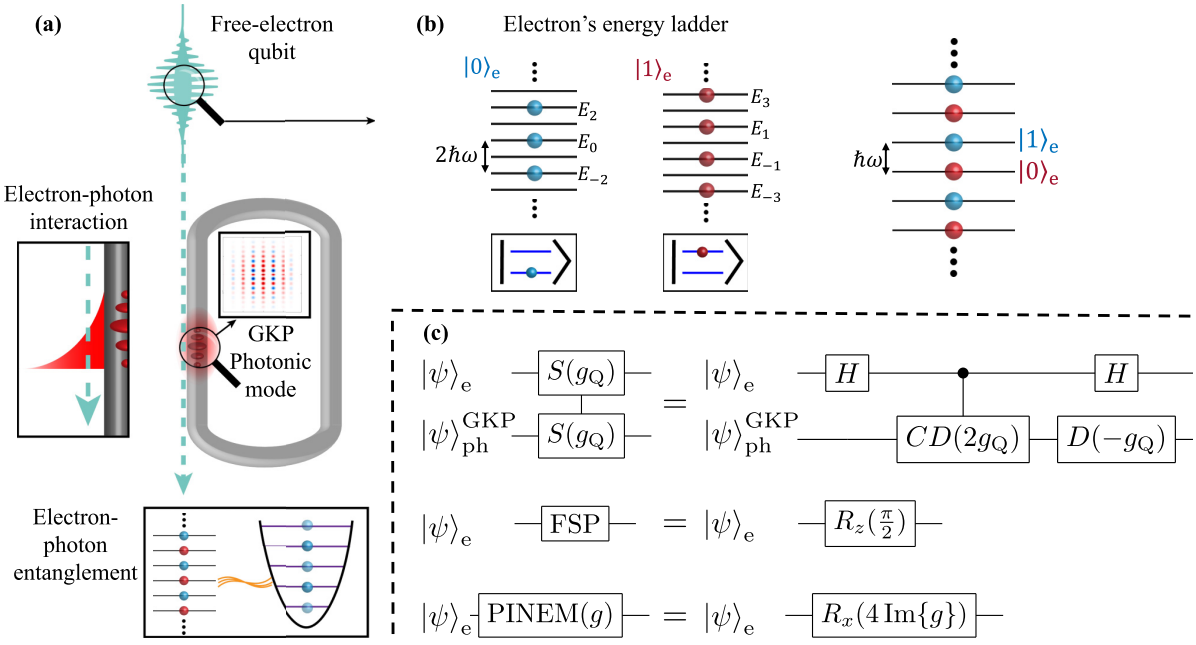


Figure 4.15: The free-electron-photon interaction as a fundamental building block for quantum information processing. (a) The free electron is preshaped into a free-electron qubit state (e.g., using laser interactions), which interacts with the photonic mode through a near-field coupling. The photonic mode contains a GKP state. The interaction entangles the electron with the GKP state. (b) The free-electron qubit states are shown by their energy spectra, as the even and odd comb electrons with $2\hbar\omega$ energy spacing. (c) Building blocks for universal quantum computation on the free-electron qubit and the GKP state (left) and their corresponding circuits (right).

Free Electrons as Ancillas for Conditional Displacement on Photonic States

We define the electron coherent energy comb as a superposition of electron energy states with a Gaussian envelope around a central energy E_0:

$$|comb\rangle_e \propto \sum_{n=-\infty}^{\infty} e^{-\frac{n^2}{2\sigma^2}} |E_0 + n\hbar\omega\rangle \tag{4.86}$$

Here $|E_0\rangle$ is the state of an electron with mean energy E_0 and narrow energy distribution compared to $\hbar\omega$, ω is the modulating laser frequency, and σ is the dimensionless energy width describing the number of energy states in the electron comb. This electron comb can be created by shaping a monoenergetic electron using multiple laser harmonics [100] or multiple interaction stages [119].

In this paper, we consider the limit of $\sigma \gg 1$, and omit the σ in the electron comb notation. In this case, the electron comb becomes an approximate eigenstate of the energy displacement operators b_ω, $b_\omega^\dagger$. The electron comb can be described as a qubit, encoded in the rotor GKP encoding [207], with the following basis:

$$|0\rangle_e = \sum_n |E_0 + 2n\hbar\omega\rangle, \quad |1\rangle_e = \sum_n |E_0 + (2n+1)\hbar\omega\rangle \tag{4.87}$$

We denote $|\psi\rangle_e = \alpha|0\rangle_e + \beta|1\rangle_e$ as a general free-electron qubit state. Universal single-qubit gates [210] over such free-electron qubit states are achievable by multiple PINEM interactions separated by free-space propagation, i.e., drift.

To describe the interaction of such modulated electrons with quantum photonic states, we quantize the electromagnetic field [34, 35]. Since photonic modes have multiple frequency components, the interaction can be described using the scattering matrix [170]:

$$S = \exp\left[\int d\omega \left(g_{Q,\omega} b_\omega a_\omega^\dagger - g_{Q,\omega}^* b_\omega^\dagger a_\omega\right)\right] \tag{4.88}$$

We consider the case where the coupling is with the multifrequency photonic mode, omitting them in the notation. The scattering matrix is then reduced to a conditional displacement (CD) operator, controlled in the X basis:

$$\begin{aligned} S(g_Q) &= \exp\Big(g_Q \sigma_x a^\dagger - g_Q^* \sigma_x a\Big) = D(g_Q \sigma_x) \\ &= |+\rangle_e\langle +| \otimes D(g_Q) + |-\rangle_e\langle -| \otimes D(-g_Q) = CD(g_Q) \end{aligned} \tag{4.89}$$

where $D(\alpha) = \exp\big(\alpha a^\dagger - \alpha^* a\big)$ is a coherent displacement operator [56]. g_Q is the coupling strength for a mode family, describing the interaction strength and the relative phase between the mode family and the free electron shaped by the modulating laser.

Universal Single-Qubit Gates with Free-Electron Ancillas

For the universality section we focus on the case where the photonic mode is an ideal GKP state [158]. GKP states form a lattice in their Wigner representation [157] and can be defined by the lattice constants $a_{x,y,z}$. Pauli gates on the GKP qubit can be achieved in two ways. The first is using the CD operator from Eq. (4) and setting the coupling constant between

the free electron and the photonic mode to be $g_Q = \pm\frac{a_i}{2}$, for $i = x, y, z$. The second is by deterministically displacing the photonic mode using a coherent light source coupled to the photonic modes containing the GKP state.

The Hadamard (H) gate acts as a rotation in phase space. Therefore, it can be replaced by adding a $\pi/2$ phase to g_Q for all the following computation steps [216]. When $g_Q = a_i/4$, Eq. (4) gives a controlled Pauli gate σ_i on the GKP state, controlled by the electron's state in the X basis. As an example, the CNOT gate between the free electron and the GKP state is given by $g_Q = a_x/4$:

$$CNOT_{e\to ph} = [H_e \otimes D(-a_x/4)]S(a_x/4)(H_e \otimes I) \tag{4.90}$$

Controlled Pauli gates give the ability to create maximum entanglement between the electron qubit and the GKP state. Moreover, controlled Pauli gates can be used to read out the GKP state by measuring the electron's energy as an ancilla [70].

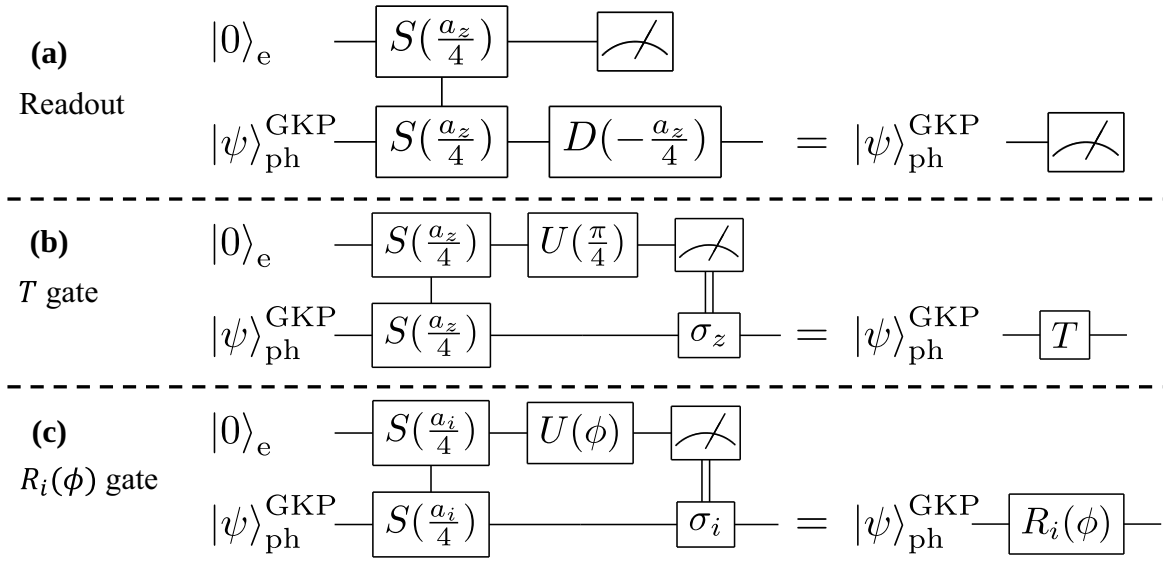


Figure 4.16: Single-qubit gates induced by the free-electron ancilla. (a) Readout operation: using electron ancilla qubit followed by measurement. (b) Rotation gate $R_i(\phi)$ utilizing teleported gates with feedforward. (c) T gate, an example of a rotation gate with $\phi = \pi/4$ and $i = z$.

The CD operator and rotation gates on the ancilla qubit can be used to implement a universal set of gates on the GKP state with an additional feedforward mechanism. Rotation gates around $i = x, y, z$ axis with angle ϕ, $R_i(\phi)$, are achieved with teleported gates by an ancilla qubit [216, 217], as shown in Fig. 4.16(c). The initial state of the electron is $|0\rangle_e$. The electron interacts with the GKP state with $g_Q = a_i/4$ according to the rotation axis and is then measured. If the measurement result is $|\phi_-\rangle_e$, the Pauli gate σ_i is applied to the GKP state, and if the measurement result is $|\phi_+\rangle_e$, there is no need to apply any gate.

Free-Electron Interaction as a Stabilizer and Error Correction Tool

This section describes the stabilization and error correction process with the free electron. General error correction involves measurements of the stabilizers and correcting accordingly.

The CD operator from Eq. (4) can stabilize the GKP manifold. Some schemes for GKP manifold stabilization [204, 218] use multiple consecutive CD interactions, performing the error correction without feedforward of the measurement result. On the contrary, the free-electron ancilla can interact only once with the photonic mode before propagating, necessitating a feedforward mechanism as in other more conventional approaches [219].

Measurement of the stabilizers is achieved by interaction with a coupling constant equal to the lattice constant, $g_Q = \pm a_i$ followed by a measurement of the free electron. Combining the free-electron-photon interaction and feedforward mechanism allows for error correction and stabilization of the GKP manifold. Furthermore, applying a single round of stabilizer measurement and correction improves the fidelity of the photonic mode state compared to a desired GKP state for any initial state.

Free Electron as a Flying Qubit: Creation of GHZ and Cluster States

The unique property of a free-electron ancilla as a flying qubit is that a single electron can be used for entangling multiple GKP states. The protocol for a $CNOT_{ph1\to ph2}$ gate between two GKP states in two separated photonic modes is described in Fig. 4.17(a), where one electron qubit interacts with two GKP states. The $CNOT_{ph1\to ph2}$ and the universal set of one qubit gates shown in the previous section are sufficient for universal quantum computing [70].

The maximally entangled GHZ state can be produced using one electron qubit interacting with multiple photonic GKP states. Each interaction is a $CNOT_{e\to ph}$, which can be implemented with $g_Q = a_x/4$. In the final step of creating the GHZ state, the Hadamard gate is applied to the electron. The electron is then measured to disentangle it from the GKP states. The procedure is shown in Fig. 4.17(b).

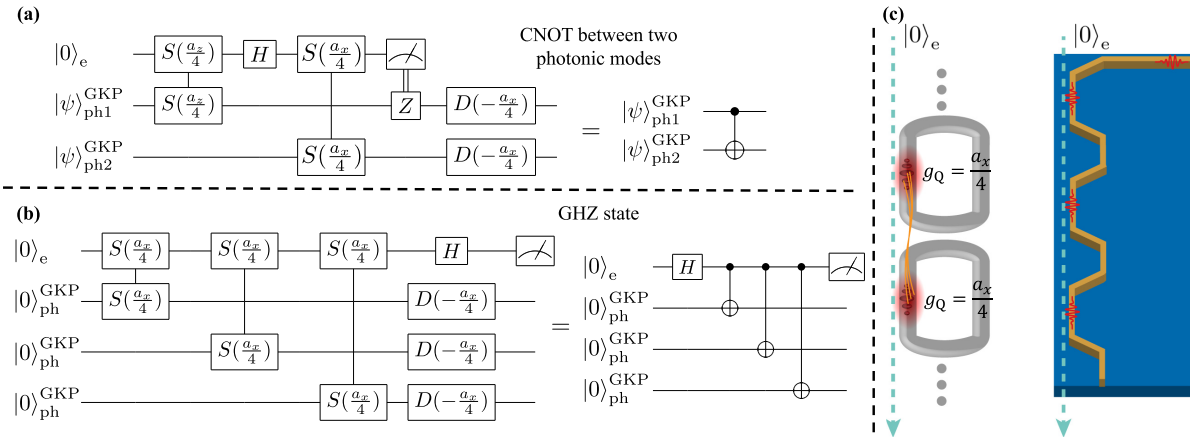


Figure 4.17: Creation of multiqubit entanglement using free electrons. (a) $CNOT_{ph1\to ph2}$ gate between two GKP states. (b) The scheme for generating a GHZ state of three GKP states. (c) Two approaches for implementing the GHZ state: stationary GKP states in cavities (left) and propagating GKP states in a waveguide (right).

The prospects of free-electron flying qubits include the potential to create the cluster states needed for measurement-based quantum computation schemes. Clusters of GKP states [220] are especially desirable because GKP states are robust against photon loss errors [158], and can be easily measured in a different basis with the same operation. Following [221], we can add appropriate propagation distances between the subsequent interactions in the GHZ-creation

scheme to add single-qubit rotation on the electron and create a one-dimensional (1D) cluster of GKP states using a single electron [Fig. 4.18(a)]. Additionally, combining multiple electron channels can create two-dimensional (2D) and potentially higher-dimensional cluster states, as shown in Fig. 4.18(b). These higher-dimensional schemes are based on the protocol presented in [222].

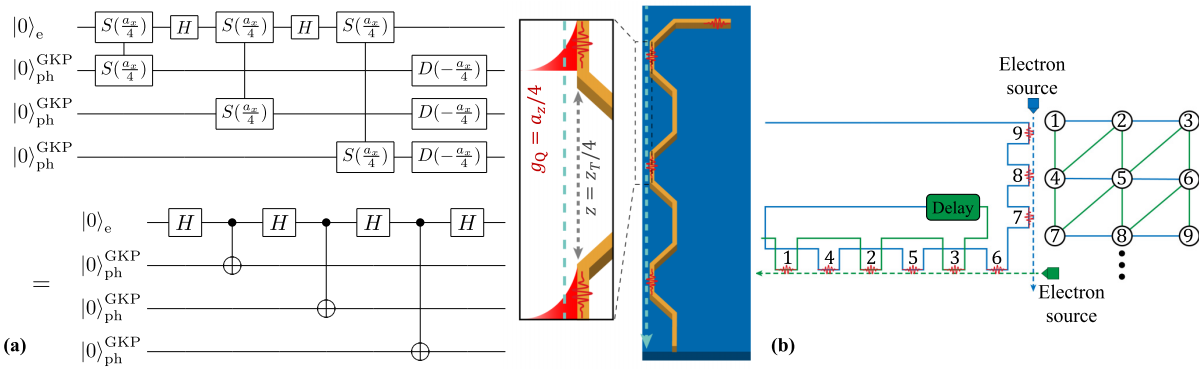


Figure 4.18: Using flying qubits for the generation of cluster states. (a) A scheme for generating a 1D cluster state of GKP states in a photonic waveguide. (b) Generation of 2D cluster states of GKP states using two free-electron sources and a delay.

Discussion and Outlook

In summary, this paper demonstrates how the coherent interaction between free electrons and GKP states enables projective measurements, error correction, and universal control over the GKP states. This paper also demonstrates how the interaction of multiple GKP states with the same electron enables the creation of highly entangled states such as GHZ and cluster states. The key to these possibilities is the creation of CD based on the electron interaction. The electron-photon interaction thus reproduces other protocols for GKP state generation in superconducting qubits [204] and ion traps [202].

Going beyond these demonstrations, the free-electron implementation provides additional degrees of freedom to the interaction due to the intrinsic nature of the free electron as a flying qubit. The use of free electrons as matter ancilla qubits is intriguing for a few practical reasons. In contrast to currently used matter ancilla qubits in circuit QED, trapped ions, and cavity QED counterparts [202–205], free electrons are versatile in their energy spectrum and can access a large range of frequencies. Second, the most significant difference is that the free-electron ancilla is a flying qubit. While photons also act as flying qubits, they do not exhibit the strong interactions usually needed to realize the operations required from ancilla qubits, such as CD. A flying ancilla qubit allows for high connectivity between the electron and multiple spatially separated photonic modes. This fact can enable possibilities that are hard to create in other systems, such as the generation of highly entangled GHZ and cluster states with only one ancilla electron (rather than multiple ancilla qubits [223, 224] or multimode coupling [225]), which further limits the coherence times and exponentially complicates the physical realization.

The flying qubit nature of the electron also implies that it interacts with the GKP state only for a short time (typically single-picosecond timescales [37, 96]). In "aloof"/grazing angle experiments [111, 226], electrons fly by tens of nanometers from the surface to minimize radiation damage. From this distance, the electrons can only excite lower-energy excitations and do not typically cause damage to the sample. Therefore, the coherence time of the photonic qubit is

not significantly reduced by the free-electron interaction (unlike the case of interaction with ancilla qubits in circuit QED [227]).

It is also interesting to compare the interaction of free-electron qubits with GKP states to other schemes that can be realized in the optical range, such as the beam-splitter interaction of optical cat states [39, 201]. Beam splitters can generate GKP states with low success probability using postselection. They can also enable entangling photonic states and creating cluster states for fault-tolerant measurement-based quantum computation. The free electron enables this, but can also apply additional operations, such as efficient GKP generation [39], operation, stabilization, and gate-based universal quantum computation.

Another aspect that makes free-electron-based schemes promising arises from developments in fast electron counting detectors (especially direct detection schemes) [228]. Since free electrons are energetic particles, it is easier to achieve number-resolved electron detection than similar detection with photons.

As presented in this work, the electrons can stabilize the quantum state by performing error correction. The importance of GKP stabilization and error correction was demonstrated in microwave cavities [204, 229]. The electron flying qubit can perform gates on such stationary modes in a manner that photonic flying qubits can only apply on traveling modes. Currently, to the best of our knowledge, there is no way to generate, stabilize, or manipulate GKP states while performing error correction inside optical cavities. Such abilities, if achieved, can open up new opportunities in quantum technologies, such as optical quantum memories [230], full-on error-correction gate-based quantum computation using stored GKP states at room temperature, or the integration of GKP states into other optical quantum computational systems such as optical cavity QED.

Since current electron sources are not deterministic, heralding the application of the gates or using feedforward is necessary. Recent experiments have shown opportunities for both photon-heralded electron sources by time-resolved detection [38, 215] and electron-heralded electron sources by antibunching [44, 45]. Such heralding abilities, together with multiplexing, can be used for deterministic single-electron sources, similar to the current common approach for continuous-variable (CV) optical quantum computation [220, 231].

Realizing free-electron-driven optical GKP states requires addressing crucial challenges in each of the two main stages of the process: initial electron qubit preparation and efficient electron-photon quantum interaction. Both stages are currently extensively investigated theoretically and experimentally. For the first, free-electron qubits and single-qubit operations of limited fidelity are already generated in PINEM experiments [96, 212, 232]. Some of these experiments realized free-electron combs even before the theory work showed how such combs implement qubits [210]. Methods for increasing the fidelities of such combs (and thus of the qubits) are being developed (e.g., [100, 119]). Other relevant ways of encoding qubits on free electrons (not via combs) were also demonstrated, as in [28], where the Bloch-sphere algebra of the qubit was demonstrated.

For the second, efficient electron-photon quantum interaction is now at the frontier of research and is advancing quickly (e.g., [170]). The realization of integrated photonic structures inside ultrafast electron microscopes contributed to these efforts [38, 212]. The necessary coupling strengths have been recently realized using plasmonic structures [171] and photonic flat-bands [233]. Our recent work [39] summarized these advances and drew a roadmap toward free-electron quantum information processing with continuous variables.

The electron detectors' response time limits the number of feedforward operations possible before the photonic mode loses coherence. Electron detectors' response times can be very fast [comparable to Avalanche photodiodes (APDs)], on the order of hundreds of picoseconds [234]. However, electronic latency delays the feedforward process to the order of 10 ns (the electron detector and the photonic chip are separated by a meter-scale distance). In the optical range, most optical material-limited loss time for a cavity with high confinement is on the order of 10 ns

[235]. The current parameters indicate that it is possible to do approximately one feedforward operation. As discussed in Sec. IV, a single feedforward's time is sufficient since, in a quantum circuit application, the Pauli operations applied in the feedforward process can be commuted to the end of the quantum circuit in a procedure known as modifying the Pauli frame [206, 220, 236]. This circuit modification enables the computation of circuits with many feedforward gates, applying the total correction at the end, utilizing the same electronic latency in parallel. It is also important to note that electron cameras and detection technologies are not optimized for feedforward operation, and with time, the numbers are expected to improve.

The free electron can also be shaped to multilevel qudits with the GKP rotor encoding. By changing the electron comb energy gap from $2\hbar$ to $N\hbar$ [39, 211], the free electron encodes an N-level qudit in the rotor encoding [207]. One can compare the rotor states to Pegg-Barnett phase states [237]; like the rotor states, they are not normalizable, but their approximation can still be used. Based on this analogy, the approximated free-electron normalized states compare to the bosonic rotation codes state of qudit binomial or N-legged cat state. These states approximate the not-normalizable Pegg-Barnett phase states and can also be used to encode qudits by changing the spacings [238]. The binomial qudit code state and N-legged cat state can provide additional degrees of freedom that can be exploited for generating and controlling GKP states. However, they are extremely difficult to generate in optics. Free electrons can substitute these useful states and provide additional degrees of freedom. This research direction facilitates the tunability of free electrons to provide degrees of freedom that fundamentally differ from their circuit QED or trapped-ion counterparts.

4.2 Free-Electron Ramsey-Type Interferometry for Enhanced Amplitude and Phase Imaging of Nearfields

This section is based on the publication:
Tomer Bucher†, Ron Ruimy†, Shai Tsesses, Raphael Dahan, Guy Bartal, Giovanni Maria Vanacore, and Ido Kaminer.
"Free-electron Ramsey-type interferometry for enhanced amplitude and phase imaging of nearfields."
Science Advances 9, no. 51 (2023): eadi5729.
† These authors contributed equally to this work.

Abstract

The complex range of interactions between electrons and electromagnetic fields gave rise to countless scientific and technological advances. A prime example is photon-induced nearfield electron microscopy (PINEM), enabling the detection of confined electric fields in illuminated nanostructures with unprecedented spatial resolution. However, PINEM is limited by its dependence on strong fields, making it unsuitable for sensitive samples, and its inability to resolve complex phasor information. Here, we leverage the nonlinear, overconstrained nature of PINEM to present an algorithmic microscopy approach, achieving far superior nearfield imaging capabilities. Our algorithm relies on free-electron Ramsey-type interferometry to produce orders-of-magnitude improvement in sensitivity and ambiguity-immune nearfield phase reconstruction, both of which are optimal when the electron exhibits a fully quantum behavior. Our results demonstrate the potential of combining algorithmic approaches with state-of-the-art modalities in electron microscopy and may lead to various applications from imaging sensitive biological samples to performing full-field tomography of confined light.

Introduction

The interaction of electrons with static and dynamic electromagnetic fields lies at the center of numerous discoveries and applications. This interaction serves as the basic principle behind achieving atomic resolution [239]; it can result in important methods for characterizing the electronic [240] and magnetic [241] properties of materials, allows to promote and explore chemical processes [242], and helps in understanding many key cellular functions by visualizing macromolecular machines [243]. In all abovementioned examples, the nontrivial and multifaceted nature of the interaction is essential.

A prime example for the interaction of electrons with electromagnetic fields is photon-induced nearfield electron microscopy (PINEM) [12, 14, 23]. PINEM is an imaging technique relying on the inelastic scattering of free electrons from illuminated structures to reconstruct nearfield amplitudes on the nanoscale with potentially subnanometer [**lummen2016**] and subpicosecond [23, 82] spatiotemporal resolutions. Beyond the time-resolved imaging of field dynamics [244], PINEM enables a plethora of additional abilities [30, 245] such as detecting quantum emitter decoherence [246], reconstructing the quantum state of free electrons [82, 247], generating attosecond electron bunches [98, 99], and performing free-electron wavefront shaping [83, 248–251].

However, when used for imaging, PINEM extracts only the amplitude of the nearfield without any information about its phase and routinely neglects the inherent nonlinear connection

between the nearfield and electron distributions [100, 252]. Therefore, it is clear that a large amount of latent information still exists in PINEM and can be exploited for the efficient electromagnetic investigation of nanoscale objects including weakly interacting ones. This can only be achieved by integrating PINEM with another methodology, to increase the possible degrees of freedom for investigation.

In recent years, multiple techniques that rely on interferometry of electrons and light were developed to extend the abilities of PINEM. Notable examples include free-electron Ramsey-type phase control [85], which relies on premodulating free electrons with a reference field while scanning over their relative phase. Inelastic electron holography [247, 253] relies on premodulating free electrons with a reference field to generate an electron hologram of the sample field via the electron energy spectrum. Attosecond-pulse train techniques [28, 119] are based on premodulation of the free electrons followed by free propagation that shapes their charge distribution into short attosecond trains. All these techniques enable phase-resolved measurement of nearfields due to their interferometric nature. However, these techniques primarily focused on the ability to perform phase-resolved (i.e., subcycle) measurements and did not consider the possibility of enhancing the imaging sensitivity.

In this work, we will focus on Ramsey-type free-electron interactions. Although sharing similar names, this phenomenon fundamentally differs from conventional, atom-based Ramsey interferometry schemes [254], primarily because free electrons do not have a fixed set of internal degrees of freedom. Hence, the evolution of their quantum state under an applied ac electric field involves only a change in their total kinetic energy via photon absorption/emission [255], therefore applicable at arbitrary frequencies [110] and with a diverse range of samples. It boasts a large, multidimensional parameter space, including the intensities and relative phase of the applied reference and sample fields, as well as the spectral and temporal properties of the fields and the free electron itself. Thus, integrating Ramsey-type control with PINEM is highly suitable for an algorithmic approach to optimize the extracted sample information, while potentially gaining added advantage from the quantum dynamics the electron undergoes by changing its kinetic energy.

Here, we propose free-electron Ramsey-type imaging (FERI) to achieve enhanced imaging of both amplitude and phase of electromagnetic nearfields. We develop an algorithmic approach that optimizes the signal extracted from the overconstrained interaction, showing imaging with orders-of-magnitude less illumination power compared to conventional PINEM. We exemplify the approach by simulating FERI with illuminated gold nanospheres, which are potential markers in bioimaging [256–258]. FERI also enables ambiguity-immune phase-resolved nearfield imaging, requiring no prior knowledge regarding the sample, which we demonstrate by simulating the interaction of electrons with a hexagonal array of plasmonic vortices [259].

Instead of relying on transverse electron coherence, as in electron holography methods [160, 162, 260], FERI relies on temporal (longitudinal) coherence, greatly simplifying the electron source and optics, at the expense of more complex electromagnetic optics and addressing scheme. While our scheme is compatible with both quantum and classical, point-particle electrons, we provide analytical and numerical evidence that it performs optimally when the free electrons behave entirely as quantum particles. Thus, our approach promotes the use of light-driven electron microscopy in a plethora of platforms that could not have been investigated before and allows sensitive, low-dose characterization of materials, gaining advantage from the quantum nature of the free electron.

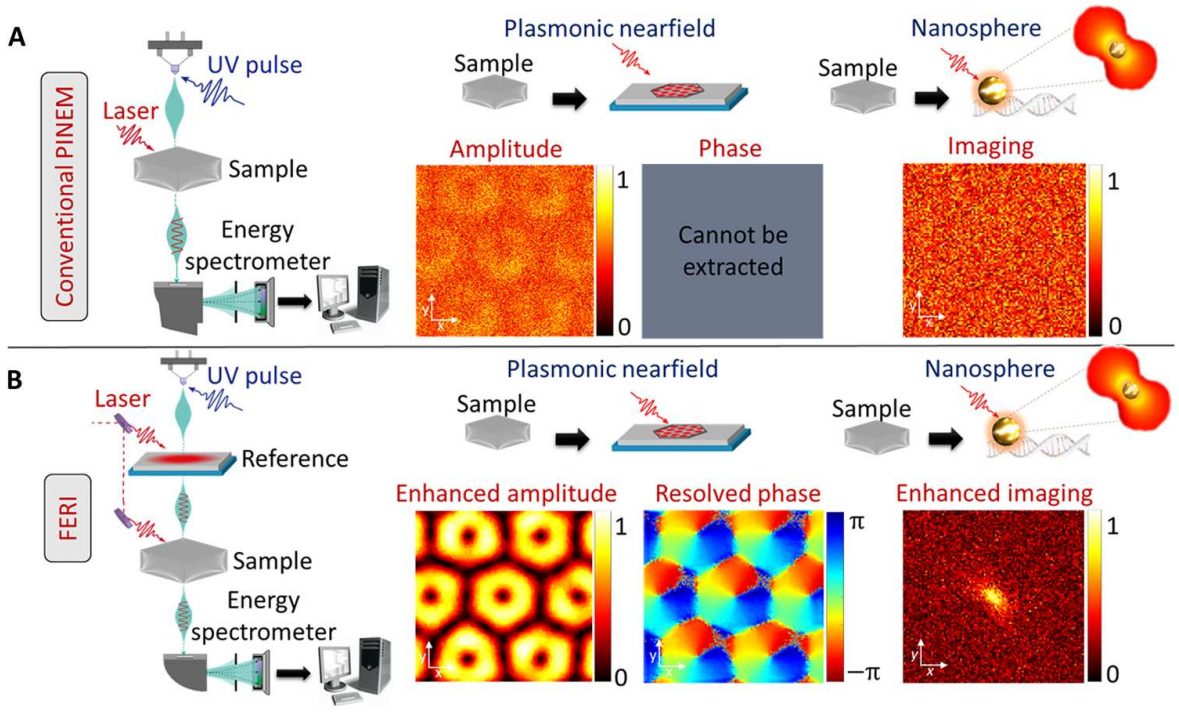


Figure 4.19: FERI: Leveraging the complex free-electron interaction with confined fields for enhanced imaging. (A) Conventional photon-induced nearfield electron microscopy (PINEM) imaging versus (B) free-electron Ramsey-type imaging (FERI). Left: The interaction configuration. Middle: Reconstruction of the amplitude and phase of plasmonic nearfields with hexagonal symmetry, at a similar noise floor and laser intensity. Right: Reconstruction of the weak nearfield induced by a gold nanosphere, which can be used as a marker for bioimaging.

Results

Imaging via premodulated electron pulses (FERI)

We begin by describing the interaction of electrons with nearfields—the theory that lies at the core of PINEM. The conventional PINEM theory usually considers an approximately monoenergetic electron of mean energy E_0 that interacts with a nearfield of central frequency ω [13]. In addition, it is assumed that the electron energy spread σ_E, which is much smaller than E_0, is also smaller than the light quanta $\hbar\omega$, such that energy measurements distinguish between different number of absorbed/emitted quanta by the electron. This situation, commonly occurring in optical and near-infrared (IR) frequencies, is akin to requiring a quantum behavior of the electron. The majority of our analysis will focus on this case, but special attention will be given to the scenario $\sigma_E \gg \hbar\omega$ when analyzing the difference between a classical and quantum electron in FERI.

PINEM theory further assumes a paraxial electron with energy substantially higher compared to the light it interacts with ($E_0 \gg \hbar\omega$), such that the dispersion of the electron can be linearized. All the abovementioned approximations are typically satisfied under the operating conditions of ultrafast scanning and transmission electron microscopes as shown in previous works in the field [12, 14, 23, 82–85, 96–99, 261]. In this case, the Hamiltonian describing the

interaction between the electromagnetic field and the electron is given by:

$$H = E_0 - i\hbar v\partial_z + \frac{evE_z(x,y,z)}{\omega} \tag{4.91}$$

Here, v is the velocity of the electron, e is the fundamental charge, and z is the direction of propagation of the electron. According to this Hamiltonian, interactions between the electron matter wave and the electromagnetic wave result in a discrete energy exchange, such that the probability P_l to measure the electron with energy $E_0 + l\hbar\omega$ (with l being an integer) is given by $|J_l(2|g|)|^2$, where $g = \frac{e}{2\hbar\omega}\int_{-\infty}^{\infty} dz E_z(x,y,z)e^{-i\omega z/v}$ is the dimensionless interaction constant. This parameter is thus the field's spatial Fourier component with wave vector ω/v.

In general, $g = g(x,y)$ is a complex number and a function of the transverse coordinates (x,y). Because of the integral linear relation between $g(x,y)$ and the electric field, the amplitude and phase of g are proportional to those of the electric field along a specific line parallel to the z axis. One can recover both the amplitude and the phase of a specific Fourier component of the nearfield $E_z(x,y,k_z = \omega/v)$, which in the case of a single nearfield mode can suffice to reconstruct the full field information [262].

In any case, currently, measuring $g(x,y)$ is the most that can be done in terms of nearfield imaging using the kind of interaction of PINEM. Using different sample tilts and electron velocities, one can in principle measure additional Fourier components of the nearfield. However, any energy-filtered spectrum measurement $\sum_{l\in L_{filter}} P_l$ can only extract information about the absolute value of the interaction constant, $|g|$.

This is the case in conventional measurement schemes (Fig. 4.19A), where one filters the signal over the entire gain side ($l > 0$) to extract the nearfield at the sample, given by the interaction constant $g_s(x,y)$. In this case, we can use identities of Bessel functions [263] to conclude:

$$Signal(x,y) \propto \sum_{l=1}^{\infty} P_l(x,y) = \frac{1}{2}\{1 - J_0[2|g_s(x,y)|]^2\} \approx |g_s(x,y)|^2 \tag{4.92}$$

In the weak field regime ($|g| \ll 1$), the signal is directly proportional to the field intensity. The quadratic dependence requires relatively intense fields to collect enough signal, making conventional PINEM inappropriate for sensitive samples.

Because g is linear in the electric field, it can contain the superposition of two spatially separated fields, one acting as a reference and the other is the unknown sample field [264]. Figure 4.19B presents the FERI scheme: It relies on the electron temporal (longitudinal) coherence to improve the detected PINEM signal at the sample by exploiting the additional coherent interaction with the reference field (with interaction constant g_r).

Figure 4.20 shows the working mechanics of the FERI scheme for phase reconstruction. By adding an additional subcycle phase delay $\Delta\phi$ between the reference and sample fields, it is possible to extract both the amplitude and phase of the sample field using energy filtering on the postinteraction electron. The relative phase delay overconstrains the measurement, as it adds up several images taken with different relative phases. The different raw measurements are sampled from different distributions, thus enhancing image contrast rather than just improving signal-to-noise ratio.

In the particularly interesting case of samples characterized by weak fields, we can replace Eq. 2 using a modified formula that takes directly into account the presence of a reference field:

$$Signal(x,y) \propto \sum_{l=1}^{\infty} P_l \approx \frac{1}{2}[1 - J_0(2|g_r|)^2] + 2J_0(2|g_r|)J_1(2|g_r|)|g_s(x,y)|\cos[\angle g_s(x,y) - \Delta\phi] \tag{4.93}$$

A critical point in Eq. 3 is the fact that the signal range of the measurement (in the limit of $|g_s| \ll 1$) scales as $|g_s|$ rather than as $|g_s|^2$. This fact alone results in substantial enhancement of the sensitivity of FERI when compared to conventional PINEM. Furthermore, using Eq. 3,

we find the optimal amplitude of the reference field interaction constant ($|g_r^{optimal}|$) for any given case where $|g_s| \ll 1$. It is given by the first positive solution to the equation $J_0(2x)^2 - J_2(2x)J_0(2x) - 2J_1(2x)^2 = 0$, which yields $|g_r^{optimal}| \approx 0.541$—a value well within reach of typical PINEM experiments [97, 246]. Using this optimal reference interaction, the signal range of the signal in a sample with maximal interaction $|g_s^m| \ll 1$ increases by the factor of $2J_1(2|g_r^{optimal}|)J_0(2|g_r^{optimal}|)/|g_s^m| \sim 0.678/|g_s^m|$. It is noteworthy that more degrees of freedom arise from this analysis, such as scanning over different reference field interaction constants $|g_r|$, or by introducing and varying free-space propagation.

This section discussed the limit of small $|g_s|$, which is the most interesting limit for sensitive samples, limited to weak illumination intensities. The analysis shows why and how FERI provides enhancement in this limit. In the following section, we describe our reconstruction algorithm, which applies for arbitrary values of $|g_s|$. The algorithm uses additional degrees of freedom of the interaction between electrons and nearfield to provide a general imaging enhancement, even in the limits of relatively large $|g_s|$.

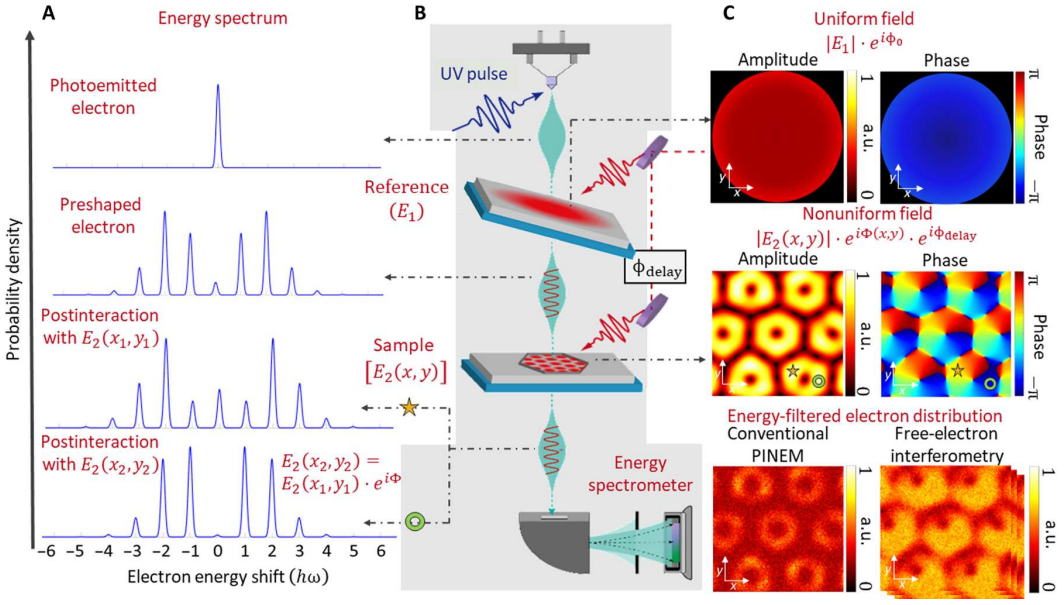


Figure 4.20: FERI measurement scheme. A free electron in an ultrafast transmission electron microscope is premodulated via an interaction with a reference field. The premodulated electron probes the sample field, which is delayed by less than an optical cycle relative to the reference field. The complex value of the field is probed by measuring the distribution of energy-filtered electrons.

Enhanced and phased-resolved nearfield imaging

PINEM applications for field imaging have thus far used energy-filtered transmission electron microscopy (EFTEM), filtering electrons over a certain range, only extracting part of the spatial information of the field. The signal in such cases is linear in the field intensity. Once we perform a premodulating interaction, the field at the sample can interfere with different interaction orders l, and by energy filtering the electrons, the nonlinearity of the relation between field and electron distributions provides substantial additional information.

The general energy-filtered electron distribution measurement can be described as $M = \sum_{l\in L_{filter}} P_l = \sum_{l\in L_{filter}} |J_l(2|g_{total}|)|^2$, with $g_{total} = g_r + g_s$ and L_{filter} being the range of filtered energies. The measured signal for each relative subcycle delay $\Delta\phi$ and each transverse

sample coordinate (x, y) is:

$$M_{x,y,\Delta\phi,L_{filter}}(|g_r|, |g_s(x,y)|) = \sum_{l \in L_{filter}} \Big| J_l \Big(2\big(|g_r|^2 + |g_s(x,y)|^2 + 2|g_r||g_s(x,y)| \cos[\angle g_s(x,y) - \Delta\phi]\big)^{1/2} \Big) \Big|^2 \tag{4.94}$$

The measurement model expression is ambiguous, i.e., multiple values of $\{|g_s|, \angle g_s\}$ can output the same value of energy-filtered electron distribution measurement, denoted as $Y(x, y, \Delta\phi, L_{filter})$. To remove this ambiguity and extract the correct field g_s, the optimization procedure (Fig. 4.21) scans over the relative phase between the reference field and sample field. By using maximum likelihood estimation (MLE) with the measurement model M, the reconstruction of the amplitude and phase of the sample is performed per (x, y) coordinate by minimizing the following expression:

$$\text{argmin}_{|g_s(x,y)|, \angle g_s(x,y)} \sum \left| Y(x, y, \Delta\phi, L_{filter}) - M_{x,y,\Delta\phi,L_{filter}}(|g_r|, |g_s(x,y)|, \angle g_s(x,y)) \right|^2 \tag{4.95}$$

The measurement scheme can also be more generally performed with scanning TEM electron energy loss spectroscopy (STEM-EELS), where the entire electron energy spectrum is measured per point.

As the MLE expression in Eq. 5 is not convex, gradient descent can converge to a local minimum. To solve this issue, the minimization method used is summation of MLE heatmaps for all relative phases, while choosing the minimum value of the joint MLE heatmap. This approach guarantees convergence to the global minima, as exemplified in Fig. 4.21 for an arbitrary phase profile and for plasmonic optical vortices simulated using the Huygens principle method [265]. After reconstructing $|g_s(x, y)|, \angle g_s(x, y)$ for every coordinate, we further use a denoising convolutional neural network (DnCNN) [266] for further signal improvement, making use of natural image prior knowledge.

Many phase retrieval methods require solving optimization problems for the transverse plane, but they often encounter ambiguities such as global phase shifts, conjugate inversions, and spatial shifts. More complex ambiguities stem from the nonconvexity of the optimization problem [267, 268]. However, FERI prevents these ambiguities because its optimization is performed per pixel instead of on the entire transverse plane.

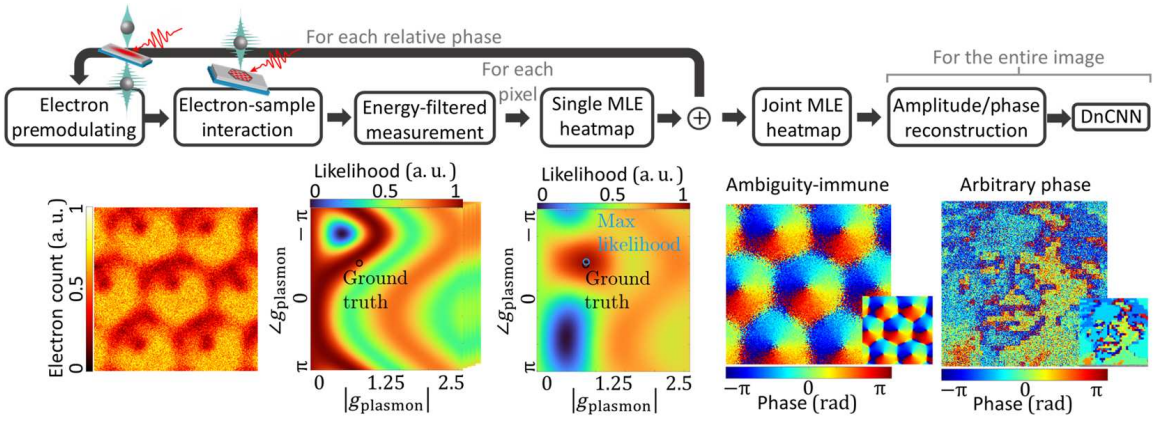


Figure 4.21: Phase-resolved optimization. Block scheme (top) and visualization (bottom) of the optimization process. For each transverse pixel, several maximum likelihood estimation (MLE) heatmaps are generated for different relative phases. The summed joint MLE heatmap enables the accurate estimation of the amplitude and phase for each pixel.

We exemplify this procedure on plasmonic standing waves with hexagonal geometry, which can be measured in PINEM experiments [269]. We measure the reconstruction fidelity relative to the ground truth using the structural similarity index measure (SSIM) [270] and use it to compare our FERI scheme with conventional PINEM. The SSIM comparison shows an improvement by almost two orders of magnitude for the minimal interaction strength necessary for the reconstruction (Fig. 4.22A).

The signal in our simulation is the empirical probability of the electron to pass a given energy filter, which then gets an additional white Gaussian noise with SD σ_N. We derive the minimal interaction strength needed to successfully image a given σ_N. For conventional PINEM, it follows $|g_{min}^{PINEM}| \approx 0.315\sqrt{\sigma_N}$; when with FERI, $|g_{min}^{FERI}| \approx 0.15\sigma_N$; and when introducing DnCNN, $|g_{min}^{DnCNN-FERI}| \approx 0.075\sigma_N$. The difference in scaling follows an approximate analytical relation for the minimal interaction strength:

$$|g_{min}^{PINEM}| \approx \frac{1}{\sqrt{2}} \cdot \sqrt{|g_{min}^{FERI}|} \approx \sqrt{2} \cdot \sqrt{|g_{min}^{DnCNN-FERI}|} \tag{4.96}$$

This square relation between PINEM and FERI is consistent with Eqs. 2 and 3.

Such improvements in sensitivity and low-dose operation are especially important when attempting to image sensitive materials or objects weakly interacting with the applied electromagnetic field. To quantify these prospects, we analyze the FERI-based enhancement of PINEM signals from gold nanospheres, which can be used as part of markers in bioimaging, sequencing, and diagnosis [258, 271–274]. Detection of nanospheres induced by weak laser fluence can be used in DNA labeling to enhance or replace fluorescence markers [**csaki2003**, 256, 275]. We envision nanospheres that are attached to DNA molecules (as illustrated in Fig. 4.22B) to help visualize, detect, and label DNA inside light-driven electron microscopes. By using laser intensities that are conventional in such experiments and identical noise floor [252], we demonstrate a quantitative advantage of FERI over PINEM. We simulated the nanosphere based on [276].

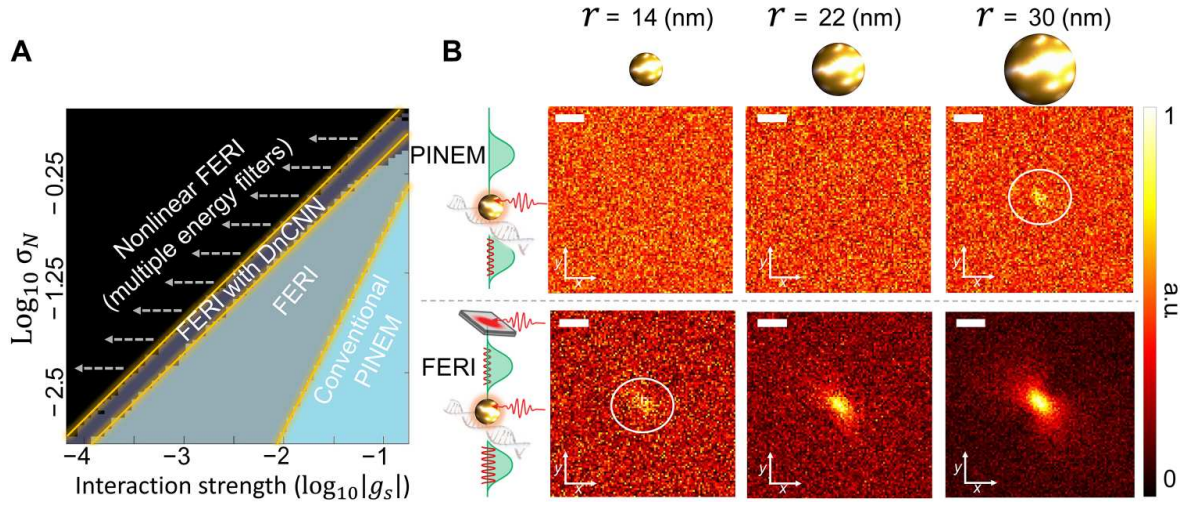


Figure 4.22: Enhanced nearfield imaging using FERI. (A) Successful amplitude reconstruction for the plasmonic field for conventional PINEM (turquoise), FERI (light gray), and with an added DnCNN (dark gray). (B) Imaging of laser-excited gold nanospheres for different sphere radii. The figure shows the reconstructed $|g_s|$ using (top) conventional PINEM imaging and (bottom) FERI.

The quantum nature of free electrons and its effect on FERI

Up until now, we only considered the electron as a quantum particle, i.e., having energy spread σ_E smaller than the light energy quantum $\hbar\omega$. In the limit $|g_s| \ll |g_r| \ll 1$, Eq. 3 directly reproduces the result of using the quantum coherence of a free electron for sensing applications [277]. In the following section, we consider the case of an electron as a classical particle, i.e., that its energy spread σ_E is larger than the light energy quantum $\hbar\omega$.

One might initially think that FERI would not be effective under these conditions, as it may appear impossible to resolve the PINEM peaks, for example, in the case of mid-IR PINEM [278]. However, even this classical electron should gain substantial improvement in sensitivity by using our scheme. The reason is that the electron-mediated interference term between the fields in Eq. 3 relies solely on the coherence of the fields, regardless of the electron energy spread. The information is then stored in the classical analog of the quantum phase—the electron velocity.

A classical, point particle electron can be directly defined by the limit $\sigma_E \gg \hbar\omega$, and it produces a conventional PINEM signal only when $|g|\hbar\omega > \sigma_E$ requiring a substantial investment of energy ($|g| \gg 1$). Although FERI should improve sensitivity, the interference term within the PINEM signal is reduced by the factor $\mathrm{erf}\left(\frac{\hbar\omega}{\sigma_E}\right)$ [210]. The direct consequence of this reduced sensitivity is a rescaling of interaction constants, increasing both the optimal reference interaction constant and the required sample interaction constant by the same factor.

In the classical regime, some electrons always pass the energy filter due to the error function, contributing a constant background signal. In this case, even in the limit of shot-noise-limited measurements, FERI introduces an additional enhancement exemplified in the linear regime by:

$$\delta g_s^{classical} = \frac{1}{2\sqrt{N}}\sqrt{\frac{a}{b^2}\cdot\frac{1}{g_{total}}+\frac{1}{b}}, \quad a=\frac{1}{2}-\frac{1}{2}\mathrm{erf}\left(\frac{E_f}{\sqrt{2}\sigma_E}\right), \quad b=\frac{\hbar\omega}{\sqrt{2\pi}\sigma_E}\cdot e^{-\frac{E_f^2}{2\sigma_E^2}} \tag{4.97}$$

where E_f is the energy filter with respect to the electron's initial mean energy E_0. Equation 7 shows that the estimation error is decreasing with respect to g_r because of the background signal, making FERI particularly useful in the case where the zero-loss peak spread is wider than the photon energy $\hbar\omega$.

Discussion

The enhancement of FERI fundamentally arises from the longitudinal (temporal) coherence of the electron (either quantum or classical). It is intriguing to compare this approach with more conventional methods that rely on transverse coherence, such as electron holography [160–162], which were recently studied with ultrafast electron microscopes [279]. Using longitudinal coherence avoids limitations due to electron beam quality and could enable operation with simpler, higher-flux electron sources. Because longitudinal electron coherence represents a robust parameter, FERI measurements can even be performed with slower electrons in scanning electron microscopes [280]. Thus, FERI seems to be a route that is easier to follow.

Possible extensions of our work can explore increasing the spatial resolution to the atomic scale, using sample tilt to perform full-field tomography, and operate at low temperatures using liquid helium cryo-holders [281], providing a unique probe for cold condensed matter physics. The sensitivity enhancement showed in this work also makes FERI a promising approach to demonstrate enhanced cathodoluminescence [32, 33, 282] as well as free-electron-bound-electron resonant interaction [41], which had not been realized experimentally so far, due to its intrinsically weak interaction.

4.3 Coherently Amplified Ultrafast Imaging Using a Free-Electron Interferometer

This section is based on the publication:
Tomer Bucher†, Harel Nahari†, Hanan Herzig Sheinfux, Ron Ruimy†, Arthur Niedermayr, Raphael Dahan, Qinghui Yan, Yuval Adiv, Michael Yannai, Daniel J. Masiel, Jialin Chen, Yaniv Kurman, Sang Tae Park, Eli Janzen, James H. Edgar, Fabrizio Carbone, Guy Bartal, Shai Tsesses, Giovanni Maria Vanacore, Frank H. L. Koppens, and Ido Kaminer.
Nature Photonics 18, 809–815 (2024).
† *These authors contributed equally to this work.*

Abstract

Accessing the low-energy non-equilibrium dynamics of materials and their polaritons with simultaneous high spatial and temporal resolution has been a bold frontier of electron microscopy in recent years. One of the main challenges lies in the ability to retrieve extremely weak signals and simultaneously disentangling the amplitude and phase information. Here we present free-electron Ramsey imaging—a microscopy approach based on light-induced electron modulation that enables the coherent amplification of optical near fields in electron imaging. We provide simultaneous time-, space- and phase-resolved measurements of a micro-drum made from a hexagonal boron nitride membrane, visualizing the sub-cycle dynamics of two-dimensional polariton wavepackets therein. The phase-resolved measurement reveals vortex–anti-vortex singularities on the polariton wavefronts, together with an intriguing phenomenon of a travelling wave mimicking the amplitude profile of a standing wave. Our experiments show a 20-fold coherent amplification of the near-field signal compared with conventional electron near-field imaging, resolving peak field intensities in the order of a few watts per square centimetre, corresponding to field amplitudes of a few kilovolts per metre. As a result, our work paves the way for the spatiotemporal electron microscopy of biological specimens and quantum materials, exciting yet delicate samples that are currently difficult to investigate.

Introduction

Free-electron physics has had a profound impact on many areas of science and technology, from electron microscopes and X-ray sources to microwave sources and accelerators. At the heart of all these applications lies the fundamental interaction between free electrons and electromagnetic fields [30, 50, 283]. This interaction can be enhanced by modulating the electrons before (and in some cases, after) the interaction [280, 284]. This electron modulation is key to applications such as electron radiation and electron acceleration, as recently demonstrated in dielectric laser accelerators [285, 286].

Electron modulation can be achieved through either classical or quantum-mechanical methods, by shaping the longitudinal electron distribution or electron wavepacket, respectively. In both cases, electron modulation can be performed by laser interaction, as inspired by research into photon-induced near-field electron microscopy (PINEM) [12]. PINEM was originally conceived as an imaging technique realized via ultrafast transmission electron microscopy (UTEM). Nevertheless, at its core, PINEM relies on a fundamental interaction: inelastic scattering of free-electron pulses by optical near fields.

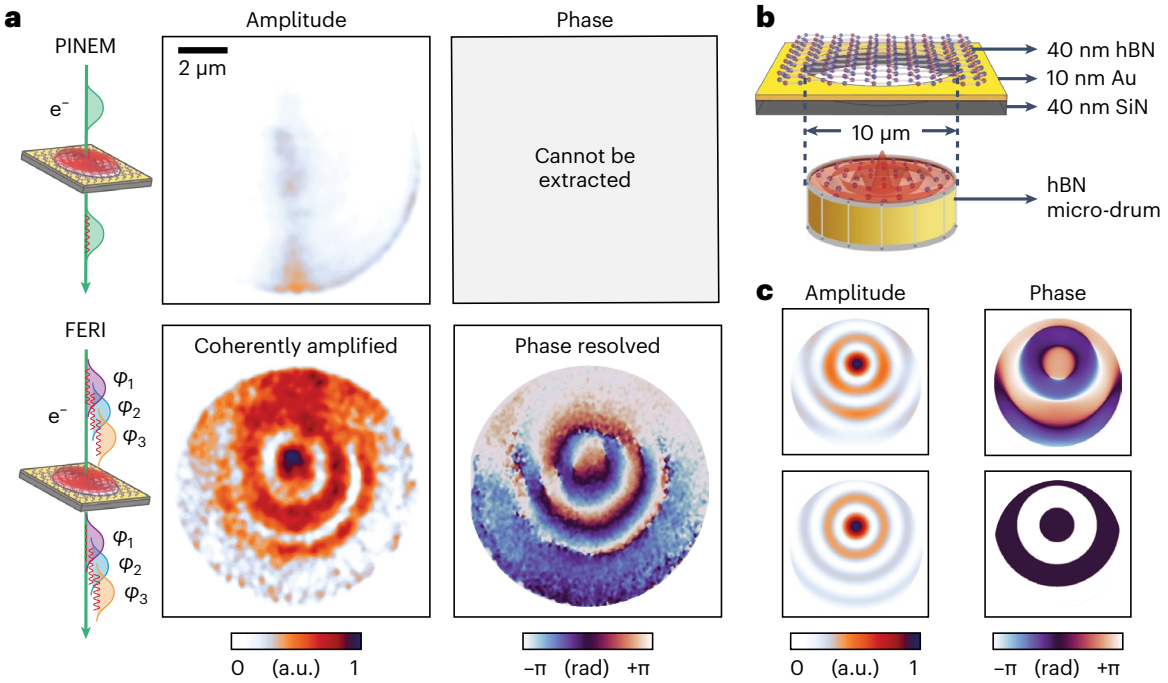


Figure 4.23: FERI: utilizing electron modulation for coherently amplified imaging of optical near fields. a, Conventional PINEM (top) scheme compared with FERI (bottom). Modulated electron interference enables the measurement of weaker field intensities and phase resolution, which are inaccessible using conventional PINEM with the same electron dose and laser intensity. The FERI and PINEM amplitude images under the "amplitude" title are normalized to have the same contrast as achieved experimentally. **b**, Platform in which we demonstrate the concepts of this work via a micro-drum made from an hBN membrane. A pump pulse in the mid-IR range couples at the circular boundary, exciting a phonon-polariton wavepacket that propagates and interferes, resulting in a wave pattern with an amplitude profile that resembles a standing wave in a drum. **c**, Simulations show that waves of fundamentally different types can look similar in their amplitude profiles and have drastically different phase profiles. Conventional PINEM extracts the amplitude profile, whereas FERI additionally extracts the phase profile and can, therefore, distinguish between the different wave types. For example, the amplitude profile in **a** resembles a standing-wave mode of a drum. However, the phase profile reveals that the wave is, in fact, not a standing wave, but a different wave phenomenon with a phase resembling that of a travelling wave. The polaritons travel inside a 40-nm-thick layer of hBN, which is held on top of a 10-nm-thick gold frame situated on a 40-nm-thick silicon nitride substrate. A circular hole with a radius of 5 μm is drilled through the gold and silicon nitride layers. Notice that the illumination angle breaks the up–down symmetry, inducing a progressive phase that shifts the interference pattern from the centre.

This interaction allows one to reconstruct the near-field amplitudes down to a single-nanometre spatial resolution [12, 97, 244, 246] and sub-picosecond temporal resolution [278]. In fact, PINEM enabled a range of imaging modalities in a variety of nanophotonic and condensed-matter systems, including surface polaritons [244, 252, 278], nanocavities [97, 246] and nanoscale plasma or charge distributions [287, 288].

Apart from imaging applications, the electron–laser interaction in PINEM-type experiments has also inspired various electron modulation schemes. This modulation allows one to recon-

struct the electron's quantum state [23, 289] and to extract the coherence and decoherence times of quantum emitters [82]. A notable application of PINEM-modulated electrons is to retrieve the temporal phase information of the optical field in a scheme coined as free-electron Ramsey-type phase control [36]. Such a scheme has been used to reconstruct the sub-cycle dynamics of terahertz [85] and optical [24, 98, 247, 290] fields. However, despite the wide range of applications enabled by electron modulation, this approach has never been used to amplify microscopy itself, that is, it was not used to increase the sensitivity in near-field imaging with electron microscopes.

Here we propose and demonstrate the coherent amplification of the electron imaging of optical near fields, relying on optically modulated free electrons for probing the investigated sample (Fig. 4.23a). Conceptually, our imaging scheme can be thought of as a frequency-tunable Ramsey interferometer [291], performing measurements simultaneously at each point in the sample. Thus, we dubbed this imaging scheme as free-electron Ramsey imaging (FERI). We use FERI to specifically demonstrate the coherently amplified imaging of polariton dynamics in a hexagonal boron nitride (hBN) flake held on a gold frame, forming a micro-drum structure supporting novel phonon-polariton wave excitations (Fig. 4.23b,c). Compared with conventional PINEM, we show that FERI yields a 20-fold coherent amplification of the raw signal contrast, with further enhancement owing to the electron–field interaction theory that underlies the algorithmic scheme. The overall enhancement enables the retrieval of an image when adopting incident intensities as low as a few watts per square centimetre, paving the way to new kinds of microscopy experiment in scenarios that were previously beyond reach due to electron or laser dose sensitivity. Examples include quantum materials like high-T_c superconductors [292], and even soft matter, where maximizing the signal with a limited dose is essential.

It should be noted that recent advances in ultrafast electron diffraction and microscopy have enabled the imaging of phonon dynamics [293]. In particular, UTEM has been applied to visualize the dynamics of acoustic phonon wave propagation in two-dimensional (2D) materials [293, 294]. Our work takes a completely different path, investigating optical phonons hybridized with electromagnetic fields, also known as phonon polaritons [295–297]. Compared with acoustic phonons, the (optical) phonon polaritons have completely different dispersion relations, for example, hyperbolic dispersion as in the hBN phonon polaritons that we investigate in this work. The phonon polaritons also evolve on shorter timescales (from a few femtoseconds to a few picoseconds) relative to their acoustic counterparts. Such timescales necessitate a method like FERI to investigate the sub-cycle oscillations, that is, study the complete phase dynamics. The sub-cycle dynamics was impossible to observe without FERI, by just using conventional PINEM [278].

Standing-wave profiles and travelling-wave phases

Combining the phase- and time-resolved capabilities of FERI reveals a surprising polariton phenomenon. The polaritonic wavepacket (whose amplitude is linear to that of the excitation pump laser) exhibits a multi-ring amplitude profile resembling a standing wave (Fig. 4.23c, left). Indeed, based on the amplitude measurements alone (that is, using conventional PINEM), the polariton could be identified as a standing wave. However, extracting the phase information from FERI reveals that the wavepacket acquires a continuous phase as it propagates, in stark contrast with a standing wave (Fig. 4.23c, right). Therefore, the polariton wavepacket cannot be classified as either a conventional travelling wave or as a standing wave. This is a new and intriguing observation in an hBN phonon-polariton micro-drum, which is reminiscent of known effects in acoustics [298]. The observation of such a behaviour has been made possible only owing to the phase-resolving capability of our FERI technique and warrants additional future research.

Experimental system for phase- and time-resolved imaging

We realize FERI in a modified UTEM (Fig. 4.24a). In a conventional system, a femtosecond laser pulse is split into two pulses. One pulse (pump) impinges on the investigated sample, and the other pulse (probe) is frequency upconverted into an ultraviolet (UV) pulse using fourth-harmonic generation, which photoemits an electron pulse from the cathode. Together, such a system implements a pump–probe scheme with an electron as the probe. In contrast, in our modified system, the pump pulse is split into two pulses (Fig. 4.24a). Specifically, for the experiments shown here, the pulse is frequency downconverted into the mid-infrared (mid-IR) range using difference-frequency generation (DFG) in an optical parametric amplifier (OPA) before being split. The first pump pulse impinges on the investigated sample, whereas the second pump pulse does not interact with the sample, and instead modulates the electron before that electron probes the sample (the reference and sample order can be changed with similar outcomes). Together, the modified system implements a pump–pump–probe scheme, with the electron as the probe. Variants of this scheme were realized in transmission electron microscopy (TEM) instruments under different constraints, for example, using separate light-coupling ports for a continuous-wave operation [24, 247] or combined into a single port for pulsed operations, splitting the two points of interaction [85] or keeping them together [252].

We modify the conventional operation of a UTEM instrument by installing a specially designed component called the photonic electron modulator (PELM). This modification enables the independent tunability of the two pulses in two separate light-coupling ports, controlling their relative delay, intensity and polarization, as well as other options. Specifically, the electron modulation is implemented by a flat aluminium (Al)-coated Si_3N_4 membrane, which is tilted at an angle of 41° with respect to the electron propagation direction to ensure transverse electron–light phase matching. The electrons penetrate through this membrane simultaneously with the laser pulse impinging on it. The flat membrane acts as a light-reflecting mirror, providing the reference interaction shown in Fig. 4.24a, as well as being relatively electron transparent to allow further interaction with our micro-drum.

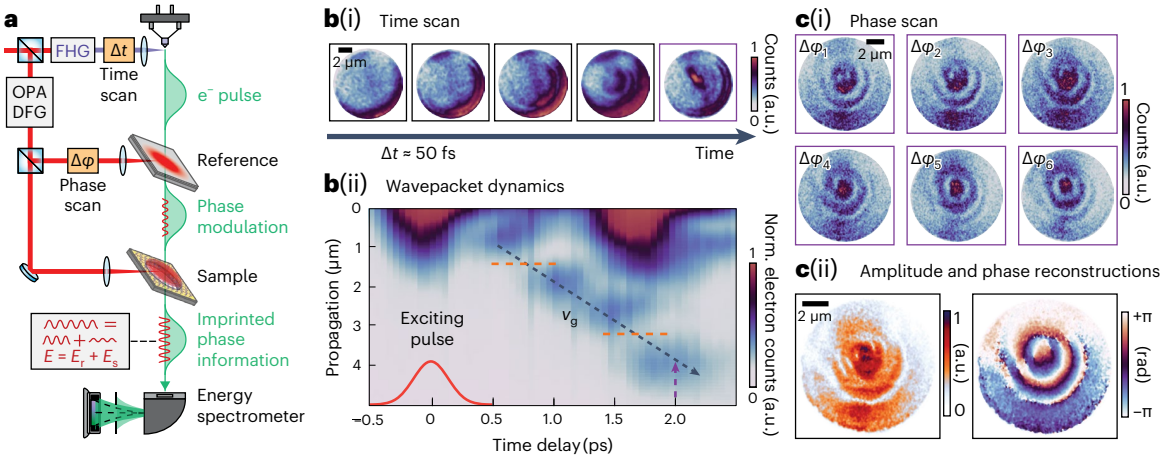


Figure 4.24: Time- and phase-resolved imaging of polariton wavepackets. a, FERI scheme: splitting a femtosecond laser pulse into three parts, enabling both ultrafast time-resolved and phase-resolved imaging. Two delay stages are used to control the timing of the laser pulses with respect to the electron pulse. The effective field modulating the electron after both interactions (E) is the superposition of the field at the reference (E_r) and the field at the sample (E_s)—an interference mediated by the electron. FHG, fourth-harmonic generation. **b**, Time-resolved imaging (i) presenting selected raw PINEM data frames at different time delays between the UV pulse and the exciting laser with 50 fs time differences. The dark parts correspond to the polaritonic wavepacket propagating from the edges to the centre and undergoing interference with other parts of the wavepackets. The polariton wavepacket dynamics is presented in a map (ii) where the propagation axis represents the dynamics along the radius, averaged along a semicircle. The polariton wavepacket propagates with a group velocity of $v_g \approx c/200$, marked by a black dashed arrow. The wavepacket "hops" over certain radii at which we observe a very low intensity (dashed orange lines). This behaviour is not expected from conventional travelling waves that continuously propagate, and is not expected for conventional standing waves that do not propagate. Instead, this behaviour is consistent with the observation (Fig. 4.23) of a simultaneous standing-wave amplitude and travelling-wave phase profiles. The red feature at the top right of the map is due to the arrival of a second excitation pulse, coupling at the edge. **c**, Phase-resolved imaging (i) presenting selected raw FERI data frames at different sub-cycle delays, corresponding to different relative phases between the modulation and sample excitation. Algorithm-aided reconstruction of the amplitude and phase profiles from the raw FERI data frames using all the phases (ii). The phase scan is performed around a time delay of 2 ps, marked by the purple frame in **b**(i) and a purple dashed arrow in **b**(ii).

FERI: concept and results

Our FERI experiment extends on previous works [24, 85, 247, 252] by one important development: coherent amplification of electron imaging. All the above-mentioned modified UTEM instruments provide a controllable phase relation between the electron modulation and the induced near field on the investigated sample (this is possible because both pump pulses were split from the same laser pulse). Our demonstration of coherently amplified imaging requires an additional development, which can be summarized in two stages: (1) acquiring raw modulated electron images, by uniformly scanning over the relative phase; (2) applying a reconstruction

algorithm on the raw images, extracting high-contrast phase and amplitude of the sample near field. We calibrate our measurement by acquiring electron-energy-filtered images without inducing field on the sample, and by taking separate electron energy spectra measurements to estimate the strength of the reference interaction. After its interaction with the sample, each modulated electron can be characterized by measuring its electron energy spectrum, which depends on the sample near field and its phase relative to the reference interaction. We specifically use electron energy filtering on the electron image. Consequently, for each choice of modulation phase, the raw electron image provides different information about the near field at the sample. By combining the raw images, our algorithm yields the phase and amplified contrast in the amplitude profile, meaning that weaker fields can be reconstructed with the same electron dose. For example, Fig. 4.23a compares two images acquired with the same total electron dose and same field intensity on the sample, showing the advantage of FERI over conventional PINEM, with a 20-fold increase in the resulting signal contrast.

At every pixel, our scheme is analogous to Ramsey interferometry in atomic physics [254] or to homodyne detection in optics [299]. However, this analogy is not precise. Only for special cases, depending on the interaction strength and on the distance between the modulation stage and sample, our algorithm reproduces the regime where the Radon transform is used in conventional homodyne detection. However, for the general case, our algorithm goes beyond the Radon transform [48]. This more general case is necessary for our experiment.

Next, we apply FERI to investigate phonon-polariton wavepackets in hBN and measure their group and phase dynamics. Figure 4.24b illustrates the wavepacket propagation from the Au edge of the micro-drum towards its centre (a radial half-circle profile). The slope of the dashed black arrow (Fig. 4.24b(ii)) corresponds to the group velocity of the excited wavepacket, which is measured to be $v_g \approx c/200$. By using modulated electrons and by performing a sub-cycle delay scan between the two points of interaction, the phase dynamics of the phonon-polariton wavepacket is retrieved.

A peculiar feature of the polariton wavepacket dynamics is highlighted in Fig. 4.24b, where we present the polaritonic field intensity averaged along a semicircle as a function of radius. The laser pulse excites a narrow wavepacket (roughly 1 μm wide) that propagates from the edge towards the centre. The black dashed arrow marks the polariton wavepacket propagation, revealing the unusual feature of wavepacket "hopping": certain rings at fixed radii remain low in their intensity throughout the dynamics. These rings appear as dark lines in Fig. 4.24b (marked by the dashed orange lines). One typically expects stationary features of zero intensity to be a hallmark of standing waves. But this is not the case here, since the polariton wavepacket has a wide bandwidth and its width is too small. Rather, this hopping behaviour is consistent with the observation from Fig. 4.23 about the polariton wavepacket simultaneously having a standing-wave-like amplitude profile and a travelling-wave-like phase accumulation.

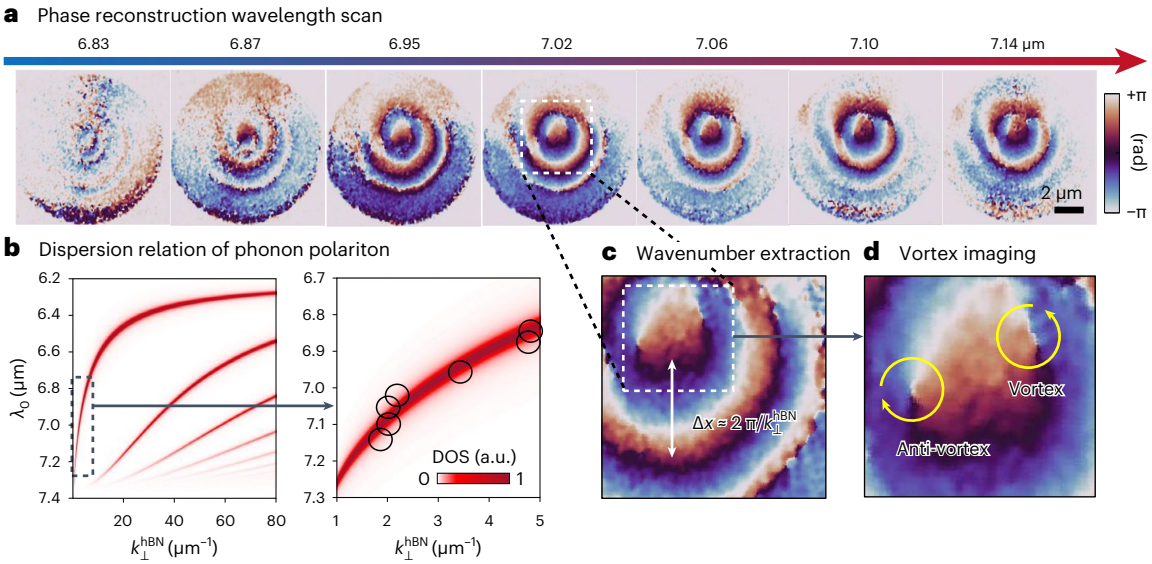


Figure 4.25: Intrinsic phonon-polariton properties extracted via FERI: direct measurement of the polariton phase velocity and identification of a vortex–anti-vortex pair. a, FERI phase reconstruction for different wavelengths. The exciting laser power at the presented different wavelengths is around 2 nW. **b**, We use the distance between consecutive equal-phase circles for the direct extraction of the polariton's wavenumber (and phase velocity). The dispersion relation of phonon polaritons in hBN, with circles marking the extracted wavenumbers. The density of states (DOS) dispersion relation is achieved by calculating the reflection coefficient of air–hBN–air scattering, where the thickness of the hBN is taken to be 45 nm, as estimated from a TEM measurement. **c**,**d**, Zoomed-in views of a phonon-polariton phase profile reveal that the nodal point at the centre of the micro-drum wave comprises a vortex–anti-vortex pair, an inevitable result of symmetry breaking in the system [300]. By extracting the exact phase, FERI enables measuring the chirality of each vortex.

Sub-cycle dynamics of polariton wavepackets

Figure 4.25a depicts the phase profiles for different excitation wavelengths, each retrieved from a scan of sub-cycle time delays on the modulated electrons (Fig. 4.24c). These phase profiles provide a direct measurement of the phonon-polariton wavenumber. We extract the wavenumbers from the inverse distance over which the phase of the wavepacket accumulates 2π, and compare them with theory (Fig. 4.25b; black circles on top of the theoretical dispersion of hBN phonon polaritons). The direct measurement of dispersion further establishes that the phenomenon we observe is phonon-polariton dynamics.

The phase reconstruction capability of FERI enables to pinpoint another intriguing phonon-polariton phenomenon. We show the coexistence of vortex–anti-vortex singularities at the nodal point located in the centre of the micro-drum wave (Fig. 4.25c). This occurrence is a consequence of symmetry breaking. The circular symmetry of the geometry is broken by the exciting laser pulse, which comes from a particular direction, splitting the original nodal lines of zero amplitude and no orbital angular momentum into a pair of polariton vortices of opposite chirality [300]. The opposite chirality of the vortices guarantees that the left–right mirror symmetry is preserved (as the laser comes from the up–down direction, breaking only this symmetry). We note that vortices have been previously observed in conventional PINEM [23], but identifying the vortex

chirality is only made possible in FERI.

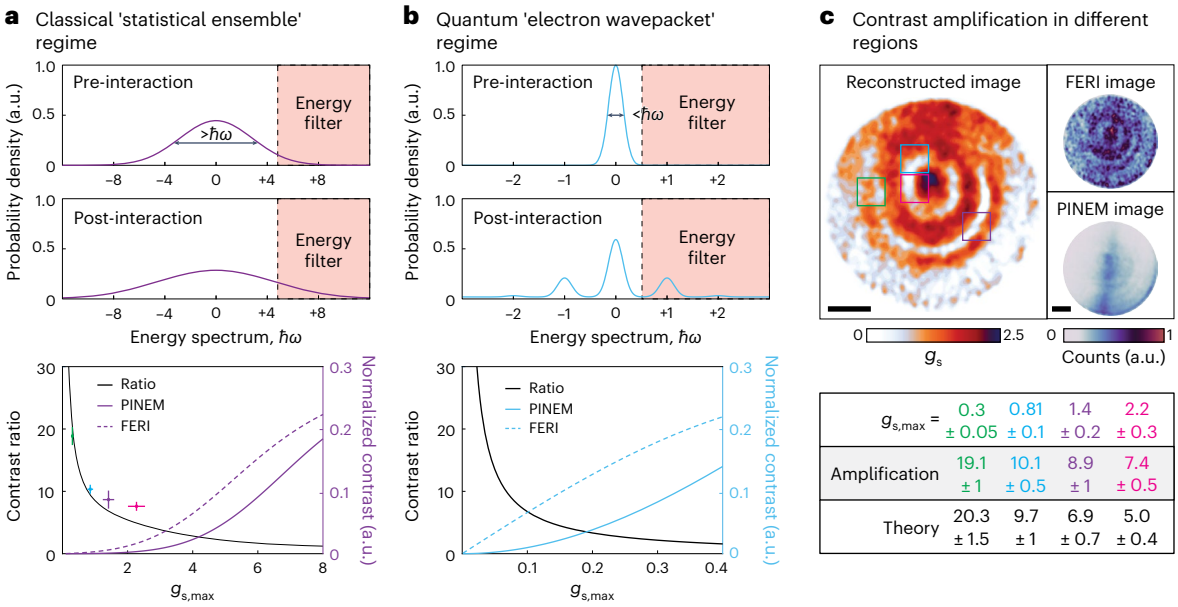


Figure 4.26: Prospects of FERI for precision measurements of weak fields, and comparison between classical and quantum regimes. **a**, Coherent amplification in the classical regime (electron energy spread wider than $\hbar\omega$, taken in our simulation to be $3.5\hbar\omega$ corresponding to our experiment), which is demonstrated in this work. The values from the table in **c** are marked on the theoretical curve (error bars correspond to the values in the table). The experimental parameters are used to draw the theory curves. **b**, Coherent amplification in the quantum regime (electron energy spread narrower than $\hbar\omega$), showing prospects for additional amplification beyond the classical regime, achieving higher contrast for smaller signals at the sample [48]. **c**, Coherent amplification of electron imaging, showing the contrast amplification in different regions of the sample. The regions from which we extract the corresponding values of g_s are marked on the reconstructed image (top left). The table presents experimentally measured g_s values with the corresponding extracted and theoretical amplification factors (bottom). The error values assigned to $g_{s,\max}$ are defined by the difference between the 90th percentile to the maximum value of the region. This derives the error values of the contrast. We extract the contrast from the regions in the raw data collected by FERI and by conventional PINEM (top right). Although the collection time in FERI (20 s) is 21 times shorter than that of the PINEM image (420 s), the features of the phonon-polariton near field are already more visible in the FERI image. The total integration time of 420 s corresponds to an electron dose of roughly $0.2e\,\mathrm{nm}^{-2}$ (estimated from measuring the electron counts on the camera without the sample). Scale bars, 2 μm.

Coherent amplification of electron imaging contrast

In this section, we quantify the coherent amplification of the electron image contrast (defined as the difference between the upper and lower tenth percentile of the signal). The signal is normalized by having the same electron dose on the sample in all the measurements. Recalling that the conventional PINEM signal of an electron with velocity v moving along z depends on a dimensionless parameter $g(x,y) = \frac{q_e}{\hbar\omega}\int_{-\infty}^{\infty} dz\, E_z(x,y,z)e^{-iz\omega/v}$ [13, 14], where q_e is the

electron charge and ω is the angular laser frequency. Here g_s denotes the PINEM parameter for the sample signal field E_s, and g_r denotes the PINEM parameter for the reference field E_r. Figure 4.26c presents the contrast values extracted from the measurements of FERI in different areas of the image that have different field intensities. In each region, we choose the relative phase in FERI such that the maximum contrast is achieved. In all these cases, the contrast is larger than the contrast in conventional PINEM. A comparison of the raw data from FERI and PINEM (Fig. 4.26c) already shows the enhanced contrast by coherent amplification (despite an acquisition time shorter by a factor of 21). Overall, the contrasts ratios qualitatively correspond to the theory shown in Fig. 4.26a. In some areas of the sample, the amplification factor approaches 20, exemplifying the advantage of coherent amplification.

Discussion

When applying FERI theory in actual experiments, we separate between two cases: (1) electron energy spread ΔE larger than the photon energy $\hbar\omega$ (classical regime; Fig. 4.26a), and (2) ΔE smaller than $\hbar\omega$ (quantum regime; Fig. 4.26b). Comparing these two regimes shows the advantage of the quantum regime for small $|g_s|$, whereas the situation is more complex for larger $|g_s|$ as in our experiment. The advantage of the quantum regime lies in the fact that it is easier to distinguish electrons that absorb or emit even just one photon from those that did not change their energy.

To estimate the minimum field amplitude E_s that is possible to image with FERI, consider that the PINEM parameter interaction strength satisfies $g_s \approx E_s q_e L/(\hbar\omega)$ [13, 14], where L is an effective interaction length between the electron and field. For the phonon polaritons we observed, L is typically in the range of a few micrometres. We estimate the weaker features that were successfully resolved in Fig. 4.26 to have $g_s \approx 0.2$ (as extracted from the reconstruction), corresponding to a field E_s of a few kV m^{-1} or intensities at around 1 W cm^{-2}.

It is important to differentiate the phase-resolved near-field imaging capabilities enabled by modulated electrons from the most established methods of phase-resolved near-field measurements. In particular, photoemission electron microscopy [301] is based on the nonlinear response of the target sample, which becomes less efficient for low-energy photons as in the mid-IR range. Hence, this approach is not easily applied to investigate phonon polaritons in 2D materials, which are typically present in the mid-IR range or at lower photon energies. Moreover, photoemission electron microscopy is limited to probing phenomena near surfaces, unlike FERI, which is inherently sensitive to the bulk. The ability to probe the internal optical field inside the bulk is relevant in scenarios where the fields are strongly confined inside the bulk (more than that in our work), such as guided optical modes in semiconductors or polaritons in hyperbolic materials in the optical range. This latter difference also distinguishes FERI from scattering-type scanning near-field optical microscopy [302, 303]. Generally, near-field measurements using scanning tips are well established over wide spectral bandwidths and can be performed with an ultrafast source [301], too. However, the reconstruction of the polaritonic field from the measurement is often limited by requiring precise modelling and assumptions on the tip–field interaction. More generally, unlike tip-based techniques that inevitably disturb the near field, the electron probe can measure the near field without altering it.

Outlook

The ability of FERI to measure the amplitude and phase of the fields inside the bulk of a sample, too, opens a set of intriguing capabilities. By collecting angle-dependent measurements, FERI can be used for full tomography and extract the three-dimensional profile of an electromagnetic

mode. This would be a completely new type of measurement. A notable application that could arise from full tomography is imaging deeply confined polaritons, such as acoustic graphene polaritons [304] and picocavity polaritons [305, 306]. These polaritons are often inaccessible by conventional surface techniques. FERI facilitates the detection of such polaritons also by coherently amplifying their low intensity.

The coherently amplified sensitivity of FERI to low-intensity fields may also provide access to highly desired polariton nonlinearities in van der Waals and phononic materials [307]. Such nonlinearities are typically challenging to observe due to the small variation in their polaritonic wavelengths. Looking forward, FERI's ability to image low-intensity fields may open new modalities for imaging biological samples and other dose-sensitive materials [308, 309], which were, so far, beyond the reach of PINEM because they necessitated field intensities that were too high [14]. Electron modulation in FERI reduces the necessary field intensity and increases the amount of information that can be extracted by each electron. Thus, FERI reduces the number of electrons needed to pass by the sample, minimizing both laser damage and electron radiation damage.

Enticing goals that could now be attempted include quantum materials [310, 311], such as encapsulated 2D superconductors [292] and others that were, so far, beyond reach. From a fundamental perspective, the coherent amplification of the intrinsic electron–photon interaction of quantum electrodynamics could eventually enable the observations of electron interactions with few-photon states or with squeezed vacuum fluctuations [34, 35, 171, 312].

Chapter 5

Unpublished Works

5.1 Engineering Free-Electron Entanglement via Virtual Cavity-Photon Exchange

This section is based on yet to be published work which is the final theoretical work of my PhD:
Ron Ruimy, Zhexin Zhao, Ido Kaminer, and Aviv Karnieli

abstract

The ability to shape and control the quantum states of free electrons has established a new paradigm, free-electron quantum optics. However, generating deterministically entangled states of multiple free electrons remains a fundamental challenge. Here, we propose a general mechanism to engineer controllable multi-electron entanglement through dispersive interactions with a photonic cavity mode. We develop a formalism to describe the interaction of paraxial electrons with a general electromagnetic environment in thermal equilibrium. By operating in the strongly detuned, virtual-photon exchange regime, free electrons have limited dissipative coupling to the environment, which either causes decoherence or requires probabilistic post-selection on the photonic state. Bypassing this limit allows us to induce coherent many-body interactions. We specialize this framework into two distinct regimes: an energy-entanglement regime mediated by optical cavities, and a spatial-entanglement regime mediated by microwave cavities. The energy entanglement generates an entangled energy comb that can be directly diagnosed using photon-induced near-field electron microscopy (PINEM). Furthermore, we demonstrate that the spatial entanglement regime is highly relevant for quantum metrology; the interaction naturally maps to a collective one-axis twisting Hamiltonian, yielding optimal spin squeezing and enhanced Quantum Fisher Information for sub-shot-noise phase measurements in Ramsey-type electron interferometers.

Introduction

Recent theoretical and experimental breakthroughs have given rise to the emerging field of free-electron quantum optics [1, 30, 283, 313]. Free-electron quantum optics treats electrons and electromagnetic fields as unified quantum entities, placing them on equal footing within the frameworks of quantum electrodynamics and quantum optics. This shift positions the free electron as a quantum resource that combines nanometer-scale spatial resolution with femtosecond timescales. Consequently, free electrons have been proposed for numerous quantum information applications, including the manipulation and measurement of atomic excitations [41–43, 110] and photonic quantum states [37, 38, 40, 115, 170, 277, 314, 315].

A central goal in the field is the generation of deterministically entangled states of multiple free electrons [34, 36, 49, 316]. However, this remains an open problem. While electrons interact via free-space Coulomb forces [44, 45], generating genuine quantum entanglement through this channel requires their spatial separation to be strictly smaller than their coherent position spread to introduce 'which-is-ahead' quantum ambiguity [46, 317]. However, this overlapping regime is, as of now, practically inaccessible in free space.

Alternatively, electrons can be coupled to optical fields such as cavity modes. However, typical free-electron–light interactions, such as those driving photon-induced near-field electron microscopy (PINEM) [12–14, 23, 26, 37, 38, 97, 246], are predominantly inelastic. When the electron velocity matches the phase velocity of the light, the particles exchange real quanta of energy and momentum [13, 34, 35]. This real photon emission or absorption unavoidably couples

the electron to the lossy photonic environment (see Fig. 5.27a1). Relying on such dissipative, inelastic processes to generate or infer multi-electron states either induces rapid decoherence or requires probabilistic, heralded post-selection on the emitted photons [34, 49]. Another recent proposal suggested to utilize elastic ponderomotive interactions with electromagnetic fields [318], however such method is also non deterministic by nature and requires integrating high-precision optical interferometry measurements into an electron microscope.

Here, we propose a general mechanism to engineer deterministic, controllable multi-electron entanglement through dispersive interactions with a photonic cavity mode (see Fig. 5.27a2). We develop a theoretical formalism based on macroscopic quantum electrodynamics (MQED) in the temporal gauge [94, 319] to describe the interaction of paraxial electrons with a general quantized electromagnetic environment in thermal equilibrium. By operating in the strongly detuned, virtual-photon exchange regime, we deliberately phase-mismatch the real photon emission (Fig. 5.27b). This suppresses the non-unitary dissipative channels that lead to environmental decoherence, isolating a purely coherent many-body interaction mediated exclusively by virtual cavity photons. This cavity-mediated mechanism is conceptually analogous to dispersive cavity quantum electrodynamics (cQED). In those architectures, far-detuned optical or microwave modes are routinely utilized to generate entanglement between stationary atoms or superconducting qubits without suffering from spontaneous emission decay [320, 321].

We specialize this framework into two distinct physical regimes (outlined in Fig. 5.27c):

- **Energy Entanglement via Optical Cavities:** In the longitudinal degree of freedom, the dispersive interaction generates a perfectly correlated, continuous-variable entangled energy comb. Unlike free-space Coulomb interactions, which require the electrons to be closer than their coherence length to create "which-is-ahead" quantum ambiguity, our cavity mechanism only requires the electrons to occupy the cavity at the same time while their individual coherent position spreads exceed the optical wavelength ($\sigma_z > \lambda_{\mathrm{mode}}$). Because this matches the typical operating conditions found in PINEM experiments, the discrete energy correlations can be diagnosed via electron multi-electron PINEM experiments with coincidence detectors [46], opening new avenues for quantum-enhanced spectroscopy and free-electron quantum information processing.

- **Spatial Entanglement via Microwave Cavities:** In the transverse degree of freedom, we map the continuous electron wavepacket onto a discrete path-qubit basis. We operate in the regime where the spatial extent of the entire electron bunch is much smaller than the microwave wavelength. We demonstrate that the cavity interaction naturally maps to a collective one-axis twisting ($\hat{H}_{\mathrm{eff}} \propto \hat{S}_z^2$) Hamiltonian, where $\hat{S}_z$ is the collective spin operator. This interaction redistributes quantum noise to generate spin-squeezed states [322, 323], enabling Ramsey-type electron interferometers [324] to surpass the Standard Quantum Limit and achieve sub-shot-noise phase sensitivity with an enhanced Quantum Fisher Information approaching the fundamental Heisenberg limit for quantum-enhanced metrology [325]. This paves the way toward the sought-after goal of constructing a quantum-enhanced electron microscope [21, 146, 147, 149, 150, 326, 327].

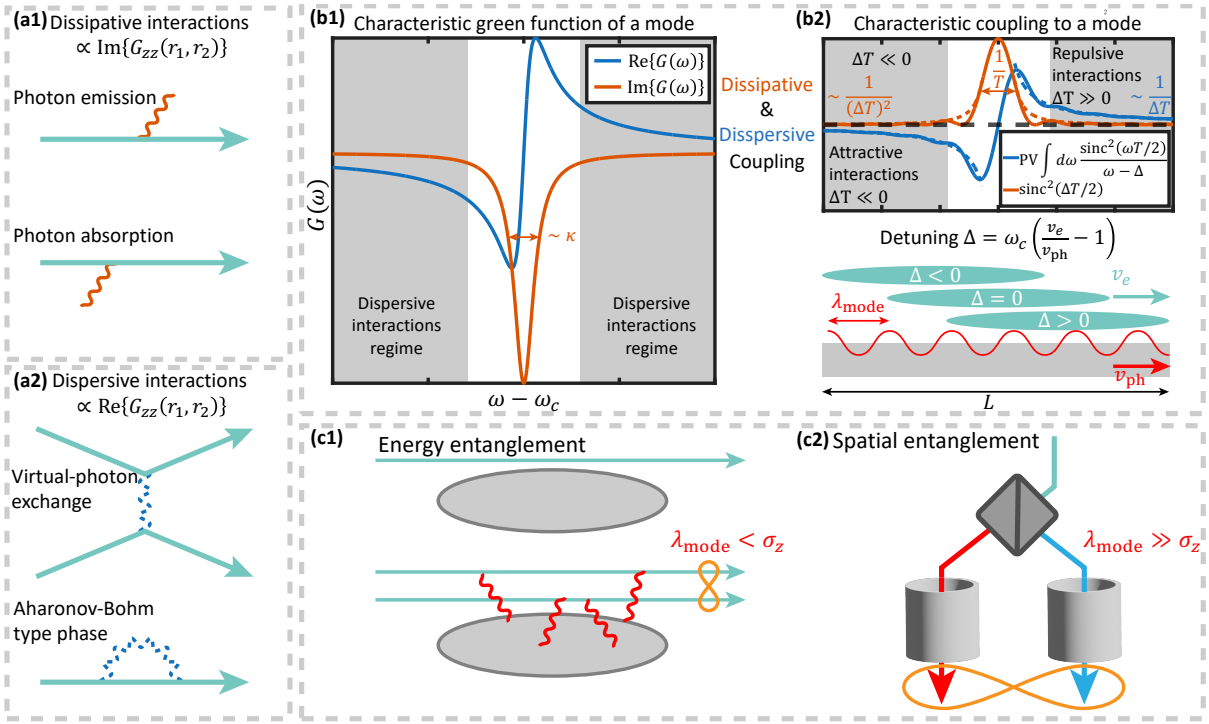


Figure 5.27: Conceptual framework of cavity-mediated free-electron entanglement. (a) The dyadic Green's function dictates the probability amplitudes of Feynman diagrams involving photon emission and absorption. (a1) Processes involving real (on-shell) photons are proportional to the imaginary part of the Green's function. These processes include the exchange of energy with the environment due to photon emission or absorption, and evaluate to zero in free space. (a2) Processes involving virtual (off-shell) photons are proportional to the real part of the Green's function. Such processes do not exchange energy with the environment, but can mediate energy exchange between the electrons or induce an environment-dependent Aharonov-Bohm-type phase shift on the electron. In free space, these diagrams reduce to the typical Coulomb (or more generally Liénard-Wiechert) potential. (b) Characteristic spectral shape of the Green's function with a Lorentzian resonance and effective electron coupling. (b1) For narrow resonance the dissipative part decays much faster, allowing for purely dispersive interactions in the detuned regime. (b2) The electron coupling is dictated by integrating the mode's profile along the electron trajectory. For a mode with defined momentum along the electron propagation this dictates well-defined phase-matching conditions. (c) The two proposed entanglement modalities. (c1) Continuous-variable energy entanglement is achieved in the limit where $\lambda_{\mathrm{mode}} < \sigma_z$. (c2) Transverse spatial entanglement is achieved when the electron trajectories are coherently split across different paths and $\lambda_{\mathrm{mode}} \gg \sigma_z$.

Interaction with a General Electromagnetic Environment

In this section, we derive the exact joint evolution of paraxial free electrons interacting with a general quantized electromagnetic environment [94]. By tracing out the photonic degrees of freedom, we analytically isolate the coherent multi-electron interaction phase and the non-unitary dissipative kernel. We consider N electrons propagating with mean velocity v along the z axis. The position of electron j is denoted by $\hat{\mathbf{r}}_j = (\hat{\mathbf{r}}_{\perp j}, \hat{z}_j)$, where $\hat{\mathbf{r}}_{\perp j}$ denotes its transverse

coordinates $(\hat{x}, \hat{y})$.

To describe the interaction of these electrons with a quantized electromagnetic environment, we start from the full Hamiltonian evaluated in the temporal gauge ($\phi = 0$) [319],

$$\hat{H} = \hat{H}_e + \hat{H}_{\rm ph} + \hat{V} = -\mathrm{i}\hbar v \sum_{j=1}^{N} \frac{\partial}{\partial \hat{z}_j} + \hat{H}_{\rm ph} - ev \sum_{j=1}^{N} \hat{A}_z(\hat{\mathbf{r}}_{\perp j}, \hat{z}_j). \tag{5.98}$$

Here $\hat{H}_e$ is the free-electron Hamiltonian in the paraxial approximation, $\hat{H}_{\rm ph}$ is the Hamiltonian of the photonic excitations, $\hat{A}_z$ is the longitudinal component of the vector-potential operator, and e is the elementary charge. Because $\hat{H}_e$ is the generator of longitudinal spatial translations, moving to the interaction picture, $\hat{V}_I(t) = \mathrm{e}^{\mathrm{i}(\hat{H}_e + \hat{H}_{\rm ph})t/\hbar} \hat{V} \mathrm{e}^{-\mathrm{i}(\hat{H}_e + \hat{H}_{\rm ph})t/\hbar}$, shifts the longitudinal electron coordinate according to $\hat{z}_j(t) = \hat{z}_j + vt$. The interaction Hamiltonian in Eq. (5.98) therefore takes the form

$$\hat{V}_I(t) = -ev \sum_{j=1}^{N} \hat{A}_z(\hat{\mathbf{r}}_{\perp j}, \hat{z}_j + vt, t). \tag{5.99}$$

The exact joint evolution of the system is governed by the scattering operator,

$$\hat{S} = \mathcal{T} \exp\left[-\frac{\mathrm{i}}{\hbar} \int_{-\infty}^{\infty} dt\, \hat{V}_I(t) \right], \tag{5.100}$$

where $\mathcal{T}$ denotes time ordering. Applying the Magnus expansion [328] allows us to express this as $\hat{S} = \exp\Big(\hat{\Omega}_1 + \hat{\Omega}_2 + \dots\Big)$, where the first- and second-order terms are explicitly defined using the interaction Hamiltonian (Eq. 5.99) as

$$\begin{aligned} \hat{\Omega}_1 &= -\frac{\mathrm{i}}{\hbar} \int_{-\infty}^{\infty} dt\, \hat{V}_I(t), \\ \hat{\Omega}_2 &= -\frac{1}{2\hbar^2} \int_{-\infty}^{\infty} dt \int_{-\infty}^{t} dt'\, [\hat{V}_I(t), \hat{V}_I(t')]. \end{aligned} \tag{5.101}$$

Because the interaction Hamiltonian is strictly linear in the bosonic field operators, the nested commutator $[\hat{V}_I(t), \hat{V}_I(t')]$ evaluates to a c-number. Consequently, all higher-order nested commutators vanish ($\hat{\Omega}_n = 0,\ n \geq 3$), truncating the expansion exactly at the second order.

The first-order term generates the effective electron-photon displacement operation. The second-order term, $\hat{\Omega}_2$, encodes the pure electron-electron interactions mediated by the electromagnetic vacuum. Evaluating $\hat{\Omega}_2$ requires the MQED vacuum commutator. We use the Fourier convention in which positive-frequency components evolve as $\mathrm{e}^{-\mathrm{i}\omega t}$, and $G_{\mu\nu}(\mathbf{r}, \mathbf{r}'; \omega)$ denotes the dyadic Green's function of the electromagnetic environment. Crucially, combining the field commutator with the time-ordering Heaviside step function $\Theta(t - t')$ naturally yields the Green's function:

$$[\hat{A}_\mu(\mathbf{r}, t), \hat{A}_\nu(\mathbf{r}', t')]\Theta(t - t') = -\frac{\mathrm{i}\hbar}{\epsilon_0 c^2} \int_{-\infty}^{\infty} \frac{d\omega}{2\pi} \mathrm{e}^{-\mathrm{i}\omega(t-t')} G_{\mu\nu}(\mathbf{r}, \mathbf{r}'; \omega). \tag{5.102}$$

We consider reciprocal media, such that Onsager reciprocity gives $G_{zz}(\mathbf{r}, \mathbf{r}'; \omega) = G_{zz}(\mathbf{r}', \mathbf{r}; \omega)$. Establishing an Aharonov-Bohm-like phase convention [329], we define the coherent Hermitian phase operator as $\hat{\Phi} = \mathrm{i}\hat{\Omega}_2$.

To organize the coherent and dissipative interactions, we define the master coupling kernel Γ as the longitudinal path integral over the Green's function:

$$\Gamma(\mathbf{r}_{\perp i}, \mathbf{r}_{\perp j}; \omega) \equiv \frac{e^2}{2\pi\epsilon_0 c^2 \hbar} \int_{-\infty}^{\infty} dz \int_{-\infty}^{\infty} dz'\, \mathrm{e}^{\mathrm{i}\omega(z-z')/v} G_{zz}(\mathbf{r}_{\perp i}, z; \mathbf{r}_{\perp j}, z'; \omega). \tag{5.103}$$

This kernel decomposes into its Hermitian and anti-Hermitian parts in the electron-coordinate space:

$$\begin{aligned}\Gamma_+(\mathbf{r}_{\perp i},\mathbf{r}_{Tj},,\omega) &\equiv \frac{1}{2}\left[\Gamma(\mathbf{r}_{\perp i},\mathbf{r}_{\perp j},\omega)+\Gamma^*(\mathbf{r}_{\perp j},\mathbf{r}_{\perp i},\omega)\right] \\ &= \frac{e^2}{2\pi\varepsilon_0 c^2\hbar}\int_{-\infty}^{\infty}\mathrm{d}z\int_{-\infty}^{\infty}\mathrm{d}z'\,\mathrm{e}^{\mathrm{i}\omega(z-z')/v}\mathrm{Re}G_{zz}(\mathbf{r}_{\perp i},z;\mathbf{r}_{\perp j},z';\omega).\end{aligned} \tag{5.104}$$

$$\begin{aligned}\Gamma_-(\mathbf{r}_{\perp i},\mathbf{r}_{\perp i},\omega) &\equiv \frac{1}{2\mathrm{i}}\left[\Gamma(\mathbf{r}_{\perp i},\mathbf{r}_{\perp j},\omega)-\Gamma^*(\mathbf{r}_{\perp j},\mathbf{r}_{\perp i},\omega)\right] \\ &= \frac{e^2}{2\pi\varepsilon_0 c^2\hbar}\int_{-\infty}^{\infty}\mathrm{d}z\int_{-\infty}^{\infty}\mathrm{d}z'\,\mathrm{e}^{\mathrm{i}\omega(z-z')/v}\mathrm{Im}G_{zz}(\mathbf{r}_{\perp i},z;\mathbf{r}_{\perp j},z';\omega),\end{aligned} \tag{5.105}$$

With the above reciprocity and Fourier conventions, Γ_+ is determined by the reactive, real part of the Green's function and generates the coherent interaction phase, while Γ_- is determined by the dissipative, imaginary part of the Green's function. To isolate the electronic dynamics, we define the $3N$-dimensional collective coordinate vector $\mathbf{R}\equiv(\mathbf{r}_1,\ldots,\mathbf{r}_N)$. The coherent phase evaluated on these spatial coordinates is

$$\Phi(\mathbf{R}) = -\sum_{i,j=1}^{N}\int_0^{\infty} d\omega\,\Gamma_+(\mathbf{r}_{\perp i},\mathbf{r}_{\perp j};\omega)\mathrm{e}^{-\mathrm{i}\omega(z_i-z_j)/v}. \tag{5.106}$$

The terms with $i=j$ represent one-body Aharonov-Bohm phases induced by the electromagnetic environment, while the $i\neq j$ terms describe the coherent pairwise interaction between distinct electrons.

We obtain the final reduced electronic density matrix elements $\rho_f(\mathbf{R},\mathbf{R}')\equiv\langle\mathbf{R}|\hat{\rho}_e^{(f)}|\mathbf{R}'\rangle$ by tracing out the photonic degrees of freedom, assuming an initially separable state with no electron-photon correlations and with the photonic bath in thermal equilibrium. The trace is evaluated analytically using the Baker-Campbell-Hausdorff (BCH) formula [330]. Since the thermal bath has a vanishing mean field, $\langle\hat{A}\rangle_T=0$, and the relevant exponent is linear in the bosonic field operators, we invoke the Gaussian Weyl characteristic identity [330], $\langle\mathrm{e}^{\hat{X}}\rangle_T=\exp\left(\frac{1}{2}\langle\hat{X}^2\rangle_T\right)$ to evaluate the trace.

The resulting quadratic moments are evaluated via the fluctuation-dissipation theorem [331], which relates the finite-temperature field correlators to the imaginary part of the Green's function:

$$\langle\hat{A}_\mu(\mathbf{r},\omega)\hat{A}_\nu^\dagger(\mathbf{r}',\omega')\rangle_{\mathrm{ph}} = \frac{\hbar}{\pi\epsilon_0 c^2}[n_{th}(\omega)+1]\mathrm{Im}G_{\mu\nu}(\mathbf{r},\mathbf{r}';\omega)\delta(\omega-\omega'), \tag{5.107}$$

where $n_{\mathrm{th}}(\omega)$ is the Bose-Einstein distribution. Collecting these thermal averages yields the exact non-unitary dissipative kernel $K(\mathbf{R},\mathbf{R}')$, which is driven entirely by Γ_-:

$$\begin{aligned}K(\mathbf{R},\mathbf{R}') = \sum_{i,j=1}^{N}\int_0^{\infty} d\omega\Big\{ &-\left[2n_{th}(\omega)\mathrm{i}\sin\left(\frac{\omega}{v}(z_i-z_j)\right)+\mathrm{e}^{\mathrm{i}\frac{\omega}{v}(z_i-z_j)}\right]\Gamma_-(\mathbf{r}_{\perp i},\mathbf{r}_{\perp j},\omega) \\ &-\left[2n_{th}(\omega)\mathrm{i}\sin\left(\frac{\omega}{v}(z_i'-z_j')\right)+\mathrm{e}^{\mathrm{i}\frac{\omega}{v}(z_i'-z_j')}\right]\Gamma_-(\mathbf{r}'_{\perp i},\mathbf{r}'_{\perp j},\omega) \\ &+\left[2n_{th}(\omega)\mathrm{i}\sin\left(\frac{\omega}{v}(z_i-z_j')\right)\right]\Gamma_-(\mathbf{r}_{\perp i},\mathbf{r}'_{\perp j},\omega) \\ &+\left[2n_{th}(\omega)\mathrm{i}\sin\left(\frac{\omega}{v}(z_j'-z_i)\right)+2\mathrm{e}^{\mathrm{i}\frac{\omega}{v}(z_j'-z_i)}\right]\Gamma_-(\mathbf{r}'_{\perp j},\mathbf{r}_{\perp i},\omega)\Big\}.\end{aligned} \tag{5.108}$$

The exact reduced density matrix evolution takes the final form:

$$\rho_f(\mathbf{R},\mathbf{R}') = \mathrm{e}^{-\mathrm{i}\Phi(\mathbf{R})}\rho_0(\mathbf{R},\mathbf{R}')\mathrm{e}^{-K(\mathbf{R},\mathbf{R}')}\mathrm{e}^{\mathrm{i}\Phi(\mathbf{R}')}. \tag{5.109}$$

This exact result (Eq. 5.109) physically isolates the two fundamental interaction channels. The real part of the Green's function, encoded in Γ_+, drives the coherent, multi-particle virtual photon exchange phase $\Phi(\mathbf{R})$. Conversely, the imaginary part, encoded in Γ_-, governs the dissipative kernel $K(\mathbf{R}, \mathbf{R}')$. This kernel captures energy exchange with the environment due to real photon emission and absorption, while its cross terms dictate collective subradiant and superradiant emission [36]. Concurrently, K represents the non-unitary loss of spatial coherence, manifesting as which-particle information leaking into the photonic bath and causing decoherence.

Finally, in the homogeneous free-space limit for uniformly moving paraxial electrons with $v < c$, the absence of phase matching for real photon emission ensures that the dissipative kernel vanishes, $K = 0$, within the recoil-free approximation. In this regime, after removing one-body self-phases and avoiding double counting, the coherent pair-interaction phase strictly evaluates to the classical Liénard-Wiechert potential integrated over the interaction time T, $\Phi_{\text{int}} = \sum_{i<j} \frac{e^2 T}{4\pi\epsilon_0 \hbar \gamma \sqrt{\gamma^2 \Delta z_{ij}^2 + \Delta r_{\perp ij}^2}}$.

Interaction with an isolated mode

To engineer deterministic entanglement, we route the electron bunch through a photonic cavity designed to support a single dominant quasinormal mode (QNM). Assuming a high quality factor ($\kappa \ll \omega_c$), near the resonance frequency ω_c with linewidth κ, the relevant longitudinal component of the Green's tensor can be approximated by a single Lorentzian pole:

$$G_{zz}(\mathbf{r}, \mathbf{r}'; \omega) \simeq -\frac{c^2}{2\omega_c} \frac{u_z^*(\mathbf{r}) u_z(\mathbf{r}')}{\omega - \omega_c + \mathrm{i}\kappa/2}. \tag{5.110}$$

We assume the mode profile factorizes into a transverse envelope, a longitudinal window of length L, and a carrier wave carrying momentum q_0, such that $u_z(\mathbf{r}_\perp, z) = u(\mathbf{r}_\perp) W(z) \mathrm{e}^{\mathrm{i}q_0 z}$.

Substituting this mode profile (Eq. 5.110) into the general master kernel Γ derived in Eq. (5.103) and evaluating the longitudinal spatial integrals over the finite interaction length yields a phase-matching spectral response characterized by a sinc^2 function. To quantify the interaction, we define the dimensionless transverse coupling strength:

$$g(\mathbf{r}_\perp) \equiv \frac{e}{\hbar\omega_c} \sqrt{\frac{\hbar\omega_c}{2\epsilon_0}} u(\mathbf{r}_\perp) L. \tag{5.111}$$

This parameter represents the fundamental figure of merit for the electron-photon interaction strength commonly investigated in free-electron quantum optics literature [34, 315, 332, 333]. Using this, the macroscopic interaction kernel becomes:

$$\Gamma(\mathbf{r}_{\perp i}, \mathbf{r}_{\perp j}; \omega) \simeq -g^*(\mathbf{r}_{\perp i}) g(\mathbf{r}_{\perp j}) \frac{\mathrm{sinc}^2\left[\frac{(\omega - \omega_{\text{PM}})L}{2v}\right]}{2\pi(\omega - \omega_c + \mathrm{i}\kappa/2)}, \tag{5.112}$$

where $\omega_{\text{PM}} = v q_0$ is the phase-matching frequency. The dynamics are dictated by the frequency detuning $\Delta \equiv \omega_{\text{PM}} - \omega_c$, which governs the accumulated phase slip $\phi_{\text{slip}} = \Delta \frac{L}{v}$ of the electron relative to the cavity mode.

We operate in the strongly detuned, low-loss limit where the cavity linewidth is much narrower than both the detuning, the transit-time bandwidth, and the mode resonant frequency ($\kappa \ll |\Delta|, v/L$). In this large detuning regime, the dissipative and coherent channels behave fundamentally differently. Crucially, the ratio of the dissipative to dispersive coupling naturally scales as $\sim 1/\Delta$.

For the dissipative kernel K, the imaginary part of the Lorentzian acts as a narrow spectral filter, evaluating the phase-matching envelope exactly at resonance. This yields a dissipative

rate strictly proportional to $\mathrm{sinc}^2(\phi_{\mathrm{slip}}/2)$. Consequently, choosing a phase slip of $\phi_{\mathrm{slip}} \simeq 2\pi$ deliberately lands exactly on the first zero of the sinc function. This completely suppresses the real excitation of the mode, protecting the system from decoherence ($K \to 0$).

Conversely, the coherent phase Φ is driven by the symmetric kernel Γ_+, which is governed by the real part of the Green's function ($\mathrm{Re}[G_{zz}]$). Integrating this over frequency involves the broad sinc^2 phase-matching window multiplied by the principal value of the dispersive Lorentzian, $\mathcal{P}\frac{1}{\omega-\omega_c}$. Because this principal value integral scales asymptotically as $1/\Delta$, the coherent phase avoids the sinc^2 zero suppression and remains finite. Evaluating this integral to leading order yields a pure, dimensionless many-body interaction phase:

$$\Phi(\mathbf{R}) \simeq \frac{1}{\phi_{\mathrm{slip}}} \sum_{i,j=1}^{N} g^*(\mathbf{r}_{\perp i}) g(\mathbf{r}_{\perp j}) \mathrm{e}^{-\mathrm{i}q_0(z_i - z_j)} \Lambda\left(\frac{z_i - z_j}{L}\right), \tag{5.113}$$

where $\Lambda(x) = \max(1 - |x|, 0)$ is a triangular window function dictating the spatial overlap of the electrons within the cavity length. Thus, operating at a $\phi_{\mathrm{slip}} \simeq \pm 2\pi$ naturally isolates a purely coherent, fully tunable long-range entanglement mechanism mediated exclusively by virtual cavity photons.

Energy entanglement using optical cavities

To explore continuous-variable energy correlations, we specialize our formalism to a two-electron bunch ($N = 2$) traversing approximately identical transverse paths through an optical cavity, such that $g(\mathbf{r}_{\perp 1}) \approx g(\mathbf{r}_{\perp 2}) \equiv g$ (see Fig. 5.28a). We operate at the optimized phase slip $\phi_{\mathrm{slip}} \equiv \Delta L/v \simeq \pm 2\pi$, where the dissipative kernel completely vanishes ($K \to 0$), suppressing real cavity excitations. Dropping the unobservable self-interaction global phases, the interaction phase operator simplifies to:

$$\Phi_{\pm}(z_1, z_2) = \pm \frac{|g|^2}{\pi} \cos\left[q_0(z_1 - z_2)\right] \Lambda\left(\frac{z_1 - z_2}{L}\right). \tag{5.114}$$

The sign of the phase accumulation $\Phi_{\pm}$ is strictly governed by the cavity detuning (see Fig. 5.28b). Operating under positive blue detuning ($\Delta > 0, \phi_{\mathrm{slip}} \simeq 2\pi$) dictates a purely repulsive interaction, whereas negative red detuning ($\Delta < 0, \phi_{\mathrm{slip}} \simeq -2\pi$) mediates an attractive interaction (see Fig. 5.27b2).

In the close-proximity regime where the longitudinal separation is much smaller than the cavity length ($|z_1 - z_2| \ll L$), the spatial window approaches unity ($\Lambda \to 1$). Promoting the coordinates to quantum operators, the cosine modulator maps onto a beam-splitter-like exchange interaction, $\cos[q_0(\hat{z}_1 - \hat{z}_2)] = \frac{1}{2}(\hat{b}_1\hat{b}_2^\dagger + \hat{b}_1^\dagger\hat{b}_2)$, where $\hat{b}_j \equiv \mathrm{e}^{-\mathrm{i}q_0\hat{z}_j}$ and $\hat{b}_j^\dagger = \mathrm{e}^{\mathrm{i}q_0\hat{z}_j}$ are the electron energy ladder operators.

Evaluating the unitary evolution $\hat{U} = \mathrm{e}^{-\mathrm{i}\hat{\Phi}_{\pm}}$ on an initial state where both electrons occupy identical kinetic energy states E_0, we expand the phase modulation via the Jacobi-Anger identity. Defining the discrete single-particle energy-ladder basis as $|n\rangle \equiv |E_0 + n\hbar\omega_{\mathrm{PM}}\rangle$, the final joint electronic state vector evaluates to:

$$|\psi_f\rangle = \sum_{m=-\infty}^{\infty} (\mp\mathrm{i})^m J_m\left(\frac{|g|^2}{\pi}\right) |m, -m\rangle, \tag{5.115}$$

where J_m is the m-th order Bessel function of the first kind. This state describes a perfectly correlated *entangled energy comb* (Fig. 5.28e). Written in its orthogonal Schmidt decomposition, its quantum entanglement is quantified directly by the negativity [334, 335] $\mathcal{N}$ (Fig. 5.28c,d):

$$\mathcal{N} = \frac{1}{2}\left[\left(\sum_{m=-\infty}^{\infty}\left|J_m\left(\frac{|g|^2}{\pi}\right)\right|\right)^2 - 1\right]. \tag{5.116}$$

Crucially, this energy entanglement is uniquely suited for practical verification using PINEM [46]. In standard free-space Coulomb interactions, generating energy entanglement relies on the quantum ambiguity of which electron precedes the other, which strictly requires their initial spatial separation to be smaller than their coherent position spread. In our cavity-mediated scheme, this stringent spatial constraint is bypassed: the electrons simply need to interact with the cavity mode simultaneously, and their individual coherent position spread must exceed the optical wavelength ($\sigma_z > \lambda_{\mathrm{mode}}$), the typical condition for PINEM experiments, which also hold for multi-electron bunches as recently demonstrated.

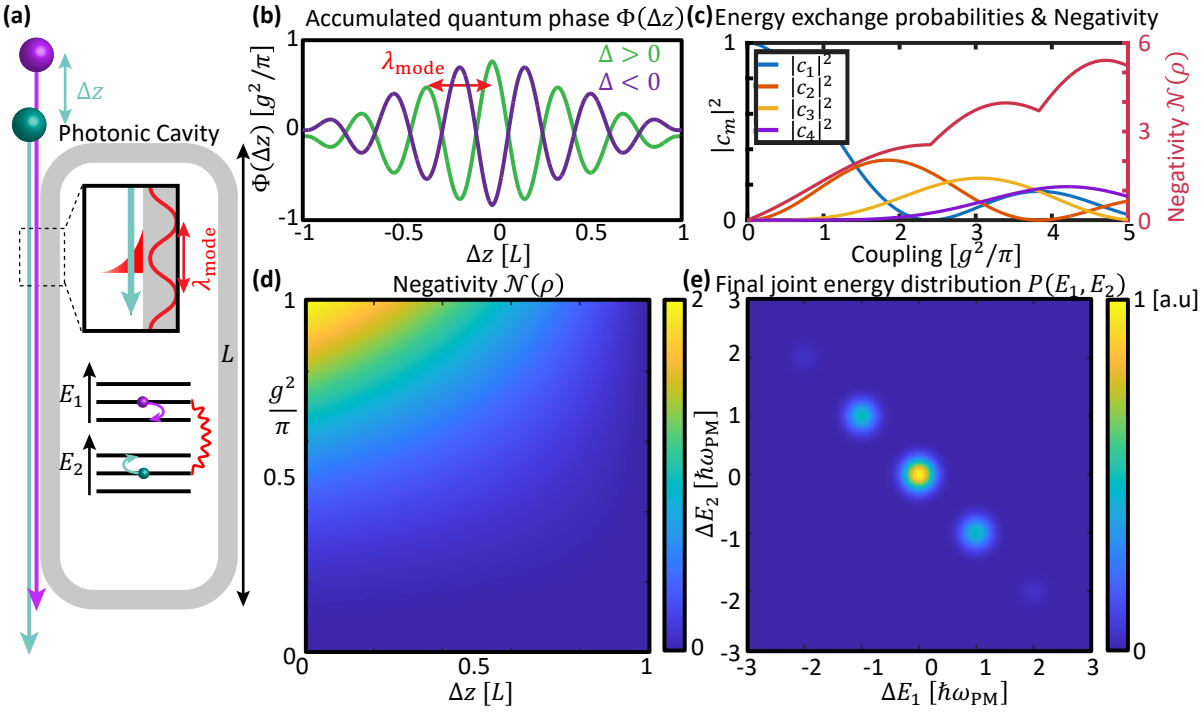


Figure 5.28: Deterministic energy entanglement mediated by optical cavities. (a) Schematic of the optical cavity energy entanglement scheme. Two electrons moving parallel to a cavity exchange virtual photons, generating correlations across their discrete energy ladders. (b) The accumulated effective two-particle quantum phase. The phase is plotted for both negative ($\Delta < 0$) and positive ($\Delta > 0$). The oscillations in the phase implies that if Δz varies coherently on the scale of λ_{mode} entanglement would emerge. (c) Energy exchange probabilities and entanglement negativity ($\mathcal{N}$). These are evaluated in the ideal limit where the electron spacing is much smaller than the interaction length ($\Delta z \ll L$). (d) Entanglement robustness mapping. A color map displaying the negativity as a continuous function of the longitudinal separation (Δz) and the dimensionless coupling strength (g). (e) Simulated post interaction Electron Energy-Loss Spectroscopy (EELS). The electron energies are distributed across the anti-diagonal, demonstrating the energy exchange between the electrons. The parameters used for the simulations are coherent electron spread of 20nm and, $\lambda_{\mathrm{mode}} = 1500$nm and $L = 100\mu$m and $\Delta z = 10\mu$m for (e).

Spatial entanglement using microwave cavities

We now use the dispersive cavity-mediated interaction to generate entanglement in the transverse path degree of freedom. Each electron is restricted to a two-path basis, $|R\rangle$ and $|L\rangle$,

which defines a path qubit (see Fig. 5.29a). Exploiting this transverse spatial entanglement inherently relies on the precision of coherent electron manipulation. Recent advances in low-loss beam splitters—ranging from free-space diffraction gratings to chip-based microwave and electrostatic ponderomotive potentials—provide the requisite interferometric stability to route and recombine these continuous wavepackets as discrete path qubits [166, 168, 169, 324, 336–339]. We denote the Pauli operator of electron j by $\hat{\sigma}_z^{(j)} = |R\rangle_j\langle R|_j - |L\rangle_j\langle L|_j$, and the collective spin by $\hat{S}_\alpha = \frac{1}{2}\sum_{j=1}^{N}\hat{\sigma}_\alpha^{(j)}$. We move to the microwave-cavity regime, where the longitudinal bunch length is much shorter than both the cavity wavelength and the interaction length. The relative longitudinal phase across the bunch can then be neglected, $e^{iq_0(z_i-z_j)} \approx 1$, so that all electrons sample the same cavity phase. In this limit, the general dispersive phase reduces to a purely transverse, path-dependent interaction,

$$\Phi_\pm \simeq \pm\frac{1}{2\pi}\sum_{i,j}\mathrm{Re}\left[g(\hat{\mathbf{r}}_{\perp i})g^*(\hat{\mathbf{r}}_{\perp j})\right]. \tag{5.117}$$

We suggest a dual-cavity geometry, where one cavity couples only to the right arm and the other identical one couples only to the left arm (see Fig. 5.29b),

$$g^{(R)}(\hat{\mathbf{r}}_\perp) = g|R\rangle\langle R|, \qquad g^{(L)}(\hat{\mathbf{r}}_\perp) = g|L\rangle\langle L|. \tag{5.118}$$

Substituting these two couplings into the transverse phase, the linear $\hat{S}_z$ rotations from the two cavities cancel, while the quadratic terms add. Dropping the global phase gives $\Phi = \pm\frac{|g|^2}{\pi}\hat{S}_z^2$.

Equivalently, over the interaction time T, the same phase can be written as an effective one-axis-twisting Hamiltonian,

$$\hat{H}_{\mathrm{eff}} = \frac{\chi}{T}\hat{S}_z^2, \qquad \hat{U} = \exp\left[-\frac{i}{\hbar}\hat{H}_{\mathrm{eff}}T\right] = \exp\left(-i\chi\hat{S}_z^2\right), \qquad \chi = \pm\frac{|g|^2}{\pi}. \tag{5.119}$$

This is the standard one-axis-twisting (OAT) unitary, familiar from spin squeezing in atomic ensembles. Its importance is that it is not a product of independent single-electron phases: the phase acquired by each many-electron configuration depends on the collective path-population imbalance. Therefore, an initially separable path state is converted into a genuinely entangled many-electron spatial state [322].

Starting from a balanced interferometer, the input state is a coherent spin state polarized along x, corresponding to each electron occupying an equal superposition of the two paths. The OAT phase generated by Eq. (5.119) then shears the collective spin distribution: one transverse quadrature is squeezed, while the conjugate quadrature is anti-squeezed. In interferometric language, this squeezing reduces the uncertainty of an appropriate collective path observable below the projection noise of independent electrons.

The metrological consequence of this OAT interaction is the generation of spin squeezing, as standard in collective spin systems [322, 323, 325]. For standard Ramsey interferometry, the operational phase sensitivity is dictated by the Wineland squeezing parameter ξ_R^2. For weak twisting and large N, the optimal Ramsey gain is reached at

$$|g|_{\mathrm{opt}} \simeq \sqrt{\pi}\cdot 3^{1/12}N^{-1/3}, \qquad \xi_{R,\mathrm{opt}}^2 \simeq \frac{3^{2/3}}{2}N^{-2/3}. \tag{5.120}$$

Thus, increasing the number of electrons improves the achievable phase sensitivity to a sub-shot-noise scaling of $\Delta\varphi \propto N^{-5/6}$ (for optimal squeezing), while simultaneously relaxing the required single-electron cavity coupling (see Fig. 5.29c): the optimal coupling strength decreases as $|g|_{\mathrm{opt}} \propto N^{-1/3}$. The squeezed quadrature is generally tilted relative to the native path-population axis, so a final collective rotation is required to map the reduced-noise quadrature onto the measured output ports.

While the optimal Wineland parameter identifies the practical limit for standard interferometric measurements, further twisting continues to increase the ultimate theoretical sensitivity formalized by the Quantum Fisher Information (QFI). Ultimately, the OAT evolution can generate GHZ [340] states that achieve the Heisenberg limit (see Fig. 5.29d). However, extracting this enhanced sensitivity requires complex readout protocols that severely complicate the measurement, making the Wineland-squeezed states the most relevant and robust target for near-term implementation.

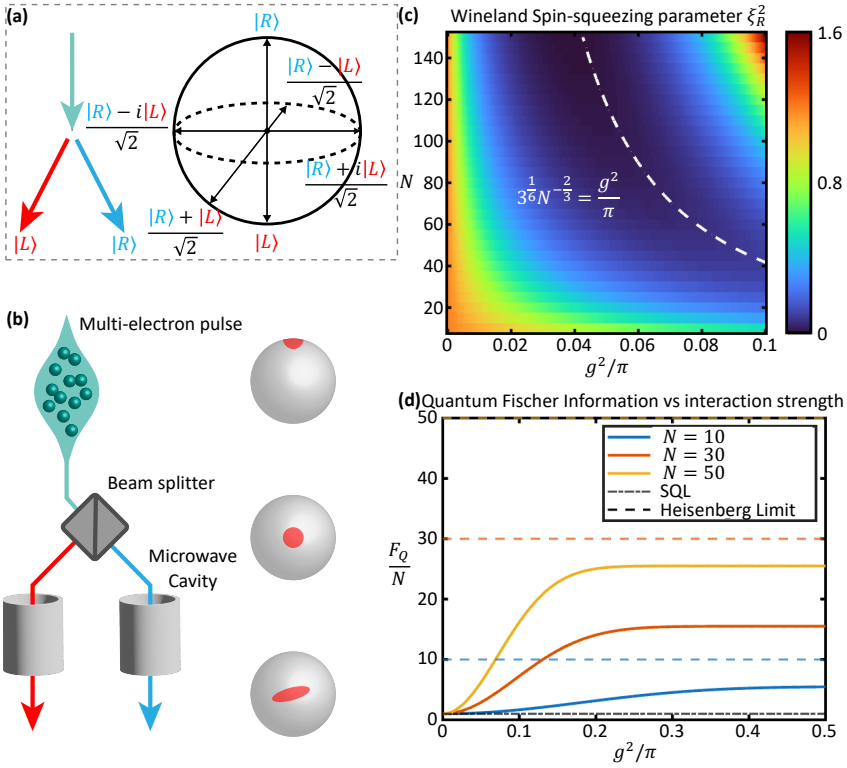


Figure 5.29: Spatial entanglement and quantum metrology using microwave cavities. (a) Electron trajectory-qubit equivalence. The continuous transverse electron wavepacket is mapped onto a discrete two-level path basis ($|L\rangle$ and $|R\rangle$). (b) Dual-cavity experimental scheme. Electron pulses traverse two independent microwave cavities, a symmetry that perfectly cancels linear single-particle rotations. Accompanying Bloch spheres [**arecchi1972**] illustrate the collective spin state dynamics evolving during the experiment. (c) The Wineland spin squeezing parameter (ξ_R^2). Plotted as a function of the particle number (N) and electron-photon coupling strength (g), demonstrating the achievement of optimal sub-shot-noise scaling. (d) Normalized Quantum Fisher Information (F_Q/N). Displayed as a function of g across various bunch sizes (N), highlighting the parametrically enhanced phase sensitivity approaching the fundamental Heisenberg scaling.

Discussion and Outlook

In this work, we have established a deterministic framework for generating multi-electron entanglement in free-electron beams through dispersive interactions with a photonic environment. By completely bypassing the dissipative real-photon emission channels, our mechanism protects the quantum state from environmental decoherence. In the optical regime, this interaction yields a pristine, continuous-variable entangled energy comb that can be directly mapped and diagnosed

utilizing existing PINEM [46]. In the microwave regime, the spatial interaction maps onto a collective one-axis twisting Hamiltonian, generating highly squeezed spin states that provide a robust pathway toward quantum-enhanced electron metrology.

Crucially, the practical implementation of this spatial entanglement does not strictly require the system to reach the strong single-particle coupling regime ($g \sim 1$). As we have shown, the optimal dimensionless coupling required to maximize the Wineland squeezing parameter and achieve sub-shot-noise sensitivity scales as $N^{-1/3}$. However, this collective enhancement is not without practical experimental trade-offs. While microwave architectures support the longitudinal compression of multiple electrons within a single wavelength fraction ($\sigma_z \ll \lambda_{\mathrm{mode}}$), dense bunching ($N \gg 1$) invariably exacerbates space-charge effects. This complicates beam manipulation and degrades the transverse emittance, which can ultimately lower the spatial resolution of the microscope. Consequently, realizing this scaling law in practice becomes an optimization problem of tolerance: determining the maximal macroscopic bunch size that can be utilized before the classical beam degradation outweighs the metrological advantage of collective spin squeezing.

Interestingly, the dense electron bunching required for large N naturally bridges our cavity-mediated scheme with recent metrological proposals utilizing free-space electrostatic (Coulomb) interactions to generate spin squeezing [341]. It is important to emphasize that our general MQED formalism inherently encapsulates these Coulombic interactions, together with additional relativistic corrections and thermal noise fluctuations. Our framework shows that cavity-mediated squeezing and electrostatically induced squeezing are not mutually exclusive, the tunable cavity interaction can be physically stacked on top of such electrostatic interactions, offering a hybrid pathway to push the signal-to-noise ratio even further beyond the Standard Quantum Limit.

We note that maximizing the dimensionless coupling g remains a highly sought-after goal in free-electron quantum optics [315, 332, 333], particularly for generating. Ongoing advancements in integrated nanophotonics, such as high-Q micro-resonators and near-field dielectric structures, offer highly promising experimental routes toward the $g \sim 1$ limit. Our proposal also motivate this ongoing research, and extends it also into the microwave regime where less effort has been invested.

Looking forward, the versatility of our general multi-electron formalism allows for theoretical analysis and structural optimization well beyond the single-mode approximation presented here. By engineering multi-mode photonic environments, tailored dispersion relations, or structured continuum baths, the interaction kernel can be customized to yield even stronger, highly specific many-body potential landscapes. Ultimately, deterministic cavity-mediated interactions establish the free electron not merely as a high-resolution probe, but as a fully programmable, flying quantum resource for precision metrology and a novel quantum information processing tool.

5.2 Additional Theoretical Derivations

The preceding sections present the formal, published body of work that constitutes this thesis. However, the trajectory of theoretical research is rarely captured in its entirety by peer-reviewed manuscripts alone; it is equally shaped by the private derivations, toy models, and exploratory mathematics investigated along the way. This chapter is dedicated to a curated selection of unpublished calculations that were profoundly instructive to my own scientific development.

The inclusion of these specific derivations is motivated by several factors. Some hold deep sentimental value, marking the initial steps into my PhD journey, while others are included for their pedagogical clarity and the physical insights they provide. Furthermore, I believe that each of these sections contains a genuine kernel of novelty, often framing established physics from a perspective that highlights connections others have overlooked. These calculations were not merely academic exercises; they served as the blueprints for multiple research directions I pursued throughout my PhD.

5.2.1 The Kapitza-Dirac Effect and Stimulated Compton Scattering in the PINEM Formalism

A cornerstone of free-electron quantum optics is the coherent exchange of energy and momentum between electrons and photons. Traditionally, such interactions—like those measured in standard photon-induced near-field electron microscopy (PINEM)—rely on optical near-fields. The near-field boundary breaks the continuous translational symmetry of free space, allowing for phase-matching between the electron and the light. However, coherent modulation can also be achieved in completely free space using nonlinear multi-photon processes.

The most famous example of free-space electron-light interaction is the Kapitza-Dirac (KD) effect, first proposed in 1933. In the standard KD effect, an electron beam diffracts off a stationary standing wave of light, treating the periodic intensity grating of the electromagnetic field as a physical diffraction grating. If the two counter-propagating laser beams forming the grating have slightly different frequencies ($\omega_1 \neq \omega_2$), the standing wave moves. In the comoving rest frame of the electron, the Doppler shift equalizes the frequencies, reducing the system back to the standard, stationary Kapitza-Dirac effect. In the laboratory frame, however, this process is understood as stimulated Compton scattering: the electron absorbs a photon from one beam and undergoes stimulated emission into the other, exchanging the energy difference $\hbar(\omega_1 - \omega_2)$ and the momentum difference $\hbar(q_1 - q_2)$.

Recently, this free-space coherent modulation was experimentally realized by Tsarev *et al.* [342], demonstrating nonlinear-optical quantum control of free-electron matter waves without the need for near-field nanostructures. The standard approach to analyzing such experiments relies on numerically solving the Time-Dependent Schrödinger Equation (TDSE). However, it is illuminating to show that this stimulated Compton process can be captured entirely analytically using the elegant scattering matrix (S-matrix) formalism developed for standard PINEM.

We begin with the Klein-Gordon Hamiltonian for a relativistic spin-less electron in an electromagnetic field. Using minimal coupling, $\mathbf{p} \to \mathbf{p} + e\mathbf{A}$, the Hamiltonian is:

$$H = \sqrt{m^2c^4 + (\mathbf{p} + e\mathbf{A})^2c^2}. \tag{5.121}$$

Assuming the interaction energy is small relative to the electron's total energy $E_0 \approx \gamma mc^2$, we can Taylor expand the square root. Standard near-field PINEM relies on the linear term proportional to $\mathbf{p} \cdot \mathbf{A}$. However, in free space, this linear term cannot be phase-matched and averages to zero. Instead, the dominant interaction is governed by the second-order diamagnetic term (the ponderomotive potential):

$$H_{int} \approx \frac{e^2c^2}{2E_0}\mathbf{A}^2(\mathbf{r}, t) \approx \frac{e^2}{2m_0\gamma}\mathbf{A}^2(\mathbf{r}, t). \tag{5.122}$$

Consider two classical plane waves in vacuum with frequencies ω_1, ω_2 and amplitudes E_1, E_2, propagating at angles θ_1, θ_2 in the $x-z$ plane. The vector potential is:

$$\mathbf{A}(z,t) = -\mathbf{e}_1 \frac{E_1}{\omega_1} \sin\left(\omega_1 t - \frac{\omega_1 \cos\theta_1}{c} z\right) - \mathbf{e}_2 \frac{E_2}{\omega_2} \sin\left(\omega_2 t - \frac{\omega_2 \cos\theta_2}{c} z\right). \tag{5.123}$$

When we calculate $\mathbf{A}^2$, the single-beam terms oscillate too rapidly to phase-match. The interaction is driven entirely by the cross-term representing the beat note between the two fields. Defining the polarization overlap factor $F(\theta) = \cos\theta_1 \cos\theta_2 + \sin\theta_1 \sin\theta_2$, we extract the relevant slowly varying components:

$$\mathbf{A}^2(z,t) \approx -F(\theta) \frac{E_1 E_2}{4\omega_1 \omega_2} \left[e^{i\left((\omega_2-\omega_1)t - \left(\frac{\omega_2 \cos\theta_2}{c} - \frac{\omega_1 \cos\theta_1}{c}\right)z\right)} + \text{h.c.} \right]. \tag{5.124}$$

To find the scattering matrix S, we must integrate this interaction potential over the electron's unperturbed classical trajectory $z \to z + vt$ during an interaction time T. The scattering operator is $S = \exp\left(-\frac{i}{\hbar}\int_0^T H_{int}(z+vt,t)dt\right)$. Focusing on the time integral of the phase term, we have:

$$I = \int_0^T \exp\left[i(\omega_2 - \omega_1)t - i\left(\frac{\omega_2 \cos\theta_2}{c} - \frac{\omega_1 \cos\theta_1}{c}\right)(z+vt) \right] dt. \tag{5.125}$$

To evaluate this, we change variables from the laboratory time t to the electron's co-moving longitudinal position $\zeta = z + vt$. Consequently, $t = (\zeta - z)/v$ and $dt = d\zeta/v$. The integration limits transform from $t \in [0, T]$ to spatial limits $\zeta \in [z, z+L]$, where $L = vT$ is the interaction length:

$$I = \frac{1}{v} \exp\left(-i\frac{\omega_2 - \omega_1}{v} z\right) \int_z^{z+L} \exp\left[i\left(\frac{\omega_2 - \omega_1}{v} - \left(\frac{\omega_2 \cos\theta_2}{c} - \frac{\omega_1 \cos\theta_1}{c}\right)\right)\zeta \right] d\zeta. \tag{5.126}$$

For this integral to not average to zero, the spatial oscillation in the exponent must vanish. This imposes the exact free-space phase-matching condition:

$$v = \frac{\omega_2 - \omega_1}{\frac{\omega_2 \cos\theta_2}{c} - \frac{\omega_1 \cos\theta_1}{c}}. \tag{5.127}$$

This condition perfectly reflects energy and momentum conservation for an electron absorbing a photon at ω_2 and emitting one at ω_1. When phase-matched, the integral evaluates trivially to L, leaving:

$$I = \frac{L}{v} e^{-i\frac{\omega_2 - \omega_1}{v} z}. \tag{5.128}$$

We define the translation operator $b = \exp\left(-i\frac{\omega_2-\omega_1}{v} z\right)$, which acts on the electron wavefunction to shift its energy by exactly $\hbar(\omega_2 - \omega_1)$. Re-inserting the evaluated integral into the S-matrix yields:

$$S = \exp\left(gb - g^* b^\dagger\right), \quad \text{where} \quad = i\frac{e^2 E_1 E_2 F(\theta)}{8\hbar m_0 \gamma v \omega_1 \omega_2} L. \tag{5.129}$$

Remarkably, this free-space S-matrix takes the exact same mathematical form as the standard near-field PINEM interaction.

Because the algebra matches PINEM perfectly, applying this operator to an initial monoenergetic electron state $|E_0\rangle$ immediately yields the standard discrete energy sidebands. The probability P_n of the electron absorbing n net energy quanta $\hbar(\omega_2 - \omega_1)$ is exactly given by the Bessel functions of the first kind:

$$P_n = J_n^2(2|g|). \tag{5.130}$$

By reframing stimulated Compton scattering within the PINEM formalism, we reveal a theoretical unity. Whether an electron interacts with an evanescent near-field via the linear momentum term, or with free-space standing waves via the nonlinear ponderomotive term, the resulting quantum coherent modulation is identically governed by the same continuous-variable displacement operators.

5.2.2 Single-Mode Toy Model of Electron-Cavity Interactions

Throughout this thesis, the interaction between free electrons and photonic environments has been primarily treated using the full, multi-mode framework of macroscopic quantum electrodynamics (MQED). While rigorous, these broadband continuum models can sometimes obscure the intuitive quantum dynamics at play. To build a clearer physical picture, it is often illuminating to map the system onto a simplified, single-mode toy model.

By treating the electron-photon interaction in the style of cavity QED—conceptually akin to the Jaynes-Cummings model but adapted for free electrons—we can analytically solve the time-evolution operator. This single-mode Hamiltonian elegantly reveals how the interaction naturally partitions into three distinct physical phenomena: cavity phase accumulation, coherent cavity displacement, and cavity-mediated electron-electron entanglement.

We consider a beam of electrons interacting with a single confined electromagnetic mode (e.g., inside a photonic cavity). The single-mode Hamiltonian is given by:

$$H = H_e + \hbar\omega_c a^\dagger a + \sum_j \hbar\left(\beta_j a^\dagger b_j + \beta_j^* a b_j^\dagger\right), \tag{5.131}$$

where H_e is the free-electron Hamiltonian, ω_c is the cavity resonance frequency, and $a^\dagger, a$ are the standard photon creation and annihilation operators. The parameter β_j represents the coupling strength to the j-th electron. The operator b_j is the longitudinal momentum translation operator for the j-th electron, defined as $b_j = e^{-iq_z\hat{z}_j}$, where q_z is the phase-matched longitudinal wavevector of the cavity mode.

For highly energetic electrons moving at a constant velocity v, the translation operator satisfies the commutation relation $[H_e, b_j] \approx -\hbar q_z v b_j$. This allows us to transition into a comoving rotating frame (the interaction picture with respect to the electron motion). In this frame, the effective Hamiltonian simplifies to:

$$H_{\text{eff}} = \hbar\Delta a^\dagger a + \sum_j \hbar\left(\beta_j a^\dagger b_j + \beta_j^* a b_j^\dagger\right), \tag{5.132}$$

where we have defined the detuning parameter $\Delta = \omega_c - q_z v$. To compact the notation, we introduce a collective electron drive operator $B = \sum_j \beta_j b_j$. The Hamiltonian then takes the elegant form of a driven quantum harmonic oscillator:

$$H_{\text{eff}} = \hbar\Delta a^\dagger a + \hbar\left(a^\dagger B + a B^\dagger\right). \tag{5.133}$$

Because the Hamiltonian is linear in the optical field operators, it can be exactly diagonalized by completing the square. We can rewrite the effective Hamiltonian as:

$$H_{\text{eff}} = \hbar\Delta\left(a^\dagger + \frac{B^\dagger}{\Delta}\right)\left(a + \frac{B}{\Delta}\right) - \hbar\frac{B^\dagger B}{\Delta}. \tag{5.134}$$

To find the final state of the system after the electrons traverse an interaction length L, we must compute the time-evolution operator $U(t) = \exp(-iH_{\text{eff}}t/\hbar)$ evaluated at the transit time $t = L/v$. Let us define the dimensionless transit angle $\theta = \Delta L/v$.

Using the Baker-Campbell-Hausdorff (BCH) lemma and the algebra of coherent displacement operators, the total unitary evolution can be analytically factored into three distinct operations:

$$U(L) = \exp\left[i\frac{B^\dagger B}{\Delta^2}(\theta - \sin\theta)\right]\mathcal{D}\left(\frac{B}{\Delta}(e^{-i\theta} - 1)\right)\exp\left(-i\theta a^\dagger a\right), \tag{5.135}$$

where $\mathcal{D}(\alpha) = \exp\left(\alpha a^\dagger - \alpha^* a\right)$ is the Glauber displacement operator.

This exact factorization provides a profound physical interpretation of the electron-cavity interaction. Reading the operator from right to left, the interaction imposes three effects on the joint system:

1. $\exp\big(-i\theta a^\dagger a\big)$: **Cavity Phase Delay.** The bare cavity accumulates a phase proportional to the detuning and the interaction length.

2. $\mathcal{D}\big(\frac{B}{\Delta}(e^{-i\theta}-1)\big)$: **Coherent Displacement.** The electrons act as a classical current, displacing the cavity field into a coherent state. The amplitude of this displacement is directly proportional to the collective electron operator B.

3. $\exp\left[i\frac{B^\dagger B}{\Delta^2}(\theta-\sin\theta)\right]$: **Electron-Electron Coupling.** The most intriguing term is a purely electronic phase shift generated by the operator $B^\dagger B = \sum_{j,k}\beta_j^*\beta_k b_j^\dagger b_k$. This represents a cavity-mediated, dispersive interaction between the electrons.

If the interaction length and detuning are engineered such that $\theta = 2\pi m$ (where m is an integer), the cavity displacement term perfectly vanishes, $\mathcal{D}(0) = \mathbb{1}$. At these "magic angles," the electrons emit and subsequently reabsorb the cavity field entirely. No real photons are left in the cavity, yet the electrons still experience the $B^\dagger B$ evolution. This leaves the system with a purely virtual, cavity-mediated electron-electron interaction, providing the mechanism for generating deterministic free-electron entanglement.

5.2.3 Classical vs. Quantum Regimes of Free-Electron Bunching

While the PINEM formalism is inherently quantum mechanical—treating the exchange of energy between the electron and the field in discrete photon units—it is highly instructive to compare these results to the classical limit. This comparison reveals profound physical differences between classical ballistic electron kinematics and quantum matter-wave interference, specifically regarding the energy spectrum and the subsequent spatial density modulation (bunching) of the electron beam.

In the quantum formalism, an electron interacting with a continuous-wave optical field of frequency ω with a coupling strength g evolves into a superposition of discrete energy states. The probability P_n of emitting or absorbing n photons is given by the Bessel functions of the first kind:

$$P_n = J_n^2(2|g|). \tag{5.136}$$

In the purely classical regime, the electron is treated as a point particle arriving at the interaction region at a random phase $\phi \in [0, 2\pi]$ relative to the optical cycle. The continuous energy shift it experiences is $\Delta E(\phi) = 2|g|\hbar\omega\cos(\phi)$. Because the initial phase is uniformly distributed, the probability density function for the electron's final energy is found via the Jacobian transformation $P(\Delta E) = P(\phi)|d\phi/d\Delta E|$. This yields the classical arcsine distribution:

$$P_{class}(\Delta E) = \frac{1}{\pi\sqrt{(2|g|\hbar\omega)^2 - (\Delta E)^2}} \quad \text{for} \quad |\Delta E| < 2|g|\hbar\omega, \tag{5.137}$$

and zero otherwise. The quantum distribution $J_n^2(2|g|)$ smoothly recovers this classical arcsine envelope in the correspondence limit where $|g| \gg 1$ and n is treated as a continuous variable $E/\hbar\omega$.

While the energy modulation occurs instantaneously at the interaction plane ($z = 0$), the conversion of this energy modulation into spatial density modulation (bunching) requires free-space propagation. Sispersion causes components with different energies to travel at different velocities, transforming the phase modulation into an amplitude modulation.

Before diving into the mathematics, it is crucial to establish the conceptual distinction between the classical and quantum regimes. In classical klystron theory, "bunching" is strictly a macroscopic phenomenon: it describes an *ensemble* of many point-particle electrons catching

up to one another to create a varying macroscopic charge density $\rho(z,t)$. A single classical electron cannot bunch with itself. Quantum mechanically, however, the "bunching" describes the probability density $|\psi(z,t)|^2$ of a *single* electron. As the electron's discrete energy sidebands propagate, they accumulate different quantum phases and interfere with one another. Thus, quantum bunching is a single-particle matter-wave interference effect.

To calculate the spatial density modulation, we define the normalized dispersion parameter $\theta = \frac{\pi z}{z_T}$, where $z_T = \frac{4\pi m_0 \gamma^3 v^3}{\hbar \omega^2}$ is the Talbot distance. We seek the fundamental bunching factor b_1, defined as the first Fourier harmonic of the density at the optical frequency ω.

1. The Classical Klystron Derivation

Classically, an ensemble of electrons arrives at the interaction region with a uniform time distribution t_0. They experience a continuous energy modulation $E = E_0 + \Delta E \cos(\omega t_0)$, where $\Delta E = 2|g|\hbar\omega$. Because velocity depends on energy ($dv/dE = 1/m_0\gamma^3 v$), the electrons acquire a velocity modulation:

$$v(t_0) \approx v_0 + \frac{2|g|\hbar\omega}{m_0\gamma^3 v_0}\cos(\omega t_0). \tag{5.138}$$

Following ballistic trajectories $z = v(t_0)(t - t_0)$, the arrival time t at a distance z is:

$$t \approx t_0 + \frac{z}{v_0} - \frac{z}{v_0^2}\left(\frac{2|g|\hbar\omega}{m_0\gamma^3 v_0}\right)\cos(\omega t_0). \tag{5.139}$$

The classical bunching factor is the ensemble average of the fundamental harmonic, $b_{1,c} = \langle e^{i\omega t}\rangle$. Substituting the arrival time and normalizing the constants to the dispersion parameter θ, we find:

$$b_{1,c}(z) = \frac{1}{2\pi}\int_0^{2\pi} e^{i\omega t_0 - i(4|g|\theta)\cos(\omega t_0)} d(\omega t_0). \tag{5.140}$$

Using the Jacobi-Anger expansion, this integral evaluates exactly to the first Bessel function, yielding the classical ballistic bunching factor:

$$b_{1,c}(z) = J_1(4|g|\theta). \tag{5.141}$$

2. The Quantum Matter-Wave Derivation

In the quantum regime, we propagate the single-electron wavefunction. Immediately after the PINEM interaction, the electron is in a superposition of discrete sidebands: $\psi(0,t) \propto \sum_n J_n(2|g|)e^{in\omega t}$. As the state propagates to a distance z, each sideband n accumulates a longitudinal geometric phase $k_n z$. Expanding the dispersion relation $k(E)$ to second order, $k_n \approx k_0 + \frac{n\omega}{v_0} - \frac{n^2\omega^2}{2m_0\gamma^3 v_0^3}$, the wavefunction becomes:

$$\psi(z,t) \propto \sum_{n=-\infty}^{\infty} J_n(2|g|)e^{in\omega(t - z/v_0)}e^{-in^2\theta}. \tag{5.142}$$

The single-particle probability density is $|\psi(z,t)|^2$. The fundamental bunching factor $b_{1,q}$ is extracted by taking the expectation value of the electron ladder operator $b = e^{-i\omega z}$, or equivalently by calculating the cross-terms of the amplitudes where the sideband index differs by one ($m = n - 1$):

$$b_{1,q}(z) = \sum_{n=-\infty}^{\infty} J_n(2|g|)J_{n-1}(2|g|)e^{-i(n^2-(n-1)^2)\theta} = \sum_{n=-\infty}^{\infty} J_n(2|g|)J_{n-1}(2|g|)e^{-i(2n-1)\theta}. \tag{5.143}$$

Using Graf's addition theorem for Bessel functions, this infinite sum evaluates analytically:

$$b_{1,q}(z) = J_1(4|g|\sin\theta). \tag{5.144}$$

The simple mathematical substitution of $\theta \to \sin\theta$ between the classical and quantum bunching factors yields two physical consequences:

1. The Quantum Talbot Effect (Periodicity):
Classically, as the propagation distance $z \to \infty$, the dispersion parameter $\theta \to \infty$. The argument of the classical bunching factor $J_1(4|g|\theta)$ grows indefinitely, causing the bunching amplitude to oscillate and eventually decay to zero as $1/\sqrt{z}$. This represents washout of the density modulation. Quantum mechanically, the argument of the Bessel function is bounded by the sine function. The density modulation is strictly periodic in space, $b_1(z) = b_1(z + z_T)$. This revival of the electron bunching is the temporal Talbot effect, a purely quantum phenomenon arising from the discrete nature of the electron energy sidebands.

2. Shift in the Optimal Bunching Distance:
To achieve maximum compression (the highest possible bunching factor), the argument of the Bessel function must be tuned to its first maximum, $x_0 \approx 1.84$. In the classical regime, the optimal propagation distance is purely linear with respect to the coupling: $\theta_c^{opt} = \frac{1.84}{4|g|}$. In the quantum regime, the optimal distance satisfies $\sin\left(\theta_q^{opt}\right) = \frac{1.84}{4|g|}$. Expanding the arcsine function for low coupling strengths reveals a fundamental shift:

$$\theta_q^{opt} \approx \theta_c^{opt} + \frac{(\theta_c^{opt})^3}{6}. \tag{5.145}$$

Thus, for weak field interactions (low g), the focal plane of the electron wavepacket occurs at a distinctly different, longer propagation distance than predicted by classical kinematics. Furthermore, if the interaction is exceedingly weak such that $4|g| < 1.84$, the argument $4|g|\sin\theta$ can never reach the Bessel maximum. In this deep quantum regime, classical "optimal bunching" is strictly impossible, and the highest achievable bunching is physically capped by the Talbot limit at $\theta = \pi/2$.

5.2.4 Photon Statistics in Free-Electron Lasers

A long-standing, formidable goal in the accelerator community is the generation of non-classical light—such as Fock states, squeezed states, or entangled photons—directly from a free-electron laser (FEL). Before exploring advanced quantum interactions, it is crucial to understand the baseline photon statistics of spontaneous emission in an FEL, and specifically, how the longitudinal distribution of the electron beam governs these statistics.

In this section, we analyze the intensity fluctuations of FEL emission and demonstrate a surprising result: while an unbunched beam produces thermal statistics, and a beam bunched at the emission frequency produces coherent statistics, a beam bunched at *double* the emission frequency produces highly noisy, *super-thermal* (super-Poissonian) statistics. This behavior can be elegantly understood by mapping the multi-electron emission process onto one-dimensional and two-dimensional random walks in the complex plane.

Consider a beam of N non-interacting electrons arriving at an interaction region (e.g., an undulator) at times t_j. The complex amplitude of the emitted spontaneous radiation at frequency ω is given by the sum of the individual electron contributions:

$$A(\omega) = g\sum_{j=1}^{N} e^{i\phi_j}, \tag{5.146}$$

where g represents the single-electron emission amplitude and $\phi_j = \omega t_j$ is the phase of the j-th electron. The total radiated intensity is $I(\omega) = |A(\omega)|^2$.

To quantify the statistics of the emitted light, we define the generalized bunching factors of the electron beam at the m-th harmonic:

$$b_m = \langle e^{im\phi_j} \rangle = \int d\phi\, \rho(\phi) e^{im\phi}, \tag{5.147}$$

where $\rho(\phi)$ is the phase distribution of the electron bunch. The mean intensity emitted by the beam is:

$$\langle I(\omega)\rangle = g^2 \left\langle \sum_{j,k} e^{i(\phi_j - \phi_k)} \right\rangle = g^2 \left[N + N(N-1)|b_1|^2\right]. \tag{5.148}$$

The variance of the intensity, $\mathrm{Var}(I) = \langle I^2\rangle - \langle I\rangle^2$, dictates the nature of the photon statistics. By expanding the four-fold sum of $\langle I^2\rangle = g^4\langle\sum_{j,k,l,m} e^{i(\phi_j-\phi_k+\phi_l-\phi_m)}\rangle$ and grouping the non-vanishing terms, we find the general expression for the variance. For a beam with no fundamental bunching ($b_1 = 0$), the variance simplifies exactly to:

$$\mathrm{Var}(I) = g^4 N(N-1)\left[1 + |b_2|^2\right]. \tag{5.149}$$

This equation reveals that the intensity fluctuations at frequency ω are highly sensitive to b_2, the electron bunching at the *second harmonic* (i.e., bunching at $\omega/2$).

To characterize the photon statistics of the FEL emission, we utilize the normalized second-order coherence function, $g^{(2)}(0)$, defined classically in terms of the intensity I:

$$g^{(2)}(0) = \frac{\langle I^2\rangle}{\langle I\rangle^2} = 1 + \frac{\mathrm{Var}(I)}{\langle I\rangle^2}. \tag{5.150}$$

In quantum optics, this observable classifies the nature of the emitted light: $g^{(2)}(0) = 1$ corresponds to Poissonian (coherent) light, $g^{(2)}(0) > 1$ indicates super-Poissonian statistics, $g^{(2)}(0) = 2$ defines standard thermal light, and values $g^{(2)}(0) > 2$ represent super-thermal light.

By evaluating the intensity and its variance under different electron bunching conditions, three distinct statistical regimes emerge:

1. The Unbunched Beam (Thermal Statistics):
For a completely uniform (unbunched) beam, the electron phases ϕ_j are uniformly distributed in $[0, 2\pi]$. Consequently, all bunching factors vanish ($b_1 = b_2 = 0$). The mean intensity is $\langle I\rangle = Ng^2$, and the variance is:

$$\mathrm{Var}(I) = N(N-1)g^4 \approx \langle I\rangle^2. \tag{5.151}$$

This results in $g^{(2)}(0) = 2$, which is the hallmark of a thermal (exponential) distribution. Physically, adding independent complex vectors with random phases constitutes a **2D random walk** in the complex plane. The resulting field amplitude follows a 2D Gaussian distribution, yielding standard thermal intensity statistics.

2. Bunched at ω (Coherent Statistics):
If the beam is perfectly bunched at the emission frequency ω, all electrons emit strictly in phase ($\phi_j = 0$). In this case, $b_1 = 1$, and the intensity scales coherently as $\langle I\rangle = N^2g^2$. The classical phase space is restricted to a single point, meaning the variance approaches zero, yielding $g^{(2)}(0) = 1$. This represents the classical limit of a Poissonian coherent state.

3. Bunched at 2ω (Super-Thermal Statistics):
A qualitatively different statistical regime occurs when the beam is bunched at the second harmonic of the emission frequency (2ω). In this configuration, the physical spacing between electron micro-bunches is $\lambda_{em}/2$, meaning the electrons arrive at phases restricted to $\phi_j \in \{0, \pi\}$.

Because the electrons populate the 0 and π phase buckets equally, the fundamental bunching factor vanishes ($b_1 = \langle\pm 1\rangle = 0$), and the mean intensity remains spontaneous: $\langle I\rangle = Ng^2$. However, the second harmonic bunching factor is maximized ($b_2 = \langle(\pm 1)^2\rangle = 1$). Substituting $b_2 = 1$ into the general variance equation yields:

$$\mathrm{Var}(I) = 2N(N-1)g^4 \approx 2\langle I\rangle^2. \tag{5.152}$$

This results in $g^{(2)}(0) = 3$. The variance is exactly twice that of a thermal source, indicating super-thermal statistics.

This effect is understood through the random walk model. Because the allowed phases are strictly 0 or π, the individual emission amplitudes are entirely real ($\pm g$). The emission process reduces from a 2D random walk in the complex plane to a **1D random walk** along the real axis. Statistically, the square of a 1D Gaussian distribution produces a Chi-squared distribution with one degree of freedom (χ_1^2), which inherently possesses twice the normalized variance of the 2D case (χ_2^2).

This mechanism provides a novel approach to manipulating the emission statistics and noise profile of free electrons lasers, relying entirely on kinematics rather than nonlinear optical interactions. Notably, this operates in direct contrast to typical FEL schemes, such as High-Gain Harmonic Generation (HGHG). In standard practice, FELs are bunched at a sub-harmonic (e.g., $\omega/2$ or $\omega/3$) to drive coherent Poissonian emission at the higher harmonics. By instead bunching at a higher harmonic (2ω) to observe the fundamental (ω), coherent emission is entirely suppressed, but the underlying spontaneous noise profile is fundamentally altered into a highly correlated, super-thermal state.

5.2.5 Electrostatic Fields as Vacuum Displacement in QED

A fundamental pedagogical question in quantum electrodynamics (QED) is the origin of static electric fields. The standard quantization of the free electromagnetic field is performed in the Coulomb gauge, where only the propagating, transverse modes ($\omega_k = ck > 0$) are quantized as photons. This raises the question: how does a static electrostatic field (which has no frequency) emerge from a framework that only describes oscillating transverse photons?

In this section, we provide a mathematically rigorous toy model demonstrating that the presence of a static point dipole does not require the introduction of new "static" photon modes. Instead, the interaction with the dipole shifts the ground state of the entire electromagnetic field from the bare vacuum $|0\rangle$ into a multi-mode coherent state. The expectation value of the quantized transverse electric field operator in this new, displaced vacuum precisely recovers the classical macroscopic dipole field.

We begin with the free Hamiltonian of the transverse electromagnetic field:

$$H_0 = \sum_{\mathbf{k},\lambda} \hbar\omega_k \left(a^\dagger_{\mathbf{k},\lambda} a_{\mathbf{k},\lambda} + \frac{1}{2} \right), \tag{5.153}$$

where $\mathbf{k}$ sums over all momentum modes, $\lambda \in \{1, 2\}$ represents the two transverse polarizations, and $\omega_k = c|\mathbf{k}|$. The quantized electric field operator evaluated at position $\mathbf{r}$ is:

$$\hat{\mathbf{E}}(\mathbf{r}) = i \sum_{\mathbf{k},\lambda} \sqrt{\frac{\hbar\omega_k}{2\varepsilon_0 V}} \mathbf{e}_{\mathbf{k},\lambda} \left(a_{\mathbf{k},\lambda} e^{i\mathbf{k}\cdot\mathbf{r}} - a^\dagger_{\mathbf{k},\lambda} e^{-i\mathbf{k}\cdot\mathbf{r}} \right), \tag{5.154}$$

where $\mathbf{e}_{\mathbf{k},\lambda}$ are the transverse polarization unit vectors, satisfying $\mathbf{e}_{\mathbf{k},\lambda} \cdot \mathbf{k} = 0$.

We introduce a point dipole $\mathbf{d}$ located at the origin $\mathbf{r} = 0$. The interaction Hamiltonian in the dipole approximation is $H_{int} = -\mathbf{d} \cdot \hat{\mathbf{E}}(0)$. The total Hamiltonian is therefore:

$$H = \sum_{\mathbf{k},\lambda} \left[\hbar\omega_k a^\dagger_{\mathbf{k},\lambda} a_{\mathbf{k},\lambda} - i \left(\mathbf{d} \cdot \mathbf{e}_{\mathbf{k},\lambda} \right) \sqrt{\frac{\hbar\omega_k}{2\varepsilon_0 V}} \left(a_{\mathbf{k},\lambda} - a^\dagger_{\mathbf{k},\lambda} \right) \right]. \tag{5.155}$$

Because the interaction is strictly linear in the creation and annihilation operators, we can exactly diagonalize this Hamiltonian by completing the square. We define a multi-mode coherent displacement operator:

$$\mathcal{D}(\{\alpha_{\mathbf{k},\lambda}\}) = \prod_{\mathbf{k},\lambda} \exp\left(\alpha_{\mathbf{k},\lambda} a^\dagger_{\mathbf{k},\lambda} - \alpha^*_{\mathbf{k},\lambda} a_{\mathbf{k},\lambda} \right). \tag{5.156}$$

Applying this transformation to the annihilation operators, $a_{\mathbf{k},\lambda} \to a_{\mathbf{k},\lambda} + \alpha_{\mathbf{k},\lambda}$, we eliminate the linear terms in the Hamiltonian by choosing the displacement amplitudes:

$$\alpha_{\mathbf{k},\lambda} = -i \frac{\mathbf{d} \cdot \mathbf{e}^*_{\mathbf{k},\lambda}}{\hbar\omega_k} \sqrt{\frac{\hbar\omega_k}{2\varepsilon_0 V}}. \tag{5.157}$$

Consequently, the new ground state of the system is no longer the bare vacuum $|0\rangle$, but rather a coherently displaced vacuum $|\psi_0\rangle = \mathcal{D}(\{\alpha_{\mathbf{k},\lambda}\})|0\rangle$. This new state contains an infinite number of virtual transverse photons.

To observe the macroscopic field generated by the dipole, we calculate the expectation value of the electric field operator in this new coherent ground state. Since $\langle\psi_0|a_{\mathbf{k},\lambda}|\psi_0\rangle = \alpha_{\mathbf{k},\lambda}$, the expectation value is simply:

$$\begin{aligned} \langle\hat{\mathbf{E}}(\mathbf{r})\rangle &= i \sum_{\mathbf{k},\lambda} \sqrt{\frac{\hbar\omega_k}{2\varepsilon_0 V}} \mathbf{e}_{\mathbf{k},\lambda} \left(\alpha_{\mathbf{k},\lambda} e^{i\mathbf{k}\cdot\mathbf{r}} - \alpha^*_{\mathbf{k},\lambda} e^{-i\mathbf{k}\cdot\mathbf{r}} \right) \\ &= i \sum_{\mathbf{k},\lambda} \sqrt{\frac{\hbar\omega_k}{2\varepsilon_0 V}} \mathbf{e}_{\mathbf{k},\lambda} \left[\left(-i \frac{\mathbf{d} \cdot \mathbf{e}^*_{\mathbf{k},\lambda}}{\sqrt{2\varepsilon_0 V \hbar\omega_k}} \right) e^{i\mathbf{k}\cdot\mathbf{r}} - \left(i \frac{\mathbf{d} \cdot \mathbf{e}_{\mathbf{k},\lambda}}{\sqrt{2\varepsilon_0 V \hbar\omega_k}} \right) e^{-i\mathbf{k}\cdot\mathbf{r}} \right]. \end{aligned} \tag{5.158}$$

Simplifying the terms, the $\hbar\omega_k$ dependence perfectly cancels out, yielding a purely geometric sum:

$$\langle\hat{\mathbf{E}}(\mathbf{r})\rangle = \frac{1}{2\varepsilon_0 V} \sum_{\mathbf{k}} \sum_{\lambda=1,2} \mathbf{e}_{\mathbf{k},\lambda} \left(\mathbf{e}^*_{\mathbf{k},\lambda} \cdot \mathbf{d} \right) \left(e^{i\mathbf{k}\cdot\mathbf{r}} + e^{-i\mathbf{k}\cdot\mathbf{r}} \right). \tag{5.159}$$

We now evaluate the polarization sum using the completeness relation for transverse modes, $\sum_\lambda (\mathbf{e}_{\mathbf{k},\lambda})_i (\mathbf{e}^*_{\mathbf{k},\lambda})_j = \delta_{ij} - \hat{k}_i \hat{k}_j$. Since this tensor is symmetric with respect to $\mathbf{k} \to -\mathbf{k}$, the two exponential terms $e^{i\mathbf{k}\cdot\mathbf{r}}$ and $e^{-i\mathbf{k}\cdot\mathbf{r}}$ contribute equally when integrated over all $\mathbf{k}$-space. Taking the continuum limit $\frac{1}{V}\sum_{\mathbf{k}} \to \int \frac{d^3k}{(2\pi)^3}$, the field component $\langle E_i \rangle$ becomes:

$$\langle\hat{E}_i(\mathbf{r})\rangle = \frac{d_j}{\varepsilon_0} \int \frac{d^3k}{(2\pi)^3} \left(\delta_{ij} - \frac{k_i k_j}{k^2} \right) e^{i\mathbf{k}\cdot\mathbf{r}}. \tag{5.160}$$

This integral defines the transverse delta-function tensor. We can solve it rigorously by separating the two terms in the parentheses. The first term evaluates trivially to a Dirac delta function: $\int \frac{d^3k}{(2\pi)^3} \delta_{ij} e^{i\mathbf{k}\cdot\mathbf{r}} = \delta_{ij}\delta(\mathbf{r})$. The second term can be extracted from the Fourier transform of the Coulomb potential:

$$\int \frac{d^3k}{(2\pi)^3} \frac{k_i k_j}{k^2} e^{i\mathbf{k}\cdot\mathbf{r}} = -\partial_i \partial_j \int \frac{d^3k}{(2\pi)^3} \frac{e^{i\mathbf{k}\cdot\mathbf{r}}}{k^2} = -\partial_i \partial_j \left(\frac{1}{4\pi r} \right). \tag{5.161}$$

Combining these, the expectation value of the field is exactly:

$$\langle\hat{E}_i(\mathbf{r})\rangle = \frac{d_j}{\varepsilon_0} \left[\delta_{ij}\delta(\mathbf{r}) + \frac{1}{4\pi} \partial_i \partial_j \left(\frac{1}{r} \right) \right]. \tag{5.162}$$

Applying the spatial derivatives for $r \neq 0$, where $\partial_i \partial_j (1/r) = (3\hat{r}_i \hat{r}_j - \delta_{ij})/r^3$, we arrive at our final result in vector notation:

$$\langle\hat{\mathbf{E}}(\mathbf{r} \neq 0)\rangle = \frac{1}{4\pi\varepsilon_0} \left(\frac{3\hat{\mathbf{r}}(\mathbf{d} \cdot \hat{\mathbf{r}}) - \mathbf{d}}{r^3} \right). \tag{5.163}$$

Thus, without ever quantizing a static Coulomb interaction, the classical electrostatic dipole field perfectly emerges from the coherent displacement of the transverse quantum vacuum.

5.2.6 Quantum Noise Limits and Correlated Electron Imaging

A fundamental limit in all forms of electron microscopy is the intrinsic noise of the electron beam. In standard transmission electron microscopy (TEM), electrons are emitted from a thermal or field-emission source via independent, uncorrelated stochastic processes. This lack of correlation manifests as a fundamental noise floor that obscures the imaging of dose-sensitive, fragile materials.

To bypass this limit, one must engineer "quiet" electron beams. In this section, we analyze the transmission of an electron beam through a semi-transparent sample. By decomposing the total image noise into distinct fundamental components—*shot noise* and *partition noise*—we demonstrate that they are governed by entirely different physical mechanisms and require distinct forms of electron correlations (temporal vs. spatial) to be suppressed.

Consider a transmission imaging experiment where an incident electron beam illuminates a specific spatial region of a sample. Let N be the number of incident electrons hitting this region, and let $T \in [0, 1]$ be the transmission probability of the sample. The number of electrons successfully transmitted and detected is n.

Because the transmission of each individual electron is an independent Bernoulli trial (it either passes or is scattered/absorbed), the conditional probability of detecting n electrons given N incident electrons follows a binomial distribution. The conditional expectation value is $E[n|N] = TN$, and the conditional variance is $\mathrm{Var}(n|N) = NT(1 - T)$.

In a real experiment, the number of incident electrons N is not fixed; it fluctuates due to the emission statistics of the source. To find the total variance of the detected signal, we apply the law of total variance:

$$\mathrm{Var}(n) = \mathrm{Var}(E[n|N]) + E[\mathrm{Var}(n|N)]. \tag{5.164}$$

Substituting the binomial expectation and variance, we obtain the fundamental noise equation for transmission imaging:

$$\mathrm{Var}(n) = T^2\mathrm{Var}(N) + \langle N\rangle T(1 - T). \tag{5.165}$$

This equation elegantly separates the noise into two distinct physical origins:

1. $T^2\mathrm{Var}(N)$: **Shot Noise.** This term originates entirely from the statistical fluctuations of the electron source itself. It is the uncertainty in the total number of electrons arriving at the sample.

2. $\langle N\rangle T(1 - T)$: **Partition Noise.** This term arises from the probabilistic nature of the scattering process inside the sample. Even if the incident beam is perfectly noiseless, the quantum mechanical "choice" of each electron to transmit or scatter injects binomial noise into the final image.

In a standard TEM, the electron source emits a Poissonian beam, meaning the variance of the incident beam equals its mean: $\mathrm{Var}(N) = \langle N\rangle$. Substituting this into our equation yields $\mathrm{Var}(n) = T^2\langle N\rangle + \langle N\rangle T - \langle N\rangle T^2 = \langle N\rangle T$. Because the total detected mean is $\langle n\rangle = \langle N\rangle T$, we find that $\mathrm{Var}(n) = \langle n\rangle$. The transmitted beam remains purely Poissonian. Both noises scales linearly with $\langle N\rangle$ leading to the confusion between them in the literature.

To improve the signal-to-noise ratio beyond the Poisson limit, we must first eliminate the source fluctuations. This is achieved by introducing *temporal anti-bunching* into the electron beam.

If the electron source is engineered to emit exactly one electron at a time at perfectly regular intervals (e.g., using a single-electron pump or a Coulomb-blockaded emitter). In this idealized temporally correlated state, there are absolutely no fluctuations in the incident particle rate: $\mathrm{Var}(N) = 0$.

Under this condition, the shot noise term in our variance equation vanishes. The total noise in the image is reduced to the partition noise:

$$\mathrm{Var}_{anti-bunched}(n) = \langle N \rangle T(1-T). \tag{5.166}$$

Because $T \leq 1$, this variance is strictly less than the Poissonian variance $\langle n \rangle = \langle N \rangle T$. The transmitted beam exhibits sub-Poissonian statistics. However, the partition noise $T(1-T)$ remains a hard physical limit. As long as the electrons act as independent particles sampling a probabilistic cross-section, the partition noise cannot be beaten by temporal correlations alone.

It is crucial to recognize that the binomial partition noise $T(1-T)$ calculated above represents a fundamental quantum limit of the scattering process. For a single pixel, if an incident electron encounters a partially transparent barrier, the "choice" to transmit or scatter is an inherent quantum superposition collapse. No degree of beam engineering can mitigate this fundamental partition noise for a single pixel. This distinction clarifies a common ambiguity in the literature, where "shot noise" is frequently used interchangeably with the "standard quantum limit", as this single-pixel example demonstrates, the ultimate quantum limit of a transmission measurement fundamentally arises from the Bernoulli partition noise of the sample's scattering process, rather than the shot noise of the incident beam.

However, practical imaging does not consist of a single pixel; it involves an array of M spatial pixels. This multi-pixel geometry introduces a second, entirely distinct form of noise: *spatial partition noise*.

Suppose the total beam consists of N_{tot} electrons. If the beam lacks transverse spatial correlations, each electron randomly lands on the sample, hitting a given pixel i with probability p_i (where $p_i \approx 1/M$ for uniform illumination). The number of electrons incident on pixel i, denoted N_i, is therefore a binomial random variable.

Crucially, even if the electron source is perfectly temporally anti-bunched such that the total number of emitted electrons is absolute and noiseless ($\mathrm{Var}(N_{tot}) = 0$), the local number of incident electrons at pixel i still fluctuates due to this random transverse distribution:

$$\mathrm{Var}(N_i) = N_{tot} p_i (1-p_i). \tag{5.167}$$

Because the incident illumination N_i fluctuates, we must reapply the law of total variance for the detected electrons n_i at pixel i, which yields:

$$\mathrm{Var}(n_i) = T_i^2 \mathrm{Var}(N_i) + \langle N_i \rangle T_i (1-T_i). \tag{5.168}$$

Substituting the spatial variance, the total noise at pixel i becomes:

$$\mathrm{Var}(n_i) = T_i^2 N_{tot} p_i (1-p_i) + \langle N_i \rangle T_i (1-T_i). \tag{5.169}$$

The first term is the spatial partition noise (the illumination noise caused by random transverse sampling), and the second term is the sample's inherent scattering partition noise.

To eliminate the spatial partition noise, one must introduce *spatial homogeneity* (transverse spatial correlations) into the beam. Such homogenization could potentially arise naturally from strong Coulomb repulsion between the particles. In the extreme limit of this interaction, mutual repulsion forces the electrons to spontaneously organize into a rigid, highly ordered spatial lattice (known as Wigner crystal).

When such a spatially correlated beam illuminates a multi-pixel sample, the randomness of the transverse sampling is eliminated. Assuming the density of this electron beam matches the pixel density, exactly the same number of electrons strikes pixel i during every exposure. The spatial partitioning across the image is no longer a probabilistic Bernoulli trial, but deterministic.

Consequently, the spatial variance vanishes ($\mathrm{Var}(N_i) = 0$). The total noise at each pixel is driven down to the absolute quantum minimum dictated solely by the sample's physical opacity:

$$\mathrm{Var}_{correlated}(n_i) = \langle N_i \rangle T_i(1 - T_i). \tag{5.170}$$

Therefore, while temporal anti-bunching eliminates the longitudinal shot noise of the source, transverse spatial homogenization is required to eliminate the spatial partition noise across a multi-pixel array. True noiseless illumination requires a synthesis of both, systematically stripping away the beam's stochastic degrees of freedom until only the fundamental quantum scattering limit of the sample itself remains.

5.2.7 Electron Mass Renormalization in a Macroscopic Medium

Throughout this thesis, macroscopic quantum electrodynamics (MQED) has been utilized primarily to describe the coherent exchange of photons between free electrons and engineered photonic environments. However, a profoundly intriguing question arises when we consider "hard-core" QED phenomena—such as the Casimir effect, the Lamb shift, and mass renormalization—within the context of macroscopic nanophotonics. Does the presence of a macroscopic medium fundamentally alter the intrinsic properties of a free elementary particle?

In this section, we provide a theoretical proof of concept demonstrating that the effective kinetic mass of an electron is indeed renormalized by its macroscopic environment. By calculating the second-order self-energy of a moving electron interacting with the quantized electromagnetic field inside a homogeneous dispersive plasma, we show how the electron's mass diverges from its standard vacuum value.

In standard non-relativistic QED, the observable mass of an electron m^* is not its "bare" mass m_0. The bare mass is dynamically dressed by the electron's continuous emission and reabsorption of virtual photons. For a moving electron, this manifests as a correction to its kinetic energy, which renormalizes the mass governing its parabolic dispersion relation ($E = p^2/2m^*$).

We begin with the minimal coupling Hamiltonian:

$$H = \frac{(\mathbf{p} - e\mathbf{A})^2}{2m_0} = \frac{\mathbf{p}^2}{2m_0} - \frac{e}{m_0}\mathbf{p}\cdot\mathbf{A} + \frac{e^2}{2m_0}\mathbf{A}^2. \tag{5.171}$$

While the $\mathbf{A}^2$ term provides a constant, momentum-independent shift to the rest energy, the momentum-dependent correction arises from the linear $\mathbf{p}\cdot\mathbf{A}$ term evaluated to second-order in perturbation theory. The energy shift for an electron with initial momentum $\mathbf{p}$ and a photon vacuum state $|0\rangle$ is given by the sum over all intermediate states $|I\rangle$ (where the electron has momentum $\mathbf{p} - \hbar\mathbf{k}$ and one virtual photon of momentum $\hbar\mathbf{k}$ is created):

$$\Delta E^{(2)}(\mathbf{p}) = \sum_I \frac{|\langle I| - \frac{e}{m_0}\mathbf{p}\cdot\mathbf{A}|\mathbf{p};0\rangle|^2}{E_{initial} - E_I}. \tag{5.172}$$

When the electron propagates inside a dispersive medium, the virtual photons are governed by the medium's dispersion relation, and the density of states is modified by the dielectric function $\epsilon(\omega)$.

When formulating macroscopic QED in a dispersive medium, the quantized vector potential requires a modified normalization to ensure each mode correctly possesses a zero-point energy of $\frac{1}{2}\hbar\omega_k$. This introduces a scaling factor that depends on the dielectric function:

$$\widehat{\mathbf{A}}(\mathbf{r}) = \sum_{\mathbf{k},\lambda} \sqrt{\frac{\hbar}{2\varepsilon_0\omega_k V D(\omega_k)}}\widehat{\mathbf{e}}_{\mathbf{k},\lambda}\left(\hat{a}_{\mathbf{k},\lambda}e^{i\mathbf{k}\cdot\mathbf{r}} + \text{h.c.}\right), \quad \text{where } D(\omega) = \frac{1}{2\omega}\frac{d(\omega^2\epsilon)}{d\omega}. \tag{5.173}$$

To look at a simple case, we consider a free-electron propagating in an homogeneous plasma. The plasma dielectric function is given by, $\epsilon(\omega) = 1 - \omega_p^2/\omega^2$, where ω_p is the plasma frequency. Taking the derivative yields $\frac{d}{d\omega}(\omega^2\epsilon) = 2\omega$, meaning $D(\omega) = 1$. The quantized field amplitude matches the vacuum form, albeit subject to the modified dispersion relation $\omega_k^2 = c^2k^2 + \omega_p^2$.

To evaluate the transition matrix element analytically, we apply the dipole approximation ($\hbar k \ll p$), meaning the momentum of the virtual photon is negligible compared to the electron's momentum. The energy denominator is therefore dominated entirely by the photon energy ($E_i - E_f \approx -\hbar\omega_k$). Expanding the squared matrix element and averaging over the photon polarizations λ, the angular dependence $\sum |\mathbf{p} \cdot \mathbf{e}_{\mathbf{k},\lambda}|^2$ yields $p^2 \sin^2\theta$.

Taking the continuum limit ($V \to \infty$), the discrete sum transitions into an integral over the modified photonic modes. The angular integration of $\sin^2\theta$ over the solid angle yields $8\pi/3$, leaving a momentum-dependent energy shift:

$$\Delta E^{(2)}(\mathbf{p}) = -\frac{e^2p^2}{6\pi^2\varepsilon_0 m_0^2}\int_0^{k_c}\frac{k^2}{\omega_k^2}dk \equiv -\alpha p^2. \tag{5.174}$$

Because the integral evaluates over the continuum of photon frequencies, it inherently depends on the plasma dispersion. Substituting $\omega_k^2 = c^2k^2 + \omega_p^2$, we can evaluate the integral exactly:

$$\int_0^{k_c}\frac{k^2}{c^2k^2+\omega_p^2}dk = \frac{1}{c^2}\int_0^{k_c}\left(1 - \frac{\omega_p^2}{c^2k^2+\omega_p^2}\right)dk = \frac{k_c}{c^2} - \frac{\omega_p}{c^3}\arctan\left(\frac{ck_c}{\omega_p}\right). \tag{5.175}$$

As in all non-relativistic QED self-energy calculations, the integral requires a high-frequency cutoff (such as the Compton limit $k_c = m_0c/\hbar$) to converge. In the large cutoff limit ($ck_c \gg \omega_p$), the arctangent asymptotically approaches $\pi/2$. Thus, the coupling constant evaluates to:

$$\alpha \approx \frac{e^2}{6\pi^2\varepsilon_0 m_0^2c^2}\left(k_c - \frac{\pi\omega_p}{2c}\right). \tag{5.176}$$

The total kinetic energy of the electron is therefore the sum of the bare parabolic kinetic energy and this second-order QED shift:

$$E_{total} = \frac{p^2}{2m_0} - \alpha p^2 = \frac{p^2}{2}\left(\frac{1}{m_0} - 2\alpha\right). \tag{5.177}$$

By defining the total energy strictly in terms of an effective kinetic mass, $E_{total} \equiv p^2/2m^*$, we extract the renormalized mass $m^* \approx m_0(1 + 2m_0\alpha)$, which yields:

$$m^* = m_0 + \frac{e^2k_c}{3\pi^2\varepsilon_0c^2} - \frac{e^2\omega_p}{6\pi\varepsilon_0c^3}. \tag{5.178}$$

This derivation naturally the mass renormalization into two distinct components: $m^* = m_0 + \delta m_{vac} + \delta m_{plasma}(\omega_p)$.

The first term, $\delta m_{vac} \propto k_c$, emerges from the high-frequency limit where the plasma cannot respond. This term is independent of ω_p and represents the standard linear divergence of the vacuum mass renormalization in non-relativistic QED. In standard physics, this unobservable shift is absorbed into the definition of the physical mass $m_e = m_0 + \delta m_{vac}$.

The second term, $\delta m_{plasma}(\omega_p) \propto -\omega_p$, is entirely novel to the MQED framework. It depends explicitly on the plasma frequency, representing the additional dynamical dressing of the electron's kinetic mass by the collective macroscopic excitations of the environment.

While evaluating this medium-induced mass shift yields an incredibly tiny numerical correction to the electron's inertia, it serves as a proof of concept that the fundamental dynamical properties of elementary particles are dynamically coupled to, and altered by, their macroscopic dielectric boundary conditions. Exploring how this medium-dependent renormalization scales in highly confined nanophotonic geometries remains a compelling direction for future research.

Chapter 6

Discussion

The overarching objective of this thesis has been to elevate the free electron from a classical, passive imaging probe into an active, highly tunable quantum resource. By systematically exploring and expanding the "triangle of quantum interactions" in free-electron quantum optics, we have established rigorous theoretical frameworks and proposed concrete experimental pathways for utilizing free electrons in advanced quantum metrology, many-body spectroscopy, and quantum information processing.

In this chapter, we synthesize the findings from the research papers comprising this thesis. We discuss how the coherent manipulation of the free electron transforms the interaction with quantum matter (Electron-Matter interactions), sensing and generating quantum light (Electron-Light interactions), and finally, pushing beyond single-electron paradigms to generate multi-electron entanglement. By integrating these distinct domains, we highlight the overarching innovation of this work: laying the foundational blueprint for the electron microscope as a fully coherent, versatile quantum laboratory.

6.1 The Electron-Matter Edge: From Single Qubits to Macroscopic Ensembles

Probing and Controlling Individual Qubits (3.1)

Through the theoretical development of the Free-Electron-Bound-Electron Resonant Interaction (FEBERI), we demonstrated that coherently shaped free electrons can act as ultrafast, atomic-resolution probes capable of determining a qubit's state and extracting vital quantum characteristics. The fundamental concept of utilizing the electron as a flying quantum gate is depicted in Figure 3.3. As our findings indicate, this interaction can achieve extraordinary spatiotemporal resolution, reaching single nanometers spatially and hundreds of femtoseconds temporally, bounded primarily by the excitation laser bandwidth.

The innovation here lies in the ability to access individual quantum emitters within dense ensembles—such as semiconductor quantum dots (SCQDs)—which is typically obscured by the optical diffraction limit. As shown in Figure 3.4, our framework enables the extraction of the longitudinal relaxation time (T_1) and transverse coherence time (T_2). Furthermore, by measuring the final electron state, we can non-destructively measure the initial quantum state of the material qubit (Figure 3.5).

A critical discussion point is the validity of modeling real, complex materials as idealized two-level systems. Free electrons are highly energetic and can trigger numerous off-resonant material excitations, serving as unwanted decoherence channels. However, we showed that by employing post-selection (via stringent energy filtering), one can isolate only those electrons that exchanged

the exact qubit transition energy. This ensures that the measured electron-qubit density matrix remains robust against environmental noise, particularly in thin samples. Looking forward, we envision combining this diagnostic capability with coherent control techniques to construct a new class of nanoscale quantum simulators, where shaped electrons read, write, and simulate many-body Hamiltonians with deep sub-wavelength resolution.

Superradiant Electron Energy Loss Spectroscopy (3.2)

Expanding the FEBERI framework to multiple spatially distributed emitters, we introduced Superradiant Electron Energy Loss Spectroscopy (SREELS). This work broadens the context of conventional EELS. Traditional EELS relies heavily on linear response theory and assumes the target material is in thermal equilibrium. In contrast, our findings demonstrate the critical role of mutual quantum coherence within the material.

As illustrated by the phase-matched resonances in the EELS spectrum (Figure 3.8), when a single free electron interacts with an extended coherent ensemble, the interaction cross-section is drastically modified even if the electron itself is not pre-modulated. SREELS provides a novel diagnostic tool to directly extract the superradiant quantum state of the ensemble (Figure 3.9) and map its ultrafast cooperative dynamics (Figure 3.10).

The primary contribution of this work to the field of quantum optics is the introduction of a spatial probe for Dicke superradiance. Typically, superradiance is probed optically by measuring the far-field emitted photon pulse. SREELS allows us to image the intermediate populations along the superradiant ladder with simultaneous high spatial and temporal resolution. Importantly, our theoretical analysis shows that this resonant enhancement is robust against realistic experimental imperfections, including variations in emitter energies and positions (governed by the T_2^* decoherence time). With effective coupling strengths predicted to exceed unity for large ensembles, SREELS presents an immediate, feasible target for current ultrafast electron microscopes.

6.2 The Electron-Light Edge: Enhanced Metrology and Quantum State Engineering

The second major pillar of this thesis investigated the interaction between free electrons and the electromagnetic fields, leading to innovations in both the classical sensing of weak optical fields and the deterministic generation and manipulation of complex quantum light.

Manipulating Quantum States of Light (4.1)

We demonstrated that the free electron can be utilized as a flying ancilla to generate, manipulate, and correct continuous-variable quantum states of light. By mapping the PINEM interaction onto generalized displacement operators, we showed how the electron can perform precise quantum gates on Gottesman-Kitaev-Preskill (GKP) error-correcting codes (Figure 4.15).

The innovation here lies in the unique physical nature of the free electron. Unlike stationary ancilla qubits (such as superconducting transmons or trapped ions) which are limited by fixed spatial connectivity and specific resonance frequencies, the free electron is a highly energetic, versatile flying qubit. This allows a single electron to sequentially interact with multiple, spatially separated photonic cavities. As shown in Figure 4.17, this mechanism can efficiently generate highly entangled multimode states—such as GHZ and cluster states—without the exponential complexity typically associated with scaling multi-qubit architectures.

Furthermore, the "aloof" or grazing-angle geometry typical in these interactions ensures that the electron does not degrade the coherence time of the photonic qubit, as it interacts

strictly via the near-field for only a few picoseconds. When combined with fast, number-resolved direct electron detectors, our framework establishes a viable roadmap for continuous-variable quantum computing, offering a completely new paradigm for optical quantum memories and room-temperature fault-tolerant computation.

Free-Electron Interferometry (4.2, 4.3)

By exploiting the longitudinal (temporal) coherence of the free electron, we developed Free-Electron Ramsey-type Interferometry (FERI). Traditional phase-resolved electron microscopy methods, such as holography, rely on transverse spatial coherence, which places stringent demands on electron beam quality and source brightness. In contrast, longitudinal coherence is a highly robust parameter, allowing FERI to operate efficiently even with simpler, higher-flux sources, including scanning electron microscopes (SEMs).

Our experimental and theoretical results established FERI as a tool for sensing optical near-fields. The basic measurement scheme (Figure 4.20) and the optimization of the extracted phase (Figure 4.21) demonstrate sensitivity to both the amplitude and phase of the field. A key property of this approach is the ability to coherently amplify the electron's interaction with weak optical fields. By transitioning from the classical continuous-energy regime into the quantum regime (where the energy spread is smaller than the photon energy), the discrimination of single-photon absorption/emission events is drastically improved.

As demonstrated by the combined temporal and phase-resolved measurements (Figure 4.24), FERI provides access to deeply confined polaritonic fields (such as phonon polaritons in 2D materials) that are often inaccessible or destructively perturbed by scanning probe techniques like s-SNOM or PEEM. The coherent amplification of the signal (Figure 4.26) enables high-contrast imaging of fields as weak as a few kV/m without requiring high-intensity pump lasers. This non-destructive imaging modality holds promise for characterizing dose-sensitive biological samples and delicate van der Waals heterostructures, mitigating both laser-induced and electron-induced radiation damage.

6.3 Multi-Electron Entanglement

The final, and perhaps most conceptually profound, section of this thesis transcends the single-electron interactions to address the generation of quantum entanglement between distinct free electrons. This is a crucial frontier, as enabling collective electron dynamics is the key to surpassing classical shot-noise limits in microscopy.

Path Entanglement via "Which-Path" Information (3.3)

First, we explored the generation of spatial entanglement through the lens of a multi-particle "which-path" experiment. By designing an interaction where a quantum detector (e.g., a photonic cavity) interacts with multiple free electrons while maintaining its quantum coherence, we found that the electrons inherently develop strong non-local correlations. The core concept and its equivalent quantum logic gate description are illustrated in Figure 3.11.

We demonstrated that measuring the electrons can project the detector into highly useful non-classical states (such as optical cat states or GKP states). Conversely, measuring the state of the detector collapses the multi-electron wavefunction into an entangled state (Figure 3.12). A key theoretical insight is the mapping of this continuous-variable interaction onto a discrete fermionic detector model featuring conditional "yes/no" degrees of freedom. This shows that our free-electron which-path mechanism is mathematically isomorphic to the conditional phase gates used to generate multi-partite entanglement in leading quantum computing platforms,

highlighting the universality of this approach. By simply breaking the spatial or temporal symmetry of the electron arrivals, this interaction scales to explore exponentially large many-body Hilbert spaces.

Cavity-Mediated Interactions (5.1)

Finally, addressing the fundamental physical limitation that native free-space Coulomb repulsion cannot generate usable electron energy entanglement, we proposed a paradigm shift: utilizing macroscopic nanophotonic environment to mediate the electron-electron interactions.

By tracing out the photonic degrees of freedom in an arbitrary environment, we established a framework for generating multi-electron entanglement. By tuning the interaction with a photonic cavity to highly detuned phase-matching conditions, we effectively suppress dissipative real-photon emission (environmental decoherence) while maximizing the reversible exchange of virtual photon exchange. In the optical regime, this yields an entangled continuous-variable energy comb (Figure 5.28). Distinctly, in the microwave regime, mapping the transverse spatial paths of the electrons to a two-level qubit, the cavity-mediated dispersive interaction takes the mathematical form of a One-Axis Twisting (OAT) Hamiltonian. This native twisting interaction generates collective spatial entanglement and spin squeezing across the electron bunch (Figure 5.29).

We shows that this spatial entanglement provides a robust pathway toward quantum-enhanced electron metrology. To achieve sub-shot-noise sensitivity, the optimal dimensionless coupling required scales favorably as $N^{-1/3}$. However, a critical discussion point is the practical trade-off involving classical beam dynamics. The dense electron bunching ($N \gg 1$) required to maximize collective squeezing inevitably exacerbates space-charge effects, which degrade the transverse beam emittance and spatial resolution. Thus, future implementations will require precise optimization to balance the metrological quantum advantage against classical beam degradation.

6.4 Future Outlook: Experimental Realization and Technological Roadmaps

To successfully translate the theoretical frameworks established in this thesis into routine laboratory practice, several experimental hurdles must be overcome. The generation of complex quantum states, such as GKP and optical cat states using free electrons, inherently relies on the phase stability of the exciting optical fields and the rigorous coherence of the electron source. This necessitates unprecedented synchronization between the femtosecond laser excitation systems and the electron emission mechanisms. Minimizing timing jitter and actively stabilizing the optical phase drifts over extended acquisition times will be paramount to preserving the delicate quantum fidelities predicted by our models. Current ultrafast transmission electron microscopes (UTEMs) are undergoing rapid advancements; however, achieving the predicted strong-coupling regimes requires integrating high-quality-factor (high-Q) nanophotonic cavities directly into the electron beam path. Maintaining these delicate, high-Q optical resonances while preventing electron-induced damage, structural degradation, and localized charging effects on the dielectric cavities presents a significant, yet solvable, nanofabrication challenge.

Furthermore, as highlighted in our investigation of multi-electron entanglement, there exists a fundamental tension between establishing quantum correlations and managing classical beam dynamics. The cavity-mediated One-Axis Twisting (OAT) Hamiltonian requires dense electron bunching to maximize collective spin squeezing. Yet, pushing multiple electrons into tight spatiotemporal confinement inevitably exacerbates the aforementioned space-charge effects—the classical Coulomb repulsion that degrades beam emittance and blurs spatial resolution. Future

experimental designs will need to navigate this exact trade-off, potentially by utilizing highly relativistic electron regimes where transverse space-charge forces are intrinsically mitigated, or by employing advanced radio-frequency (RF) bunching cavities to precisely control electron arrival times without sacrificing transverse beam coherence.

6.5 Broader Impacts: Bridging Quantum Optics and Materials Science

Beyond fundamental physics, the methodologies developed herein offer transformative, highly practical tools for materials science, nanophotonics, and structural biology. The Free-Electron Ramsey-type Interferometry (FERI) technique represents a crucial leap toward truly non-destructive quantum metrology. By coherently amplifying the interaction between the probing electron and weak optical near-fields, FERI drastically reduces the required electron dose and optical pump intensities. This capability is exceptionally vital for the study of dose-sensitive specimens, such as cryogenic biological samples, delicate van der Waals heterostructures, and functional soft matter, where traditional continuous-wave or high-intensity pulsed probing often induces irreversible structural damage.

Similarly, the introduction of Superradiant Electron Energy Loss Spectroscopy (SREELS) provides a highly localized, precise probe for cooperative material dynamics. By granting access to the intermediate rungs of the Dicke superradiant ladder with nanometer spatial resolution, SREELS bridges the historical gap between macroscopic optical spectroscopy and atomic-scale electron microscopy. This unprecedented capability will be instrumental in designing and characterizing next-generation optoelectronic devices, dense quantum dot arrays, and topological photonic materials where localized coherence directly dictates macroscopic device performance and efficiency. By providing a direct window into these previously hidden nanoscale dynamics, the frameworks established here equip researchers with the diagnostic precision needed to iteratively refine and optimize quantum materials from the bottom up.

6.6 Concluding Remarks

Taken together, the research presented in this thesis constitutes a comprehensive theoretical and methodological expansion of free-electron quantum optics. We have shown that by controlling the longitudinal and transverse phase space of the free electron, we can interface it with the broader ecosystem of quantum technologies.

From executing atomic-scale quantum gates and mapping superradiant dynamics, to coherently amplifying weak optical fields and engineering macroscopic continuous-variable entanglement, the innovations detailed here solve fundamental limitations in current electron microscopy and quantum optics. Ultimately, this work envisions and actively drives the transition of the electron microscope from an indispensable classical imaging tool into a fully coherent, programmable quantum laboratory. A century after the free electron was first utilized merely to resolve the structural outlines of matter, it is now poised to actively participate in the quantum information revolution. By successfully bridging macroscopic quantum electrodynamics with advanced electron microscopy, this thesis charts a course toward that future.

References

1. Ruimy, R., Karnieli, A. & Kaminer, I. Free-electron quantum optics. *Nat. Phys.* (2025).
2. Thomson, J. J. Cathode rays. *The London, Edinburgh, and Dublin Philosophical Magazine and Journal of Science* **44,** 293–316 (1897).
3. Madey, J. M. Stimulated emission of bremsstrahlung in a periodic magnetic field. *Journal of Applied Physics* **42,** 1906–1913 (1971).
4. De Broglie, L. A tentative theory of light quanta. *The London, Edinburgh, and Dublin Philosophical Magazine and Journal of Science* **47,** 446–458 (1924).
5. Thomson, G. P. Experiments on the diffraction of cathode rays. *Proceedings of the Royal Society of London. Series A, Containing Papers of a Mathematical and Physical Character* **117,** 600–609 (1928).
6. Davisson, C. & Germer, L. H. Diffraction of electrons by a crystal of nickel. *Physical Review* **30,** 705 (1927).
7. Knoll, M. & Ruska, E. Beitrag zur geometrischen Elektronenoptik I und II. *Annalen der Physik* **404,** 607–661 (1932).
8. Kühlbrandt, W. The resolution revolution. *Science* **343,** 1443–1444 (2014).
9. Einstein, A., Podolsky, B. & Rosen, N. Can quantum-mechanical description of physical reality be considered complete? *Physical review* **47,** 777 (1935).
10. Bell, J. S. On the Einstein Podolsky Rosen paradox. *Physics Physique Fizika* **1,** 195 (1964).
11. Dowling, J. P. & Milburn, G. J. Quantum technology: the second quantum revolution. *Philosophical Transactions of the Royal Society of London. Series A: Mathematical, Physical and Engineering Sciences* **361,** 1655–1674 (2003).
12. Barwick, B., Flannigan, D. J. & Zewail, A. H. Photon-induced near-field electron microscopy. *Nature* **462,** 902 (2009).
13. García de Abajo, F. J. *et al.* Multiphoton absorption and emission by interaction of swift electrons with evanescent light fields. *Nano Lett.* **10,** 1859 (2010).
14. Park, S. T., Lin, M. & Zewail, A. H. Photon-induced nearfield electron microscopy (PINEM): Theoretical and experimental. *New J. Phys.* **12,** 123028 (2010).
15. Shiloh, R., Lereah, Y., Lilach, Y. & Arie, A. Sculpturing the electron wave function using nanoscale phase masks. *Ultramicroscopy* **144,** 26–31 (2014).
16. Verbeeck, J. *et al.* Demonstration of a 2x2 programmable phase plate for electrons. *Ultramicroscopy* **190,** 58–65 (2018).

17. Verbeeck, J., Tian, H. & Schattschneider, P. Production and application of electron vortex beams. *Nature* **467,** 301–304 (2010).

18. Grillo, V. *et al.* Measuring the orbital angular momentum spectrum of an electron beam. *Nat. Commun.* **8,** 15536 (2017).

19. Guzzinati, G. *et al.* Probing the symmetry of the potential of localized surface plasmon resonances with phase-shaped electron beams. *Nat. Commun.* **8,** 14999 (2017).

20. McMorran, B. J. & Cronin, A. D. An electron Talbot interferometer. *New J. Phys.* **11,** 033021 (2009).

21. Turner, A. E. *et al.* Interaction-free measurement with electrons. *Phys. Rev. Lett.* **127,** 110401 (2021).

22. Mohler, K. J. *et al.* Ultrafast electron diffraction from nanophotonic waveforms via dynamical Aharonov-Bohm phases. *Sci. Adv.* **6,** eabc8804 (2020).

23. Feist, A. *et al.* Quantum coherent optical phase modulation in an ultrafast transmission electron microscope. *Nature* **521,** 200 (2015).

24. Nabben, D. *et al.* Attosecond electron microscopy of sub-cycle optical dynamics. *Nature* **619,** 63–67 (2023).

25. Gaida, J. H. *et al.* Attosecond electron microscopy by free-electron homodyne detection. *Nat. Photon.* **18,** 509–515 (2024).

26. Bucher, T. *et al.* Coherently amplified ultrafast imaging using a free-electron interferometer. *Nat. Photon.* **18,** 809–815 (2024).

27. Reinhardt, O., Gorlach, A. & Kaminer, I. *Superradiant Cathodoluminescence* in *Conference on Lasers and Electro-Optics (CLEO)* (2021), FW2Q.6.

28. Tsarev, M. V., Ryabov, A. & Baum, P. Free-electron qubits and maximum-contrast attosecond pulses via temporal Talbot revivals. *Phys. Rev. Res.* **3,** 043033 (2021).

29. Jaynes, E. T. & Cummings, F. W. Comparison of quantum and semiclassical radiation theories with application to the beam maser. *Proc. IEEE* **51,** 89–109 (1963).

30. De Abajo, F. J. G. Optical excitations in electron microscopy. *Rev. Mod. Phys.* **82,** 209 (2010).

31. Cherenkov, P. A. Visible Emission of Clean Liquids by Action of γ radiation. *Dokl. Akad. Nauk SSSR* **2,** 541 (1934).

32. Meuret, S. *et al.* Photon bunching in cathodoluminescence. *Phys. Rev. Lett.* **114,** 197401 (2015).

33. Sola-Garcia, M. *et al.* Photon statistics of incoherent cathodoluminescence with continuous and pulsed electron beams. *ACS Photon.* **8,** 916–925 (2021).

34. Kfir, O. Entanglements of Electrons and Cavity Photons in the Strong-Coupling Regime. *Phys. Rev. Lett.* **123,** 103602 (2019).

35. Di Giulio, V., Kociak, M. & de Abajo, F. J. G. Probing quantum optical excitations with fast electrons. *Optica* **6,** 1524 (2019).

36. Karnieli, A., Rivera, N., Arie, A. & Kaminer, I. The coherence of light is fundamentally tied to the quantum coherence of the emitting particle. *Sci. Adv.* **7,** eabf8096 (2021).

37. Dahan, R. *et al.* Imprinting the quantum statistics of photons on free electrons. *Science* **373,** eabj7128 (2021).

38. Feist, A. *et al.* Cavity-mediated electron-photon pairs. *Science* **377,** 6607 (2022).

39. Dahan, R. *et al.* Creation of optical cat and GKP states using shaped free electrons. *Phys. Rev. X* **13,** 031001 (2023).

40. Baranes, G. *et al.* Free-electron interactions with photonic GKP states: universal control and quantum error correction. *Phys. Rev. Res.* **5,** 043271 (2023).

41. Gover, A. & Yariv, A. Free-Electron-Bound-Electron Resonant Interaction. *Phys. Rev. Lett.* **124,** 064801 (2020).

42. Ruimy, R. *et al.* Toward Atomic-Resolution Quantum Measurements with Coherently Shaped Free Electrons. *Phys. Rev. Lett.* **126,** 233403 (2021).

43. Zhao, Z., Sun, X.-Q. & Fan, S. Quantum Entanglement and Modulation Enhancement of Free-Electron-Bound-Electron Interaction. *Phys. Rev. Lett.* **126,** 233402 (2021).

44. Meier, S., Heimerl, J. & Hommelhoff, P. Few-electron correlations after ultrafast photoemission from nanometric needle tips. *Nat. Phys.* **19,** 1402–1409 (2023).

45. Haindl, R. *et al.* Coulomb-correlated electron number states in a transmission electron microscope beam. *Nat. Phys.* **19,** 1410–1417 (2023).

46. Tziperman, O. *et al.* Two-electron quantum walks for probing entanglement and decoherence in an electron microscope. *Nature Physics* **22,** 763–769 (2026).

47. Ruimy, R., Gorlach, A., Baranes, G. & Kaminer, I. Superradiant electron energy loss spectroscopy. *Nano Letters* **23,** 779–787 (2023).

48. Bucher, T. *et al.* Free-electron Ramsey-type interferometry for enhanced amplitude and phase imaging of nearfields. *Sci. Adv.* **9,** eadi5729 (2023).

49. Ruimy, R., Tziperman, O., Gorlach, A., Mølmer, K. & Kaminer, I. Many-body entanglement via 'which-path' information. *npj Quantum Information* **10,** 121 (2024).

50. Polman, A., Kociak, M. & de Abajo, F. J. G. Electron-beam spectroscopy for nanophotonics. *Nat. Mater.* **18,** 1158 (2019).

51. Kociak, M. Cathodoluminescence in the scanning transmission electron microscope. *Ultramicroscopy* **176,** 112 (2017).

52. Kuttge, M. Local density of states, spectrum, and far-field interference of surface plasmon polaritons probed by cathodoluminescence. *Phys. Rev. B* **79,** 113405 (2009).

53. De Abajo, F. J. G. Probing the Photonic Local Density of States with Electron Energy Loss Spectroscopy. *Phys. Rev. Lett.* **100,** 106804 (2008).

54. Malis, T., Cheng, S. C. & Egerton, R. F. EELS log-ratio technique for specimen-thickness measurement in the TEM. *J. Electron Microsc. Tech.* **8,** 193–200 (1988).

55. Novotny, L. *Principles of Nano-Optics* (Cambridge University Press, New York, 2012).

56. Scully, M. O. & Zubairy, M. S. *Quantum Optics* (Cambridge University Press, New York, 1997).

57. Bechtold, A. *et al.* Three-stage decoherence dynamics of an electron spin qubit in an optically active quantum dot. *Nat. Phys.* **11,** 1005 (2015).

58. Bechtold, A. *et al.* Quantum Effects in Higher-Order Correlators of a Quantum-Dot Spin Qubit. *Phys. Rev. Lett.* **117,** 027402 (2016).

59. Grelich, A., Carter, S. G., Kim, D., Bracker, A. S. & Gammon, D. Optical control of one and two hole spins in interacting quantum dots. *Nat. Photonics* **5,** 702 (2011).

60. Economou, S. E. & Reinecke, T. L. Theory of Fast Optical Spin Rotation in a Quantum Dot Based on Geometric Phases in Trapped States. *Phys. Rev. Lett.* **99,** 217401 (2007).

61. Godden, T. M. *et al.* Coherent Optical Control of the Spin of a Single Hole in an InAs/GaAs Quantum Dot. *Phys. Rev. Lett.* **108,** 017402 (2012).

62. Khanonkin, I. *et al.* Ultra-fast charge carrier dynamics across the spectrum of an optical gain media on INAs/AlGaInAs/InP quantum dots. *AIP Adv.* **7,** 035122 (2017).

63. Ledentsov, N. N. *et al.* Quantum dot heterostructures: Fabrication, properties, lasers. *Semiconductors* **32,** 343 (1998).

64. Bimberg, D. & Pohl, U. W. Quantum dots: Promises and accomplishments. *Mater. Today* **14,** 388 (2011).

65. Shen, H. *et al.* Visible quantum dot light-emitting diodes with simultaneous high brightness and efficiency. *Nat. Photonics* **13,** 192 (2019).

66. Banyoudeh, S. & Reithmaier, J. P. High-density 1.54 μ m InAs/InGaAlAs/InP (100) based quantum dots with reduced size inhomogeneity. *J. Cryst. Growth* **425,** 299 (2015).

67. Choi, H. *et al.* Ultrafast Rabi flopping and coherent pulse propagation in a quantum cascade laser. *Nat. Photonics* **4,** 706 (2010).

68. Bayer, M. & Forchel, A. Temperature dependence of the exciton homogeneous linewidth in In0.60 Ga0.40As/GaAs self-assembled quantum dots. *Phys. Rev. B* **65,** 041308 (2002).

69. Loss, D. & DiVincenzo, D. P. Quantum computation with quantum dots. *Phys. Rev. A* **57,** 120 (1998).

70. Nielsen, M. A. & Chuang, I. *Quantum Computation and Quantum Information* (Cambridge University Press, New York, 2002).

71. Bose, R., Sridharan, D., Kim, H., Solomon, G. S. & Waks, E. Low-Photon-Number Optical Switching with a Single Quantum Dot Coupled to a Photonic Crystal Cavity. *Phys. Rev. Lett.* **108,** 227402 (2012).

72. Alivisatos, A. P., Harris, A. L., Levinos, N. J., Steigerwald, M. L. & Brus, L. E. Electronic states of semiconductor clusters: Homogeneous and inhomogeneous broadening of the optical spectrum. *J. Chem. Phys.* **89,** 4001 (1988).

73. Deng, Y. & Chu, D. Coherence properties of different light sources and their effect on the image sharpness and speckle of holographic displays. *Sci. Rep.* **7,** 5893 (2017).

74. Allen, L. & Eberly, J. H. *Optical Resonance and Two-level Atoms* (Dover Publications, New York, 1987).

75. Borri, P. *et al.* Ultrastrong Dephasing Time in InGaAs Quantum Dots. *Phys. Rev. Lett.* **87,** 157401 (2001).

76. Novoselov, K. S., Mishchenko, A., Carvalho, A. & Neto, A. H. C. 2D materials and van der Waals heterostructures. *Science* **353,** aac9439 (2016).

77. Jena, A. K., Kulkarni, A. & Miyasaka, T. Halide perovskite photovoltaics: background, status, and future. *Chem. Rev.* **119,** 3036 (2019).

78. Akkerman, Q. A., Rainò, G., Kovalenko, M. V. & Manna, L. Genesis, challenges and opportunities for colloidal lead halide perovskite nanocrystals. *Nat. Mater.* **17,** 394 (2018).

79. Sutherland, B. R. & Sargent, E. H. Perovskite photonic sources. *Nat. Photonics* **10,** 295 (2016).

80. Hulet, R. G., Hilfer, E. S. & Kleppner, D. Inhibited Spontaneous Emission by a Rydberg Atom. *Phys. Rev. Lett.* **55,** 2137 (1985).

81. Jones, R. R., You, D. & Bucksbaum, H. B. Ionization of Rydberg Atoms by Subpicosecond Half-Cycle Electromagnetic Pulses. *Phys. Rev. Lett.* **70,** 1236 (1993).

82. Priebe, K. E. *et al.* Attosecond electron pulse trains and quantum state reconstruction in ultrafast transmission electron microscopy. *Nat. Photonics* **11,** 793 (2017).

83. Vanacore, G. M. *et al.* Ultrafast generation and control of an electron vortex beam via chiral plasmonic near fields. *Nat. Mater.* **18,** 573 (2019).

84. Vanacore, G. M. *et al.* Attosecond coherent control of free-electron wave functions using semi-infinite light fields. *Nat. Commun.* **9,** 2694 (2018).

85. Echternkamp, K. E., Feist, A., Schäfer, S. & Ropers, C. Ramsey-type phase control of free-electron beams. *Nat. Phys.* **12,** 1000 (2016).

86. Pan, Y. & Gover, A. Spontaneous and stimulated emission of a preformed quantum free-electron wave function. *Phys. Rev. A* **99,** 052107 (2019).

87. Dicke, R. H. Coherence in spontaneous radiation processes. *Phys. Rev.* **93,** 99 (1954).

88. Gross, M. & Haroche, S. Superradiance: An essay on the theory of collective spontaneous emission. *Phys. Rep.* **93,** 301 (1982).

89. Peskin, M. E. & Schroeder, D. V. *An Introduction to Quantum Field Theory* (CRC Press, Reading, 2018).

90. Williams, D. B. & Carter, C. B. *Transmission Electron Microscopy* (Springer, Boston, 2009).

91. Jackson, J. D. *Classical Electrodynamics* (Wiley, New York, 1999).

92. Baryshevsky, V. *et al. Parametric X-Ray Radiation in Crystals* (Springer, Berlin, 2005).

93. Magnus, W. On the exponential solution of differential equations for a linear operator. *Commun. Pure Appl. Math.* **7,** 649 (1954).

94. Rivera, N. & Kaminer, I. Light-matter interactions with photonic quasiparticles. *Nat. Rev. Phys.* **2,** 538 (2020).

95. Breuer, H.-P. *The Theory of Open Quantum Systems* (Oxford University Press, New York, 2002).

96. Dahan, R. *et al.* Resonant phase-matching between a light wave and a free-electron wavefunction. *Nat. Phys.* **16,** 1123 (2020).

97. Wang, K. *et al.* Coherent interaction between free electrons and a photonic cavity. *Nature* **582,** 50–54 (2020).

98. Morimoto, Y. & Baum, P. Diffraction and microscopy with attosecond electron pulse trains. *Nat. Phys.* **14,** 252 (2018).

99. Kozák, M., Schönenberger, N. & Hommelhoff, P. Ponderomotive Generation and Detection of Attosecond Free-Electron Pulse Trains. *Phys. Rev. Lett.* **120,** 103203 (2018).

100. Reinhardt, O. & Kaminer, I. Theory of Shaping Electron Wavepackets with Light. *ACS Photonics* **7,** 2859 (2020).

101. Bell, D. C. & Erdman, N. *Low Voltage Electron Microscopy: Principles and Applications* (Wiley, New York, 2012).

102. Bracco, G. & Holst, B. *Surface Science Techniques* (Springer, Berlin, 2013).

103. Pomarico, E. *et al.* meV resolution in laser-assisted energy-filtered transmission electron microscopy. *ACS Photonics* **5,** 759 (2018).

104. Karni, O. *et al.* Rabi oscillations and self-induced transparency in InAs/InP quantum dot semiconductor optical amplifier operating at room temperature. *Opt. Express* **21,** 26786 (2013).

105. Khanonkin, I. *et al.* Ramsey fringes in room-temperature quantum-dot semiconductor optical amplifier. *Phys. Rev. B* **97,** 241117 (2018).

106. Khanonkin, I. *et al.* Room Temperature Quantum Coherent Revival in an Ensemble of Artificial Atoms. *Phys. Rev. Research* **3,** 033073 (2021).

107. Nazarov, V. U. Multipole surface-plasmon-excitation enhancement in metals. *Phys. Rev. B* **59,** 9866 (1999).

108. Nazarov, V. U., Silkin, V. M. & Krasovskii, E. E. Role of the kinematics of probing electrons in electron energy-loss spectroscopy of solid surfaces. *Phys. Rev. B* **93,** 035403 (2016).

109. Nazarov, V. U., Silkin, V. M. & Krasovskii, E. E. Probing mesoscopic crystals with electrons: One-step simultaneous inelastic and elastic scattering theory. *Phys. Rev. B* **96,** 235414 (2017).

110. Ratzel, D. *et al.* Controlling quantum systems with modulated electron beams. *Phys. Rev. Research* **3,** 023247 (2021).

111. Krivanek, O. *et al.* Vibrational spectroscopy in the electron microscope. *Nature* **514,** 209 (2014).

112. Pan, Y. & Gover, A. Beyond Fermi's golden rule in free-electron quantum electrodynamics: acceleration/radiation correspondence. *New J. Phys.* **23,** 063070 (2021).

113. Zhang, B. *et al.* Quantum state interrogation using a preshaped free electron wavefunction. *Phys. Rev. Res.* **4,** 033071 (2022).

114. Ran, D. *et al.* Coherent Excitation of Bound Electron Quantum State With Quantum Electron Wavepackets. *Front. Phys.* **10,** 920701 (2022).

115. Baranes, G. *et al.* Free electron can induce entanglement between photons. *NPJ. Quantum Inf.* **8,** 32 (2022).

116. Kfir, O. *et al.* Optical coherence transfer mediated by free electrons. *Sci. Adv.* **7,** eabf6380 (2021).

117. García de Abajo, F. J. *et al.* Complete Excitation of Discrete Quantum Systems by Single Free Electrons. *Phys. Rev. Lett.* **129,** 093401 (2022).

118. Karnieli, A. *et al. Probing strongly coupled light-matter interactions using quantum free electrons* in *2022 Conference on Lasers and Electro-Optics (CLEO)* (2022).

119. Yalunin, S. V. *et al.* Tailored high-contrast attosecond electron pulses for coherent excitation and scattering. *Phys. Rev. Research* **3,** 032036 (2021).

120. Bonifacio, R. *et al.* Quantum Statistical Theory of Superradiance. I. *Phys. Rev. A* **4,** 302 (1971).

121. Bonifacio, R. *et al.* Quantum Statistical Theory of Superradiance. II. *Phys. Rev. A* **4,** 854 (1971).

122. Bonifacio, R. *et al.* Cooperative radiation processes in two-level systems: Superfluorescence. *Phys. Rev. A* **11,** 1507 (1975).

123. Rainò, G. *et al.* Superfluorescence from lead halide perovskite quantum dot superlattices. *Nature* **563,** 671–675 (2018).

124. Garrison, J. & Chiao, R. *Quantum Optics* (Oxford University Press, 2008).

125. Tamm, I. E. & Frank, I. M. Coherent In-Medium Fast-Electron Radiation. *Dokl. Akad. Nauk SSSR* **14,** 109 (1937).

126. Kaminer, I. *et al.* Quantum Cerenkov radiation: spectral cutoffs and the role of spin and orbital angular momentum. *Phys. Rev. X* **6,** 011006 (2016).

127. Smith, S. J. & Purcell, E. M. Visible Light from Localized Surface Charges Moving Across a Grating. *Phys. Rev.* **92,** 1069 (1953).

128. Van den Berg, P. M. Smith-Purcell Radiation from a Point Charge Moving Parallel to a Reflection Grating. *J. Opt. Soc. Am.* **63,** 1588 (1973).

129. Tsesses, S. *et al.* Light generation via quantum interaction of electrons with periodic nanostructures. *Phys. Rev. A* **95,** 013832 (2017).

130. Polkovnikov, A. Phase space representation of quantum dynamics. *Ann. Phys.* **325,** 1790 (2010).

131. Halperin, A. *et al.* Electron-beam-induced super-radiant emission from a grating. *Phys. Rev. A* **50,** 3316 (1994).

132. Young, T. The Bakerian lecture. Experiments and calculation relative to physical optic. *Phil. Trans. R. Soc.* **94,** 1 (1804).

133. Thomson, G. P. & Reid, A. Diffraction of cathode rays by a thin film. *Nature* **119,** 890 (1927).

134. Merli, P. G. *et al.* On the statistical aspect of electron interference phenomena. *Am. J. Phys.* **44,** 306 (1976).

135. Carnal, O. & Mlynek, J. Young's double-slit experiment with atoms: a simple atom interferometer. *Phys. Rev. Lett.* **66,** 2689 (1991).

136. D"urr, S., Nonn, T. & Rempe, G. Origin of quantum-mechanical complementarity probed by a which-way experiment in an atom interferometer. *Nature* **395,** 33–37 (1998).

137. Aharonov, Y. *et al.* How the result of measurement of a component of the spin of a spin-1/2 particle can turn out to be 100. *Phys. Rev. Lett.* **60,** 1351 (1988).

138. Jacques, V. *et al.* Experimental realization of Wheeler's delayed-choice gedanken experiment. *Science* **315,** 966–968 (2007).

139. Kim, Y. H. *et al.* Delayed 'choice' quantum eraser. *Phys. Rev. Lett.* **84,** 1 (2000).

140. Walborn, S. P. *et al.* Double-slit quantum eraser. *Phys. Rev. A* **65,** 033818 (2002).

141. Feynman, R. *et al.* The Feynman lectures on physics. *Physics Today* **17,** 45 (1964).

142. Childs, A. M. Universal computation by quantum walk. *Phys. Rev. Lett.* **102,** 180501 (2009).

143. Lin, C. Y. *et al.* Encoding qubits into harmonic-oscillator modes via quantum walks in phase space. *Quant. Inf. Process.* **19,** 272 (2020).

144. Sheremet, A. S. *et al.* Waveguide quantum electrodynamics: collective radiance and photon-photon correlations. *Rev. Mod. Phys.* **95,** 015002 (2023).

145. Eickbusch, A. *et al.* Fast universal control of an oscillator with weak dispersive coupling to a qubit. *Nat. Phys.* **18,** 1464–1469 (2022).

146. Okamoto, H. Possible use of a cooper-pair box for low-dose electron microscopy. *Phys. Rev. A* **85,** 043810 (2013).

147. Okamoto, H. & Nagatani, Y. Entanglement-assisted electron microscopy based on a flux qubit. *Appl. Phys. Lett.* **104,** 062604 (2014).

148. Okamoto, H. Measurement errors in entanglement-assisted electron microscopy. *Phys. Rev. A* **89,** 063828 (2014).

149. Kruit, P. *et al.* Designs for a quantum electron microscope. *Ultramicroscopy* **164,** 31–45 (2016).

150. Koppell, S. A. *et al.* Transmission electron microscopy at the quantum limit. *Appl. Phys. Lett.* **120,** 190502 (2022).

151. Gerry, C. & Knight, P. *Introductory Quantum Optics* (Cambridge University Press, 2004).

152. Kuzmich, A. *et al.* Atomic quantum non-demolition measurements and squeezing. *EPL* **42,** 481 (1998).

153. Sørensen, A. & Mølmer, K. Probabilistic generation of entanglement in optical cavities. *Phys. Rev. Lett.* **90,** 12 (2003).

154. Madsen, L. & Mølmer, K. Spin squeezing and precision probing with light and samples of atoms in the Gaussian description. *Phys. Rev. A* **70,** 052324 (2004).

155. Vasilakis, G. *et al.* Generation of a squeezed state of an oscillator by stroboscopic back-action-evading measurement. *Nat. Phys.* **11,** 389–392 (2015).

156. Boto, A. N. *et al.* Quantum interferometric optical lithography: exploiting entanglement to beat the diffraction limit. *Phys. Rev. Lett.* **85,** 2733 (2000).

157. Wigner, E. P. On the quantum correction for thermodynamic equilibrium. *Phys. Rev.* **40,** 103 (1932).

158. Gottesman, D. *et al.* Encoding a qubit in an oscillator. *Phys. Rev. A* **64,** 012310 (2001).

159. Bourassa, J. E. *et al.* Blueprint for a scalable photonic fault-tolerant quantum computer. *Quantum* **5,** 392 (2021).

160. Tonomura, A. Applications of electron holography. *Rev. Mod. Phys.* **59,** 639 (1987).

161. Cowley, J. M. Twenty forms of electron holography. *Ultramicroscopy* **41,** 4 (1992).

162. Lichte, H. & Lehmann, M. Electron holography-basics and applications. *Rep. Prog. Phys.* **71,** 016102 (2008).

163. Tanigaki, T. *et al.* Split-illumination electron holography. *Appl. Phys. Lett.* **101,** 043101 (2012).

164. Fernandez, M. & Williams, S. Closed-form expression for the poisson-binomial probability density function. *IEEE Tran. Aerosp. Electron. Syst.* **46,** 2 (2010).

165. Mertens, B. M. *et al.* Off-axis holography with a crystal beam splitter. *Ultramicroscopy* **77,** 1–2 (1999).

166. Harvey, T. R. *et al.* Interpretable and efficient interferometric contrast in scanning transmission electron microscopy with a diffraction-grating beam splitter. *Phys. Rev. Appl.* **10,** 061001 (2018).

167. Dellweg, M. M. & Muller, C. Spin-polarizing interferometric beam splitter for free electrons. *Phys. Rev. Lett.* **118,** 070403 (2017).

168. Hammer, J. *et al.* Microwave chip-based beam splitter for low-energy guided electrons. *Phys. Rev. Lett.* **114,** 254801 (2015).

169. Yang, Y. *et al.* Efficient two-port electron beam splitter via a quantum interaction-free measurement. *Phys. Rev. A* **98,** 043621 (2018).

170. Huang, G. *et al.* Electron-photon quantum state heralding using photonic integrated circuits. *PRX Quant.* **4,** 020351 (2023).

171. Adiv, Y. *et al.* Observation of 2D cherenkov radiation. *Phys. Rev. X* **13,** 011002 (2023).

172. Yan, Q., Ruimy, R., Niedermayr, A. & Kaminer, I. *Single-particle–single-photon coupling using a circuital metamaterial cavity* in *CLEO 2023* (2023), FF3D.1.

173. Sonnentag, P. & Hasselbach, F. Measurement of decoherence of electron waves and visualization of the quantum-classical transition. *Phys. Rev. Lett.* **98,** 200402 (2007).

174. Kerker, N. *et al.* Quantum decoherence by Coulomb interaction. *New J. Phys.* **22,** 063039 (2020).

175. Vitanov, N. V. *et al.* Stimulated Raman adiabatic passage in physics, chemistry, and beyond. *Rev. Mod. Phys.* **89,** 015006 (2017).

176. Fabre, C. Modes and states in quantum optics. *Rev. Mod. Phys.* **92,** 035005 (2020).

177. Gardiner, C. W. & Collett, M. J. Input and output in damped quantum systems: quantum stochastic differential equations and the master equation. *Phys. Rev. A* **31,** 3761–3774 (1980).

178. Caneva, T. *et al.* Quantum dynamics of propagating photons with strong interactions: a generalized input-output formalism. *New J. Phys.* **17,** 113001 (2015).

179. Gardiner, C. W. & Zoller, P. *Quantum Noise: A Handbook of Markovian and Non-Markovian Quantum Stochastic Methods with Applications to Quantum Optics* (Springer Science & Business Media, 2004).

180. Kiilerich, A. & Mølmer, K. Input-output theory with quantum pulses. *Phys. Rev. Lett.* **123,** 123604 (2019).

181. Holstein, T. & Primakoff, H. Field dependence of the intrinsic domain magnetization of a ferromagnet. *Phys. Rev.* **58,** 1098 (1940).

182. Neeley, M. *et al.* Generation of three-qubit entangled states using superconducting phase qubits. *Nature* **467,** 570–573 (2010).

183. Rauschenbeutel, A. *et al.* Step-by-step engineered multiparticle entanglement. *Science* **288,** 2024–2028 (2000).

184. Cirac, J. I. & Zoller, P. Quantum computations with cold trapped ions. *Phys. Rev. Lett.* **74,** 4091 (1995).

185. Sørensen, A. & Mølmer, K. Quantum computation with ions in thermal motion. *Phys. Rev. Lett.* **82,** 1971 (1999).

186. Monroe, C. *et al.* Demonstration of a fundamental quantum logic gate. *Phys. Rev. Lett.* **75,** 4714–4717 (1995).

187. Kannan, B. *et al.* Waveguide quantum electrodynamics with superconducting artificial giant atoms. *Nature* **583,** 775–779 (2020).

188. Kannan, B. *et al.* On-demand directional microwave photon emission using waveguide quantum electrodynamics. *Nat. Phys.* **19,** 394–400 (2023).

189. Tiranov, A. *et al.* Collective super- and subradiant dynamics between distant optical quantum emitters. *Science* **379,** 389–393 (2023).

190. Dordevic, T. *et al.* Entanglement transport and a nanophotonic interface for atoms in optical tweezers. *Science* **373,** 1511–1514 (2021).

191. Yan, Z. *et al.* Super-radiant and sub-radiant cavity scattering by atom arrays. *Phys. Rev. Lett.* **133,** 253603 (2023).

192. Chang, D. E. *et al.* Quantum nonlinear optics - photon by photon. *Nat. Photon.* **8,** 685–694 (2014).

193. Braunstein, S. L. & van Loock, P. Quantum information with continuous variables. *Rev. Mod. Phys.* **77,** 513 (2005).

194. Takeda, S. & Furusawa, A. Toward large-scale fault-tolerant universal photonic quantum computing. *APL Photonics* **4,** 060902 (2019).

195. Imoto, N., Haus, H. A. & Yamamoto, Y. Quantum nondemolition measurement of the photon number via the optical Kerr effect. *Phys. Rev. A* **32,** 2287 (1985).

196. Pirandola, S., Mancini, S., Vitali, D. & Tombesi, P. Continuous variable entanglement and quantum-state teleportation in a macroscopic optomechanical system. *Europhys. Lett.* **68,** 323 (2004).

197. Su, D., Myers, C. R. & Sabapathy, K. K. Conversion of Gaussian states to non-Gaussian states using photon-number-resolving detectors. *Phys. Rev. A* **100,** 052301 (2019).

198. Eaton, M., Nehra, R. & Pfister, O. Non-Gaussian and Gottesman-Kitaev-Preskill state preparation by photon catalysis. *New J. Phys.* **21,** 113034 (2019).

199. Tzitrin, I. *et al.* Quantum error correction with the Gottesman-Kitaev-Preskill code. *Phys. Rev. A* **101,** 032315 (2020).

200. Glancy, S. & Vasconcelos, H. M. Methods for producing optical coherent state superpositions. *J. Opt. Soc. Am. B* **25,** 712 (2008).

201. Weigand, D. J. & Terhal, B. M. Generating grid states from Schrödinger-cat states without postselection. *Phys. Rev. A* **97,** 022341 (2018).

202. Flühmann, C. *et al.* Encoding a qubit in a trapped-ion mechanical oscillator. *Nature* **566,** 513–517 (2019).

203. De Neeve, B. *et al.* Error correction of a logical grid state qubit by dissipative pumping. *Nat. Phys.* **18,** 296 (2022).

204. Campagne-Ibarcq, P. *et al.* Quantum error correction of a qubit encoded in grid states of an oscillator. *Nature* **584,** 368 (2020).

205. Hastrup, J. & Andersen, U. L. Protocol for generating optical Gottesman-Kitaev-Preskill states with cavity QED. *Phys. Rev. Lett.* **128,** 170503 (2022).

206. Raussendorf, R. & Briegel, H. J. A one-way quantum computer. *Phys. Rev. Lett.* **86,** 5188 (2001).

207. Albert, V. V., Covey, J. P. & Preskill, J. Robust encoding of a qubit in a molecule. *Phys. Rev. X* **10,** 031050 (2020).

208. Eickbusch, A. *et al.* Fast universal control of an oscillator with weak dispersive coupling to a qubit. *Nat. Phys.* **18,** 1464–1469 (2022).

209. Wang, K. *et al.* Coherent interaction between free electrons and a photonic cavity. *Nature* **582,** 50–54 (2020).

210. Reinhardt, O., Mechel, C., Lynch, M. & Kaminer, I. Free-electron qubits. *Ann. Phys.* **533,** 2000254 (2021).

211. Braiman, G., Reinhardt, O., Mechel, C., Levi, O. & Kaminer, I. The synthetic Hilbert space of laser-driven free-electrons. *Quantum* **7,** 888 (2023).

212. Henke, J.-W. *et al.* Integrated photonics enables continuous-beam electron phase modulation. *Nature* **600,** 653–658 (2021).

213. Ben Hayun, A. *et al.* Shaping quantum photonic states using free electrons. *Sci. Adv.* **7,** eabe4270 (2021).

214. Bendaña, X., Polman, A. & García de Abajo, F. J. Single-photon generation by electron beams. *Nano Lett.* **11,** 5099–5103 (2011).

215. Varkentina, N. *et al.* Cathodoluminescence excitation spectroscopy: nanoscale imaging of excitation pathways. *Sci. Adv.* **8,** eabq4947 (2022).

216. Terhal, B. M. *et al.* Towards scalable bosonic quantum error correction. *Quant. Sci. Technol.* **5,** 043001 (2020).

217. Gottesman, D. & Chuang, I. L. Demonstrating the viability of universal quantum computation using teleportation and single-qubit operations. *Nature* **402,** 390–393 (1999).

218. Royer, B., Singh, S. & Girvin, S. M. Stabilization of finite-energy Gottesman-Kitaev-Preskill states. *Phys. Rev. Lett.* **125,** 260509 (2020).

219. Terhal, B. M. & Weigand, D. Encoding a qubit into a cavity mode in circuit QED using phase estimation. *Phys. Rev. A* **93,** 012315 (2016).

220. Bourassa, J. E. *et al.* Blueprint for a scalable photonic fault-tolerant quantum computer. *Quantum* **5,** 392 (2021).

221. Lindner, N. H. & Rudolph, T. Proposal for pulsed on-demand sources of photonic cluster state strings. *Phys. Rev. Lett.* **103,** 113602 (2009).

222. Pichler, H., Choi, S., Zoller, P. & Lukin, M. D. Universal photonic quantum computation via time-delayed feedback. *Proc. Natl. Acad. Sci. U.S.A.* **114,** 11362–11367 (2017).

223. Chou, K. S. *et al.* Deterministic teleportation of a quantum gate between two logical qubits. *Nature* **561,** 368–373 (2018).

224. Wan, Y. *et al.* Quantum gate teleportation between separated qubits in a trapped-ion processor. *Science* **364,** 875–878 (2019).

225. Rosenblum, S. *et al.* A CNOT gate between multiphoton qubits encoded in two cavities. *Nat. Commun.* **9,** 652 (2018).

226. Rez, P. *et al.* Damage-free vibrational spectroscopy of biological materials in the electron microscope. *Nat. Commun.* **7,** 10945 (2016).

227. Boissonneault, M., Gambetta, J. M. & Blais, A. Dispersive regime of circuit QED: Photon-dependent qubit dephasing and relaxation rates. *Phys. Rev. A* **79,** 013819 (2009).

228. McMullan, G., Faruqi, A. R., Clare, D. & Henderson, R. Comparison of optimal performance at 300 keV of three direct electron detectors for use in low dose electron microscopy. *Ultramicroscopy* **147,** 156–163 (2014).

229. Sivak, V. V. *et al.* Real-time quantum error correction beyond break-even. *Nature* **616,** 50–55 (2023).

230. Lvovsky, A. I., Sanders, B. C. & Tittel, W. Optical quantum memory. *Nat. Photonics* **3,** 706–714 (2009).

231. Meyer-Scott, E., Silberhorn, C. & Migdall, A. Single-photon sources: Approaching the ideal through multiplexing. *Rev. Sci. Instrum.* **91,** 041101 (2020).

232. Kfir, O. *et al.* Controlling free electrons with optical whispering-gallery modes. *Nature* **582,** 46–49 (2020).

233. Yang, Y. *et al.* Photonic flatband resonances for free-electron radiation. *Nature* **613,** 42–47 (2023).

234. Heijhoff, K. *et al.* Timing performance of the Timepix4 front-end. *J. Instrum.* **17,** P07006 (2022).

235. Puckett, M. W. *et al.* 422 Million intrinsic quality factor planar integrated all-waveguide resonator with sub-MHz linewidth. *Nat. Commun.* **12,** 3341 (2021).

236. Knill, E. Quantum computing with realistically noisy devices. *Nature* **434,** 39 (2005).

237. Barnett, S. M. & Pegg, D. T. Phase in quantum optics. *J. Phys. A: Math. Gen.* **19,** 3849 (1986).

238. Grimsmo, A. L. *et al.* Quantum computing with rotation-symmetric bosonic codes. *Phys. Rev. X* **10,** 011038 (2020).

239. Urban, K. W. Studying atomic structures by aberration-corrected transmission electron microscopy. *Science* **321,** 506–510 (2008).

240. Leamy, H. J. Charge collection scanning electron microscopy. *J. Appl. Phys.* **53,** R51–R80 (1982).

241. Fu, X. *et al.* Optical manipulation of magnetic vortices visualized in situ by Lorentz electron microscopy. *Sci. Adv.* **4,** eaat3077 (2018).

242. Thomas, J. M. & Terasaki, O. The electron microscope is an indispensable instrument for the characterisation of catalysts. *Topics Catal.* **21,** 155–159 (2002).

243. Baumeister, W. & Steven, A. C. Macromolecular electron microscopy in the era of structural genomics. *Trends Biochem. Sci.* **25,** 624–631 (2000).

244. Piazza, L. *et al.* Simultaneous observation of the quantization and the interference pattern of a plasmonic near-field. *Nat. Commun.* **6,** 6407 (2015).

245. García de Abajo, F. J. & Di Giulio, V. Optical excitations with electron beams: challenges and opportunities. *ACS Photon.* **8,** 945–974 (2021).

246. Kfir, O. *et al.* Controlling free electrons with optical whispering-gallery modes. *Nature* **582,** 46–49 (2020).

247. Ryabov, A. *et al.* Attosecond metrology in a continuous-beam transmission electron microscope. *Sci. Adv.* **6,** eabb1393 (2020).

248. Madan, I. *et al.* Ultrafast transverse modulation of free electrons by interaction with shaped optical fields. *ACS Photon.* **9,** 3215–3224 (2022).

249. Tsesses, S. *et al.* Tunable photon-induced spatial modulation of free electrons. *Nat. Mater.* **22,** 345–352 (2023).

250. García de Abajo, F. J. & Konecna, A. Optical modulation of electron beams in free space. *Phys. Rev. Lett.* **126,** 123901 (2021).

251. Mihaila, M. C. C. *et al.* Transverse electron-beam shaping with light. *Phys. Rev. X* **12,** 031043 (2022).

252. Madan, I. *et al.* Holographic imaging of electromagnetic fields via electron-light quantum interference. *Sci. Adv.* **5,** eaav8358 (2019).

253. Potapov, P. L., Lichte, H., Verbeeck, J. & van Dyck, D. Experiments on inelastic electron holography. *Ultramicroscopy* **106,** 1012–1018 (2006).

254. Ramsey, N. *Molecular Beams* (Oxford University Press, 1956).

255. Bertet, P. *et al.* A complementarity experiment with an interferometer at the quantum-classical boundary. *Nature* **411,** 166–170 (2001).

256. Sperling, R. A. *et al.* Biological applications of gold nanoparticles. *Chem. Soc. Rev.* **37,** 1896–1908 (2008).

257. De, M., Ghosh, P. S. & Rotello, V. M. Applications of nanoparticles in biology. *Adv. Mater.* **20,** 4225–4241 (2008).

258. Wu, Y. *et al.* Gold nanoparticles in biological optical imaging. *Nano Today* **24,** 120–140 (2019).

259. Tsesses, S. *et al.* Spin-orbit interaction of light in plasmonic lattices. *Nano Lett.* **19,** 4010–4016 (2019).

260. Simon, P. *et al.* Electron holography of biological samples. *Micron* **39,** 229–256 (2008).

261. Park, S. T. & Zewail, A. H. Relativistic effects in photon-induced near field electron microscopy. *J. Phys. Chem. A* **116,** 11128–11133 (2012).

262. Park, S. T. & Zewail, A. H. Photon-induced near-field electron microscopy: Mathematical formulation of the relation between the experimental observables and the optically driven charge density of nanoparticles. *Phys. Rev. A* **89,** 013851 (2014).

263. Olver, F. W. J., Lozier, D. W., Boisvert, R. F. & Clark, C. W. *NIST Handbook of Mathematical Functions* (Cambridge University Press, 2010).

264. Gaida, J. H. *et al.* Lorentz microscopy of optical fields. *Nat. Commun.* **14,** 6545 (2023).

265. Teperik, T. V. *et al.* Huygens-Fresnel principle for surface plasmons. *Opt. Express* **17,** 17483–17490 (2009).

266. Zhang, K. *et al.* Beyond a Gaussian denoiser: Residual learning of deep CNN for image denoising. *IEEE Trans. Image Process.* **26,** 3142–3155 (2017).

267. Shechtman, Y. *et al.* Phase retrieval with application to optical imaging: A contemporary overview. *IEEE Signal Process. Mag.* **32,** 87–109 (2015).

268. Taylor, L. The phase retrieval problem. *IEEE Trans. Antennas Propag.* **29,** 386–391 (1981).

269. Roitman, D. *et al.* Shaping of electron beams using sculpted thin films. *ACS Photonics* **8,** 3394–3405 (2021).

270. Wang, Z. *et al.* Image quality assessment: From error visibility to structural similarity. *IEEE Trans. Image Process.* **13,** 600–612 (2004).

271. Novotny, L. & van Hulst, N. Antennas for light. *Nat. Photonics* **5,** 83–90 (2011).

272. Storhoff, J. J. *et al.* Homogeneous detection of unamplified genomic DNA sequences based on colorimetric scatter of gold nanoparticle probes. *Nat. Biotechnol.* **22,** 883–887 (2004).

273. Sargazi, S. *et al.* Application of green gold nanoparticles in cancer therapy and diagnosis. *Nanomaterials* **12,** 1102 (2022).

274. Qiang, W. *et al.* Bioinspired polydopamine nanospheres: A super-quencher for fluorescence sensing of biomolecules. *Chem. Sci.* **5,** 3018–3024 (2014).

275. Reichert, J. *et al.* Chip-based optical detection of DNA hybridization by means of nanobead labeling. *Anal. Chem.* **72,** 6025–6029 (2000).

276. García de Abajo, F. J. & Kociak, M. Electron energy-gain spectroscopy. *New J. Phys.* **10,** 073035 (2008).

277. Karnieli, A. *et al.* Quantum sensing of strongly coupled light-matter systems using free electrons. *Sci. Adv.* **9,** eadd2349 (2023).

278. Kurman, Y. *et al.* Spatiotemporal imaging of 2D polariton wave packet dynamics using free electrons. *Science* **372,** 1181–1186 (2021).

279. Houdellier, F. *et al.* Optimization of off-axis electron holography performed with femtosecond electron pulses. *Ultramicroscopy* **202,** 26–32 (2019).

280. Shiloh, R., Chlouba, T. & Hommelhoff, P. Quantum-coherent light-electron interaction in a scanning electron microscope. *Phys. Rev. Lett.* **128,** 235301 (2022).

281. Taylor, K. A. & Glaeser, R. M. Electron diffraction of frozen, hydrated protein crystals. *Science* **186,** 1036–1037 (1974).

282. Fiedler, S. *et al.* Sub-to-super-Poissonian photon statistics in cathodoluminescence of color center ensembles in isolated diamond crystals. *Nanophotonics* **12,** 2231–2237 (2023).

283. Roques-Carmes, C. *et al.* Free-electron-light interactions in nanophotonics. *Appl. Phys. Rev.* **10,** 011303 (2023).

284. Gover, A. *et al.* Superradiant and stimulated-superradiant emission of bunched electron beams. *Rev. Mod. Phys.* **91,** 035003 (2019).

285. Schönenberger, N. *et al.* Generation and characterization of attosecond microbunched electron pulse trains via dielectric laser acceleration. *Phys. Rev. Lett.* **123,** 264803 (2019).

286. Black, D. S. *et al.* Net acceleration and direct measurement of attosecond electron pulses in a silicon dielectric laser accelerator. *Phys. Rev. Lett.* **123,** 264802 (2019).

287. Kurman, Y. *et al.* Dynamics of optical vortices in van der Waals materials. *Optica* **10,** 612–618 (2023).

288. Yannai, M. *et al.* Ultrafast electron microscopy of nanoscale charge dynamics in semiconductors. *ACS Nano* **17,** 3645–3656 (2023).

289. Madan, I. *et al.* Charge dynamics electron microscopy: nanoscale imaging of femtosecond plasma dynamics. *ACS Nano* **17,** 3657–3665 (2023).

290. Ryabov, A. & Baum, P. Electron microscopy of electromagnetic waveforms. *Science* **353,** 374–377 (2016).

291. Ramsey, N. F. A molecular beam resonance method with separated oscillating fields. *Phys. Rev.* **78,** 695–699 (1950).

292. Qiu, D. *et al.* Recent advances in 2D superconductors. *Adv. Mater.* **33,** 2006124 (2021).

293. Cremons, D. R., Plemmons, D. A. & Flannigan, D. J. Femtosecond electron imaging of defect-modulated phonon dynamics. *Nat. Commun.* **7,** 11230 (2016).

294. Zhang, Y. & Flannigan, D. J. Imaging nanometer phonon softening at crystal surface steps with 4D ultrafast electron microscopy. *Nano Lett.* **21,** 7332–7338 (2021).

295. Basov, D. N., Fogler, M. M. & García de Abajo, F. J. Polaritons in van der Waals materials. *Science* **354,** aag1992 (2016).

296. Caldwell, J. D. *et al.* Sub-diffractional volume-confined polaritons in the natural hyperbolic material hexagonal boron nitride. *Nat. Commun.* **5,** 5221 (2014).

297. Li, P. *et al.* Hyperbolic phonon-polaritons in boron nitride for near-field optical imaging and focusing. *Nat. Commun.* **6,** 7507 (2015).

298. Vered, Y. & Bucher, I. Experimental multimode traveling waves identification in an acoustic waveguide. *Mech. Syst. Signal Process.* **153,** 107515 (2021).

299. Ip, E. *et al.* Coherent detection in optical fiber systems. *Opt. Express* **16,** 753–791 (2008).

300. Ostrovsky, E. *et al.* Nanoscale control over optical singularities. *Optica* **5,** 283–288 (2018).

301. Davis, T. J. *et al.* Ultrafast vector imaging of plasmonic skyrmion dynamics with deep subwavelength resolution. *Science* **368,** eaba6415 (2020).

302. Yao, Z. *et al.* Nanoimaging and nanospectroscopy of polaritons with time resolved s-SNOM. *Adv. Opt. Mater.* **8,** 1901042 (2020).

303. Nishida, J. *et al.* Ultrafast infrared nano-imaging of far-from-equilibrium carrier and vibrational dynamics. *Nat. Commun.* **13,** 1083 (2022).

304. Lundeberg, M. B. *et al.* Tuning quantum nonlocal effects in graphene plasmonics. *Science* **357,** 187–191 (2017).

305. Yuan, Z. *et al.* Extremely confined acoustic phonon polaritons in monolayer-hBN/metal heterostructures for strong light-matter interactions. *ACS Photonics* **7,** 2610–2617 (2020).

306. Sheinfux, H. H. *et al.* High-quality nanocavities through multimodal confinement of hyperbolic polaritons in hexagonal boron nitride. *Nat. Mater.* **23,** 499–505 (2024).

307. Iyikanat, F., Konecna, A. & de Abajo, F. J. G. Nonlinear tunable vibrational response in hexagonal boron nitride. *ACS Nano* **15,** 13415–13426 (2021).

308. Flannigan, D. J., Barwick, B. & Zewail, A. H. Biological imaging with 4D ultrafast electron microscopy. *Proc. Natl Acad. Sci. USA* **107,** 9933–9937 (2010).

309. Egerton, R. F. Radiation damage to organic and inorganic specimens in the TEM. *Micron* **119,** 72–87 (2019).

310. Basov, D. N., Averitt, R. D. & Hsieh, D. Towards properties on demand in quantum materials. *Nat. Mater.* **16,** 1077–1088 (2017).

311. Liu, X. & Hersam, M. C. 2D materials for quantum information science. *Nat. Rev. Mater.* **4,** 669–684 (2019).

312. Di Giulio, V. & de Abajo, F. J. G. Optical-cavity mode squeezing by free electrons. *Nanophotonics* **11,** 4659–4670 (2022).

313. García de Abajo, F. J. *et al.* Roadmap for Quantum Nanophotonics with Free Electrons. *ACS Photon.* (2025).

314. Karnieli, A. *et al.* Universal and ultrafast quantum computation based on free-electron-polariton blockade. *PRX Quantum* **5,** 010339 (2024).

315. Di Giulio, V. *et al.* Toward optimum coupling between free electrons and confined optical modes. *ACS Nano* **18,** 14255 (2024).

316. Kumar, S. *et al.* Strongly correlated multielectron bunches from interaction with quantum light. *Sci. Adv.* **10,** adm9563 (2024).

317. Haindl, R. *et al.* Femtosecond and Attosecond Phase-Space Correlations in Few-Particle Photoelectron Pulses. *Phys. Rev. Lett.* (2025).

318. Zheng, D. & Kfir, O. Elastic Quantum Coupling Between Free Electrons and Photons. *arXiv preprint arXiv:2510.15584* (2025).

319. Di Giulio, V. & de Abajo, F. J. G. Electron diffraction by vacuum fluctuations. *New J. Phys.* **22,** 103057 (2020).

320. Zheng, S.-B. & Guo, G.-C. Efficient scheme for two-atom entanglement and quantum information processing in cavity QED. *Phys. Rev. Lett.* **85,** 2392–2395 (2000).

321. Blais, A., Huang, R.-S., Wallraff, A., Girvin, S. M. & Schoelkopf, R. J. Cavity quantum electrodynamics for superconducting electrical circuits: An architecture for quantum computation. *Phys. Rev. A* **69,** 062320 (2004).

322. Kitagawa, M. & Ueda, M. Squeezed spin states. *Phys. Rev. A* **47,** 5138 (1993).

323. Wineland, D. J., Bollinger, J. J., Itano, W. M. & Heinzen, D. J. Squeezed atomic states and projection noise in spectroscopy. *Phys. Rev. A* **50,** 67 (1994).

324. Johnson, C. W., Turner, A. E. & McMorran, B. J. Scanning two-grating free electron Mach-Zehnder interferometer. *Phys. Rev. Res.* **3,** 043009 (2021).

325. Pezzè, L., Smerzi, A., Oberthaler, M. K., Schmied, R. & Treutlein, P. Quantum metrology with nonclassical states of atomic ensembles. *Rev. Mod. Phys.* **90,** 035005 (2018).

326. Juffmann, T. *et al.* Multi-pass transmission electron microscopy. *Sci. Rep.* **7,** 1699 (2017).

327. Putnam, W. P. & Yanik, M. F. Noninvasive electron microscopy with interaction-free quantum measurements. *Phys. Rev. A* **80,** 040902 (2009).

328. Blanes, S., Casas, F., Oteo, J. A. & Ros, J. The Magnus expansion and some of its applications. *Physics Reports* **470,** 151–238 (2009).

329. Aharonov, Y. & Bohm, D. Significance of electromagnetic potentials in the quantum theory. *Physical Review* **115,** 485 (1959).

330. Wilcox, R. M. Exponential operators and parameter differentiation in quantum physics. *Journal of Mathematical Physics* **8,** 962–982 (1967).

331. Callen, H. B. & Welton, T. A. Irreversibility and generalized noise. *Physical Review* **83,** 34 (1951).

332. Zhao, Z. *et al.* Upper bound for the quantum coupling between free electrons and photons. *Phys. Rev. Lett.* **134,** 043804 (2025).

333. Xie, Z. *et al.* Maximal Quantum Interaction between Free Electrons and Photons. *Phys. Rev. Lett.* **134,** 043803 (2025).

334. Peres, A. Separability criterion for density matrices. *Physical Review Letters* **77,** 1413–1415 (1996).

335. Vidal, G. & Werner, R. F. Computable measure of entanglement. *Physical Review A* **65,** 032314 (2002).

336. Caprez, A., Bach, R., McGregor, S. & Batelaan, H. A wide-angle electron grating bi-prism beam splitter. *J. Phys. B: At. Mol. Opt. Phys.* **42,** 165503 (2009).

337. Zimmermann, R., Seidling, M. & Hommelhoff, P. Charged particle guiding and beam splitting with auto-ponderomotive potentials on a chip. *Nat. Commun.* **12,** 390 (2021).

338. Zimmermann, R., Weber, P., Seidling, M. & Hommelhoff, P. Beam splitting of low-energy guided electrons with a two-sided microwave chip. *Appl. Phys. Lett.* **115,** 104103 (2019).

339. Seidling, M., Zimmermann, R. & Hommelhoff, P. Chip-based electrostatic beam splitting of guided kiloelectron volt electrons. *Appl. Phys. Lett.* **118,** 034101 (2021).

340. Greenberger, D. M., Horne, M. A. & Zeilinger, A. in *Bell's Theorem, Quantum Theory and Conceptions of the Universe* 69–72 (Springer, 1989).

341. Haim, S. E. *et al.* Spin Squeezing in Electron Microscopy. *arXiv preprint arXiv:2507.09243* (2025).

342. Tsarev, M. *et al.* Nonlinear-optical quantum control of free-electron matter waves. *Nat. Phys.* **19,** 1350–1354 (2023).

אופטיקה קוונטית של אלקטרונים חופשיים

חיבור על מחקר

לשם מילוי חלקי של הדרישות לקבלת התואר דוקטור לפילוסופיה

רון רוימי

מוגש לסנט הטכניון -- מכון טכנולוגי לישראל

אב תשפ"ו אוגוסט 2026 חיפה

המחקר נעשה בפקולטה להנדסת חשמל ומחשבים ע"ש ויטרבי, בהנחייתו של פרופ' עידו קמינר.

הצהרת אתיקה

החתום מטה מצהיר בזה כי המחקר, כולל איסוף, עיבוד והצגת הנתונים, ההתייחסות וההשוואה למחקרים קודמים וכיוצא בזה, נעשה כולו ביושר, כמצופה ממחקר מדעי המתנהל על פי הכללים המקובלים באקדמיה. כמו כן, הדיווח על המחקר ותוצאותיו בחיבור זה נעשה ביושר ובאופן שלם, על פי אותם הכללים.

תודות ותמיכה כספית

ברצוני להודות לקרן אדמס (ADAMS) ולטכניון על התמיכה הכספית הנדיבה שאפשרה מחקר זה.

תקציר

במשך למעלה ממאה שנה, האלקטרון החופשי הוביל מהפכות טכנולוגיות עמוקות, ובראשן פיתוח מיקרוסקופ האלקטרונים המהווה את אבן היסוד של המיקרוסקופיה המודרנית. באופן מסורתי, האלקטרון תואר כחלקיק קלאסי נקודתי או כגל-חומר פשוט בעל תכונות בסיסיות, ושימש בעיקר כמכשיר מדידה פאסיבי לצרכי הדמיה מבנית. עם זאת, השילוב החדשני שבין טכנולוגיית לייזרים אולטרה-מהירים לבין מיקרוסקופיה מתקדמת הוליד בשנים האחרונות את תחום המחקר של "אופטיקה קוונטית של אלקטרונים חופשיים". שינוי תפיסתי זה מקדם את האלקטרון החופשי ממעמד של צופה פסיבי למשאב קוונטי אקטיבי הניתן לשליטה מדויקת - ישות קוונטית מעופפת המסוגלת לשאת, לעבד ולהעביר מידע קוונטי ברזולוציה מרחבית אטומית וברזולוציה זמנית של תת-פיקו-שניות.

התקדמות זו נשענת רבות על היכולת החדשה לעצב את פונקציית הגל של האלקטרון במרחב ובזמן. פיתוחים במיקרוסקופיית אלקטרונים אולטרה-מהירה (UTEM) ובשיטות כמו Near-field (Photon-Induced PINEM Electron Microscopy) פתחו צוהר לחקר אינטראקציות חזקות בין אלקטרונים ושדות אופטיים. עבודת דוקטורט זו חוקרת את הגבולות התיאורטיים ואת הפוטנציאל הניסויי של תחום מתפתח זה, על ידי חקירה שיטתית של האינטראקציות הקוונטיות של אלקטרונים חופשיים עם אור, עם חומר, וזה עם זה. תוך שימוש במסגרת התיאורטית של אלקטרודינמיקה קוונטית מקרוסקופית (MQED) - המאפשרת לכמת ולתאר באופן מלא את הדינמיקה במערכות מורכבות - העבודה מבססת מתודולוגיות חדשות לרתימת חבילות גלי אלקטרונים מעוצבות קוהרנטית לטובת מטרולוגיה קוונטית מתקדמת, ספקטרוסקופיה של מערכות רבות-גופים, ועיבוד מידע קוונטי.

החלק הראשון של החיבור בוחן את האינטראקציה שבין אלקטרונים חופשיים למערכות קוונטיות קשורות (כגון אטומים או נקודות קוונטיות). העבודה מדגימה כי אלקטרונים חופשיים יכולים לפעול כגלאים אולטרה-מהירים לשם קריאה וכתיבה של מידע קוונטי על גבי קיוביטים (qubits) בקנה מידה אטומי, ובכך לבצע למעשה פעולות לוגיות קוונטיות. בהרחבת אינטראקציה זו לצברים (ensembles) מקרוסקופיים, מוצגת מסגרת ספקטרוסקופית חדשנית המאפשרת לאלקטרון בודד החולף בסמוך לדוגמה למדוד בו-זמנית דינמיקה מורכבת של מערכות רבות-גופים. בפרט, מודגם כיצד ניתן למדוד תופעות כמו פליטה קו-אופרטיבית סופר-רדיאנטית (Superradiant EELS) - תופעות שנותרו עד כה בלתי נגישות לגלאים אופטיים קונבנציונליים בשל מגבלות עקיפה מובנות. יכולת זו מספקת תובנות קריטיות על קוהרנטיות ודעיכה קולקטיבית.

בחלקה השני, העבודה חוקרת לעומק את האינטרקציה הקוהרנטית שבין אלקטרונים חופשיים לשדות אלקטרומגנטיים מְקוֻנָתִים. המחקר מראה כי אלקטרונים חופשיים יכולים לשמש ככלים דטרמיניסטיים ליצירה ושליטה של מצבי אור מורכבים ולא-קלאסיים, כולל אותם מצבים הנדרשים לתיקון שגיאות קוונטי במשתנים רציפים (CV) ,(QEC דוגמת מצבי GKP (Gottesman-Kitaev-Preskill) ומצבי חתול שרדינגר. יתרה מזאת, על ידי ניצול הקוהרנטיות הקוונטית האורכית של האלקטרון, אנו מפתחים טכניקות אינטרפרומטריה מתקדמות לאלקטרונים חופשיים. שיטות אינטרפרומטריות אלו מגבירות באופן קוהרנטי את האינטראקציה של האלקטרון עם שדות אופטיים קרובים חלשים במיוחד, ובכך משפרות באופן דרמטי את הרגישות והניגודיות של דימות אולטרה-מהיר, ללא שום צורך בלייזרי שאיבה עוצמתיים והרסניים.

לבסוף, החיבור מתמודד עם אחד האתגרים היסודיים ביותר בתחום: יצירת שזירה (Entanglement) רב-אלקטרונית איתנה. בעוד שדחייה קולונית Coulomb) (repulsion טבעית בין אלקטרונים בחלל החופשי מניבה לרוב קורלציות קלאסיות בלבד, עבודה זו מציעה שינוי פרדיגמה העושה שימוש בסביבות ננו-פוטוניות מהונדסות. אנו מראים כיצד שימוש באינטראקציות מתווכות-חלל Cavity-mediated) (interactions - באמצעות חילוף של פוטונים וירטואליים - מאפשר להתגבר על מגבלות אלו, ומדגימים כיצד ניתן לייצר שזירה חזקה, נקייה וניתנת לשליטה בין אלקטרונים נפרדים. הישג זה פותח דלת לחקר מצבים שזורים מקרוסקופיים של חלקיקים מסיביים.

העמקת ההבנה של שזירה רב-אלקטרונית אף סוללת דרך לבחינת מודלים תיאורטיים בסיסיים כגון תיאוריות קריסה אובייקטיבית Objective) collapse) הנובעות ממורכבות קוונטית מתהווה. ניתוח דקדקני של משוואות המאסטר ומנגנוני הדיפוזיה - תוך הבחנה מדויקת ומהותית בין מצבים תואמים matching) (states

לאלו שאינם - מאפשר לנו להציע פרוטוקולים חדשים לשמירה על הקוהרנטיות הנדרשת למצבי מולטי-קיוביט דוגמת מצבי GHZ (Greenberger-Horne-Zeilinger) במרחב החופשי. מערכות אלו עשויות להוות פלטפורמה לא רק למטרולוגיה עדינה אלא גם כבסיס עתידי ליישום אלגוריתמים קוונטיים מורכבים (כגון אלו של שור או גרובר) בתצורות של אינפורמציה קוונטית רציפה. לסיכום, המשוואות, המסגרות התיאורטיות וטכניקות האבחון שפותחו בחיבור זה מדגישות את הפוטנציאל העצום של האלקטרון החופשי, מניחות את התשתית לדור הבא של מיקרוסקופיית אלקטרונים משופרת-קוונטית, ומבססות את מעמדו כמעבדה קוונטית רב-תכליתית לחקר יסודות מכניקת הקוונטים.